This electronic thesis or dissertation has been downloaded from the King's Research Portal at https://kclpure.kcl.ac.uk/portal/

Improving Data Quality for Functional Magnetic Resonance Imaging

Wastling, Stephen James

Awarding institution:
King's College London

The copyright of this thesis rests with the author and no quotation from it or information derived from it may be published without proper acknowledgement.

END USER LICENCE AGREEMENT

Unless another licence is stated on the immediately following page this work is licensed

under a Creative Commons Attribution-NonCommercial-NoDerivatives 4.0 International

licence. https://creativecommons.org/licenses/by-nc-nd/4.0/

You are free to copy, distribute and transmit the work

Under the following conditions:

- Attribution: You must attribute the work in the manner specified by the author (but not in any way that suggests that they endorse you or your use of the work).
- Non Commercial: You may not use this work for commercial purposes.
- No Derivative Works - You may not alter, transform, or build upon this work.

Any of these conditions can be waived if you receive permission from the author. Your fair dealings and other rights are in no way affected by the above.

Take down policy

If you believe that this document breaches copyright please contact librarypure@kcl.ac.uk providing details, and we will remove access to the work immediately and investigate your claim.

Download date: 25. Dec. 2024

Institute of Psychiatry
at The Maudsley

KING'S College LONDON

Improving Data Quality for Functional Magnetic Resonance Imaging

Stephen James Wastling

A thesis submitted for the degree of
Doctor of Philosophy
for
King's College London

January 2013

Supervisors:
Professor Gareth J. Barker
Professor Steven C. R. Williams

Abstract

Functional magnetic resonance imaging (FMRI) is a non-invasive technique used to produce maps of brain activation based on the blood oxygen level dependent (BOLD) contrast. It is widely used in neuroscience research and, to a more limited extent, clinically for neurosurgical planning. A stimulus or task is conventionally used to evoke brain activity; however, functional connections in the brain can also be determined from correlations in the fluctuations of the BOLD signal observed in the absence of any external stimuli (resting-state FMRI).

Gradient-echo echo-planar imaging (GE-EPI) is the most common technique for acquiring FMRI data because of its sensitivity to the BOLD signal changes and relatively high temporal resolution. GE-EPI images are however affected by signal dropout caused by magnetic field gradients arising from the differences in the magnetic susceptibilities of materials in the head. This hampers the detection of BOLD signal changes in areas of the brain close to air-bone interfaces such as the orbitofrontal and inferior temporal regions.

Theoretical calculations and numerical simulations were performed to determine the degree of signal recovery needed to detect task-evoked and resting-state BOLD signal changes in such areas of signal dropout. Three different approaches to reducing signal dropout in GE-EPI images were then explored. The first two, z-shimming optimised to recover signal in grey matter and hyperbolic secant (HS) radiofrequency pulses aimed to reduce the dropout caused by *through-plane* susceptibility gradients. The third, using a combination of the HS pulse with compensatory gradients in the frequency encoding direction, aimed to further reduce the dropout correcting for *in-plane* susceptibility gradients. The impact of all three techniques on the ability to detect task-evoked and resting-state BOLD signal changes was investigated in a group of six healthy volunteers.

The copyright of this thesis rests with the author and no quotation from it or information derived from it may be published without proper acknowledgement.

Acknowledgements

I would like to thank my supervisors Gareth Barker and Steve Williams for giving me the opportunity to study for a Ph.D. and for all the support they have given me throughout. Gareth's close supervision, encouragement and willingness to devote large amounts of time to help me, kept the project on course. In the latter stages, his near endless supply of chocolate was invaluable! I am grateful to Dave Lythgoe and Simon Meara for supplying me with the source code for the z-shimming and DIR-EPI pulse sequences. I am also grateful to Ruth O'Gorman and Geoff Charles-Edwards who, in my previous job as a clinical scientist in the NHS, taught me so much about MRI. Joan Chick, and Catherine Morgan, with whom I shared an office in my first year, were also excellent sources of MRI knowledge as well as being wise guides in how to complete a Ph.D. My work has also benefited from discussions with Dave Lythgoe, Fernando Zelaya and Jonathan Ashmore. Without the hard work of Chris Webb and Rodney Lewis, who maintain the image processing network in the department, as well as Dave Gasston, Chris Andrew and Jeff Dalton who developed and maintain the infrastructure needed to perform functional MRI experiments, this project would have taken much longer, and been much harder to complete. I would also to thank all the volunteers who gave up their valuable time to be scanned for the experiments in this thesis.

These last three years at the CNS would have been much less fun without the many afternoon coffee breaks with Bill, Dave, Orla and Vincent; the cycle rides with Fernando, Dave, Duncan and Adam and the trips to the swimming pool with Matt, Gareth and Toby. I do not think I would have persevered without the wise encouragement and support of friends, my parents, my sister Sally and my wonderful girlfriend Alice. They have all been brilliant. It would be remiss of me not to also mention Clive Richards, my physics teacher in the sixth form, who inspired me to pursue a career in research.

My research was funded by both the Ginny Ng and King's Continuation Scholarships; I am extremely grateful for their financial support without which I would not have been able to complete this work.

Contents

List of Figures

List of Tables

Chapter 1

Introduction

Magnetic resonance imaging (MRI) [1, 2] is a widely used technique in medicine and scientific research because of its versatility and ability to non-invasively image both the structure and function of different tissues within the body. Of particular interest in this thesis are the maps of brain activation, based on the blood oxygen level dependent (BOLD) contrast [3–5], produced using functional magnetic resonance imaging (FMRI) [6–8]. Since its inception in the early 1990s, FMRI has been used extensively in neuroscience research to further expand our knowledge of the brain [9, 10]. It is also used clinically in the planning of surgery to remove tumours [11]. In the more traditional task-based FMRI experiments a stimulus or task is used to evoke a brain response [6–8]. Alternatively, in resting-state FMRI, correlations in the fluctuations of the BOLD signal, observed in the absence of any external stimuli, can be used to map functional connections in the brain [12, 13].

The technique most frequently used to acquire FMRI data is gradient-echo echo-planar imaging (GE-EPI) [14–16] because it is sensitive to the BOLD signal changes associated with brain activity and it has a relatively high temporal resolution [17]. Unfortunately, some areas of GE-EPI images are affected by signal dropout which severely reduces the detectability of BOLD signal changes [18]. The dropout is caused by signal dephasing, which results from localised magnetic field gradients that are induced by the differences in the magnetic susceptibilities of materials in the head. It is most severe in areas of the brain close to air-bone interfaces such as the orbitofrontal cortex (OFC), located superiorly to the sphenoid and ethmoid sinuses, and the inferior temporal lobes (ITL), located superiorly to the mastoid cells and ear canals [19]. The reduction in the detectability of BOLD signal changes in the orbitofrontal cortex and inferior temporal regions means that FMRI data acquired with GE-EPI cannot be used to effectively map the specific functions of these areas nor their functional connections with other regions of the brain. Alternative approaches including positron emission tomography (PET), lesion studies in humans and invasive experiments in monkey have shown the involvement of the OFC

in olfaction [20, 21], the representation of the reward of different stimuli [22, 23] and the processing of emotional facial expressions [24, 25]. The ITL has been shown to be involved in language processing [26]. Each of these have disadvantages however, and it would be ideal to be able to apply the same FMRI based approaches as in other brain regions.

As summarised in Chapter 2, an array of different techniques has been developed to reduce the signal dropout in GE-EPI images all of which have advantages and disadvantages. The aim of this thesis was to build on this work; investigating both the theoretical and practical implications of their implementation with the overall aim of devising a technique able to increase sensitivity to BOLD signal changes in the orbitofrontal and inferior temporal regions whilst retaining sensitivity in other parts of the brain.

1.1 Thesis Overview

An overview of MRI, with a focus on the techniques and concepts relevant to functional MRI is presented in Chapter 2. In Chapter 3 functional MRI is described in greater detail; included here is a discussion of both task and resting-state FMRI, as well a description of the methods commonly used to analyse both of these types of FMRI data.

In Chapter 4 the impact of signal dropout on the potential detectability of task induced brain activations, from FMRI data, is investigated using both a theoretical model and numerical simulations. Further numerical simulations are performed to determine how signal dropouts are likely to impact on the detectability of networks of resting-state brain activity.

Chapter 5 describes the development of a z-shimming technique [27] to recover signal in the inferior temporal lobes and orbitofrontal cortex. Based on the acquisition of two images with different compensatory gradients in the slice-selection direction, the method aims to recover signal in grey matter in the regions of signal dropout, whilst maintaining signal in grey matter elsewhere. The optimal difference between the two z-shim gradients is found using numerical simulations of the Bloch equations. The optimal pair of slice specific z-shim gradients is determined on the scanner using the data acquired in a calibration scan and a grey matter mask produced using a double-inversion recovery echo-planar imaging acquisition. The impact of 2-step grey matter optimised z-shimming on the ability to detect task-induced and resting-state BOLD signal changes is then assessed in a group of six healthy male volunteers. A pair of FMRI experiments, acquired using conventional GE-EPI and the z-shimming technique, while the subjects are at rest is used to measure the changes in the temporal signal to noise ratio, as well assess the changes

in the detectability of well-known resting state networks when z-shimming is used. FMRI experiments acquired when the subjects are performing a motor task are used to measure the changes in detectability of task induced BOLD signal changes. Finally the changes in BOLD sensitivity across all grey matter voxels is assessed using FMRI data acquired as the subjects perform a breath-hold task [28, 29].

Chapter 6 presents the development of a hyperbolic secant radiofrequency pulse, designed to reduce signal dropout caused by through-plane susceptibility gradients [30]. A systematic approach to determine the pulse parameters required to recover signal for a given slice thickness and echo time is presented. The impact of the new RF pulse is assessed in the same group of healthy volunteers with the same battery of tests as in the previous chapter.

In Chapter 7, a series of experiments are presented to show the effect of combining the optimised hyperbolic secant pulse with compensation of susceptibility gradients in the phase and frequency encoding directions [28, 29]. The best combination of the two is found along the optimal slice angle to maximise signal recovery in the regions affected by dropout. The impact of the chosen combination is assessed in the same group of healthy volunteers and with the same battery of tests as in the previous two chapters.

The main results and conclusions of the previous four chapters are drawn together in Chapter 8, to highlight both the contributions to the field and those areas which would merit further study.

1.2 Ethical Approval

The assessment of the efficacy of the novel acquisition methods, developed in this thesis, by scanning healthy volunteers, is covered by the ethical approval "Development of Magnetic Resonance Imaging and Spectroscopy Methods" (Study reference: 04/Q0706/72 approved by the London – Camberwell St Giles NRES Committee, formerly known as the Joint South London and Maudsley and the Institute of Psychiatry Research Ethics Committee).

All the work presented in this thesis was completed by me; I am grateful to David Lythgoe and Simon Meara for providing the source code for z-shimming and double inversion-recovery echo-planar imaging pulse sequences which I updated and used in several experiments in this thesis.

Chapter 2

Magnetic Resonance Imaging

2.1 Introduction

The discovery of Nuclear Magnetic Resonance (NMR), as first described by Bloch [31] and Purcell et al. [32], followed from the experimental observations of electron spin by Gerlach and Stern [33] along with measurements of the proton's magnetic moment by Rabi et al. [34] and the theoretical description of spin arising from Dirac's equation of relativistic quantum mechanics [35, 36]. It was on these foundations that initially Damadian [37] and then more fully Lauterbur [1] and Mansfield and Grannell [2] developed the technique of Magnetic Resonance Imaging (MRI) which is now so widely exploited in medicine.

2.2 Nuclear Magnetic Resonance

Nuclear magnetic resonance is observed in nuclei with a non-zero spin angular momentum. Due to its abundance in the human body the most commonly encountered nucleus in MRI is ^{1}H although applications utilising ^{13}C,^{19}F and ^{31}P are also seen in research and clinical practice. Associated with their spin angular momentum these nuclei also have a magnetic dipole moment. In a static magnetic field these dipole moments have a discrete set of spin eigenstates that are populated according to the Boltzmann distribution. The result is a net magnetisation parallel to the applied field which can be manipulated by means of radiofrequency (RF) pulses applied perpendicular to the static field at the Larmour frequency. A measurable RF signal results when the net magnetisation is rotated into the transverse plane by the application of an RF pulse. Following this irradiation the spins return to their equilibrium state via both transverse and longitudinal relaxation mechanisms.

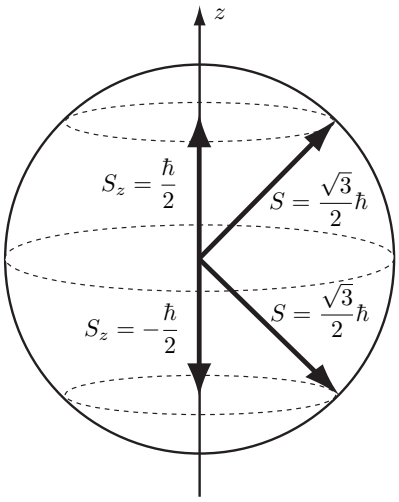

Figure 2.1: The spin-up and spin-down states of a proton

2.2.1 Spin

In addition to mass and charge, protons have a further fundamental property; spin angular momentum, $\boldsymbol{S}$, and associated with this a spin magnetic moment, $\boldsymbol{\mu}$. These two quantities are related by:

$$\boldsymbol{\mu} = \gamma \boldsymbol{S} \tag{2.1}$$

Where γ is the gyromagnetic ratio. For protons $\gamma = \frac{g_p e}{2m_p} = 2.675 \times 10^8$ rad s^{-1}T^{-1} where g_p is the proton g-factor, e is the electronic charge and m_p is the proton mass.

Protons are spin-1/2 particles; as such the magnitude of their spin angular momentum $S = \hbar\sqrt{3/2}$ and the z-component of the spin angular momentum has two eigenstates $m_s = \pm 1/2$. These two states are commonly referred to as spin-up ($\uparrow$) and spin-down ($\downarrow$); they are shown schematically in Figure 2.1.

2.2.2 Nuclear Zeeman Splitting

In the absence of an external magnetic field the spin-up and spin-down states of the proton have the same energy. However, in an external magnetic field with magnitude B_0 directed along the z-axis, the energy levels of the spin-up and spin-down states split. The spin-up state, in which the z-component of the spin angular momentum is aligned with the external field has a lower energy $E_\uparrow = -\frac{1}{2}\gamma\hbar B_0$, and the spin-down state has a higher energy $E_\downarrow = \frac{1}{2}\gamma\hbar B_0$, this effect is shown in Figure 2.2. The energy difference between the two eigenstates is $\Delta E = \gamma\hbar B_0 = \hbar\omega_0$. Therefore the frequency of radiation required to stimulate transitions between the spin-up and spin-down states is the Larmor frequency $\omega_0 = \gamma B_0$.

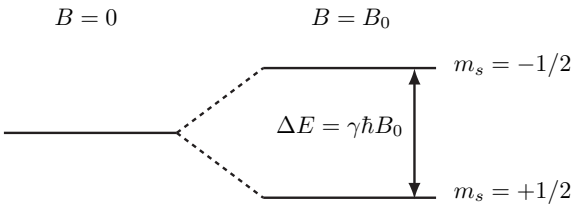

Figure 2.2: Nuclear Zeeman splitting of the spin energy levels in an external magnetic field

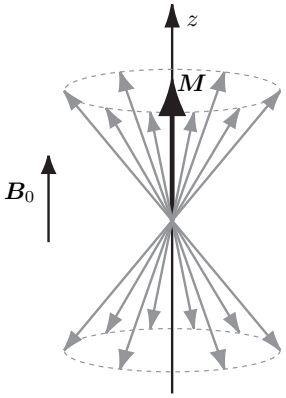

Figure 2.3: The net magnetisation resulting from the vector sum of the individual spin magnetic moments

2.2.3 The Boltzmann Distribution and the Net Magnetisation

In an NMR experiment, it is the effect of the net magnetisation, rather than that of single spins, that is measured. The z-component of the net magnetisation M_z of a group of proton spins is proportional to the population difference $(n_\uparrow - n_\downarrow)$ between the spin-up and spin-down states:

$$M_z = \frac{\gamma\hbar}{2}(n_\uparrow - n_\downarrow) \tag{2.2}$$

The formation of the net magnetisation from the vector sum of the spin magnetic moments is shown schematically in Figure 2.3. The populations of each state are given by the Boltzmann distribution, therefore at equilibrium the z-component of the bulk magnetisation, $M_{z,0}$ is:

$$M_{z,0} = N\frac{\hbar^2\gamma^2 B_0}{4k_B T} \tag{2.3}$$

Where N is the total number of spins $(n_\downarrow + n_\uparrow)$, k_B is the Boltzmann constant and T is the temperature of the system. The greater the magnetic field strength and the lower the temperature the greater the net magnetisation of the sample.

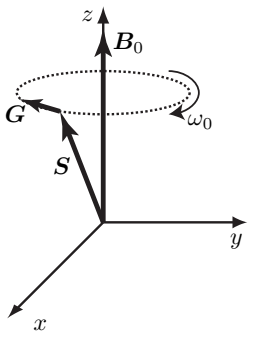

Figure 2.4: Schematic showing the torque $\boldsymbol{G}$ exerted on the spin angular momentum $\boldsymbol{S}$ by the external magnetic field $\boldsymbol{B}$ causing precession

2.2.4 Larmor Precession

As shown in Figure 2.4 the spin angular momentum $\boldsymbol{S}$ and magnetic moment $\boldsymbol{\mu}$ precess about the applied magnetic field at the Larmor frequency. This precession occurs because the the magnetic field $\boldsymbol{B}$ exerts a torque $\boldsymbol{G}$ on the spin magnetic moment $\boldsymbol{\mu}$, causing a change in the spin angular momentum $\mathrm{d}\boldsymbol{S}/\mathrm{d}t$ that is perpendicular to $\boldsymbol{B}$ and $\boldsymbol{S}$. For a bulk sample of non-interacting protons the net magnetisation $\boldsymbol{M}$ precesses about the applied field in the same manner:

$$\frac{\mathrm{d}\boldsymbol{M}}{\mathrm{d}t} = \gamma \boldsymbol{M} \times \boldsymbol{B} \tag{2.4}$$

2.2.5 Excitation and the Rotating Frame of Reference

The direction of the net magnetisation can manipulated using radio-frequency (RF) pulses at the Larmor frequency. The combined effects of the static $\boldsymbol{B}_0$ and RF magnetic fields $\boldsymbol{B}_1$ on the net magnetisation can be greatly simplified by transforming from the laboratory frame of reference $(\hat{\boldsymbol{x}}, \hat{\boldsymbol{y}}, \hat{\boldsymbol{z}})$ to a frame of reference $(\hat{\boldsymbol{x}}', \hat{\boldsymbol{y}}', \hat{\boldsymbol{z}})$ rotating about the z-axis, $\boldsymbol{\Omega} = -\omega\hat{\boldsymbol{z}}$ [38]. In a frame rotating at the Larmor frequency, the net magnetisation $\boldsymbol{M}$ is stationary and the effect of an RF pulse with a frequency ω_0 applied along $\hat{\boldsymbol{x}}'$ on the net magnetisation is simply a rotation about the $\hat{\boldsymbol{x}}'$-axis. The angle of rotation, or flip angle, is given by the area under the RF pulse envelope:

$$\theta = \gamma \int_0^t B_1(t')\mathrm{d}t' \tag{2.5}$$

This linear relationship between $B_1(t)$ and θ only holds if either the excitation is on resonance or for small flip angles ($\theta < 90°$) [39]. The behaviour of the net magnetisation during a 90° RF pulse as viewed from the laboratory and rotating frames is shown in Figure 2.5.

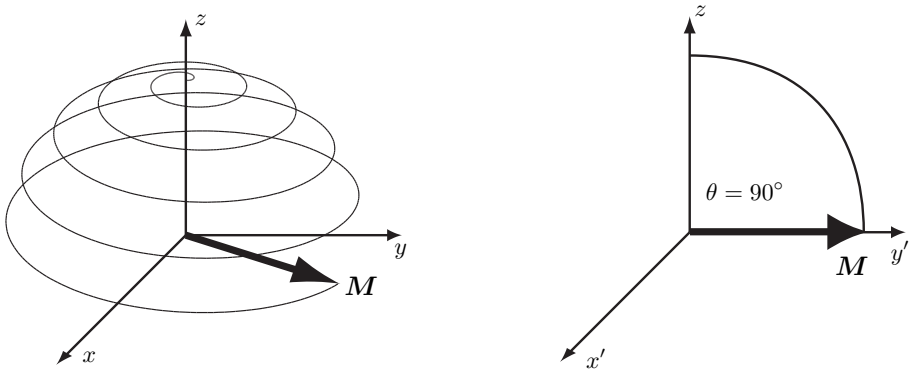

(a) Laboratory frame (b) Rotating frame

Figure 2.5: Behaviour of the net magnetisation during a 90° RF pulse as viewed from the laboratory and rotating frames

2.2.6 Signal Detection

In the laboratory frame, following an RF pulse that tips the net magnetisation vector away from the direction of $\boldsymbol{B}_0$, the net magnetisation has a transverse component that precesses around the static magnetic field. This can then be detected using a wire coil whose axis is perpendicular to $\boldsymbol{B}_0$. The electromotive force $\mathcal{E}$ induced in the coil by the rotating magnetic flux is given by Faraday's law:

$$\mathcal{E} = -\frac{\mathrm{d}\Phi}{\mathrm{d}t} \tag{2.6}$$

Where $\Phi = \int \mathrm{d}\boldsymbol{S} \cdot \boldsymbol{B}$ is the magnetic flux. In the case of NMR, $\mathcal{E}$ is given by:

$$\mathcal{E} = -\frac{\mathrm{d}}{\mathrm{d}t} \int_{sample} \mathrm{d}^3\boldsymbol{r}\boldsymbol{M}(\boldsymbol{r},t) \cdot \boldsymbol{B}_c(\boldsymbol{r}) \tag{2.7}$$

where $\boldsymbol{M}(\boldsymbol{r},t)$ is the magnetisation of the sample and $\boldsymbol{B}_c(\boldsymbol{r})$ is the magnetic field per unit current that would be produced by the coil at $\boldsymbol{r}$ [40]. As shown in Figure 2.6 the precession of the magnetisation at the Larmor frequency leads to an induced voltage, or signal, in the coil that varies sinusoidally at ω_0 but which also decays away exponentially because of the effects of relaxation described below.

2.2.7 Relaxation

Following rotation of the magnetisation into the transverse plane, $\hat{\boldsymbol{x}}'$-$\hat{\boldsymbol{y}}'$, by a 90° RF pulse, Bloch [31] described two mechanisms by which the magnetisation returns to its equilibrium state, spin-lattice and spin-spin relaxation.

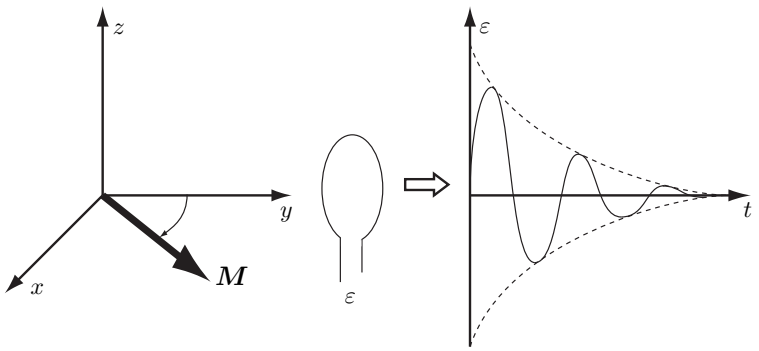

Figure 2.6: Schematic showing the detection of the free induction decay signal using a wire coil

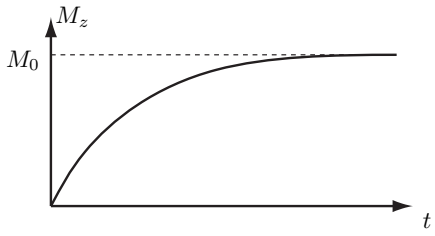

Figure 2.7: Behaviour of the longitudinal magnetisation following a 90° RF pulse

Spin-Lattice Relaxation

Spin-lattice relaxation is the process by which the longitudinal magnetisation M_z returns to equilibrium, by a loss of energy from the spins to the lattice, as spins in the higher energy state return to the lower energy state. T_1 is the characteristic decay time of the longitudinal relaxation given in the Bloch equation:

$$\frac{\mathrm{d}M_z}{\mathrm{d}t} = -\frac{1}{T_1}\left(M_z(t) - M_0\right) \tag{2.8}$$

Here M_0 is the equilibrium longitudinal magnetisation. The dependence of the longitudinal magnetisation on T_1, the time, t, and its initial value $M_z(0)$ is therefore given by:

$$M_z(t) = M_z(0)e^{-t/T_1} + M_0\left(1 - e^{-t/T_1}\right) \tag{2.9}$$

The behaviour of the longitudinal magnetisation following a 90° RF pulse is shown schematically in Figure 2.7.

Spin-Spin Relaxation

Spin-spin relaxation is the process by which the transverse magnetisation $\boldsymbol{M}_{xy} = M_x\hat{\boldsymbol{x}}' + M_y\hat{\boldsymbol{y}}'$ decays, T_2 is the characteristic decay time of the spin-spin relaxation

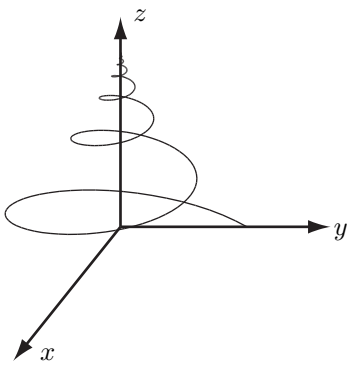

Figure 2.8: Return of the net magnetisation to equilibrium following a 90° RF pulse as viewed from the laboratory frame

process given in the Bloch equation:

$$\frac{\mathrm{d}\boldsymbol{M}_{xy}}{\mathrm{d}t} = -\frac{\boldsymbol{M}_{xy}}{T_2} \tag{2.10}$$

The dependence of the transverse magnetisation on T_2, the time, t, and its initial value $\boldsymbol{M}_{xy}(0)$ is therefore given by:

$$\boldsymbol{M}_{xy}(t) = \boldsymbol{M}_{xy}(0)e^{-t/T_2} \tag{2.11}$$

T_2 decay occurs because each spin experiences local magnetic field inhomogeneities resulting from the interactions with neighbouring spins. This leads to local variations in the spins' precession frequencies, therefore, over time, the spins dephase relative to one another, causing a decay of the net magnetisation. In addition to the intrinsic inhomogeneities arising from spin-spin interactions, extrinsic inhomogeneities in the static magnetic field lead to dephasing with a time constant T_2', the combined effect of the two decay processes is free induction decay with a time constant T_2^*. The relationship between T_2, T_2' and T_2^* is:

$$\frac{1}{T_2^*} = \frac{1}{T_2} + \frac{1}{T_2'} \tag{2.12}$$

Bloch incorporated the relaxation behaviour in Equations (2.8) and (2.10) into Equation (2.4) resulting in the phenomenological Bloch equation[31]:

$$\frac{\mathrm{d}\boldsymbol{M}}{\mathrm{d}t} = \gamma\boldsymbol{M} \times \boldsymbol{B} - \frac{(M_z - M_0)\,\hat{\boldsymbol{z}}}{T_1} - \frac{\boldsymbol{M}_{xy}}{T_2} \tag{2.13}$$

The combined effects of T_1 and T_2 decay on the magnetisation initially in the transverse plane, following a 90° RF pulse, is shown in Figure 2.8.

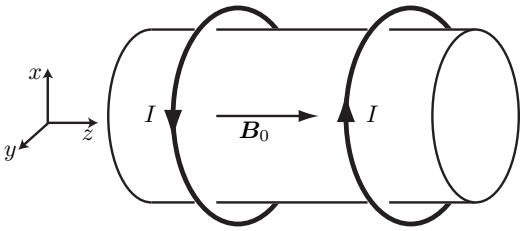

(a) Maxwell pair consisting of two coaxial coils with current I flowing in opposite directions used to generate a magnetic field gradient in the z-direction

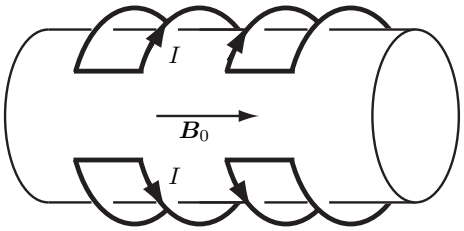

(b) Golay coil used to generate a magnetic field gradient in the x-direction

Figure 2.9: Schematic of the coils used to generate magnetic field gradients

2.3 Magnetic Resonance Imaging

2.3.1 Frequency Encoding and the Fourier Transform

The introduction of frequency encoding by Lauterbur [1] and Mansfield and Grannell [2] formed the basis of the Magnetic Resonance Imaging (MRI) technique, as it enabled the NMR signal to be spatially localised. It is possible to encode spatial information into the frequency of the NMR signal by applying a magnetic field gradient $\boldsymbol{G}$ across the object of interest. Here $\boldsymbol{G}$ is:

$$\boldsymbol{G} = \nabla \boldsymbol{B}_z = \left(\frac{\partial \boldsymbol{B}_z}{\partial x}, \frac{\partial \boldsymbol{B}_z}{\partial y}, \frac{\partial \boldsymbol{B}_z}{\partial z} \right) \tag{2.14}$$

The application of magnetic field gradients produces a linear variation in the static field $\boldsymbol{B}_0$ as a function of position $\boldsymbol{r}$:

$$\boldsymbol{B}_z(t) = \boldsymbol{B}_0 + \boldsymbol{G}(t) \cdot \boldsymbol{r} \tag{2.15}$$

In a typical superconducting magnet MRI system the z-axis gradients are generated using a Maxwell pair and the x-axis and y-axis gradients are generated using Golay coils, Figure 2.9.

Given that $\boldsymbol{\omega} = \gamma \boldsymbol{B}$, it can be seen from Equation 2.16 that the addition of a magnetic field gradient causes the proton precession frequency $\boldsymbol{\omega}(\boldsymbol{r}, t)$ to vary as a function of position $\boldsymbol{r}$.

$$\boldsymbol{\omega}(\boldsymbol{r}, t) = \gamma \left(\boldsymbol{B}_0 + \boldsymbol{G}(t) \cdot \boldsymbol{r} \right) \tag{2.16}$$

This linear dependence of NMR signal frequency on spatial position allows the spatial distribution of spins $\rho(\boldsymbol{r})$ to be extracted using a Fourier transform on the measured signal, s:

$$\rho(\boldsymbol{r}) = \int s(\boldsymbol{k}) e^{2\pi i \boldsymbol{k} \cdot \boldsymbol{r}} \mathrm{d}^3 \boldsymbol{k} \tag{2.17}$$

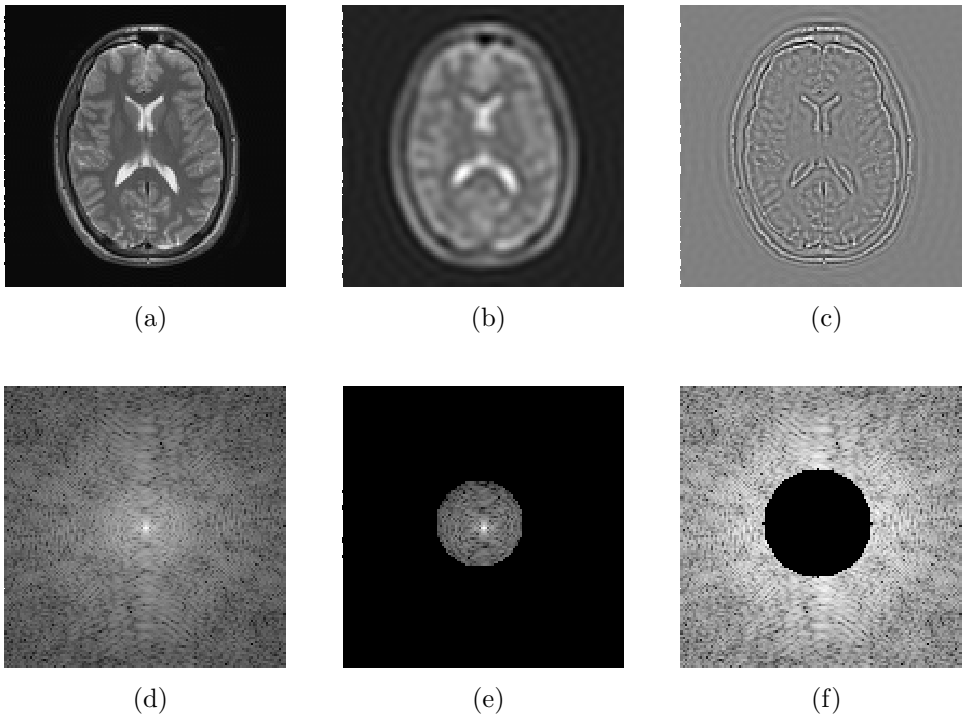

Figure 2.10: The real-space (a-c) and corresponding k-space (d-f) representations of an axial slice through the head of a healthy male volunteer showing the information contained within the inner and outer portions of k-space, that is, at low and high spatial frequencies

Here $\boldsymbol{k} = \frac{\gamma}{2\pi} \int_0^t \boldsymbol{G}(t')\mathrm{d}t'$ is the position in k-space at which the signal is measured.

2.3.2 k-space

To accurately reconstruct the spin density $\rho(\boldsymbol{r})$ using Equation 2.17 the NMR signal must be sampled from a sufficient number of points in k-space [41, 42]. This can be achieved by the combination of slice selection, frequency and phase encoding as described in the following section. As illustrated in Figure 2.10 k-space contains information about the spatial frequencies of an object. The central portion of k-space corresponding to low spatial frequencies encodes contrast information whereas the outer portions of k-space, corresponding to high spatial frequencies encode information about the edges of objects. The order of sampling is determined by the magnitude, direction and duration of the applied magnetic field gradients. The k-space trajectory resulting from the application of a bipolar gradient in the x-direction is shown as illustrative example in Figure 2.11.

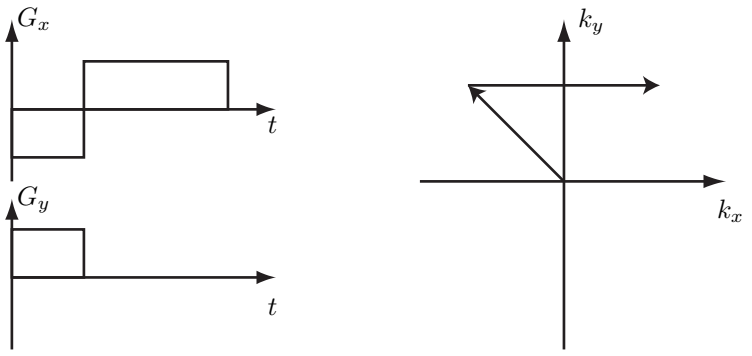

(a) A bipolar magnetic field gradient in the x-direction and a positive magnetic field gradient in the y-direction

(b) The k-space trajectory resulting from the gradients in (a)

Figure 2.11: The k-space trajectory resulting from magnetic field gradients in the x and y-directions

2.3.3 Multi-Slice Imaging

In multi-slice imaging the NMR signal is first restricted to a two-dimensional plane by slice-selection, localisation in the plane is then achieved by a combination of frequency and phase-encoding as described below.

Slice Selection

The NMR signal can be restricted to a two-dimensional plane or 'slice'; by applying a magnetic field gradient along, for example, the z-axis, such that the precession frequency of the protons varies linearly along the z-axis, as shown by Equation 2.16. An RF pulse is then applied with a frequency bandwidth $\Delta\omega$ such that only protons within the slice are excited. The slice thickness Δz and position z are given by Equations 2.18 and 2.19 respectively.

$$\Delta z = \frac{\Delta\omega}{\gamma G_z} \tag{2.18}$$

$$z = \frac{\omega_1 - \omega_0}{\gamma G_z} \tag{2.19}$$

where ω_1 is the RF carrier frequency. The linear relationship between position and frequency produced by the z-gradient means that to uniformly excite the spins in a rectangular slice the RF excitation pulse is top-hat shaped in the frequency domain. For small flip-angles ($\theta < 90°$) the slice profile is approximately equal to the inverse Fourier transform of the RF envelope [39, 43]. Therefore a sinc shaped RF envelope can be used to produce a rectangular slice profile, Figure 2.12. An infinitely long pulse would be required to produce a perfectly rectangular slice, therefore in practice

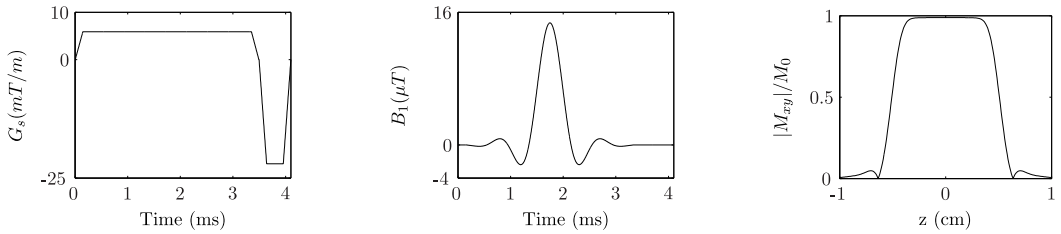

(a) Slice Selection Gradient (b) RF Pulse (c) Slice Profile

Figure 2.12: The slice profile for a 1 cm thick slice resulting from a 3.2 ms symmetric Hamming windowed sinc RF pulse, with a time-bandwidth product of 8 and a flip angle of 90°, applied in conjunction with a 5.87 mT/m slice-selection gradient (with maximum slew rate 150 $\mathrm{Tm^{-1}s^{-1}}$ and maximum gradient amplitude 22 $\mathrm{mTm^{-1}}$). The slice profile was calculated by numerically solving the Bloch equations in MATLAB (The MathWorks Inc., Natick, MA.) using code provided by Dr. Brian Hargreaves (www-mrsrl.stanford.edu/∼brian/blochsim)

either windowed sinc RF envelopes or RF pulses designed using the Shinnar-Le Roux (SLR) algorithm are used [44–49].

Frequency and Phase Encoding

Following slice selection, in-plane localisation is achieved using a combination of frequency and phase encoding of the NMR signal. Frequency encoding involves applying a gradient, along for example the x-axis, as the NMR signal is being acquired. The signal frequency then depends on the position of the object along the frequency encode axis. The signal is localized along the third spatial dimension by phase encoding where a gradient is applied in, for example, the y-direction, after slice selection but before the signal is read out [50].

Phase encoding is explained pictorially in Figure 2.13. Initially all the spins are in phase in the y-direction. A gradient G_y is then applied for a given duration, during which the spins experiencing a higher static field due to the gradient will precess at a higher frequency and accrue a positive phase shift relative to spins experiencing a reduced static field. When the phase encoding gradient is turned off the resonance frequencies of the spins return to the Larmor frequency, but the phase shift remains, hence the spatial position of the spins are encoded in their phase. The sequence is then repeated after the repetition time, TR, with a different phase encoding gradient, such that the signal from a different line of k-space is acquired.

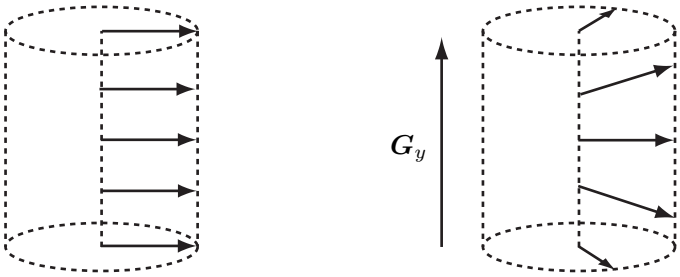

(a) Alignment of spins before the application of the phase encoding gradient

(b) The effect of phase encoding in the y-direction on spin's phase

Figure 2.13: A schematic diagram illustrating the effect of a phase encoding upon the distribution of spin phases

2.3.4 Gradient and Spin Echo Imaging

Direct measurement of the free induction decay (FID) signal is impractical as the signal readout cannot begin immediately following the signal excitation due to hardware limitations, therefore an echo of the FID is sampled. The production of gradient and spin echoes are described below:

The Gradient Echo

The mechanism by which a gradient echo is formed is outlined schematically in Figure 2.14. Initially the net magnetisation M_0 is in equilibrium along the z-axis, following a 90° pulse the net magnetisation M_0 is rotated into the transverse plane $\hat{\boldsymbol{x}}'$-$\hat{\boldsymbol{y}}'$. If a gradient with a negative polarity is applied the spins at different positions dephase relative to one another. If this gradient polarity is then reversed the spins rephase and a gradient echo is formed when $\int \boldsymbol{G}(t)\mathrm{d}t = 0$.

Two-Dimensional Gradient Echo Imaging

The pulse sequence timing diagram for a two-dimensional gradient echo imaging acquisition is shown in Figure 2.16(a). The 90° RF pulse is made slice selective by applying it in combination with a magnetic field gradient G_s. During the 90° RF pulse the slice selection gradient causes spin-dephasing across the slice, this is refocused by the negative lobe of the slice-select gradient [50]. The area A_R of the refocusing lobe is related to the slice select gradient amplitude, the pulse isodelay Δt_I and the gradient ramp duration t_r, Figure 2.15 [39]:

$$A_R = G_s \Delta t_I + \frac{G_s t_r}{2} \tag{2.20}$$

For conventional sinc excitation pulses $A_R \sim 0.5 G_s t_{rf}$, where t_{rf} is the duration of the RF pulse. The NMR signal is localised in-plane using frequency and phase

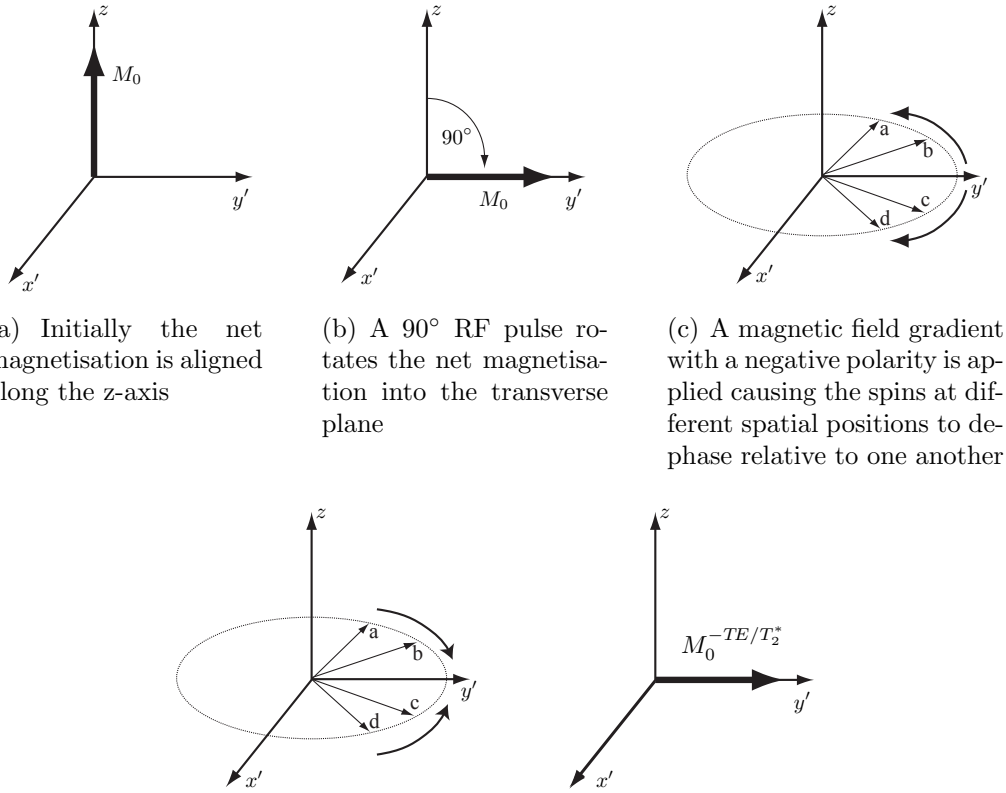

(a) Initially the net magnetisation is aligned along the z-axis

(b) A 90° RF pulse rotates the net magnetisation into the transverse plane

(c) A magnetic field gradient with a negative polarity is applied causing the spins at different spatial positions to dephase relative to one another

(d) Applying a magnetic field gradient with opposite polarity causes the spins to rephase

(e) A gradient echo forms when the overall time integral of the gradients equals zero

Figure 2.14: The formation of a gradient echo as viewed from the rotating frame. Adapted from Haacke et al. [51]

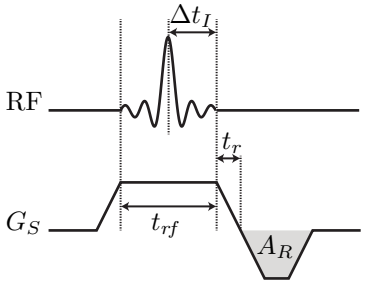

Figure 2.15: A schematic showing slice-select refocusing. Adapted from Bernstein et al. [39]

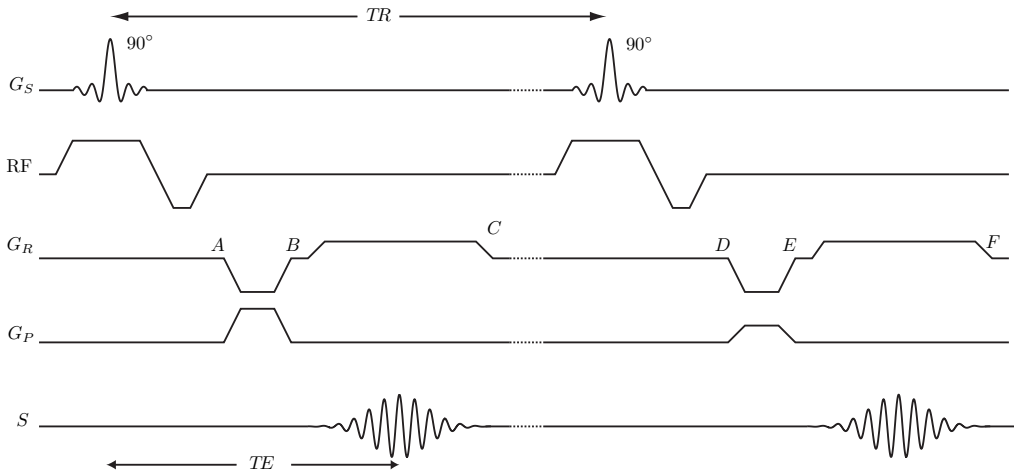

(a) Pulse sequence timing diagram showing two phase encoding steps

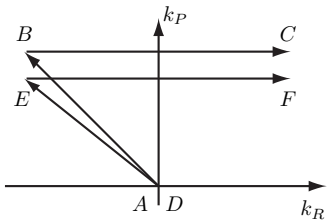

(b) k-space trajectory showing two phase encoding steps

Figure 2.16: Gradient echo pulse sequence timing diagram and k-space trajectory

encoding gradients as described in Section 2.3.3. The sequence is then repeated after the repetition time, TR, with a different phase encoding gradient, such that the signal from a different line of k-space is acquired. The time required to acquire the data for a 2D-slice is therefore:

$$T = TR \times N_{pe} \tag{2.21}$$

where N_{pe} is the number of phase encoding steps. The k-space trajectory for this sequence is shown in Figure 2.16(b). It should be noted that the effects of extrinsic magnetic field inhomogeneities are not refocused by the gradient echo and as such the image contrast will depend on T_2^* rather than T_2.

The Spin Echo

The spin, or RF echo [52], is formed by the application a 90° excitation pulse followed by a 180° refocusing pulse. The mechanism by which the echo is formed is outlined schematically in Figure 2.17. Prior to the 90° pulse the net magnetisation M_0 is in equilibrium along the z-axis. M_0 is rotated into the transverse plane $\hat{\boldsymbol{x}}'$-$\hat{\boldsymbol{y}}'$ whereupon the spins at different positions dephase relative to one another because they experience locally differing magnetic fields. After a time, τ, a 180° pulse is

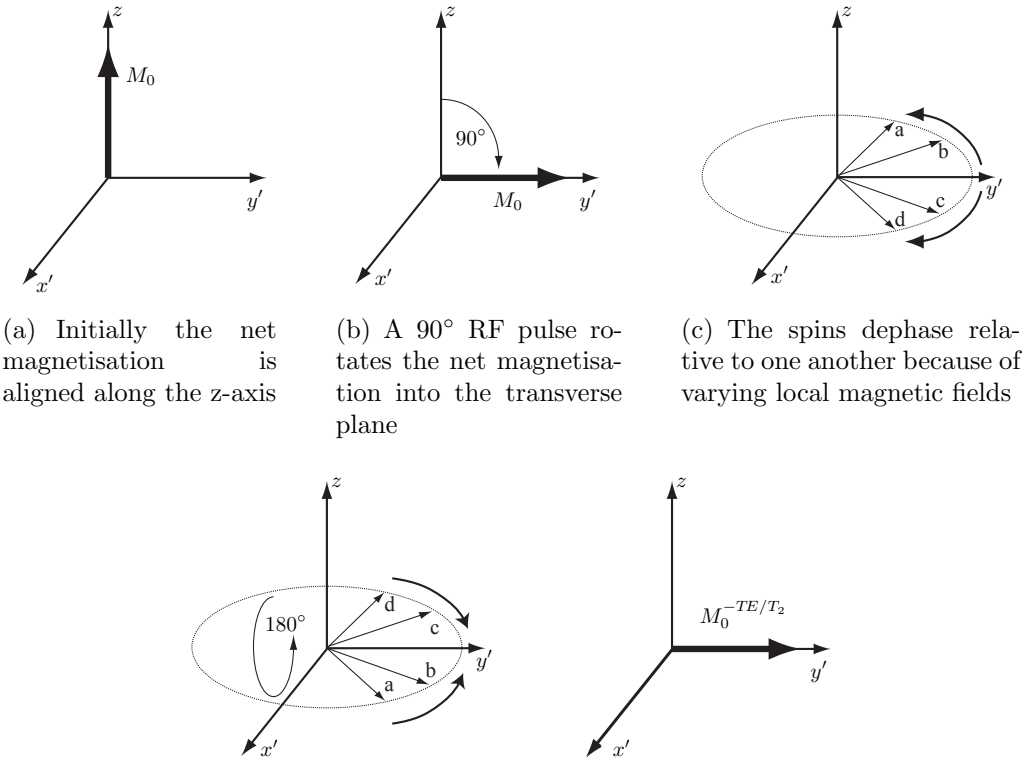

(a) Initially the net magnetisation is aligned along the z-axis

(b) A 90° RF pulse rotates the net magnetisation into the transverse plane

(c) The spins dephase relative to one another because of varying local magnetic fields

(d) Applying a 180° RF pulse about the $\hat{\boldsymbol{y}}'$-axis τ seconds after the 90° RF pulse causes the spins to rephase

(e) A spin echo forms at $t \equiv TE = 2\tau$

Figure 2.17: The formation of a spin echo as viewed from the rotating frame. Adapted from Haacke et al. [51]

applied about the $\hat{\boldsymbol{y}}'$-axis. This refocuses the dephasing due to extrinsic magnetic field inhomogeneities, and a spin echo is formed at $TE = 2\tau$. The refocusing of the dephasing due to extrinsic magnetic field inhomogeneities means that spin-echo pulse sequence can produce images T_2 contrast. The accumulated phase $\phi(\boldsymbol{r}, t) = 0$ when $t = 2\tau$ is independent of $\boldsymbol{r}$ and hence a spin-echo occurs.

Two-Dimensional Spin Echo Imaging

The pulse sequence timing diagram for a two-dimensional spin echo imaging acquisition is shown in Figure 2.18(a). The 90° and 180° RF pulses are made slice selective by applying them in combination with the G_s magnetic field gradient. The NMR signal is localised in plane using frequency and phase encoding gradients as described in Section 2.3.3. The sequence is then repeated after the repetition time, TR, with a different phase encoding gradient, such that the signal from a different line of k-space is acquired. The k-space trajectory for this sequence is shown in Figure 2.18(b). Typically the RF echo, produced by the combination of the 90° and 180° RF pulses and the gradient echo, produced by the bipolar readout gradi-

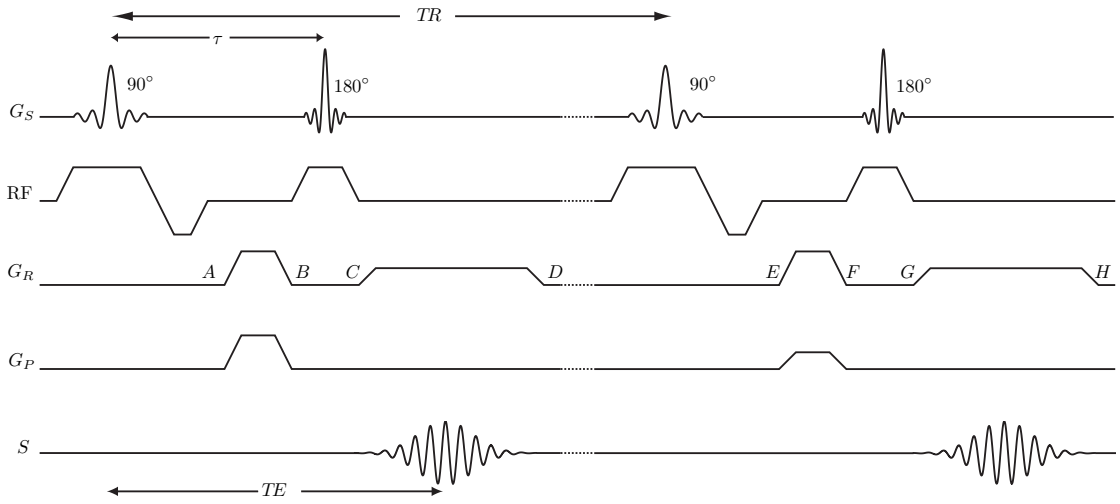

(a) Pulse sequence timing diagram showing two phase encoding steps

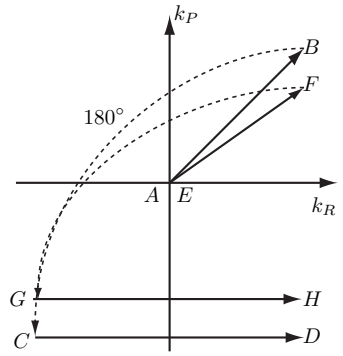

(b) k-space trajectory showing two phase encoding steps

Figure 2.18: Spin echo pulse sequence timing diagram and k-space trajectory

ent are chosen to occur simultaneously to minimise off-resonance effects. Though they are sometimes intentionally offset to sensitise the images to T_2^* and magnetic susceptibility effects [39].

2.3.5 Multi-slice Imaging

When imaging a 3D volume, such as the human head, data from multiple slices must be acquired. This can be achieved either using a sequential or interleaved acquisition. In a sequential acquisition all the k-space lines for each slice are acquired before beginning the data acquisition of the next slice. The time required to collect a 3D volumes consisting of N_{slice} slices is:

$$T = TR \times N_{pe} \times N_{slice} \tag{2.22}$$

In an interleaved acquisition data for a given k-space line are collected for each slice location before acquiring the data from the next k-space line. Interleaved

acquisitions are more time efficient because they allow multiple k-space lines to be acquired within a single TR [53] by taking advantage of the idle time during a TR in which neither gradients nor RF are active. To reduce slice cross-talk, which results from the interference of the signal of adjacent slices due imperfect slice profiles, the slice acquisition order in interleaved acquisitions is modified such that the data from adjacent slices is acquired further apart in time.

2.3.6 Image Contrast

The contrast C_{AB} between two tissues, A and B, in different voxels of an MR image is defined as the difference between their respective voxel signals S_A and S_B [51]:

$$C_{AB} \equiv S_A - S_B \tag{2.23}$$

In MRI it is possible to change this contrast because the voxel signal is dependent on both the imaging sequence parameters, such as the echo and repetition times and the flip angle, and the tissue parameters such as the proton density, and the T_1 and T_2 relaxation times. There are four commonly encountered contrasts: T_1-weighted which, as the name suggests, has a high contrast between tissues with different T_1 relaxation times, T_2-weighted which has large differences between tissues with different T_2 relaxation times, T_2^*-weighted that have large differences between regions with different T_2^* relaxation times and proton-density weighted that has large differences between tissues with different densities of protons.

2.4 Functional MRI Data Acquistion

In a comprehensive review article, Turner and Ordidge [17] outlined the technical requirements of an MRI sequence used to acquire functional MRI data. Firstly it must be sensitive to the variations in T_2^* caused by changes in deoxyhaemaglobin concentration in response to neuronal activity. Secondly it must be able to produce images with sufficient spatial resolution to allow these T_2^* changes to be localised to specific areas of the brain. Thirdly the sequence must be able to acquire images of the whole brain at a speed sufficient to capture the temporal variations in T_2^*. For these reasons gradient-echo echo-planar imaging (GE-EPI) [14–16] has become the most commonly used acquisition method in modern functional MRI studies, as it can acquire T_2^*-weighted images of the whole brain at a sufficient spatial resolution for FMRI in two seconds.

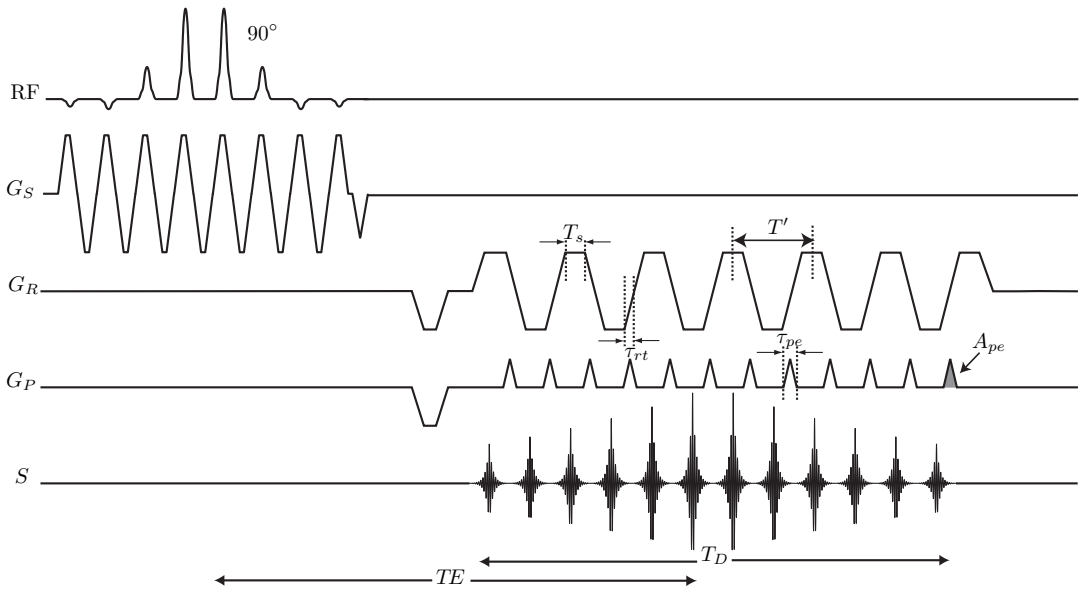

(a) Illustration of the pulse sequence timing diagram

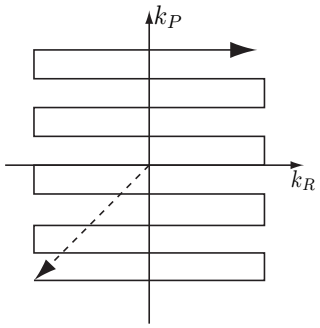

(b) k-space trajectory

Figure 2.19: Gradient echo EPI pulse sequence timing diagram and k-space trajectory [39, 51]

2.5 Gradient Echo EPI

The GE-EPI sequence is shown schematically in Figure 2.19(a) alongside its corresponding k-space trajectory in Figure 2.19(b). Following signal excitation, discussed below, an oscillating trapezoidal readout gradient is used to generate a series of echoes, under a gradient echo envelope, which have been individually phase encoded using a set of evenly spaced triangular shaped phase-encoding gradients of duration τ_{pe}. The T_2^* decay during signal readout means that each echo is acquired at a different TE; since the image contrast depends mostly on the central k-space line it is common to define the effective echo time $TE = TE(k = 0)$.

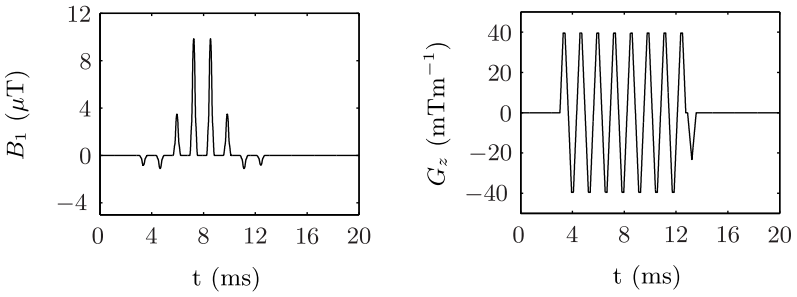

(a) RF Pulse (b) Slice-selection Gradient

Figure 2.20: SPSP RF pulse and gradient waveform captured from the 3T GE HDx scanner for an acquisition with a flip angle of 90° and a slice thickness of 2.4 mm

2.5.1 Signal Excitation

On the both the 3 T GE Discovery MR750 and GE Signa HDx systems (General Electric, Milwaukee, WI, USA) two different signal excitation approaches are available. Both of which attempt to minimise the chemical shift artefact, discussed in detail below, caused by lipid signals.

Spatial-Spectral (SPSP) RF Pulses

Spatial-Spectral (SPSP) RF pulses [54, 55] are, as their name suggests, selective both spatially and spectrally. As such they can be used to excite water protons in a specific spatial location whilst leaving fat protons unaffected. They are made up of a set of RF 'subpulses' in a broad RF envelope Figure 2.20. Their spatial selectivity is governed by the combination of the subpulses with an oscillating gradient and the RF envelope controls the spectral selectivity. The dependence of the signal as a function of spatial position and resonant frequency offset, determined by numerical simulation of the Bloch equations in MATLAB, is shown in Figure 2.22(a).

Fat Suppression and Water Excitation RF Pulses

Alternatively, a combination of a CHESS (Chemical Shift Selective) [56] pulse and an excitation pulse, designed using the SLR algorithm, can be used to excite water protons whilst suppressing the signal from lipids, Figure 2.21. For comparison with SPSP pulses the dependence of the signal as a function of spatial position and resonant frequency offset is shown in Figure 2.22(b). SPSP pulses are used by default on the GE scanners because they are shorter and less susceptible to B_1 inhomogeneities[39]

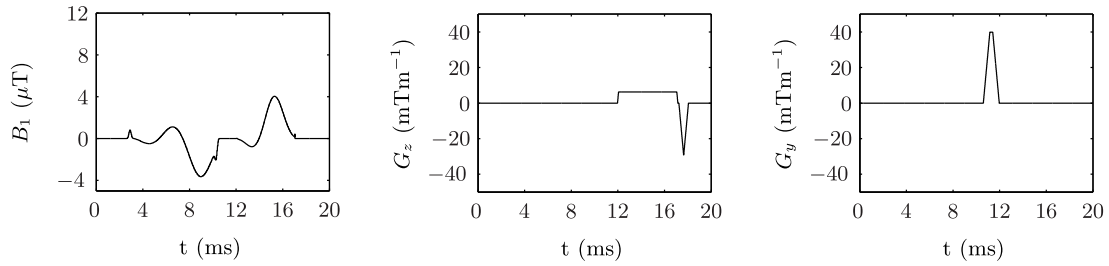

(a) CHESS and SLR RF Pulse (b) Slice-selection Gradient (c) Fat Crusher Gradient

Figure 2.21: CHESS and SLR pulses along with their accompanying gradient waveforms captured from the 3T GE HDx scanner for an acquisition with a flip angle of 90° and a slice thickness of 2.4 mm

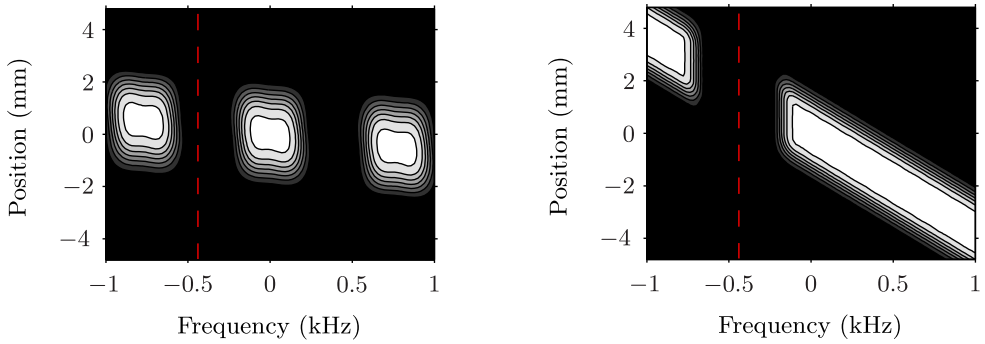

(a) SPSP Excitation Pulse

(b) Fat-sat: SLR Excitation Pulse Preceded by a Spectrally Selective Presaturation Pulse

Figure 2.22: Contour plots showing Bloch simulations of the spatial and spectral selectivity of SPSP and fat-sat pulses. Both techniques avoid exciting fat protons which have a resonant frequency offset of -440Hz (relative to water) at 3T

2.5.2 EPI Readout Gradients

The readout gradient begins with a prephasing lobe that is used to set the initial position of the k-space sampling in the readout direction. This is followed by a series of oscillating trapezoidal gradients, e.g. for a 64× 64 matrix there would be 32 positive and 32 negative read gradient lobes. In a straightforward implementation of the trapezoidal gradients the echo is sampled only in the periods of constant readout gradient for a time T_s. Sampling can be performed during the periods of gradient ramp-up and down [57] though the data must be re-gridded before reconstruction because the k-space samples no longer have a simple linear relationship with the signal in the time domain. During FMRI data acquisition on GE HDx and Discovery MR750 systems three additional read-gradient lobes, with no accompanying phase encoding precede the readout train. This internal referencing enables correction of phase differences caused by B_0 drifts over time.

2.5.3 EPI Phase Encoding Gradients

As for the readout gradients, the phase-encoding gradient begins with a prephasing lobe which sets the starting point of the k-space sampling in the phase-encoding direction. The blipped gradients, formed from a series of equally spaced triangular waveforms of the same polarity, then phase encode each echo.

2.5.4 Parallel Imaging

The combined use of EPI and parallel imaging has a threefold advantage in FMRI data acquisition [58]. Firstly it results in a reduction in signal drop-out and distortion artefacts in single-shot acquisitions, secondly it allows for an increase in the temporal or spatial resolution, and thirdly it reduces the acoustic noise caused by the gradient switching.

Parallel imaging uses phased array coils to increase the speed of acquisition. Given that, in Cartesian acquisition schemes, the scan time is linearly proportional to the number of phase encoding steps, scan time can be reduced by an acceleration factor R by increasing the distance between the phase-encoding lines in k-space, whilst maintaining the maximum k-values. Given the inverse relationship between the step size in k-space Δk and the field of view (FOV) in image space, Equation 2.24, such an increase reduces the FOV by R.

$$\Delta k = \frac{1}{FOV} \tag{2.24}$$

The FOV reduction would normally result in aliasing, Figure 2.23, but using the extra spatial information provided from the coil sensitivity profiles of the separate

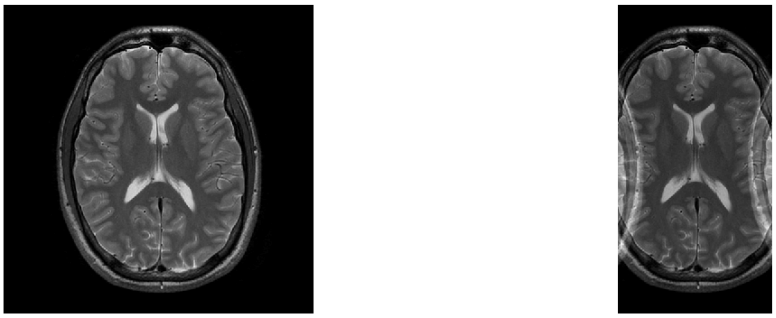

(a) Image reconstructed from full k-space

(b) Aliased image reconstructed from k-space that has been sub-sampled in the left-right direction

Figure 2.23: A demonstration of the image aliasing induced by sub-sampling k-space (only acquiring every other line) in the left-right direction. This aliasing can be unwrapped using the extra spatial information provided by the coil sensitivity profiles via the SENSE algorithm

elements of phased array coils un-aliased images can be reconstructed. On GE HDx and Discovery MR750 systems parallel imaging is implemented using ASSET, the manufacturer's implementation of sensitivity encoding, described below:

Sensitivity Encoding

Sensitivity encoding (SENSE) [59] is an image-space based technique, used to unwrap the aliased images that are produced when k-space is under-sampled. Firstly, aliased images from each coil element are reconstructed using the Discrete Fourier Transform (DFT), then, from these intermediate images a full FOV image is produced that is free from the aliasing that resulted from k-space sub-sampling. For a given pixel in the reduced FOV the signal is a superposition of the signal from that location and the signal from pixels at integer multiples of FOV/R in the phase-encoding direction. A vector $\boldsymbol{a}$, of length n_p, the number of pixels that are superimposed, is constructed from the values of the chosen pixel in the intermediate images. n_p can be calculated from the object size in the phase encoding direction determined from the coil sensitivity calibration images. If n_c coil elements are being used, an $n_c \times n_p$ sensitivity matrix $\boldsymbol{S}$ is used to store the information about the coil sensitivities at the n_p superimposed positions.

$$\boldsymbol{S}_{\gamma,p} = s_\gamma(\boldsymbol{r}_p) \tag{2.25}$$

Where s_γ is the sensitivity of coil γ and $\boldsymbol{r}_p$ is the position of pixel p. In the ASSET implementation of SENSE the sensitivity calibration is performed in a separate, low resolution, 2D fast gradient echo scan. Because the calibration scan is acquired at

a lower resolution the sensitivities at $\boldsymbol{r}_p$ are found by linear interpolation[60]. From the sensitivity matrix, and an $n_c \times n_c$ receiver noise matrix $\boldsymbol{\Psi}$, an unfolding matrix $\boldsymbol{U}$ is then constructed:

$$\boldsymbol{U} = (\boldsymbol{S}^{\dagger}\boldsymbol{\Psi}^{-1}\boldsymbol{S})^{-1}\boldsymbol{S}^{\dagger}\boldsymbol{\Psi}^{-1} \tag{2.26}$$

Here † represents the Hermitian conjugate. The diagonal elements of $\boldsymbol{\Psi}$ contain information about the noise variance from each coil and off diagonal elements the noise cross-correlation between two coils. This is then multiplied by $\boldsymbol{a}$ to produce a vector $\boldsymbol{v}$ that is a list, of length n_p, of the separated pixel values for the originally superimposed positions.

$$\boldsymbol{v} = \boldsymbol{U}\boldsymbol{a} \tag{2.27}$$

A full FOV images is produced by carrying out each of these steps for all of the pixels in the reduced field of view. The reduction in acquisition time is not achieved without cost, as the SNR is reduced by the following factors:

$$SNR_p^{\mathrm{SENSE}} = \frac{SNR_p^{full}}{g_p\sqrt{R}} \tag{2.28}$$

Here g_p is the local geometry factor:

$$g_p = \sqrt{[(\boldsymbol{S}^{\dagger}\boldsymbol{\Psi}^{-1}\boldsymbol{S})^{-1}]_{pp}(\boldsymbol{S}^{\dagger}\boldsymbol{\Psi}^{-1}\boldsymbol{S})_{pp}} \geq 1 \tag{2.29}$$

$(\boldsymbol{S}^{\dagger}\boldsymbol{\Psi}^{-1}\boldsymbol{S})_{pp}$ are the diagonal elements of the matrix $\boldsymbol{S}^{\dagger}\boldsymbol{\Psi}^{-1}\boldsymbol{S}$. g_p is dependent upon both n_p and the differences in coil sensitivity between the aliased pixels, which itself depends upon the orientations of the coil and scan plane as well as the phase encoding direction and pixel position, i.e. the greater the coil separation in the phase-encoding direction the lower the resulting noise magnification [39]. In the ASSET implementation of SENSE the matrix inversion $(\boldsymbol{S}^{\dagger}\boldsymbol{\Psi}^{-1}\boldsymbol{S})^{-1}$ is performed using LU decomposition with mild regularisation[61], which reduces the noise at the expense of some uncorrected aliasing.

2.6 GE-EPI Artifacts and Methods to Reduce their Impact

The advantages of GE-EPI over other sequences are not without cost, as the images may suffer from a range of artifacts. Much work has been done to ameliorate these problems, as outlined below, but as yet comprehensive solutions, fully compatible with the requirements of FMRI, are still to be found.

2.6.1 T_2^* Blurring

T_2^* blurring is observed in GE-EPI images because each line of k-space is acquired at a different time and hence has a different T_2^* weighting. This exponential decay causes image blurring in the phase-encoded direction as the data is effectively spatially filtered. This blurring effect is most obvious in objects with high-spatial frequencies since it is these that are affected to the largest extent by T_2^* decay during data acquisition. One way to reduce the blurring effect is to reduce the echo train length or inter-echo spacing such that, in the time over which data is acquired, T_2^* decay is not significant. This can be achieved, whilst maintaining k-space coverage, by switching to multi-shot EPI[39] or by employing parallel imaging[62], though this may result in reduced SNR and increased Nyquist ghosting.

2.6.2 Nyquist Ghosts

In single-shot EPI the reconstructed images contain 'Nyquist ghosts' that are shifted by half of the field of view in the phase encoding direction; these arise from phase inconsistencies between the odd and even lines of k-space, which were traversed in opposite directions. Phase differences result from B_0-field inhomogeneities, eddy currents, asymmetric anti-alias filter response, concomitant magnetic fields and receive chain and gradient amplifier group delays[39]. There are several different types of Nyquist ghost, as shown schematically in Figure 2.24, however the observed ghost is typically a mixture of those shown and other phase errors resulting from higher-order eddy currents and concomitant fields. On GE HDx and Discovery MR750 systems, Nyquist ghost artifacts are reduced by correcting the phase errors between the odd and even lines of k-space using the information acquired in a reference scan[63]. The reference scan consists of a single-shot EPI acquisition without any phase-encoding, such that any phase differences between the odd and even k-space lines are known to be artifactual in origin.

2.6.3 Off-Resonance Artifacts

There are a number of artifacts that arise from inhomogeneities in the static magnetic field; these include distortion and signal dropout associated with the slice selection, phase and frequency encoding processes, see Figure 2.25, in addition to the chemical shift artifact. B_0 inhomogeneities have a range of causes including imperfect scanner hardware and magnetic susceptibility variations in the object being scanned. For example in the human head artifacts are caused by differences in the magnetic susceptibilities of bone ($\chi_{bone} = -8.9 \times 10^{-6}$), soft tissue ($\chi_{water} = -9.05 \times 10^{-6}$) and air ($\chi_{air} = 0.36 \times 10^{-6}$) [65]. These differences pro-

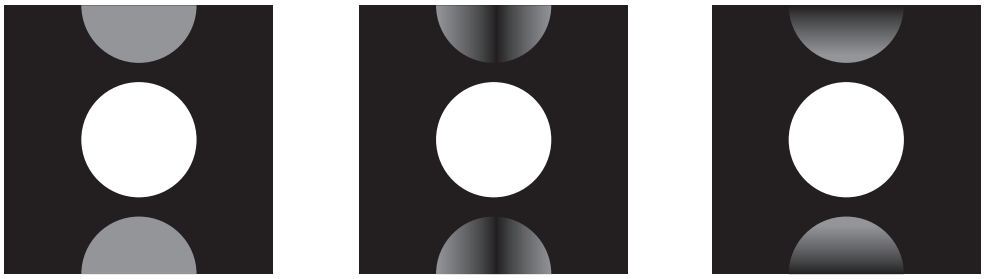

(a) Constant phase ghost (b) Linear phase ghost (c) Oblique ghost

Figure 2.24: Schematic EPI images of a spherical phantom (the readout direction is left to right in the images). A constant phase ghost results from a spatially-independent phase error that alternates between odd and even lines of k-space, typically caused by eddy currents. The linear phase ghost results from an alternate positive and negative shifting of the k-space lines in the readout direction $\pm\delta k_x$ for odd and even echoes, which can be caused by gradient group delays, gradient amplifier hysteresis and spatially linear eddy currents. An oblique ghost is due to an alternate positive and negative shifting of the k-space lines in the phase encode direction $\pm\delta k_y$ for odd and even echoes which can result from group delays among the physical gradient axes and cross-term eddy currents (figure adapted from Bernstein et al. [39]).

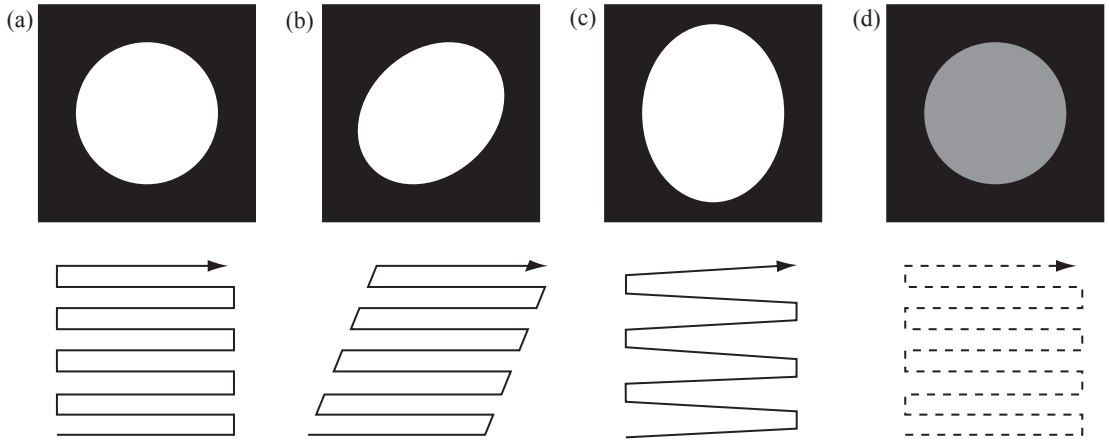

Figure 2.25: Schematic EPI images of a spherical phantom and their corresponding k-space trajectories in the case of (a) a homogeneous B_0 field (b) B_0 inhomogeneities in the readout direction causing image shearing, (c) B_0 inhomogeneities in the phase encoding direction causing image stretching and (d) B_0 inhomogeneities in the slice selection direction resulting in reduced image intensity as the excitation is off-resonance (figure adapted from Huettel et al. [64]).

duce locally varying magnetic field gradients, and hence inhomogeneities in the static magnetic field [18, 66, 67] especially in the orbitofrontal cortex and inferior temporal lobes.

Using the notation of Farzaneh et al. [68] it can be shown, see Appendix A, that the signal for the m^{th} readout point on the n^{th} phase encoding line measured during a GE-EPI acquisition of an object $\rho(x, y)$ is:

$$s_{nm} = \int_{\frac{-L_y}{2}}^{\frac{L_y}{2}} \int_{\frac{-L_x}{2}}^{\frac{L_x}{2}} \rho(x, y) e^{-i\gamma G_x x m \Delta t} e^{-i\gamma G_y n T' y} \mathrm{d}x \mathrm{d}y \tag{2.30}$$

Here x corresponds to the frequency encoding (or readout) direction and y to the phase encoding direction. n is an integer in the range $-N_y/2 \leq n < N_y/2$, m is an integer in the range $-N_x/2 \leq m < N_x/2$, $N_x \times N_y$ is the matrix size, $L_x \times L_y$ is the field of view, G_x is the amplitude of the readout gradient lobes, G_y is the change in phase-encoding gradient between each of the phase encode lines[1] i.e. $G_y = A_{pe}/T' = 2\pi/\gamma L_y T'$ where A_{pe} is the area of the phase encode blip, Δt is the time between each sampled point in the readout direction and T' is the inter-echo spacing ($T' = T_s + \tau_{pe}$).

In the presence of a B_0 inhomogeneity of the form $\Delta B(x, y, z) = \alpha + G_{x,s}x + G_{y,s}y + G_{z,s}z$ the signal equation becomes:

$$\begin{aligned} s_{nm} = \frac{\Delta z}{\lambda_y} e^{-i\gamma\alpha TE/\lambda_y} e^{-i\gamma G_{z,s}(TE \pm m\Delta t + nT')z_0} \mathrm{sinc}\left(\frac{\gamma G_{z,s}\Delta z(TE \pm m\Delta t + nT')}{2}\right) \\ \int_{\frac{-L_y}{2}}^{\frac{L_y}{2}} \int_{\frac{-L_x}{2}}^{\frac{L_x}{2}} \rho\left(x', \frac{y'}{\lambda_y} - \frac{\alpha + G_{x,s}x'}{\lambda_y G_y}, z_0\right) e^{-2\pi i(k_{x,m} + \delta k_{x,s})x'} e^{-2\pi i(k_{y,n} + \delta k_{y,s})y'} \mathrm{d}x' \mathrm{d}y' \end{aligned} \tag{2.31}$$

here Δz is the slice-thickness, TE is the echo time, and

$$\lambda_y \equiv 1 + \frac{G_{y,s}}{G_y} \tag{2.32}$$

$$k_{x,m} = \frac{\gamma G_x m \Delta t}{2\pi} \tag{2.33}$$

$$k_{y,n} = \frac{\gamma G_y n T'}{2\pi} \tag{2.34}$$

The shifts of the echo in k-space in the frequency encoding (x) and phase encoding

[1]The factor of 2π is included in the numerator to be consistent with the definition $k = \frac{\gamma}{2\pi}\int \mathrm{d}t' G(t')$ used when the k-space signal has terms in $e^{-2\pi i \boldsymbol{k}.\boldsymbol{r}}$ as is the case throughout this thesis

(y) directions caused by the susceptibility gradients are:

$$\delta k_{x,s} = \frac{\gamma G_{x,s} TE}{2\pi\lambda_y} \tag{2.35}$$

$$\delta k_{y,s} = \frac{\gamma G_{y,s} TE}{2\pi\lambda_y} \tag{2.36}$$

To gain a clearer picture of the impact of these changes upon a GE-EPI image the effect of susceptibility gradients in each direction are considered in turn below:

Constant Magnetic Field Offsets

As seen from Equation 2.31 a constant field offset α, caused for example by the chemical shift of lipids relative to water, results in translations of α/G_y in the y-direction[68].

Susceptibility Gradients in the Frequency Encoding Direction

A susceptibility gradient in the frequency encoding (x) direction $G_{x,s}$ results in:

- a shift of the data in k-space by $\delta k_{x,s}$ [17, 29, 69] :

$$\delta k_{x,s} = \frac{\gamma G_{x,s} TE}{2\pi\lambda_y} \tag{2.37}$$

- signal dropout if the echo falls outside of the k-space acquisition window [29] i.e. if the susceptibility gradient in the x-direction does not fall within the following range:

$$-\frac{\pi N_x}{\gamma TE L_x}\left(1+\frac{G_{y,s}}{G_y}\right) \leq G_{x,s} \leq \frac{\pi N_x}{\gamma TE L_x}\left(1+\frac{G_{y,s}}{G_y}\right) \tag{2.38}$$

- image shearing [17]. From Equation (2.31) it can be shown that the observed spin density ρ is sheared by the presence of a susceptibility gradient in the x-direction:

$$\rho\left(x', y' - \frac{G_{x,s}x'}{G_y}\right) \tag{2.39}$$

Susceptibility Gradients in the Phase Encoding Direction

A susceptibility gradient in the phase encoding (y) direction $G_{y,s}$ leads to:

- a shift of the data in k-space by $\delta k_{y,s}$[28, 70]:

$$\delta k_{y,s} = \frac{\gamma G_{y,s} TE}{2\pi\lambda_y} \tag{2.40}$$

- signal dropout if the echo falls outside of the k-space acquisition window [70, 71], i.e. if the susceptibility gradient in the y-direction does not fall within the following range:

$$\left(\frac{-1}{2TE/(N_yT')+1}\right)G_y \leq G_{y,s} \leq \left(\frac{1}{2TE/(N_yT')-1}\right)G_y \tag{2.41}$$

here G_y is the change in phase-encoding gradient between each phase encode line[2].

- modification of the echo time from TE to TE' resulting from the k-space shift [70, 71]:

$$TE' = \frac{TE}{\lambda_y} \tag{2.42}$$

- From Equation (2.31) it can be shown that the observed spin density is modified from ρ to ρ' [70, 71]:

$$\rho' = \frac{\rho}{\lambda_y} \tag{2.43}$$

- image stretching or compressing. Again from Equation (2.31) it can be shown the observed spin density ρ, is stretched or compressed by the presence of a susceptibility gradient in the y-direction [70, 71]:

$$\rho\left(x', y'/\lambda_y\right) \tag{2.44}$$

Susceptibility Gradients in the Slice Selection Direction

A susceptibility gradient in the slice selection (z) direction results in:

- a shift of the data in k-space by [51, 72, 73]:

$$\delta k_{z,s} = \frac{\gamma G_{z,s} TE}{2\pi} \tag{2.45}$$

- the image intensity being modulated by the modulus of a sinc function [74] (assuming rectangular slice profiles)

$$\left|\text{sinc}\left(\frac{\gamma G_{z,s}\Delta z TE}{2}\right)\right| \tag{2.46}$$

Hence, when $G_{z,s}$ is equal to an integer multiple of $\left(\frac{2\pi}{\gamma \Delta z TE}\right)$ there is complete signal dropout.

[2]Note that this may be expressed in terms of the field of view L_y using $G_y = 2\pi/(\gamma L_y T')$ taking care to account for the polarity of G_y i.e. it is negative if k-space is traversed from k_y to $-k_y$ and positive if from $-k_y$ to k_y [70]

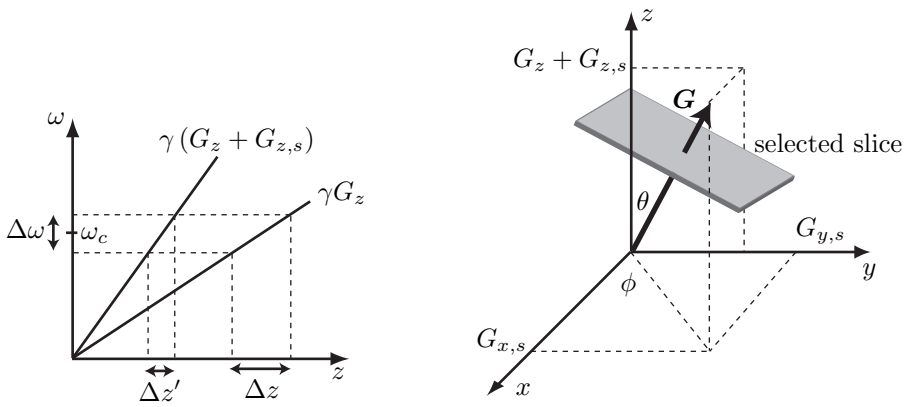

(a) Deviation from prescribed slice position and thickness due to through place susceptibility gradients

(b) Rotation of the prescribed slice due to susceptibility gradients $G_{x,s}$, $G_{z,s}$ and $G_{z,s}$

Figure 2.26: Slice selection distortion effects due to susceptibility gradients, figures adapted from Haacke et al. [51]

- a deviation from the prescribed slice thickness Δz and position z_0, Figure 2.26(a),[51]:

$$\Delta z' = \frac{\Delta\omega}{\gamma\left(G_z + G_{z,s}\right)} = \frac{\Delta z}{\lambda_z} \tag{2.47}$$

and:

$$z_0' = \frac{\omega_c - \omega_0}{\gamma\left(G_z + G_{z,s}\right)} = \frac{z_0}{\lambda_z} \tag{2.48}$$

Here ω_c is the RF carrier frequency and $\lambda_z \equiv 1 + \frac{G_{z,s}}{G_z}$.

The slice selection process is also affected by in-plane susceptibility gradients which cause local rotations of the excited slice, Figure 2.26(b). The angle between the slice selection direction and the z-axis is:

$$\theta = \tan^{-1}\frac{\sqrt{G_{x,s}^2 + G_{y,s}^2}}{G_z + G_{z,s}} \tag{2.49}$$

and the angle between its projection into the x-y plane and the x-axis is:

$$\phi = \tan^{-1}\frac{G_{y,s}}{G_{x,s}} \tag{2.50}$$

2.6.4 Techniques to Reduce Off-Resonance Artifacts

Correcting Image Distortions

A range of approaches are used to correct for EPI image distortions. Firstly magnetic field inhomogeneities, measured by static magnetic field mapping or as part of a

modified EPI sequence [75, 76], can be used to correct distortion, in image [77, 78] or k-space [79]. Magnetic field maps acquired for every brain volume using a modified EPI sequence may be better suited to FMRI applications as they account for the effects of subject motion on the magnetic field inhomogeneities throughout data acquisition. Secondly a number of variations [80–82] on the reversed gradient method [83] have also been published. Two images are acquired with opposite phase-encoding gradient polarity, such that the distortions in the second image are the opposite of those in the first. Undistorted images can then be computed in a number of ways, including performing line-integrals along the phase-encoding direction[81] or fitting a displacement field in 3D using cosine basis functions[80]. A third approach uses a map of the point spread function (PSF) [84–90], acquired using modified EPI sequences, to unwarp the EPI data. Finally, images can be reconstructed using algebraic methods [91–96], that incorporate knowledge of the B_0 inhomogeneities from a static magnetic field map, rather than the Fourier transform.

Reducing Signal Dropout

A large number of techniques have been used to reduce the problem of signal dropout, however these normally include trade-offs including reductions in the temporal resolution, increased image distortion or reduction in sensitivity to the BOLD signal in regions unaffected by the susceptibility gradients. An overview of these methods is given below:

Firstly, to reduce signal dropout, the echo time can simply be reduced since this minimises the time over which the spins dephase relative to one another. One disadvantage of this approach however, is that it leads to a reduction in the BOLD contrast, defined as the change in MR signal in an area of the brain between its baseline and stimulated states. This is maximised when the echo time is chosen to match the T_2^* of grey matter [97], see Figure 2.27.

Another straightforward approach is to reduce the voxel volume [17, 18, 98–106]. This has the added advantage of reducing the intra-voxel tissue heterogeneity. The disadvantage however, is a decrease in SNR (although this can be mitigated by combining a set of thin slices by summation into a thicker slice [102] or by using parallel imaging with a surface coil array[105]) and BOLD contrast-to-noise ratio (CNR) [102].

A family of related strategies based around magnetic field shimming [107] can be used to increase the homogeneity of magnetic field using a set of resistive shim coils. These are designed to generate fields with spherical harmonic geometries. On GE HDx and Discovery MR750 systems first and second order shims are set using fast, automatic shimming technique by mapping along projections (FASTMAP) [108–111]. Shimming is effective over small volumes, although low-order spherical

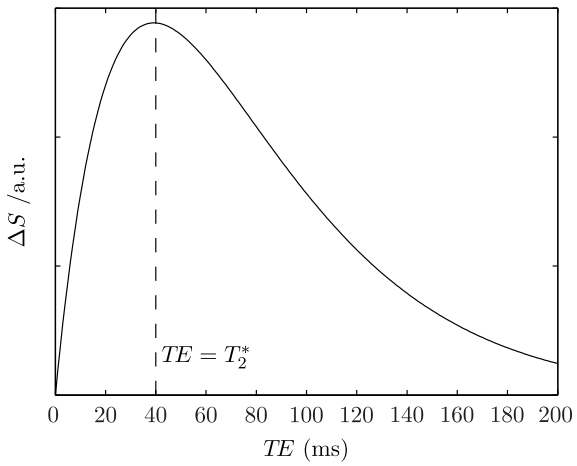

Figure 2.27: A plot demonstrating the echo time dependence of the BOLD contrast for $T_2^* = 40$ ms and $\Delta R_2^* = -1$ s^{-1} showing that the maximum change in signal, ΔS, occurs when $TE = T_2^*$.

harmonic shimming cannot sufficiently homogenise the B_0-field across the whole brain because of strong and highly localised magnetic field distortions, for example around the sinuses [112, 113]. In an effort to improve this situation, localised shimming approaches that optimise field inhomogeneity in predefined regions have been developed [114, 115]. These have the disadvantage, however, of reduced signal in areas of the brain outside the shimmed region and as such they are not ideal for whole brain applications.

Dynamic Shim Updating (DSU) [116–119], in which the shim fields are updated on a slice-by-slice basis during multi-slice data acquisition, can be used to further increase the magnetic field homogeneity, over and above first and second order volume shimming. This is a promising technique but technically challenging to implement because of eddy current effects and the need for dedicated hardware not available on many commercial scanners [112, 118].

Passive shims made from diamagnetic material, such as highly oriented pyrolytic graphite, held within a subject-customised mouth or ear mould, have been used with some success [114, 120, 121] to increase B_0 homogeneity in localised areas, such as the inferior frontal or temporal lobes. The discomfort of such device reduces possible examination times to approximately half an hour however and results in increased subject motion[122], meaning they are of limited practical use.

A range of localised active shimming techniques have also been utilised in FMRI studies. Resistive coils have been placed either inside the subject's mouth [123] or on an acrylic face mask [113] allowing the shimming field to be adjusted for each subject. Like passive shims, the resulting discomfort means it would be very difficult to apply these methods in clinical or psychiatric populations.

It is also possible to reduce the signal drop out by modifying the GE-EPI pulse

sequence itself. In one well developed method, z-shimming [27] described in detail in Chapter 5, the amplitude of the slice select gradient refocusing lobe is modified to cancel out the effects of linear through-plane susceptibility gradients reducing signal dropout.

As described in detail in Chapter 7 the amplitude of the preparation pulses in the phase encode and read-out directions may also be modified to reduce the signal dropout caused by in-plane susceptibility gradients [28, 70, 71, 124, 125].

A family of techniques using tailored radiofrequency pulses (TRF) [126–132], have been developed to reduce signal dropout by cancelling out the phase changes induced by the susceptibility gradients. These are described in more detail in Chapter 6.

Finally, a method combining both gradient and spin echoes into a single shot acquisition has been implemented [133–136], in the hope of utilising both the higher BOLD sensitivity of GE-EPI in regions unaffected by susceptibility gradients [137–141], the immunity of SE-EPI to signal dropout as well as its increased sensitivity to BOLD signal changes in affected regions [139, 142] and the reduction in the extravascular signal from large vessels [143].

Chapter 3

Functional Magnetic Resonance Imaging

3.1 Introduction

Functional magnetic resonance imaging (FMRI) is non-invasive technique used to produce spatial maps of brain activation that are based on the blood oxygen level dependant (BOLD) contrast [3–5]. It has been employed widely in basic neuroscience and psychiatry research [10] as well as clinically in the pre-surgical planning of tumour resections [11].

There are two major functional MRI methodologies; task-based and resting-state. The goal of task-based FMRI experiments is to determine which areas of the brain show changes in activity when subjects are exposed to external stimuli or are required to perform specific tasks. More recently, interest has grown in resting-state FMRI (RS-FMRI), where the brain is observed in the absence of external stimuli. In this case functional connectivity is inferred from correlations in the time varying MR signal from different regions of the brain.

3.2 Blood Oxygen Level Dependant Contrast

The BOLD contrast used in FMRI results from the differing magnetic properties of oxygenated and deoxygenated haemoglobin. Oxygenated haemoglobin is diamagnetic, and as such acts to weakly oppose the static magnetic field, B_0, whereas deoxyhaemoglobin, being paramagnetic, causes local increases in B_0 [144]. The susceptibility differences between deoxyhaemoglobin and surrounding tissues cause localised reductions in T_2^* which lead to reductions in the signal intensity in T_2^* - weighted images. BOLD contrast has both intra- and extra-vascular components; there are four mechanisms by which the signal is attenuated in the presence of

deoxyhaemoglobin [145]:

- Extravascular static dephasing: This is the dominant extravascular mechanism of BOLD contrast for vessels with diameters greater that 20 μm [146]. The voxel signal is attenuated as spins dephase relative to one another because of inhomogeneities in the magnetic field. These are caused by susceptibility differences between the deoxygenated blood and surrounding tissues.

- Extravascular dynamic dephasing: The signal is attenuated because spins diffuse a distance on the order of the size of the magnetic field distortion around the blood vessel during the echo time. The random nature of the diffusion trajectory means that the different spins accrue different phase changes. This mechanism is dominant in the areas surrounding capillaries and small post capillary vessels.

- Intravascular T_2-like effect: Signal attenuation occurs by dynamic averaging. This results from the motion of water molecules relative to the paramagnetic deoxyhaemoglobin in the erythrocytes (red blood cells).

- Intravascular frequency offsets: The signal is attenuated if there are a large number of vessels of different orientation within a voxel. This is because the precession frequency of spins within a vessel is dependent upon the concentration of deoxyhaemoglobin and relative orientation of the vessel to the static magnetic field.

Gradient-echo imaging detects contributions from all four of the signal attenuation mechanisms, whereas only extravascular dynamic dephasing and the intravascular T_2-like effect are seen when spin-echo based acquisition techniques are used [145].

It has been shown experimentally that the MR signal increases in areas of the brain undergoing functional stimulation[6–8]. This is a result of the changes in the cerebral blood flow (CBF) and the rate of metabolic consumption of oxygen ($CMRO_2$). As first observed in the Positron Emission Tomography (PET) experiments carried out by Fox et al. [147], prolonged visual stimulation results in an increase of 50% in the CBF, an increase of 51% in the rate of metabolic consumption of glucose (CMR_{glu}) but only a 5% increase in $CMRO_2$ in the visual cortex. Put simply 'more oxygen is supplied to the brain than is consumed' [64]. The difference in the relative increases in the CBF and $CMRO_2$ means that the fraction of oxygen extracted from the blood decreases with neuronal activity. Therefore, in activated regions, the blood has a higher concentration of oxyhaemoglobin and a lower concentration of deoxyhaemoglobin. It is this decrease in the amount of deoxyhaemoglobin that results in local increases in the T_2^* and hence increases in the MR signal in the regions of functional activation. A more detailed study of

the time course of the MR signal following a short stimulus, the haemodynamic response function, reveals an initial dip [148]; within the balloon model framework put forward by Buxton et al. [149] this is thought to be caused by an increase in $CMRO_2$ with no associated change in CBF and cerebral blood volume (CBV). This is then followed by an increase in the MR signal, the main BOLD response, and a post-stimulus undershoot [150] which is thought to result from a delay in the CBV returning to its baseline level [151].

3.3 Task-Based Functional MRI

Task-based FMRI experiments can be used to map the areas of the brain that are activated when subjects are exposed to external stimuli or are required to perform specific tasks. As discussed below, the experiment may have a block or event-related design.

3.3.1 Block Design Paradigms

Early task-based FMRI experiments used block designs [152]. These consist of periods (with a typical duration of between 10s to one minute [64]) during which the subject performs a task, or are exposed to a stimulus, interleaved with control periods. For example to determine the activations in the motor cortex due to finger tapping a subject could be instructed to carry out 30 s blocks of continuous finger tapping (task) interleaved with 30 s blocks of rest (control) for a total of five minutes. As explained later in this chapter, the regions of the brain showing statistically significant changes in MR signal in response to the task can then be determined using the general linear model. In general, block design experiments are good at detecting activations but they are relatively poor for characterising the timing and shape of the haemodynamic response function (HRF) [64].

3.3.2 Event-Related Paradigms

Alternatively task-based FMRI experiments can use event-related designs. In this case stimuli are presented for short durations, separated by an inter-stimulus interval (ranging from 2 to 20 s [64]). These designs are more flexible and can be used to determine the response to single events. They have a reduced power to detect activations compared to block designs, but if the acquisition has sufficient temporal resolution, they provide a greater ability to determine the timing and shape of the HRF. Therefore they can be used to separate out the distinct processes within a given task [64].

3.4 Resting-State Functional MRI

Resting-State Functional MRI provides a relatively straightforward method to map the functional relationships between different brain regions [153]. The technique is based on the assumption that, at 'rest', regions of the brain which are functionally connected have synchronised changes in neuronal activity which result in synchronised fluctuations in the MR signal from these brain regions. Collecting data in this passive manner could be advantageous in patients who find it difficult to perform a given task.

The first observations of resting-state functional connectivity using MRI were made by Biswal et al. [12], who demonstrated that, in the absence of explicit motor behaviour, low frequency fluctuations (0.01-0.08Hz) in the MR signal in the left motor cortex were temporally correlated with those in the right motor cortex and medial motor regions. These initial observations were confirmed by Lowe [154, 155], who also observed similar correlations in the visual cortex. Coherent fluctuations have also been observed, in subjects at rest, in a range of systems, including the auditory [156], language [156, 157], default mode[1] [159–162], dorsal attention [162, 163], ventral attention [163] and hippocampus or episodic memory [164, 165] networks. A consistent set of these spatially specific temporal correlations have been observed, in the absence of overt tasks, across subjects [13, 166–169]. Since these spatially specific temporal correlations are observed in the absence of overt tasks the correlated areas are commonly referred to as resting-state networks (RSNs).

More recently, as described in a review article by Greicius [170], RS-FMRI has been applied to the study of various neuropsychiatric disorders including Alzheimers disease and other dementias [171–175], autism [176–179], attention-deficit/hyperactivity disorder [180–183], depression [184–186] and schizophrenia [187, 188]. In addition it has been used to investigate aging [189, 190], multiple sclerosis [191] and pain [170]. Feasibility studies for its use in pre-surgical mapping [192, 193] have also been performed.

As outlined in a recent review by Birn [153], there was initially a significant degree of scepticism about RS-FMRI. This was because there are a number of potential sources of correlations in the MR signal apart from synchronised changes in neuronal activity. These include head motion, cardiac pulsations and inflow effects [194] and effects related to respiration such as time varying image distortion [195, 196]. It has also been suggested that correlations may be due to similarities in the vascular structure in different brain regions. The current evidence in support of the hypothesis that correlated fluctuations in the MR signal result from underlying

[1]The default mode network (DMN) is a collective name for the regions of the brain that demonstrate a decrease in activity when the brain is performing an overt task [158]

functional connectivity has been collated by Birn [153] and is summarised below.

Several studies have shown that signal changes in functionally related brain regions occur at lower frequencies than respiration and cardiac pulsations[12, 156, 197]. It has also been shown that the echo time dependence of resting-state signal changes is similar to that observed for the BOLD response in task-based FMRI experiments [198]. In addition it has been shown that when structural connections are reduced or removed completely, as is the case in patients with callosal agenesis or post-callosotomy, functional connections between the left and right hemispheres, derived from RS-FMRI, are reduced or completely absent, whilst intra-hemispheric connections are preserved [199, 200]. Countering the suggestion that correlations are due to similarities in the vascular supply of brain regions, Krienen and Buckner [201] found that, in agreement with the known structural connections, the right cerebellum was more strongly correlated with the left rather than the right motor cortex and that the left cerebellum was more strongly correlated with the right motor cortex. Since the cerebellum and motor cortex are supplied by different major arteries[2] the functional connections between them cannot be explained by similarities in the vascular structure. Finally temporal correlations have been observed in functionally related brain regions in humans using other modalities such as electroencephalography (EEG) [162] and electrocorticography (ECoG) [203].

3.5 Analysis of Functional MRI Data

The main aim of the data analysis carried out on task-based functional MRI data is to determine those regions of the brain which show significant changes in BOLD signal in response to a known external stimulus or task[152, 204]. In contrast, the aim when analysing resting-state functional MRI is to find spatial patterns of coherent BOLD activity [13].

3.5.1 Data Preprocessing

FMRI data is four-dimensional; a three-dimensional image of the brain is acquired within each repetition time resulting in a data set that contains a record of the signal intensity S at each spatial location and time point i.e. $S(x, y, z, t)$. Prior to the statistical analysis of either task-based or resting-state data, a series of preprocessing steps are typically performed.

[2]The motor cortex is supplied by the central branch of the middle cerebral artery whereas the cerebellum is supplied by the posterior inferior cerebellar, anterior inferior cerebellar and superior cerebellar arteries [202].

Slice Timing Correction

Slice timing correction is carried out by shifting the phase of the time series in each voxel in the Fourier domain, given knowledge of the slice acquisition order[152]. This correction accounts for the time differences in the acquisition of each slice within the TR period, as the following statistical analysis assumes that the signal at every brain voxel within each 3D brain volume was acquired at the same point in time.

Motion Correction

During the acquisition of the FMRI dataset the subject is liable to move their head. This means that the time series in each voxel no longer reflects the changes in the BOLD signal at a particular location within the brain, and as such this motion needs to be be corrected by realigning each 3D volume using a rigid body registration to determine the transformations that map all the volumes into the same space [204, 205]. The transformation is typically determined iteratively by minimising a cost-function, such as the normalised correlation between the volume of interest and the reference volume [205]. This could be the volume acquired at the central time point of the dataset or a mean of all the volumes. Even after motion correction, via rigid body registration, there will be a range of motion related artifacts present in FMRI data. These include the effects of motion within the acquisition of each volume, interpolation errors, and spatial distortions [204].

Spatial Smoothing

Spatial smoothing of the data is then typically performed, by convolution with a Gaussian kernel. This is carried out for two main reasons; firstly to increase the signal-to-noise ratio (SNR) and secondly to enable a correction for multiple comparisons of the final test-statistic using Gaussian random field (GRF) theory [152, 206]. The optimal full-width half-maximum (FWHM) of the Gaussian kernel is dependent upon the reason for smoothing; if GRF theory is used to correct multiple comparisons the FWHM should be approximately twice the voxel dimension; if it is solely to increase the SNR then it should not be larger the smallest activation to be detected [207].

Temporal Filtering

Temporal filtering is performed on each voxel in turn to remove unwanted components in the timeseries[152]. Depending upon the type of statistical analysis that is to be performed, different temporal filtering approaches are taken.

The statistical analysis of both task-based and resting-state FMRI datasets benefits from high-pass filtering to remove slowly varying scanner related signal drifts.

In task-based FMRI the cut-off period is typically chosen to be approximately one and a half times the period of the block design [152]. For resting-state data it has been suggested that the frequency cut-off is reduced, such that more power is preserved at lower frequencies, as these are thought to be important in resting-state networks[208].

In task-based FMRI analysis, low-pass filtering is one possible strategy to deal with temporal autocorrelations, discussed below, in the FMRI timeseries. Low-pass filtering 'colours' the data i.e. it imposes a known autocorrelation. This then enables the degrees of freedom of the null distribution used during inference to be estimated correctly [209, 210].

In seed-based resting-state FMRI data analysis low-pass filtering, with a cut-off of approximately 0.1 Hz, is sometimes performed to reduce the effects of cardiac and respiratory variations on the FMRI timeseries [13, 156]. The non-neuronal noise resulting from cardiac and respiratory activity accounts for a significant proportion of resting-state signals[211–213] but, unlike in task-based FMRI, this cannot be removed by averaging over multiple epochs of task and rest. Several strategies have been employed to remove it, including: linear regression of the measured cardiac and respiratory fluctuations, [211–213]; global signal regression [159, 214, 215] (this is controversial as it's been shown to introduce spurious negative correlations [216]); regression of white matter and CSF signal, [164]; increased sampling rates such that the cardiac and respiratory fluctuations can be filtered out [12, 155, 156]; and independent components analysis (ICA) [166, 217].

3.5.2 Statistical Analysis

In task-based FMRI the ubiquitous method to determine the regions of the brain which show significant changes in BOLD signal in response to a stimulus is to to fit a set of explanatory variables to the time series signal at each voxel location using the General Linear Model (GLM) [152, 204]. This is a mass-univariate approach in which the same analysis is performed independently on the time-series signal in each voxel.

In resting-state studies the GLM may also be used, but in this case the goal is to determine spatial patterns of coherent BOLD activity. Therefore, instead of a user generated model, the mean timeseries from a region of interest is used as an explanatory variable [12, 13]. The resulting statistical maps therefore show areas of the brain with BOLD signal changes that are significantly correlated with those changes in the selected region of interest. An alternative data-driven multivariate approach, which is described in detail below, is to use Independent Component Analysis (ICA) [218] to determine a set of spatially independent components [166,

217, 219, 220]. It is thought that these reflect both underlying functional networks within the brain as well as artefacts such as subject motion and susceptibility induced signal dropout[220].

Mass-Univariate Analysis using the General Linear Model

Within the framework of the GLM the MR signal in each voxel is fitted, using a linear least squares algorithm, to a set of explanatory variables. The variation in a voxel's signal over time is 'explained' using a linear combination of m-explanatory variables and a residual error term. Given that there are usually multiple explanatory variables, including the stimulus design convolved with a model of the haemodynamic response function, motion regressors and terms to account for intensity drifts, the problem is most easily cast in matrix form:

$$\begin{pmatrix} y(t_1) \\ y(t_2) \\ \vdots \\ y(t_n) \end{pmatrix} = \begin{pmatrix} x_{11} & \dots & x_{1m} \\ x_{21} & \dots & x_{2m} \\ \vdots & \ddots & \vdots \\ x_{n1} & \dots & x_{nm} \end{pmatrix} \begin{pmatrix} \beta_1 \\ \beta_2 \\ \vdots \\ \beta_m \end{pmatrix} + \begin{pmatrix} \varepsilon_1 \\ \varepsilon_2 \\ \vdots \\ \varepsilon_n \end{pmatrix} \tag{3.1}$$

Equation 3.1 can also be written more compactly as:

$$\boldsymbol{Y} = \boldsymbol{X}\boldsymbol{\beta} + \boldsymbol{\varepsilon} \tag{3.2}$$

Here $\boldsymbol{Y}$ is an $n \times 1$ vector of measured signal intensities from a single voxel at n time points, $\boldsymbol{X}$ is an $n \times m$ design matrix whose columns are the m explanatory variables. $\beta_1 \dots \beta_m$ are the m unknown parameter estimates corresponding to the m explanatory variables and $\varepsilon_1 \dots \varepsilon_n$ are the residuals at each timepoint.

A conventional linear least squares analysis assumes that the residuals, $\boldsymbol{\varepsilon}$, are uncorrelated in time, $\boldsymbol{\varepsilon} \sim \mathcal{N}_n(0, \boldsymbol{I}\sigma^2)$ i.e. that they are distributed according to an n-dimensional Gaussian with mean $\boldsymbol{\mu} = 0$ and covariance matrix $\sigma^2\boldsymbol{I}$, where $\boldsymbol{I}$ is an $n \times n$ identity matrix [221]. In the case of FMRI this assumption does not hold, as the data are temporally autocorrelated; i.e. the residual at time point i is related to the residual at $i-1$ [222]. In this case the residuals are distributed according to an n-dimensional Gaussian with mean $\boldsymbol{\mu} = 0$ and covariance matrix $\boldsymbol{V}\sigma^2$:

$$\boldsymbol{\varepsilon} \sim \mathcal{N}_n\left(0, \boldsymbol{V}\sigma^2\right) \tag{3.3}$$

Failure to properly account for temporal autocorrelation leads to false positive activations, as the number of degrees of freedom of the null distribution is overestimated, which in turn spuriously reduces the probability of finding a statistic as, or more extreme, than that calculated (i.e. the p-value is underestimated), hence null hy-

pothesis is rejected too readily [204]. The methods used to deal with autocorrelation in FMRI data are discussed below.

Given the autocorrelation of the residuals, the parameters $\boldsymbol{\beta}$ are estimated using generalised least squares [221]. The data are multiplied by a matrix $\boldsymbol{S}$; this can be constructed to act as a low pass filter to color the data [210] or more commonly set to $\boldsymbol{S} = \boldsymbol{K}^{-1}$ (where $\boldsymbol{V} = \boldsymbol{K}\boldsymbol{K}'$ - the Cholesky decomposition of the covariance matrix $\boldsymbol{V}$, which is unknown and is therefore iteratively estimated from the data [223, 224]) [223]. In the second case the data is whitened, i.e. the residuals are uncorrelated, and the parameter estimate $\hat{\boldsymbol{\beta}}$ is given by:

$$\hat{\boldsymbol{\beta}} = (\boldsymbol{X}'\boldsymbol{V}^{-1}\boldsymbol{X})^{-1}\boldsymbol{X}'\boldsymbol{V}^{-1}\boldsymbol{Y} \tag{3.4}$$

The estimate of the variance of the parameter estimates is:

$$\hat{\mathrm{Var}}\{\hat{\boldsymbol{\beta}}\} = \left(\boldsymbol{X}'\boldsymbol{V}^{-1}\boldsymbol{X}\right)^{-1}\hat{\sigma}^2 \tag{3.5}$$

and the estimate of the error variance is:

$$\hat{\sigma}^2 = \frac{\boldsymbol{\eta}'\boldsymbol{\eta}}{\mathrm{tr}(\boldsymbol{R})} \tag{3.6}$$

Here $\boldsymbol{\eta} = \boldsymbol{K}^{-1}\boldsymbol{\varepsilon}$ and $\boldsymbol{R} = \boldsymbol{I} - (\boldsymbol{K}^{-1}\boldsymbol{X})\,(\boldsymbol{K}^{-1}\boldsymbol{X})^{+}$.

In FMRI it is commonplace for multiple stimuli to be presented to the subject and then to compare their effects during data analysis. In the lexicon of FMRI this comparison is refered to as a 'contrast', represented by the column-vector $\boldsymbol{c}$. For example, if the functional paradigm included both visual and auditory stimuli, the first column of the design matrix $\boldsymbol{X}$ might contain the explanatory variable for the visual stimulus and the second column the explanatory variable for the auditory stimulus so that β_1 was the parameter estimate for visual activations and β_2 was the parameter estimate for auditory activations. To determine which voxels where active during visual stimulation $\boldsymbol{c}' = (1, 0)$ because $\boldsymbol{c}'\hat{\boldsymbol{\beta}} = (1, 0)\begin{pmatrix} \beta_1 \\ \beta_2 \end{pmatrix} = \beta_1$. Alternatively, to determine where in the brain the visual stimulus has a greater effect than the auditory the contrast vector would be $\boldsymbol{c}' = (-1, 1)$. The contrast of parameter estimates is given by $\boldsymbol{c}'\hat{\boldsymbol{\beta}}$ [152] and the estimator of the variance of the contrast of parameter estimates is given by:

$$\hat{\mathrm{Var}}\{\boldsymbol{c}'\hat{\boldsymbol{\beta}}\} = \boldsymbol{c}'(\boldsymbol{X}'\boldsymbol{V}^{-1}\boldsymbol{X})^{-1}\boldsymbol{c}\hat{\sigma}^2 \tag{3.7}$$

A t-statistic is calculated at each voxel from the parameters $\hat{\boldsymbol{\beta}}$ and their estimated

variances $\mathrm{Var}\{\hat{\boldsymbol{\beta}}\}$ [152, 204]:

$$t = \frac{\hat{\boldsymbol{\beta}}}{\sqrt{\hat{\mathrm{Var}}\{\hat{\boldsymbol{\beta}}\}}} \tag{3.8}$$

In the case of the contrast of parameter estimates, the t-statistic is:

$$t = \frac{\boldsymbol{c}'\hat{\boldsymbol{\beta}}}{\sqrt{\hat{\mathrm{Var}}\{\boldsymbol{c}'\hat{\boldsymbol{\beta}}\}}} \tag{3.9}$$

Statistical inference is then carried out on the resulting maps. This can be done for each voxel individually by determining the test-statistic threshold, t_α, above which the null hypothesis should be rejected at a given level of significance, α, as illustrated in Figure 3.1. Alternatively, taking account of spatial information in the maps, inference can be carried out at the cluster-level [207]. In this case groups of contiguous voxels whose t-statistic is greater than a given threshold are defined as clusters; a cluster is deemed significant if its spatial extent or mass (sum of t-statistics within a cluster) [207, 225] exceeds a given threshold. Since statistical significance is being tested in a large number of voxels (or clusters) there is a multiple comparisons problem and care must be taken to avoid type I errors (false positives). There are two main ways to quantify the risk of a type I error [207]; the familywise error rate (FWE) and the false discovery rate (FDR). FWE is defined as the probability of finding one or more false positive in the map. The significance level is adjusted to control the FWE using for example a Bonferroni correction (which assumes that each voxel is independent) or Gaussian Random Field Theory [226–228] (which estimates the number of spatially independent voxels given the spatial smoothness of the data). If the FWE corrected significance level is 0.01 then there is a maximum 1% probability of finding any false positive activations in the thresholded t-statistic map. The FDR is defined as the proportion of false positives out of those tests for which the null hypothesis was rejected [229, 230]. With FDR the correction of the significance level is more lenient [207]; if the FDR corrected significance level is 0.01 then on average 1% of the voxels (or clusters) that were deemed significant are false positives.

For the majority of FMRI studies investigating brain function there is a desire to generalise the results of the investigation across the population as a whole rather than being restricted to commenting on specific cases. This aim requires the scanning of multiple subjects and the combination of the statistics resulting from the GLM fit of each subject. Given that there is significant heterogeneity in brain size and shape between subjects the data must be transformed into the same space to allow meaningful interpretation of the final combined statistics [152, 207]. Acquiring data from multiple subjects has the added advantages that it can increase the

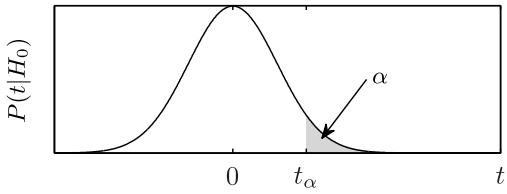

Figure 3.1: The test-statistic has a Student's t-distribution $P(t|H_0)$ with $n - m$ degrees of freedom if the null hypothesis, H_0, is true. The value of t above which the null hypothesis is rejected, t_α, is shown along with the significance level α.

sensitivity of the experiment to an effect of interest and allows comparisons between different groups of subjects [152].

It is possible to combine all the subjects' time-series data into a single linear model, however typically in FMRI data analysis a 'summary-statistics' approach is taken [231]. In such an approach, group-level inferences are made by combining the results from a set of single subject GLM fits. Several methods can be used to combine the statistical results across a group of subjects to produce a group based statistic; these include both fixed and mixed effects models. In a fixed effects analysis it is assumed that the only contribution to the variance is from within-subject variations and that there is no between subject variance, i.e. it is assumed that every subject, within a group, activates equally[152]. In contrast, a mixed effects model accounts for both within and between-subject variance [207, 231, 232]. In effect, it considers that the subjects themselves are random variables sampled from a population, and as such allows the results of the analysis to be generalised across the population as a whole.

Independent Component Analysis

The univariate methods, described above, for analysing both task-based and resting-state studies may not be adequately sensitive in detecting functional networks, since they do not fully account for the spatial relationships between voxels [219, 220]. It is therefore becoming increasingly popular to use a multivariate technique such as Independent Component Analysis (ICA) especially when analysing resting-state FMRI data [218, 233]. ICA can reduce an FMRI data set with n-time points to a set of m-component maps that are statistically independent of one another in space. The m-components are thought to represent functional networks within the brain [169], as well as artifactual signals from physiological pulsations, head movement and scanner noise [219].

Statistical independence implies that knowledge of the value of the intensity values in one independent component map gives no information about the intensity values in any of the other of the maps. That is, the joint probability density function

of the m independent components $(s_1, s_2, \ldots, s_m)$ must factorise into the product of the marginal probability density functions [219, 234] i.e.:

$$p(s_1, s_2, \ldots, s_m) = p_1(s_1)\, p_2(s_2) \ldots p_m(s_m) \tag{3.10}$$

The ICA model can only be estimated if the sources $\boldsymbol{S}$ are statistically independent or equivalently if they have non-Gaussian distributions[234].

ICA is a generative linear latent variables model [234] in that it describes how the observed data $\boldsymbol{X}$ are generated from a linear mixture of the statistically independent sources $\boldsymbol{S}$ which themselves cannot be directly observed.

$$\boldsymbol{X} = \boldsymbol{A}\boldsymbol{S} \tag{3.11}$$

For FMRI data with p-voxels and n-time points, stored in a matrix $\boldsymbol{X}$, the m spatially independent components[3] each with p-voxels are stored in a matrix $\boldsymbol{S}$, each spatially independent component has an associated time course with n-time points, which are stored in the columns of $\boldsymbol{A}$:

$$\begin{pmatrix} x_{11} & \ldots & x_{1p} \\ x_{21} & \ldots & x_{2p} \\ \vdots & \ddots & \vdots \\ x_{n1} & \ldots & x_{np} \end{pmatrix} = \begin{pmatrix} a_{11} & \ldots & a_{1m} \\ a_{21} & \ldots & a_{2m} \\ \vdots & \ddots & \vdots \\ a_{n1} & \ldots & a_{nm} \end{pmatrix} \begin{pmatrix} s_{11} & \ldots & s_{1p} \\ s_{21} & \ldots & s_{2p} \\ \vdots & \ddots & \vdots \\ s_{m1} & \ldots & s_{mp} \end{pmatrix} \tag{3.12}$$

The first step in estimating the mixing matrix, $\boldsymbol{A}$, and the independent components, $\boldsymbol{S}$, is to centre the data by subtraction of the mean. Specifically, for each brain volume in the time series, the mean voxel value for over the volume is subtracted from each voxel in that volume.

Secondly, Principal Component Analysis (PCA) is carried out; this reduces the data to a set of m components that are uncorrelated and ranked in order of explained variance. The number of components is normally unknown and therefore it must be estimated from the data; simple approaches seek to maintain a certain percentage variance or use a scree plot to infer the number of 'important' components. More sophisticated approaches such as Probabilistic PCA [236–238] have been developed that determine the number of components using Bayesian model order selection.

Following PCA, the only remaining task is to find the orthogonal transformation to ensure that the components are statistically independent. As outlined in Hyvärinen et al. [234] there are a number of different algorithms for ICA that can

[3]It is also possible, using ICA, to determine a set of components from the FMRI data that are statistically independent in time. However in the majority of cases spatial independence is used. This is because both artifactual components and those representing brain networks are relatively sparse and well localised in space [219, 235].

be used to find this transformation; maximising non-Gaussianity of the components [239–243], maximum likelihood estimation [233, 244–249], minimising the mutual information of the components [218, 243] or higher-order decorrelation using the cumulant tensor [250–253]. Maximising non-Gaussianity is probably the most intuitive method; the central limit theorem states that the sum of independent random variables tends towards a Gaussian distribution, therefore independent components are found by determining the linear combinations of the data (after PCA has been performed) which maximise the non-Gaussianity.

Finally, there is normally a need to infer which voxels in a given component are significantly modulated by the associated time course [166]. In early work this was achieved by simply thresholding the components following a z-transformation i.e. to unit variance and zero mean [219]. However a more sophisticated approach uses mixture modelling [254, 255] to produce z-score maps that are thresholded using alternative hypothesis testing [220].

Chapter 4

Simulating the Effect of the Signal-to-Noise Ratio on the Detection of BOLD Activations

4.1 Introduction

As described in Chapter 2, FMRI data acquired using a GE-EPI pulse sequence suffers from a range of artefacts that can seriously degrade image quality. In this chapter I focus on the susceptibility induced signal dropouts that hinder the detection of both resting-state and task-induced brain activations in the orbitofrontal and inferior temporal lobes. Using both direct calculation and numerical simulations, I determine the impact of the signal-to-noise ratio (SNR) in the regions of signal dropout on the statistical power of commonly used FMRI data analysis methodologies to detect both task-induced and resting-state BOLD signal changes.

In the subsequent chapters, several modified data acquisition strategies such as z-shimming and tailored RF pulses will be used to reduce signal dropout. The results of this chapter will be used to inform the likely improvements in SNR that these strategies must provide in order to detect task-induced brain activations and resting-state networks in affected areas.

4.2 Signal-to-Noise Ratio and the Detection of Task-Induced BOLD Signal Changes

As outlined in Chapter 3, the most commonly used method to determine the regions of the brain which show significant changes in MRI signal in response to a set of stimuli is to to fit a set of explanatory variables to the time varying signal in each voxel using the General Linear Model (GLM) [152, 204]. A map of the t-statistic

is calculated at each voxel using Equation 3.9 and then a voxel, or cluster-level, threshold is applied to determine those voxels with statistically significant changes in BOLD signal.

As described below it is possible, by combining two previously published models, to determine the theoretical dependence of the t-statistic (and therefore by extension the detectability of BOLD signal changes) on SNR, percentage change in BOLD signal and experimental design.

4.2.1 Dependence of the T-Statistic on the SNR, Percentage Change in BOLD Signal and Experimental Design

Using the expression for the t given in Equation 3.9 Smith et al. [256] showed that the t-statistic resulting from a GLM analysis is given by:

$$t = \frac{S}{\sigma}\frac{\Delta S_{\%}}{100}\frac{\sqrt{\boldsymbol{X}'_{eff}\boldsymbol{X}_{eff}}}{h} \tag{4.1}$$

Here S is the mean MRI signal in each voxel in the absence of any external stimuli. σ is the temporal noise; this is defined as standard deviation of the noise along the timeseries, again in the absence of external stimuli. The ratio S/σ is the temporal signal-to-noise ratio (TSNR) [105, 257, 258]. $\Delta S_{\%}$ is percentage change in the BOLD signal. Specifically, for a contrast such as $\boldsymbol{c}' = (1, 0, 0, \ldots, 0)$, used to test if β_1 (as defined in Chapter 3) is significantly different from zero, $\Delta S_{\%}$ is the change in the BOLD signal associated with the first explanatory variable expressed as a percentage of the baseline signal S. Alternatively, for a contrast like $\boldsymbol{c}' = (1, -1, 0, \ldots, 0)$, used to determine the regions where β_1 is significantly greater than β_2, $\Delta S_{\%}$ is the difference between the BOLD signal associated with the first and second explanatory variables expressed as a percentage of the baseline signal S. h is the peak-to-peak amplitude of the $n \times 1$ effective explanatory variable vector $\boldsymbol{X}_{eff}$ which is given by:

$$\boldsymbol{X}_{eff} = \boldsymbol{X}\left(\boldsymbol{X}'\boldsymbol{X}\right)^{-1}\boldsymbol{c}\left[\boldsymbol{c}'\left(\boldsymbol{X}'\boldsymbol{X}\right)^{-1}\boldsymbol{c}\right]^{-1} \tag{4.2}$$

(where again, $\boldsymbol{X}$ is as defined in Chapter 3). Inspection of Equation 4.1 shows that the t-statistic increases linearly with the TSNR, percentage change in the BOLD signal, $\Delta S_{\%}$, and $\frac{\sqrt{\boldsymbol{X}'_{eff}\boldsymbol{X}_{eff}}}{h}$. For a simple block design FMRI experiment, with a single explanatory variable, $\boldsymbol{X}_{eff} = \boldsymbol{X}$, and therefore:

$$\frac{\sqrt{\boldsymbol{X}'_{eff}\boldsymbol{X}_{eff}}}{h} = \sqrt{\frac{n}{2}} \tag{4.3}$$

where n is the number of time points, i.e. the t-statistic increases as the square root of the number of time points.

In later chapters I describe several methods to increase the SNR in the areas of GE-EPI images affected by signal dropout, therefore it helpful to express the TSNR (S/σ) in Equation 4.1 in terms of the SNR by incorporating a model of the temporal noise described by Kruger et al. [259]. They showed that the temporal noise, σ, has two main components:

$$\sigma^2 = \sigma_0^2 + \sigma_p^2 \tag{4.4}$$

The intrinsic noise, σ_0, encapsulates both the effects of thermal noise from the subject and scanner electronics, as well as noise from other scanner imperfections for example from the gradient, shim and RF systems [259]. The level of intrinsic noise is independent of the MRI signal amplitude [260]. The physiological noise σ_p results from a number of different sources including cardiac and respiratory fluctuations, as well as motion from brain pulsatility, in addition to fluctuations linked to resting-state activity[1] [259]. The physiological noise, unlike the intrinsic noise, is proportional to the baseline MR signal:

$$\sigma_p = \lambda S \tag{4.6}$$

In gray matter, $\lambda \approx 0.012$ [259]. When this noise model is incorporated into Equation 4.1 the t-statistic, with some straightforward rearrangement, can be written in terms of the signal-to-noise ratio $SNR = S/\sigma_0$:

$$t = \frac{SNR}{\sqrt{1 + \lambda^2 SNR^2}} \frac{\Delta S_{\%}}{100} \frac{\sqrt{\boldsymbol{X}'_{eff}\boldsymbol{X}_{eff}}}{h} \tag{4.7}$$

Equation 4.7 is plotted as a function of both the SNR and the percentage change in the BOLD signal, $\Delta S_{\%}$, in Figure 4.1(a), for a simple block design FMRI experiment with thirty second task and rest periods sampled every 2s for a total of five minutes. In this case the first column of the design matrix $\boldsymbol{X}$ was all ones to model the baseline MR signal and the second column contained a square-wave with a peak-to-peak amplitude of one and a period of one minute to model a stimulus with 30s task and rest blocks. The contrast $\boldsymbol{c}' = (0, 1)$. To aid interpretation of the 2D-plot in Figure 4.1(a), the t-statistic is also plotted separately as a function of

[1] As shown by Kruger et al. [259] the physiological noise σ_p can be broken down into two components:

$$\sigma_p^2 = \sigma_B^2 + \sigma_{NB}^2 \tag{4.5}$$

The first σ_B is 'BOLD-like' in the sense that it shows the same echo-time dependence as the BOLD effect and is thought to arise from resting-state activity. The second σ_{NB} is not dependent upon the echo-time and as such is 'non-BOLD-like' and is thought to arise from cardiac and respiratory fluctuations

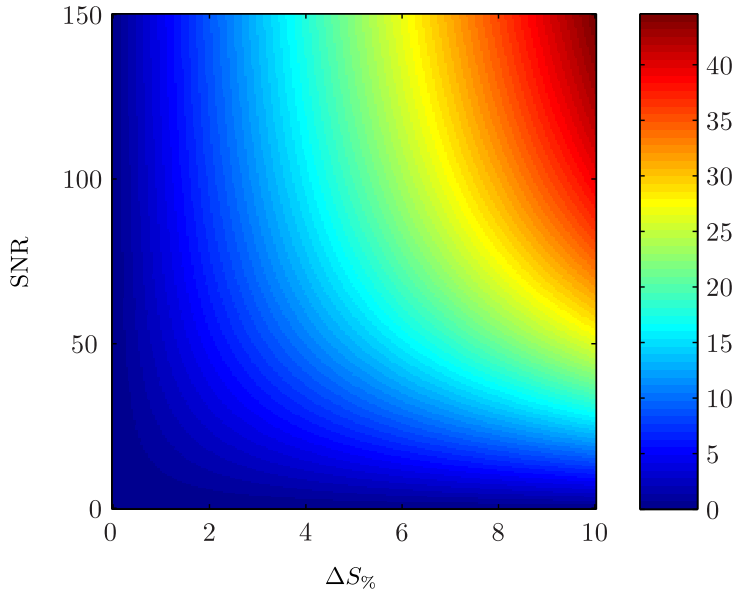

(a) t-statistic as a function of SNR and $\Delta S_{\%}$

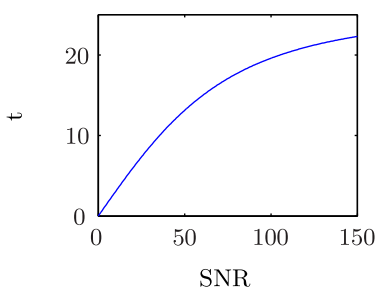

(b) t-statistic as a function of *SNR* when $\Delta S_{\%} = 5\%$

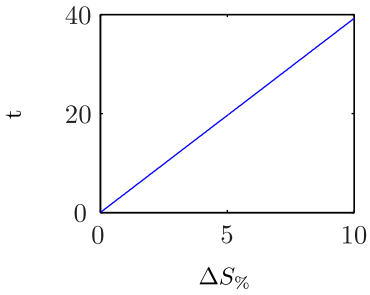

(c) t-statistic as a function of $\Delta S_{\%}$ for an SNR of 100

Figure 4.1: Plots showing the dependence of the t-statistic on the SNR and the percentage BOLD signal change, $\Delta S_{\%}$ for a simple block design FMRI experiment with thirty second task and rest periods sampled every 2s for a total of five minutes.

SNR at $\Delta S_{\%} = 5\%$ (Figure 4.1(b)) and as a function of $\Delta S_{\%}$ for an SNR of 100 (Figure 4.1(c)). Importantly, as a result including a model of the physiological noise, Equation 4.7 and Figure 4.1 show for the first time that the t-statistic does not increases linearly with SNR. Rather, smaller and smaller increases in the t-statistic are achieved with increasing SNR.

4.2.2 The Minimum SNR Required to Detect an Activation

Whilst the dependence of the t-statistic on the SNR, $\Delta S_{\%}$ and experimental design described above is useful, it is arguably more important, when designing new methods to reduce signal dropout, to determine the minimum SNR needed to find

statistically significant activations. This can be found by rearranging Equation 4.7:

$$SNR_{min} = \frac{t_\alpha}{\sqrt{\left(\frac{\Delta S_\%}{100}\right)^2 \frac{\boldsymbol{X}'_{eff}\boldsymbol{X}_{eff}}{h^2} - \lambda^2 t_\alpha^2}} \tag{4.8}$$

Here t_α is the t-statistic threshold determined using the Student's t inverse cumulative distribution function with $n - m$ degrees of freedom for a given significance level, α. Inspection of Equation 4.8 shows that minimum SNR becomes imaginary, implying that it is possible to detect an activation, when:

$$\Delta S_\% < \frac{100\lambda t_\alpha h}{\sqrt{\boldsymbol{X}'_{eff}\boldsymbol{X}_{eff}}} \tag{4.9}$$

Therefore, again as a consequence of including a model of the physiological noise, it has been shown for the first time that there is a minimum percentage BOLD signal change that depends on the experimental design, below which, regardless of the SNR, activations will never be deemed statistically significant. For example for the design matrix and contrast described above $\Delta S_{\%,min} = 0.32\%$ at a statistical significance $\alpha = 0.05$.

The minimum signal-to-noise ratio, calculated using Equation 4.8, is plotted as a function of $\Delta S_\%$ in Figure 4.2 for the design matrix and contrast described above at two different levels of statisitical significance, $\alpha = 0.05$ and $\alpha = 3.21 \times 10^{-7}$ ($\alpha = 3.21 \times 10^{-7}$ corresponds to $\alpha = 0.05$ with the most conservative correction for multiple comparisons - a Bonferroni correction - applied for a typical FMRI acquisition with $64 \times 64 \times 38$ voxels).

Incorporating Control of the Type II Error Rate

As stressed by Smith et al. [256] controlling the type I error rate via the statistical significance, α, is only one half of the picture when determining if an activation will be detected. The type II error (false negative) rate, as measured using the statistical power, π, must also be controlled. For example, at the minimum SNR given by Equation 4.8, $t = t_\alpha$ and, as shown in Figure 4.3, the statistical power is only 50%, which is less than the standard required power of 80% [256]. To, control the type II error rate and ensure that true activations are detected with a given statistical power, π , t_α in Equations 4.8 and 4.9 should be replaced by $t_{\alpha,\pi}$:

$$SNR_{min} = \frac{t_{\alpha,\pi}}{\sqrt{\left(\frac{\Delta S_\%}{100}\right)^2 \frac{\boldsymbol{X}'_{eff}\boldsymbol{X}_{eff}}{h^2} - \lambda^2 t_{\alpha,\pi}^2}} \tag{4.10}$$

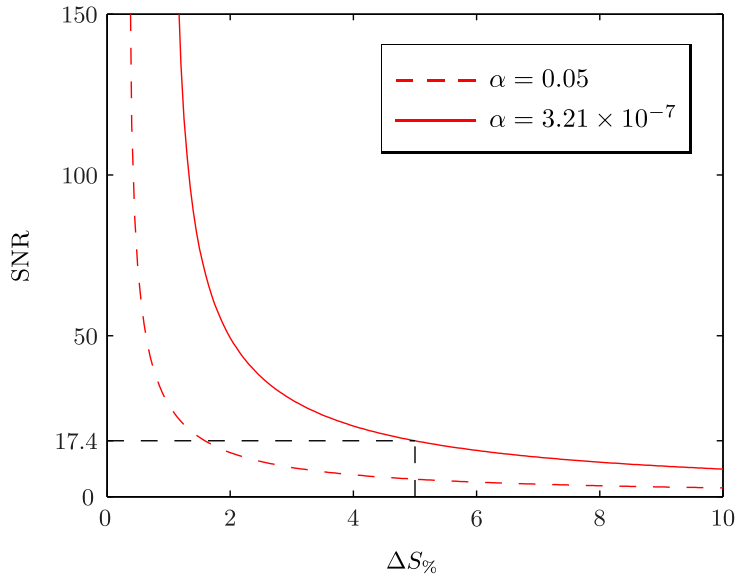

Figure 4.2: The minimum SNR as a function of the percentage change in the BOLD signal $\Delta S_{\%}$. The dashed and solid red lines correspond to a statistical significance, α, of 0.05 and 3.21×10^{-7} respectively. The minimum SNR needed to reject the null hypothesis at the Bonferroni corrected significance level $\alpha = 3.21 \times 10^{-7}$ for a percentage BOLD signal change of 5%, typically observed in the motor and visual cortex, is 17.4.

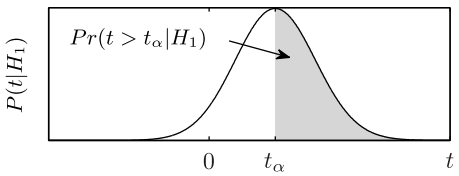

(a) When $t = t_\alpha$ there is only a 50% chance of a true positive result, i.e. the statistical power $\pi = Pr(t > t_\alpha|H_1) = 50\%$, as shown by the shaded region

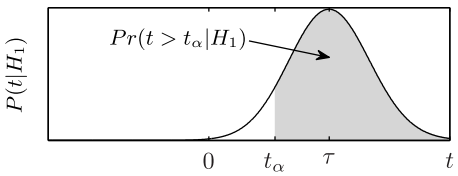

(b) When $t = \tau > t_\alpha$ the statistical power $\pi = Pr(t > t_\alpha|H_1) > 50\%$, as shown by the shaded region

Figure 4.3: Plots showing how the statistical power, $Pr(t > t_\alpha|H_1)$, varies as a function of the size of the t-statistic. Under the alternative hypothesis H_1 the test-statistic has a non central t-distribution $P(t|H_1)$ with $n - m$ degrees of freedom.

and a BOLD signal change is undetectable when:

$$\Delta S_{\%} < \frac{100\lambda t_{\alpha,\pi} h}{\sqrt{\boldsymbol{X}'_{eff}\boldsymbol{X}_{eff}}} \tag{4.11}$$

Where $t_{\alpha,\pi}$ can be determined iteratively using the following algorithm [256]:

1. Use the Student's t inverse cumulative distribution function to determine t_α given the required statistical significance, α, and the number of degrees of freedom $(n - m)$

2. Given t_α from Step 1. calculate the statistical power using non-central t cumulative distribution function with $n - m$ degrees of freedom and non-centrality parameter $\tau = 0$ (i.e. the area to the right of t_α in the non-central t-distribution).

3. Repeat Step 2. with increasing values of τ until the statistical power reaches the required level π, at this point set $t_{\alpha,\pi} = \tau$

With this modification, the novel findings described previously remain valid: there is a minimum percentage BOLD signal change below which activations can never be detected regardless of the SNR. The minimum signal-to-noise ratio, for a statistical power $\pi = 80\%$, as calculated using Equation 4.10, is plotted as a function of $\Delta S_{\%}$ in Figure 4.4 for the same design matrix, contrast and two levels of statistical significance described previously. At this power, the minimum SNR needed to reject the null hypothesis at the Bonferroni corrected significance level $\alpha = 3.21 \times 10^{-7}$ for a percentage BOLD signal change of 5% is 20.4, which compares to a minimum of 17.4 when the type II error rate was not controlled. The minimum detectable percentage BOLD signal change $\Delta S_{\%}$, calculated using Equation 4.9 with t_α replaced by $t_{\alpha,\pi}$, rises from to 1.02% to 1.19%.

Whilst the results shown Figure 4.4 and the minimum SNR and percentage BOLD signal change quoted above are instructive, they refer to a specific FMRI paradigm. However, Equation 4.10 is general and can be used on a case-by-case basis (given the specific expermental paradigm $\boldsymbol{X}$, contrast $\boldsymbol{c}$, the t-statistic threshold $t_{\alpha,\pi}$, the expected percentage change in BOLD signal $\Delta S_{\%}$ and the physiological noise constant λ) to determine the minimum SNR required to detect an activation. For example, if rather than attempting to reduce signal dropout using a novel acquisition strategy, the FMRI paradigm described above were simply doubled in length (i.e. if twice the number of data points were acquired), then the minimum SNR required to detect a BOLD signal change with $\Delta S_{\%} = 5\%$, falls to 13.9. This reduction in minimum SNR is mainly due to $\frac{\sqrt{\boldsymbol{X}'_{eff}\boldsymbol{X}_{eff}}}{h}$ in Equation 4.10, which is proportional

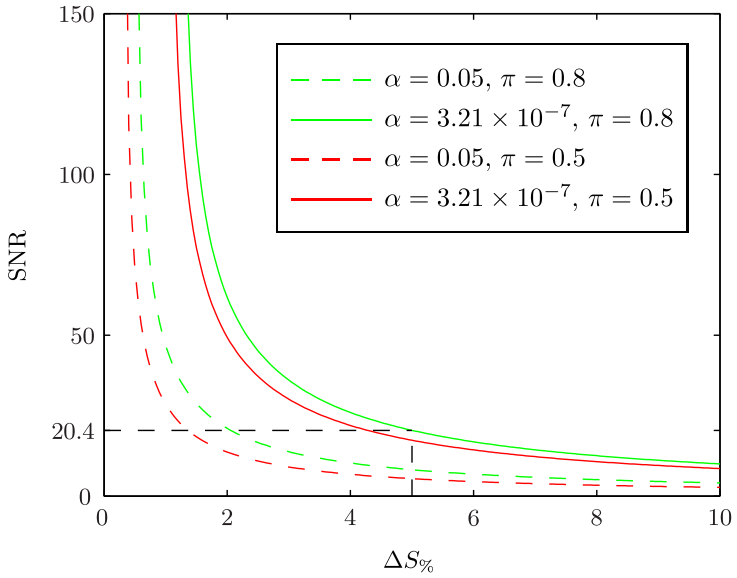

Figure 4.4: The minimum SNR as a function of the percentage change in the BOLD signal, $\Delta S_{\%}$. The dashed and solid green lines correspond to a statisitical significance $\alpha = 0.05$ and $\alpha = 3.21 \times 10^{-7}$ respectively when $\pi = 0.8$. The dashed and solid red lines, taken from Figure 4.4, are are included to demonstrate that the minimum SNR increases when the type II error rate is controlled.

to the square root of the number of timepoints. However, there is also a small effect due to $t_{\alpha,\pi}$ which increases as the number of degrees of freedom, $n - m$, increases.

Put another way, activations may become detectable by either increasing the SNR in the region of signal dropout to above the minimum level, or by reducing the minimum SNR required to detect an activation by changing the FMRI paradigm.

4.2.3 Simulations Demonstrating the Impact of Signal Dropout

Introduction

To demonstrate the impact of a region of signal dropout on the ability of a popular FMRI analysis package to detect activations, when additional processing steps such as cluster level thresholding are applied (the effect of which was not modelled in the previous section), a series of digital phantoms with varying degrees of signal dropout, were constructed in MATLAB. These were then analysed using FEAT (FMRI Expert Analysis Tool) Version 5.98, part of FSL (FMRIB's Software Library, www.fmrib.ox.ac.uk/fsl).

Methods

Each of the three-dimensional digital phantoms(64 $\times$ 64 voxels $\times$150 timepoints, representing a single slice from a task-based FMRI with a duration of 5 minutes

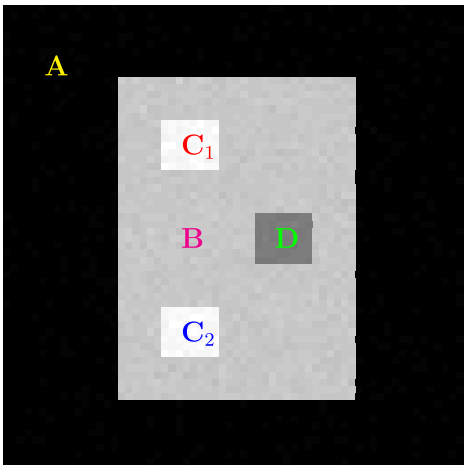

(a) A spatial map of the digital phantom showing the size and positions of the five regions described in the text

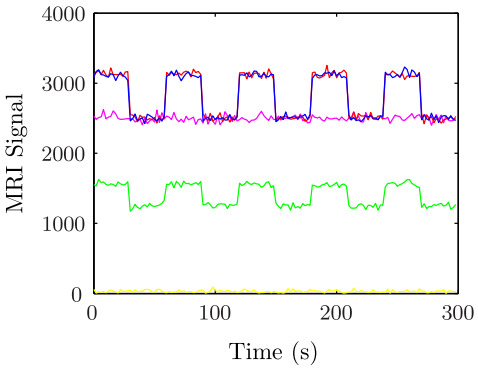

(b) Examples of the MRI signal timecourses from each of five regions, the colors match those used in Figure 4.5(a)

Figure 4.5: An example digital phantom used to determine the effect of signal dropout on the ability of FEAT to detect task-based FMRI activations (for visualisation purposes in this figure $\Delta S_{\%} = 25\%$). Region A is an area of zero signal representing the air surrounding the head. Region B is a region with a constant signal, $S = 2500$, representing the areas of the brain without any BOLD signal changes. Region C is composed of two clusters of activation (C_1 and C_2) in which square-wave modulation was added to the baseline signal with a period of one minute, representing the response to a stimulus with 30 s blocks of task and rest. The percentage change in BOLD signal was 5%. Finally region D is an area in which the baseline signal was reduced incrementally in steps of 250 from 2500 to 0 for each phantom to model the effects of increasing signal dropout. The same square-wave modulation as used in regions C_1 and C_2 was added with $\Delta S_{\%} = 5\%$.

and a repetition time, TR, of 2 s) contained five distinct regions, as shown in Figure 4.5: Gaussian noise with variance $\sigma^2 = \sigma_0^2 + \lambda^2 S^2$ ($\sigma_0 = 25$ and $\lambda = 0.012$) was added to each voxel so that the noise followed the model described previously [261]. It is recognised that the noise in MR magnitude images actually follows a Rician distribution [262], however since this is only significantly different from a Gaussian distribution at low SNR (< 3) the simpler Gaussian noise model was used here. Ten replicas of each phantom were generated; the added noise was realised afresh for each of the replicas.

Each phantom image was then processed separately using FEAT to determine the areas of significant activation. A single column design matrix[2], containing a square-wave with a peak-to-peak amplitude of one and a period of one minute, was used to model the BOLD signal change. The resulting t-statistic maps were converted to z-statistic maps and these were thresholded using clusters determined

[2]In FEAT the data, $\boldsymbol{Y}$, and design matrix, $\boldsymbol{X}$, are demeaned prior to the estimation of $\boldsymbol{\beta}$ so a column of ones to model the baseline signal is not required in the design matrix.

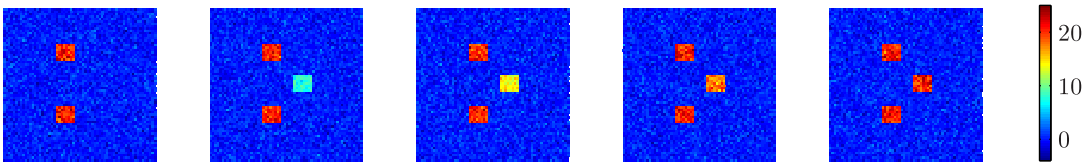

(a) $SNR_D = 0$ (b) $SNR_D = 25$ (c) $SNR_D = 50$ (d) $SNR_D = 75$ (e) $SNR_D = 100$

Figure 4.6: The raw t-statistic images from a simulation of task-based FMRI demonstrating the impact of signal dropout. In Region C, which is unaffected by signal dropout, the t-statistic remains constant, whereas in Region D the t-statistic is reduced as SNR_D goes down i.e. as signal dropout worsens the t-statistic resulting from a GLM analysis drops.

by $z > 2.3$ and a corrected cluster significance threshold of 0.05 [263].

The dependence of the number of false negatives in the thresholded z-statistic map on the SNR in the region of dropout, quantified using the observed statistic power[3], was also calculated.

Results

A selection of the resulting t-statistic maps with different amounts of signal dropout in region D are shown in Figure 4.6. A simple visual inspection suggests that, as expected because the analysis in FEAT is performed voxel-wise, the effect of signal dropout on the t-statistic is localised to the area of signal dropout. This is confirmed by the plots of the mean t-statistic in Figure 4.7, which are in exact agreement with the prediction of Equation 4.7 as plotted in Figure 4.1(b). In regions C_1 and C_2, which are unaffected by signal dropout, the t-statistic remains constant, whereas in region D the t-statistic is reduced as the signal dropout worsens.

The thresholded z-statistic maps are shown in Figure 4.8. In regions C_1 and C_2, which are unaffected by signal dropout, the z-statistic remains constant and above the threshold at which the null hypothesis is rejected. In contrast, in region D the z-statistic is reduced as SNR_D falls, resulting a reduction in the observed power, as shown in 4.9. In this specific case, the observed power falls below 100% when the SNR is less than 20. As expected, the impact of signal dropout is localised, the observed power in regions C_1 and C_2 remains at 100% regardless of the SNR in the region of signal dropout.

[3]Here the observed statistical power is defined as the ratio of the number of voxels in each region that survive in the thresholded z-statistic map divided the number of voxels in that region i.e. the probability that the alternative hypothesis was accepted. This is equal to one minus the false negative rate.

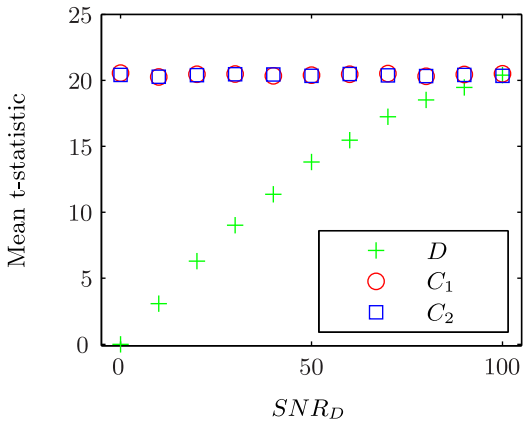

Figure 4.7: Plots of the mean t-statistic in regions C_1, C_2 and D showing quantitatively the dependence of t on the SNR in region D. The error bars representing the standard deviation across the results from the analyses of the 10 replica phantoms at each SNR_D are too small to display at this scale.

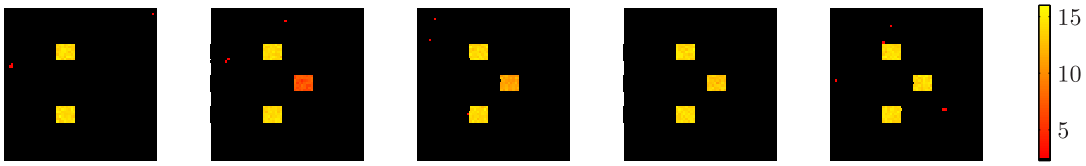

(a) $SNR_D = 0$ (b) $SNR_D = 25$ (c) $SNR_D = 50$ (d) $SNR_D = 75$ (e) $SNR_D = 100$

Figure 4.8: Thresholded z-statistic images from a simulation of task-based FMRI demonstrating the impact of signal dropout. In Region C, which is unaffected by signal dropout, the z-statistic remains constant and above the threshold, whereas in Region D the z-statistic is reduced as SNR_D goes down resulting in an increase in false negatives.

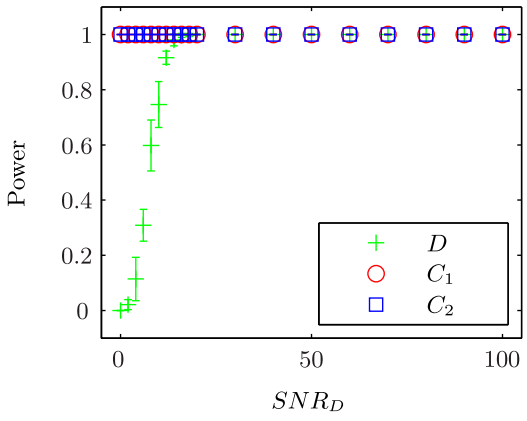

Figure 4.9: A plot of the observed statistical power in regions C_1, C_2 and D as a function of the SNR in the area of signal dropout. The error bars represent the standard deviation across the results from the analysis of the 10 replica phantoms at each signal-to-noise ratio.

Discussion and Conclusions

Reassuringly the dependence of the t-statistics resulting from a FEAT analysis match the earlier theoretical predictions. In addition it is apparent that the observed power of the cluster-level thresholded z-statistics in the region of signal dropout has a sigmoidal dependence on the SNR. The sigmoid shape results from the dependence of the probability of accepting the alternative hypothesis on the observed z-statistic. The decreases in the observed statistical power, for this type of analysis, are localised to the region of signal dropout. Promisingly the dependence of the observed statistical power on the SNR suggests that a modified FMRI acquisition technique that results in only moderate improvements in SNR may still lead to large improvements in the detection of true activations.

4.3 Signal-to-Noise Ratio and the Detection of Resting-State Networks

4.3.1 Introduction

As described in Chapter 3, seed-based and independent component analysis are two common methods to detect resting-state activations from FMRI data. In contrast to the analysis of task-based FMRI data, where the design matrix, $\boldsymbol{X}$, is based on the experimental design and therefore known prior to data acquisition, the variation with time of the resting-state BOLD signal changes are subject and session specific. This difference means that it is not possible to derive analytic expressions for the detectability of resting-state activations when either seed based or independent component analysis are used. In the case of a seed-based analysis, performed using the GLM, the design matrix $\boldsymbol{X}$ is a single column containing the mean time course from a seed region. As the seed time course is corrupted by Gaussian noise the parameters estimates, $\hat{\boldsymbol{\beta}}$, are underestimated, a phenomenon often referred to as regression dilution[264] or attenuation bias. This bias is not allowed for within the common FMRI analysis packages as they were designed to analyse task FMRI data. Therefore it is not possible to derive an expression for the dependence of the t-statistic on the SNR. In the case of probabilistic ICA, no analytic expression for the z-statistic is available because of both the multivariate and iterative natures of the technique. For these reasons, the effect of signal dropout on the detection of resting state networks can only be explored by simulation.

4.3.2 Preliminary In-vivo Experiment

Background

To ensure that the simulations provide a realistic model for the detectability of resting-state networks, estimates of the percentage BOLD signal change $\Delta S_{\%}$ and SNR for typical resting-state FMRI data are required.

Unlike task-based FMRI, only two previous studies discuss the relative magnitudes of the signal and noise observed in resting-state FMRI data sets. Using the correlation coefficients observed in seed-based analyses of RS-FMRI data, Fox and Greicius [265] suggest that resting-state activity could account for between 50-80% of the variance of the voxel signal across time. Johnson et al. [266] observed that the typical contrast-to-noise ratio (CNR) of RS-FMRI data is 0.8. To confirm these values, FMRI data were collected from a single healthy male subject.

Methods

FMRI data were acquired using a gradient-echo EPI sequence on a 3T GE Signa HDx system (General Electric, Waukesha, WI, USA). A quadrature head coil was used for RF transmission and reception. The quadrature coil was used to allow the measurement of noise in a region outside of the head, as this would be not be possible in images from mulitple channel receive-only coils since a masking step is performed when the images from each of the coils are combined. A total of 256 volumes (preceded by four dummy scans to allow the signal to reach a steady state), each with 33 slices, were acquired with a repetition time of 2 s and an echo time of 30 ms. The flip angle was 75° and the field of view was 21.9 cm with a 64×64 acquisition matrix. During the first four minutes and fifty seconds the subject was at rest with their eyes open, then for the remaining time they performed self-paced finger tapping with their right hand in 30 s blocks of rest and activity. For simplicity, the cues to start and stop finger tapping were delivered verbally. The slices were prescribed to include a region of air above the head to enable a straightforward estimation of the noise from a region free from signal.

The intrinsic noise, σ_0, was estimated from a region of interest in the slices above the head in the first volume. As the noise in this signal free region has a Rayleigh distribution the intrinsic noise, σ_0, was calculated using [262]:

$$\sigma_0 = \frac{\sigma_{ROI}}{\sqrt{2 - \frac{\pi}{2}}} \tag{4.12}$$

Assuming that, in an area known to be part of a resting-state network, the temporal variance of the signal σ^2 is simply the sum of the intrinsic variance σ_0^2 and

the variance due to resting-state activity σ^2_{BOLD}, then:

$$\sigma^2_{BOLD} = \sigma^2 - \sigma^2_0 \tag{4.13}$$

With this simplifying assumption, σ^2_{BOLD} represents an upper limit on the variance of the BOLD signal due to resting-state activity. The assumption is only valid if there is no variance due to cardiac and respiratory effects, or scanner instabilities, which cause signal variations between each volume of acquired data. To determine the spatial location of the left motor cortex, which has been previously shown to be in a resting-state network with the supplementary motor area and right motor cortex[12], the portion of the data set (the final 111 volumes) during which the subject performed the finger tapping task were analysed using FEAT. The data were preprocessed by applying motion[205] and slice timing corrections, the brain was extracted using BET [267], and spatially smoothed with a Gaussian kernel with a FWHM of 5mm. High pass temporal filtering was then performed using a Gaussian-weighted least squares fit with a standard deviation of 50s. The data were then grand-mean intensity normalised such that the mean signal across time and space was 10000. After local autocorrelation correction a linear least squares fit was performed using a single column design matrix (containing a square wave convolved with a gamma function with a phase of 0s, standard deviation of 3s and a 6s mean lag to model the HRF) using FILM [224]. The resulting z-statistic maps were thresholded using clusters determined by $z > 2.3$ and a corrected cluster significance threshold of 0.05 [263]. Using the statistically significant cluster in the left motor area as a mask the total temporal variance, σ^2, was measured from the initial resting state portion of the data. The variance of the BOLD signal due to resting-state activity was then estimated using Equation 4.13. In addition the mean signal and SNR in the same ROI were calculated.

Results

The noise in the region of interest above the head $\sigma_{ROI} = 15.9$, therefore $\sigma_0 = 24.3$. The total temporal variance in the ROI defined by the cluster of significant activation in the left motor cortex was $\sigma^2 = 1380$. Therefore, the variance due to resting state activity, calculated using Equation 4.13 was $\sigma^2_{BOLD} = 790$, which is 57% of the total variance. In the same region the mean signal was $S = 2570$ and the SNR was 114.

Discussion and Conclusions

The percentage of the variance explained by the resting-state BOLD signal (57%) fell within the range (50-80%) given previously by Fox and Greicius [265], and as such it will be used in the following simulations of the detectability of resting-

state networks. As noted above, this is an upper limit on the resting-state signal variance, as the effect of variance due to scanner instabilities, cardiac pulsatility and respiratory effects were not accounted for.

4.3.3 Simulating the Effects of SNR

Methods

A set of digital phantoms with varying degrees of signal dropout were constructed in MATLAB. Each of the three-dimensional digital phantoms (64×64 voxels ×240 time points, representing a single slice from a resting-state FMRI data set with a duration of 8 minutes acquired with a TR of 2s) contained five distinct regions as shown in Figure 4.10. Region A is an area of zero signal representing the air surrounding the head. Region B is a region with a constant signal, $S = 2500$ (rounded down from the measured in-vivo value), representing the areas of the brain without any BOLD signal changes. Regions C_1, C_2 and C_3 had a sine-wave modulation with a frequency of 0.0375 Hz added to the baseline signal, representing the time course of a resting-state network. (This model of a resting-state time course has been used previously [166]). Three different percentage changes in BOLD signal were used for the simulations $\Delta S_{\%} = 0.5$, 1 and 1.5%. (For a sine wave the peak-to-peak amplitude is equal to $\sqrt{2}$ times its standard deviation. Therefore, given that the BOLD variance measured in-vivo was 790, then the change in BOLD signal $\Delta S = \sqrt{2}\sqrt{790} = 40$, therefore $\Delta S_{\%} \approx 1.5\%$. Since the estimate of the variance was an upper bound, $\Delta S_{\%}$ of 0.5% and 1% were also simulated). In areas D_1, D_2 and D_3 a sine-wave modulation (f=0.03 Hz) was added to the baseline signal, representing the time course of a second resting-state network. The percentage change in BOLD signal was the same as regions C_1, C_2 and C_3. In region D_2 the baseline signal was reduced incrementally from 2500 to 0 for each phantom generated. In this way successive phantoms modelled the effect of increasing signal dropout in one node of a resting-state network. Gaussian noise with a standard deviation of 25 was added to each voxel. In contrast to the task-based FMRI simulation presented earlier, physiological noise was not modelled. Ten replicas of each phantom were generated (with the added noise realised afresh for each of the replicas)

Seed based analysis of the phantoms was performed separately for each seed regions shown in Figure 4.10 using FEAT. A single column design matrix containing the mean signal from the seed ROI was used. The resulting t-statistic maps were converted to z-statistic maps that were then thresholded using clusters determined by $z > 2.3$ and a corrected cluster significance threshold of 0.05 [263]. The mean t-statistic in each of the regions defined above was plotted as a function of SNR in the region of signal dropout at $\Delta S_{\%} = 0.5$, 1 and 1.5%. In addition, the observed power

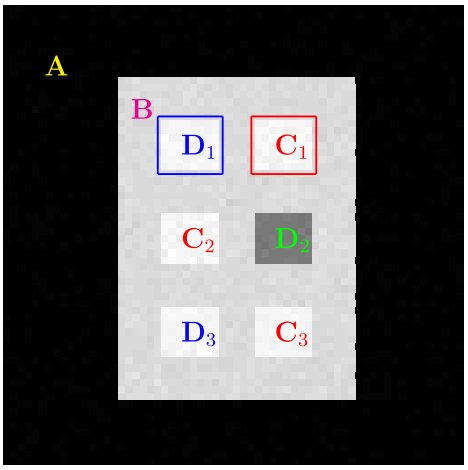

(a) A spatial map of the digital phantom showing the size and positions of the five regions described in the text

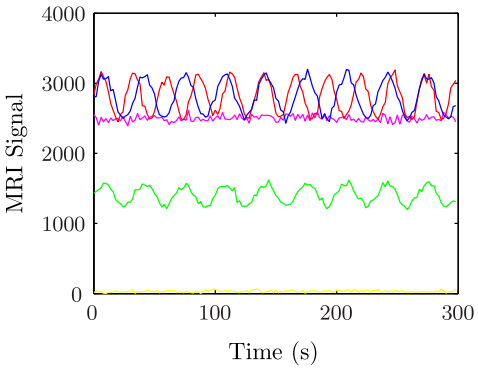

(b) Examples of the MRI signal time courses from each of five regions, the colors match those used in Figure 4.10(a)

Figure 4.10: An example of the digital phantoms used to determine the effect of signal dropout on the ability of seed-based and independent component analyses to detect resting-state networks (To allow the reader to visually differentiate the different regions of the phantom $\Delta S_{\%} = 25\%$ in this figure). The three regions C_1, C_2 and C_3 are three nodes in a resting state network and the red square denotes the location of the region-of-interest used to generate the seed time course for this network. Regions D_1, D_2 and D_3 are three nodes in a second resting state network. The blue square denotes the location of the region-of-interest used to generate the seed time course for this network.

(as defined in Section 4.2.3) in the thresholded z-statistic maps was also plotted as a function of SNR in the region of signal dropout at $\Delta S_{\%} = 0.5$, 1 and 1.5%.

Probabilistic Independent Component Analysis, discussed in Chapter 3, as implemented in MELODIC v.3.10 [220] was performed separately on each of the phantoms. Firstly the variance was normalised on a voxel-by-voxel basis; the data were then whitened and the first two principal components kept. These were decomposed into sets of time courses and spatial maps by optimising for non-Gaussian spatial source distributions using FastICA [243]. The estimated components were divided by the standard deviation of the residual noise to produce z-statistic maps. These were thresholded at p=0.05 (Bonferroni corrected for multiple comparisons for the 64×64 voxels). The mean, unthresholded, z-statistic was plotted as a function of SNR in the region of signal dropout at $\Delta S_{\%} = 0.5$, 1 and 1.5%. The observed power in the thresholded z-statistic maps was also plotted as a function of SNR in the region of signal dropout at $\Delta S_{\%} = 0.5$, 1 and 1.5%.

Results of the Seed Based Analysis Simulations

A representative selection of the t-statistic maps showing the networks correlated with each seed region at $\Delta S_{\%} = 0.5$, 1 and 1.5% for different amounts of signal dropout in region D_2 are shown in Figure 4.11. Qualitatively, these show that for a seed-based analysis the effect of signal dropout on the t-statistic is localised to Region D_2 (the area of signal dropout) for all of the percentage BOLD signal changes tested. This is confirmed by the plots of the mean t-statistic for each of the regions, Figure 4.12, which show quantitatively the dependence of t on the signal-to-noise ratio in Region D_2. In regions C_1, C_2, and C_3 the t-statistic remains constant. This is also the case for regions D_1 and D_3, which are also unaffected by signal dropout. In contrast, in region D_2, the t-statistic decreases linearly with the signal-to-noise ratio at each of the percentage BOLD signal changes tested. The t-statistic is lower for smaller percentage changes in BOLD signal.

The thresholded z-statistic maps are shown in Figure 4.13. These show qualitatively that, for a seed-based data analysis, the effect of signal dropout is localised to the area of signal dropout, region D_2. The increase in the number of false negatives with increasing signal dropout is shown quantitatively, using the observed statistical power, in Figure 4.14. For $\Delta S_{\%} = 0.5\%$ the observed power remains at an approximately constant value of 90% in regions C_1 and D_1 (the seed regions). In regions C_2, C_3 and D_3 (the resting-state network nodes unaffected by signal dropout), the observed power also remains constant, at a lower value of approximately 50%. For both $\Delta S_{\%} = 1\%$ and 1.5% the observed power remains at 100% in all the nodes unaffected by dropout. In contrast, in region D_2 the observed power has a sigmoid shape; at low SNR the power is close to zero, then as the SNR increases the

power increases to 100%. At the highest percentage BOLD signal change (1.5%) the power begins to increase at a lower SNR and the rate of increase is greater than for $\Delta S_{\%} = 0.5\%$ and 1.0%.

Results of the Probabilistic ICA Simulations

The thresholded z-statistic maps resulting from the probabilisitic independent component analysis are shown in Figure 4.15. As in the case of a seed-based analysis, these show that the effect of signal dropout is localised to the area of signal dropout, region D_2, for each $\Delta S_{\%}$ simulated. When $\Delta S_{\%} = 0.5\%$ none of the nodes are detected regardless of the degree of signal dropout. The mean unthresholded z-statistic in each of the regions, shown in Figure 4.16, shows that for $\Delta S_{\%} = 1\%$ and 1.5% z increases linearly in the region of signal dropout with the SNR. When $\Delta S_{\%} = 0.5\%$ the mean unthresholded z-statistic remains low for all SNRs simulated.

The increase in the number of false negatives with increasing signal dropout is shown quantitatively, using the observed statistical power as a metric, in Figure 4.17. When $\Delta S_{\%} = 0.5\%$ the observed statistical power in all regions is close to 0% so, regardless of the degree of signal dropout, the networks are not detected. When $\Delta S_{\%} = 1.0\%$ the observed power is approximately 80% in the regions unaffected by signal dropout, for $\Delta S_{\%} = 1.5\%$ this increases to 100%. Again, as for a seed-based analysis, in region D_2 the observed power has a sigmoid shape: at low SNR the power is close to zero, but as the SNR increases the power increases rapidly to 100%. As before the at the highest percentage BOLD signal change (1.5%) the power begins to increase at a lower SNR and the rate of increase is greater than for $\Delta S_{\%} = 1.0\%$.

Discussion and Conclusions

As outlined in the introduction to Section 4.3 it is not possible to determine analytic expressions for dependence of the t-statistic and z-statistics resulting from seed-based and independent component analyses, nor to determine the minimum SNR required to show an activation at a specified statistical significance and power. Therefore simulated data were used in conjunction with freely available and commonly used FMRI analysis software to determine the impact of a region of signal dropout on the ability to detect resting-state activations.

I have found that at a biologically plausible percentage BOLD signal change of 1.5%, the minimum SNR required to detect resting-state activations, from an eight minute acquisition, with a power of 80% was approximately 40 for a seed-based analysis and 60 for independent component analysis. However, it should be noted that these simulations used digital phantoms that only included two 'resting-

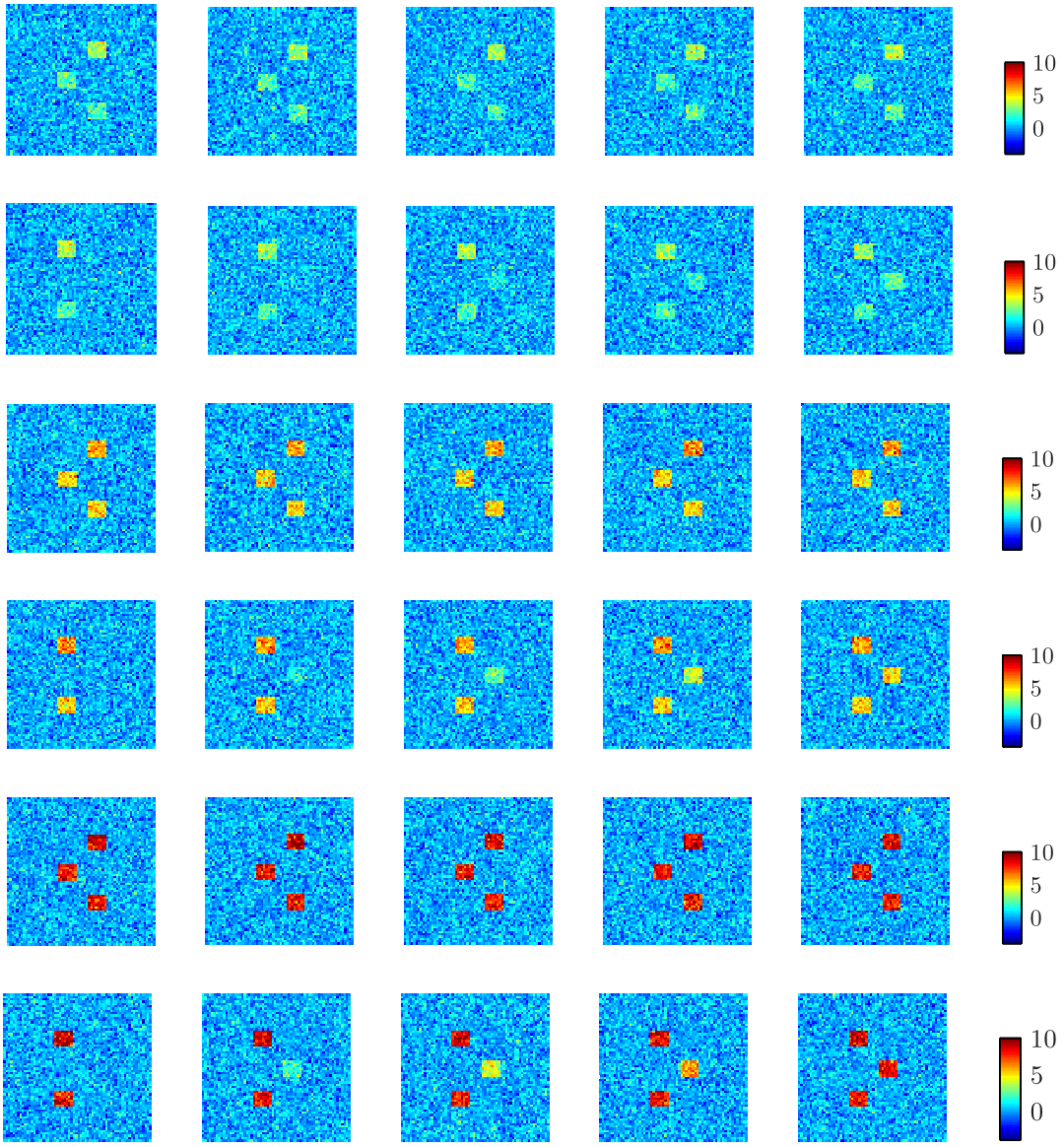

Figure 4.11: The raw t-statistic images from a simulation of seed-based resting-state FMRI analysis demonstrating the impact of signal dropout at three different percentage BOLD signal changes, 0.5%, 1% and 1.5%. The first pair of rows shows the t-statistic when $\Delta S_{\%} = 0.5\%$. The second and third pairs are for $\Delta S_{\%} = 1.0\%$ and $\Delta S_{\%} = 1.5\%$ respectively. The first row in each pair correspond to the case when C_1 was used as the seed region and the second when D_1 was used as the seed region. The SNR in region D_2 increases from zero in the first column, in steps of 25 to 100 in the final column.

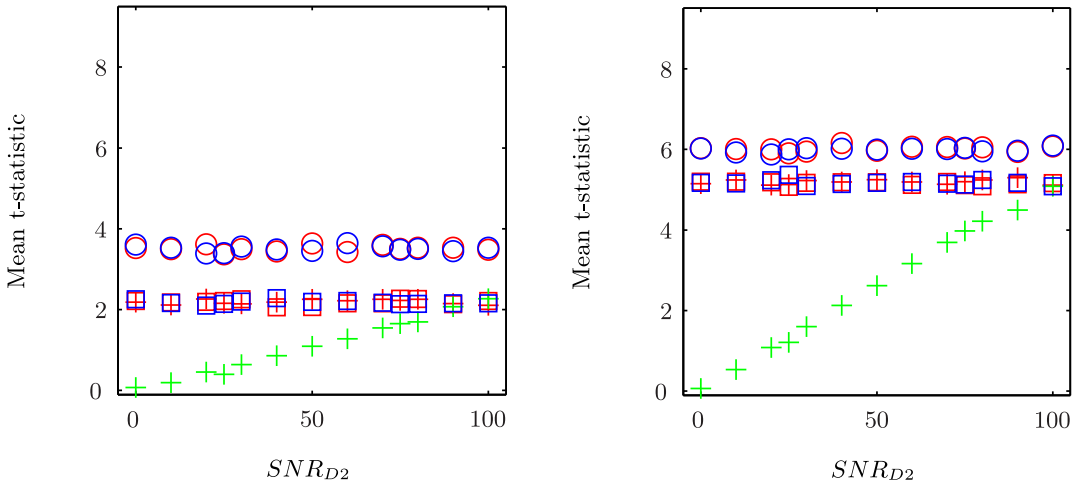

(a) $\Delta S_{\%} = 0.5\%$

(b) $\Delta S_{\%} = 1\%$

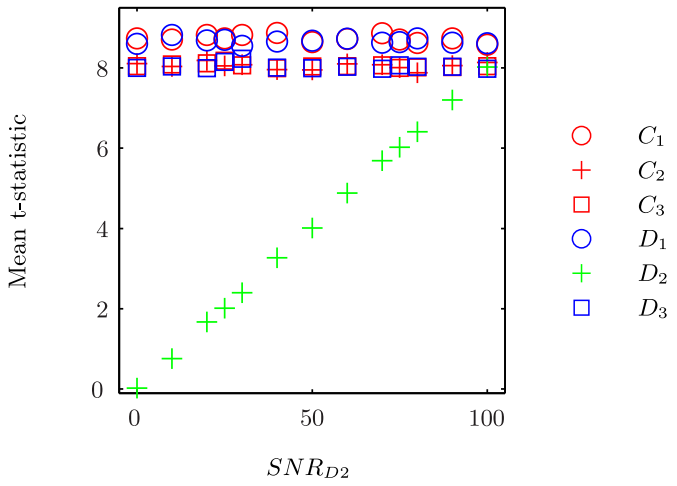

(c) $\Delta S_{\%} = 1.5\%$

Figure 4.12: Plots of the mean t-statistic in regions C_1 to D_3 showing quantitatively the dependence of t on the SNR in Region D_2, for a seed-based analysis. The standard deviation across the results from the analyses of the 10 replica phantoms at each SNR_{D2} are too small to display at this scale.

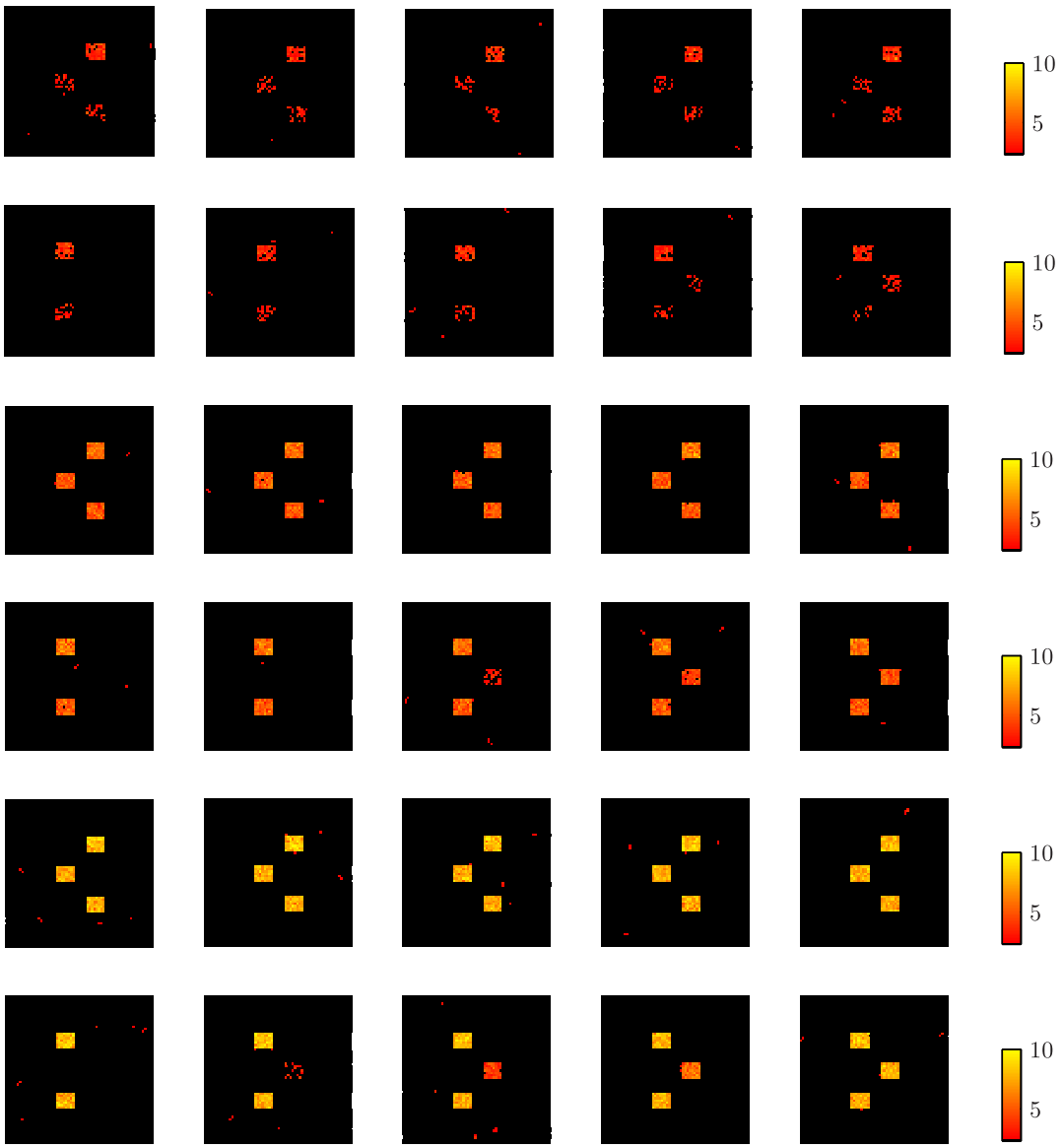

Figure 4.13: The thresholded z-statistic images from a simulation of seed-based resting-state FMRI analysis demonstrating the impact of signal dropout at three different percentage BOLD signal changes, 0.5%, 1% and 1.5%. The first pair of rows show the z-statistic when $\Delta S_{\%} = 0.5\%$. The second and third pairs are for $\Delta S_{\%} = 1.0\%$ and $\Delta S_{\%} = 1.5\%$ respectively. The first row in each pair correspond to the case when C_1 was used as the seed region and the second when D_1 was used as the seed region. The SNR in region D_2 increases from zero in the first column, in steps of 25 to 100 in the final column.

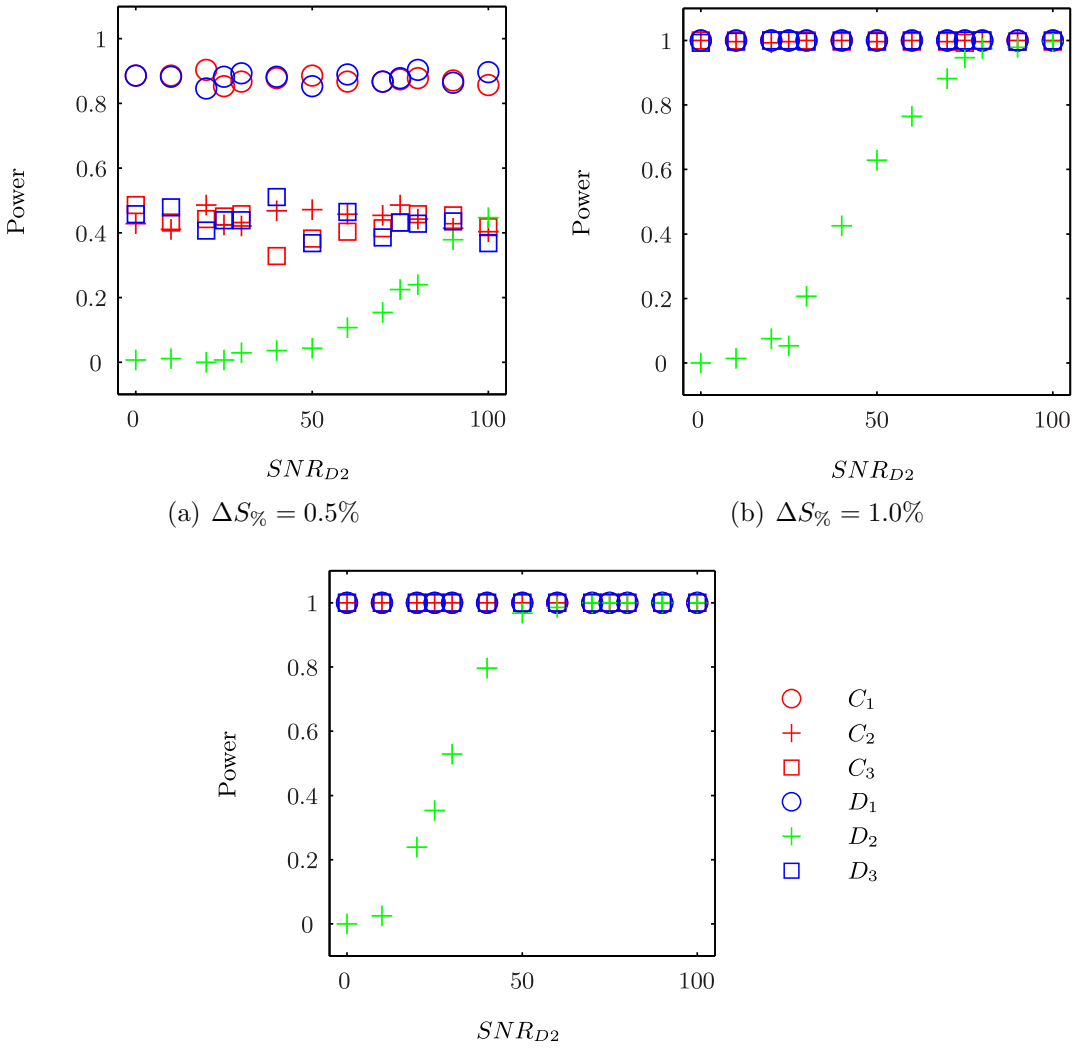

(a) $\Delta S_{\%} = 0.5\%$ (b) $\Delta S_{\%} = 1.0\%$

(c) $\Delta S_{\%} = 1.5\%$

Figure 4.14: Plots showing quantitatively the dependence of the observed power in regions C_1 to D_3 on the SNR in region D_2, for a seed-based analysis. The standard deviation across the results from the analyses of the 10 replica phantoms at each SNR_{D2} are too small to display at this scale.

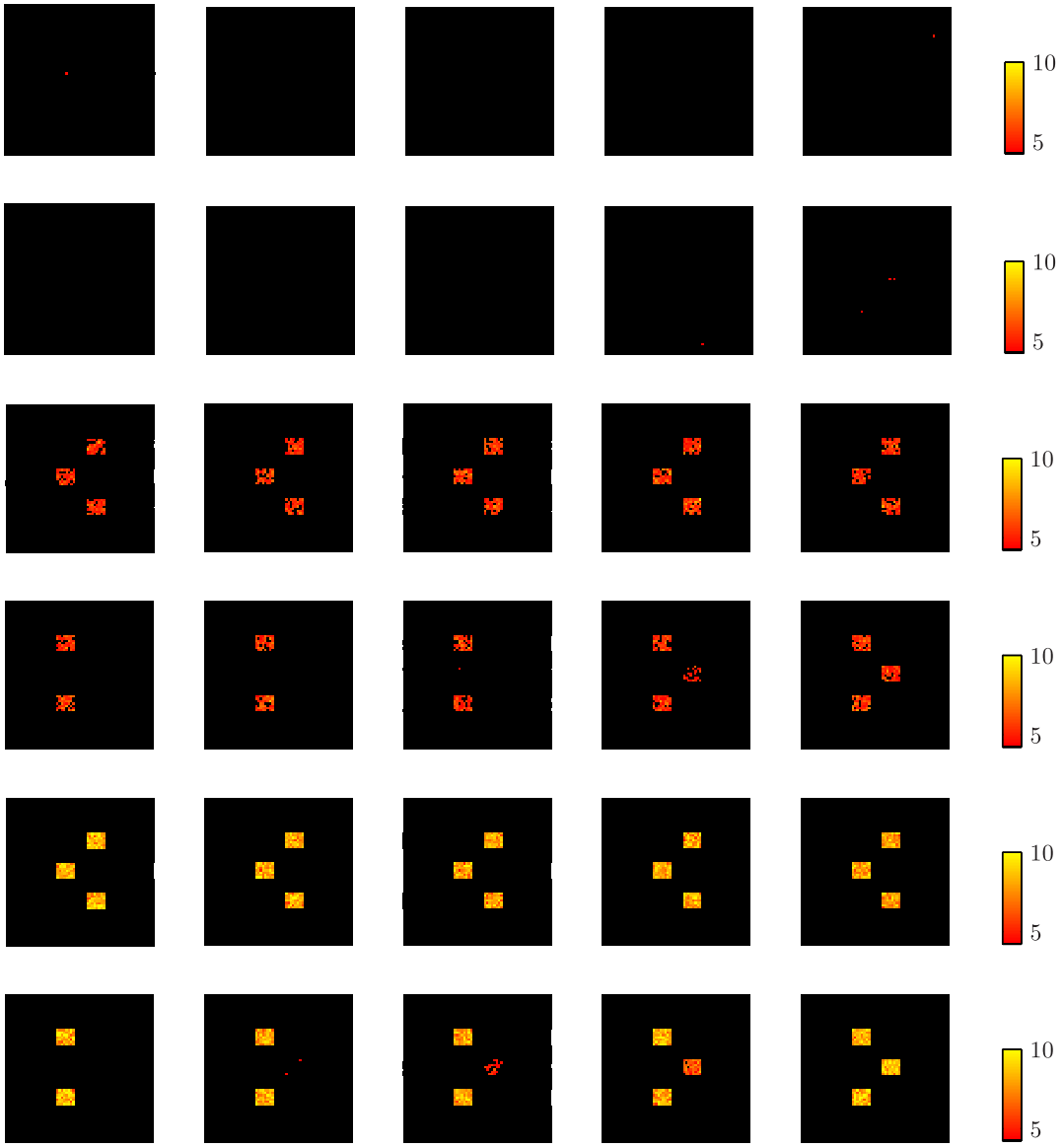

Figure 4.15: The thresholded z-statistic images from a simulation of ICA analysis resting-state FMRI data demonstrating the impact of signal dropout at three different percentage BOLD signal changes, 0.5%, 1% and 1.5%. The first pair of rows shows the z-statistic when $\Delta S_{\%} = 0.5\%$. The second and third pairs are for $\Delta S_{\%} = 1.0\%$ and $\Delta S_{\%} = 1.5\%$ respectively. The first row in each pair when C_1 was used as the seed region and the second when D_1 was used as the seed region. The SNR in region D_2 increases from zero in the first column, in steps of 25 to 100 in the final column.

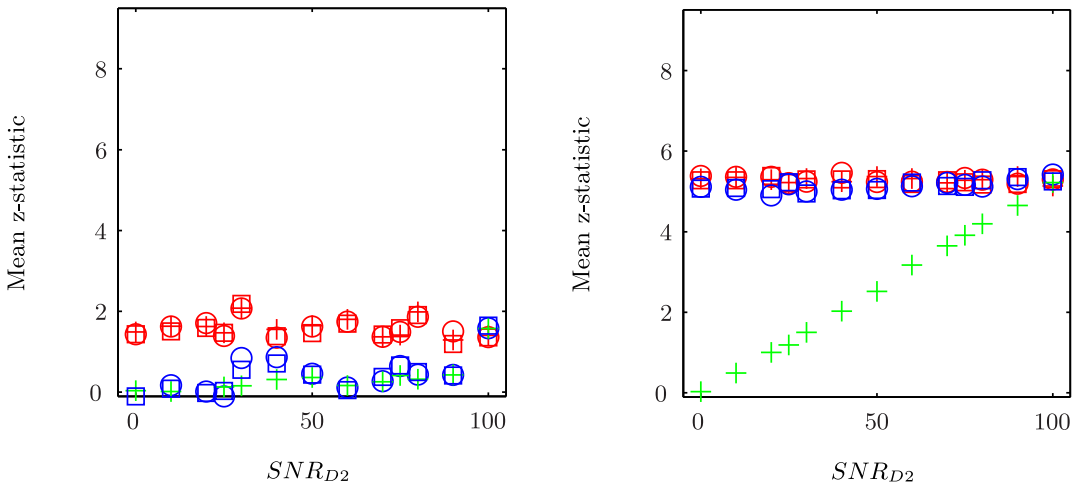

(a) $\Delta S_{\%} = 0.5\%$

(b) $\Delta S_{\%} = 1.0\%$

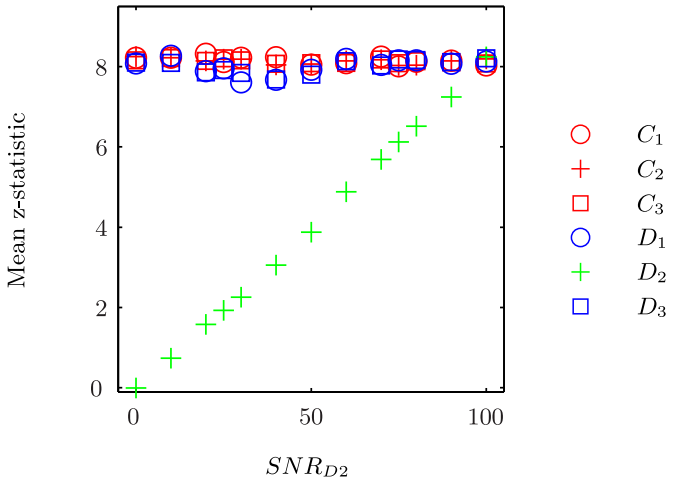

(c) $\Delta S_{\%} = 1.5\%$

Figure 4.16: Plots of the mean z-statistic in regions C_1 to D_3 showing quantitatively the dependence of z on the SNR in region D_2, the region of signal dropout for a simulation of probabilistic independent component analysis of resting-state FMRI data. The standard deviation across the results from the analyses of the 10 replica phantoms at each SNR_{D2} are too small to display at this scale.

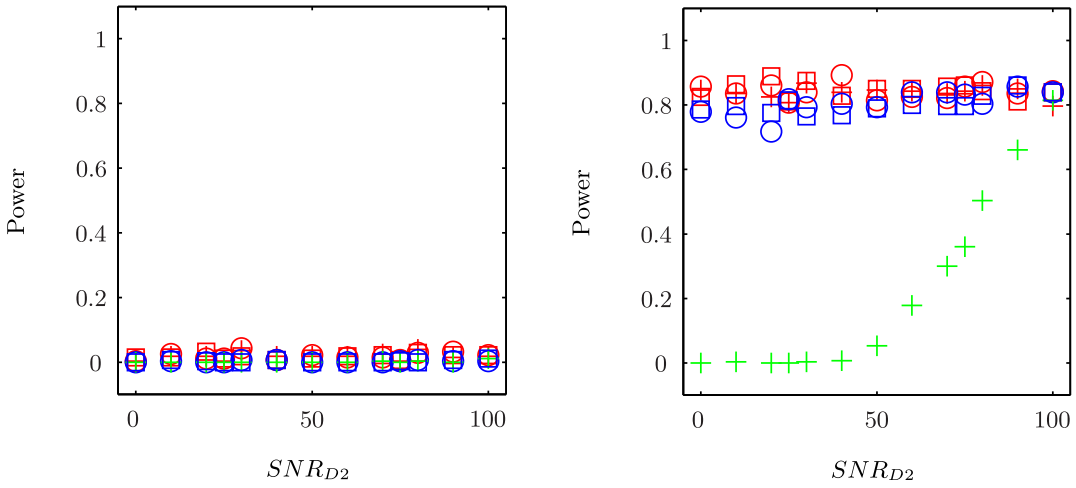

(a) $\Delta S_{\%} = 0.5\%$

(b) $\Delta S_{\%} = 1.0\%$

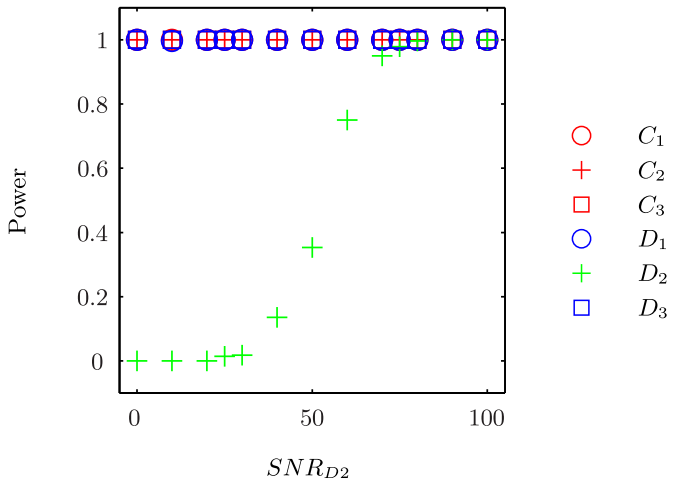

(c) $\Delta S_{\%} = 1.5\%$

Figure 4.17: Plots showing quantitatively the dependence of the observed power in regions C_1 to D_3 on the SNR in region D_2, for a probabilistic independent component analysis. The standard deviation across the results from the analyses of the 10 replica phantoms at each SNR_{D2} are too small to display at this scale.

state' networks with simple sinusoidal time courses corrupted by Gaussian noise therefore it is unclear how readily these minimum signal-to-noise levels will translate to human subjects. I have also demonstrated, using these simulations, that the impact of a region of signal dropout on the ability to detect resting-state activations is localised to the area of reduced signal-to-noise. This was seen clearly in the thresholded z-statistic resulting from both seed-based and independent component analyses, Figures 4.13 and 4.15, as well as in the graphs of the observed power in each region of the digital phantom as a function of the SNR in the region of signal dropout, Figures 4.14 and 4.17. These results could imply that there are extra nodes in commonly observed resting state networks that are currently not detected because of signal dropout in regions such as the orbitofrontal and inferior temporal regions.

4.4 Conclusion

Firstly, for task-based FMRI data, by combining the model of Smith et al. [256] with the physiological noise model of Kruger and Glover [261] I have shown that the t-statistic does not increases linearly with SNR. Rather, the rate of increase reduces until the t-statistic reaches a maximum level. A further consequence of incorporating the model of physiological noise is that there is a minimum percentage BOLD signal change that is dependent on the experimental design, below which, regardless of the SNR, activations will never be deemed to be statistically significant. This information is vital when determining whether or not a novel method to reduce signal dropout will result in an increased ability to detect brain activations.

Secondly, I have shown by simulation for task-based FMRI data that signal dropout causes a localised reduction in the observed statistical power in cluster-level thresholded z-statistic maps, i.e. there is a localised failure to detect true-activations as a result of the signal dropout.

Thirdly, by simulation, I have demonstrated that for both seed-based and independent component analyses of RS-FMRI data, the impact of a region of signal dropout on the ability to detect resting-state activations is localised to the area of reduced signal-to-noise. Since this could imply that there are nodes in commonly observed resting state networks that are currently not detected acquisition techniques will be developed in the later chapters to reduce signal dropouts in RS-FMRI data. It was also demonstrated that the observed statistical power is a sigmoid function of the SNR. Therefore, as for task-based FMRI, small improvements in the signal in regions of dropout may lead to large increases in the detectability of resting-state activations.

Chapter 5

Reducing Signal Dropout with Z-Shimming

5.1 Introduction

Z-shimming [27, 72, 74, 268–274] is a well known technique that can be used to reduce signal dropout in gradient echo images. By modifying the amplitude of the slice selection gradient refocusing lobe, the effects of linear through-plane susceptibility gradients can be cancelled out. A number of different implementations of z-shimming have been shown to increase the detectability of task induced BOLD signal changes in the regions of signal dropout such as the orbitofrontal cortex, inferior temporal and parahippocampal-amygdala regions [72, 271, 273–275].

In this chapter I describe an extension to previous studies; optimising the z-shim gradients used to correct signal dropout in grey matter on a per subject and per slice basis. I demonstrate the methods effect on the detectability of both task-based and resting-state BOLD signal changes in six healthy volunteers at 3 T.

5.2 Theoretical Background

As described briefly in Section 2.6, a linear susceptibility gradient in the direction of slice selection, $G_{z,s}$, induces a linear variation in the phase, ϕ, of the transverse magnetisation, M_{xy}, across the slice:

$$\phi = \gamma \, TE \, G_{z,s} z \tag{5.1}$$

Frahm et al. [27] showed that this could be cancelled out by modifying the area of the refocusing lobe of the slice selection gradient. Equivalently, a gradient with area $A_{z,sh}$ can be added immediately after the refocusing lobe; Figure 5.1. The dephasing

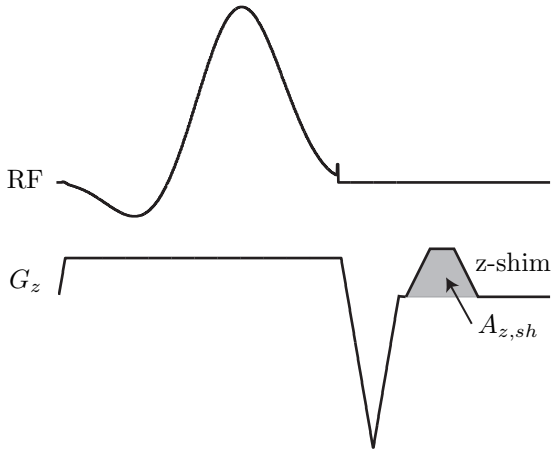

Figure 5.1: A z-shim gradient with area $A_{z,sh}$ immediately follows the refocusing lobe of the slice selection gradient.

caused by the susceptibility gradient is cancelled out when:

$$A_{z,sh} = -G_{z,s}\,TE \tag{5.2}$$

In regions of homogeneous field the additional z-shim gradient causes dephasing and therefore results in signal loss. For perfectly rectangular slice profiles it is straightforward to show that the signal in a magnitude image is a function of the echo time, TE, susceptibility gradient, $G_{z,s}$, slice thickness Δz and z-shim gradient area, $A_{z,sh}$ [74]:

$$S = M_0 \Delta z \left| \mathrm{sinc}\left(\frac{\gamma \Delta z}{2} \left[G_{z,s}\,TE + A_{z,sh} \right] \right) \right| \tag{5.3}$$

As shown in Figure 5.2 without a z-shim gradient there is complete signal dropout when $G_{z,s}$ is equal to an integer multiple of $\left(\frac{2\pi}{\gamma \Delta z TE}\right)$. For comparison with previous studies it is useful to express Equation 5.3 in terms of displacements of the signal in the slice selection (z) direction in k-space [73, 276]. The susceptibility gradient causes the maximum signal to shift in k-space by:

$$\delta k_{z,s} = \frac{\gamma}{2\pi} G_{z,s} TE \tag{5.4}$$

from $k_z = 0$ and the z-shim gradient causes a shift of:

$$\delta k_{z,sh} = \frac{\gamma}{2\pi} A_{z,sh} \tag{5.5}$$

With these two relationships Equation 5.3 is:

$$S = M_0 \Delta z \left| \mathrm{sinc}\left(\pi \Delta z \left[\delta k_{z,s} + \delta k_{z,sh} \right] \right) \right| \tag{5.6}$$

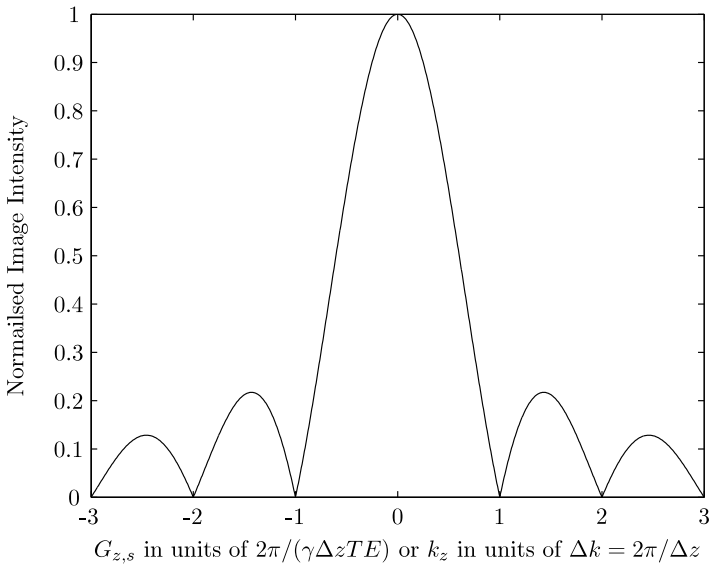

Figure 5.2: Signal intensity attenuation as a function of through-plane susceptibility gradient for an ideal rectangular slice.

When the shift in k-space caused by the susceptibility gradient is cancelled by the z-shim gradient ($\delta k_{z,sh} = -\delta k_{z,s}$) the maximum signal occurs at $k_z = 0$ and therefore the signal is completely recovered.

5.3 Existing Implementations of Z-shimming

Following the initial demonstration of signal recovery with z-shimming [27] the technique has undergone a number of developments to enable its use in FMRI experiments. Since the idea was first postulated it has been recognised that to recover signal in regions of dropout whilst maintaining signal in the regions of homogeneous field, multiple images acquired with different degrees of z-shimming must be combined [27]. Initially the sets of images were simply averaged [27], however, in more recent implementations a composite image is formed from the square root of the sum of squares (SSQ) of the z-shimmed images [74, 268, 274]. Composite images can be produced from as a few as two images acquired with different z-shim gradients [271, 274]. With conventional GE-EPI this results in a doubling of the effective repetition time. Z-shimming has also been implemented in multi-echo acquisition schemes[272, 275, 277–279] allowing images with different degrees of z-shimming to be acquired in a single shot. However, depending on the details of the implementation, the resulting images can have differing BOLD sensitivities because of the different echo times, or increased distortion because of reduced bandwidth in the phase-encoding direction. A volume-selective method, in which z-shimming is only applied to a subset of slices to reduce the loss of temporal resolution, has been shown

to increase the detectability of BOLD signal changes in the orbitofrontal cortex[273].

A range of different methods to select the optimal z-shim gradients have been proposed, requiring varying amounts of time for data acquisition, computational effort and user input. In the first method, described by Cordes et al. [271], FMRI data were acquired with interleaved volumes, the first without any z-shimming, and the second with slice specific z-shim gradients. These were determined using a semi-automated method; a calibration scan, in which 40 volumes were acquired with varying amounts of z-shimming, was parcellated into regions with similar susceptibility gradients. The experimenter then selected, for each slice, the region in which they wanted to recover signal. Whilst this user input makes the technique flexible it is also time consuming. Gu et al. [272] described the first fully-automated method. Again they collected FMRI data with interleaved volumes, however, in this case both volumes in each pair included slice specific z-shimming. These were determined from a calibration scan in which 16 volumes were acquired with varying amounts of z-shimming. All pairwise combinations of the calibration scan volumes were combined by SSQ. For each slice, the z-shim combination which most closely matched the SSQ combination of all 16 volumes was deemed optimal. Marshall et al. [274] further reduced the number of volumes in the calibration scan to just four. This saved time acquiring calibration data, however, resulted in a more computationally intensive and time consuming optimisation. This meant that a single pair of optimal shims were determined for the whole brain, rather than on a slice specific basis. Alternative, fully automated, methods described by Heberlein and Hu [280] and Truong and Song [279] used field maps, rather than calibration scans, to determine the optimal pair of z-shim gradients for each slice.

5.4 Optimising Z-shimming for Task-Based and Resting-State FMRI Experiments

5.4.1 Introduction

A method was developed to determine the slice specific z-shims which reduced signal dropout. This was based on data acquired during a calibration scan. In addition, the process was restricted to grey matter since this is the origin of the BOLD signal changes observed in task-based and resting-state FMRI. Following previous studies the composite SSQ images will be formed from pairs of images acquired using different z-shim gradients [271, 274].

5.4.2 Z-shim Pulse Sequence Programming

A GE-EPI pulse sequence with the ability to play out a slice specific z-shim gradient had previously been implemented for a 3 T GE Signa HDx system (at software release 12.0) within the Department of Neuroimaging by Dr David Lythgoe. This was upgraded for use on both a 3 T GE Signa HDx system (at software release 14.0M5) and a 3 T GE Discovery MR750 System (at software release 22.0). The pulse sequence was flexible and could be used to acquire either calibration scan or FMRI data.

The k-space shift, $\delta k_{z,sh}$, produced by the z-shim gradient was selected using three parameters. The number of shim-steps $N_{z,shim}$, a parameter β_z which allowed $k_{z,sh}$ to be set in units of $1/\Delta z$ and a shim number ζ_z that was slice and volume specific. The choice of $N_{z,shim}$, β_z and the slice thickness Δz determine the range of k-space shifts (and therefore the range of susceptibility gradients) which can be corrected for:

$$-\frac{N_{z,shim}-1}{2\beta_z\Delta z} \leq \delta k_{z,sh} \leq \frac{N_{z,shim}-1}{2\beta_z\Delta z} \tag{5.7}$$

The k-space shift for a specific shim number, ζ_z, is:

$$\delta k_{z,sh} = \frac{1}{\Delta z\beta_z}\left(\zeta_z - \frac{N_{z,shim}+1}{2}\right) \tag{5.8}$$

The values of $N_{z,shim}$, β_z and ζ_z are supplied to the pulse sequence via a text file.

Z-shim Calibration Scan

When used to acquire calibration data $N_{z,shim}$ and β_z are chosen such that the range of k-space offsets produced by the z-shim gradient covers the range of offsets induced by the susceptibility gradients in the head. For example, by using Equation 5.4, it can be seen that at an echo time of 30 ms the range of k-space offsets needed to correct susceptibility gradients, measured at 3 T in the human head, ($-250 < G_{z,s} < 250$ $\mu\mathrm{Tm}^{-1}$) [28, 29] is $-0.95/\Delta z < \delta k_{z,sh} < 0.95/\Delta z$. Using Equation 5.7 it can be seen that this range can be encompassed when $N_{z,shim} = 51$ and $\beta_z = 25$. (Other combinations of $N_{z,shim}$ and β_z could cover $-0.95/\Delta z < \delta k_{z,sh} < 0.95/\Delta z$. These specific values were chosen because preliminary experiments showed that they enabled the MR signal as a function of $G_{z,s}$ to be accurately sampled in a reasonable time of one minute and forty two seconds.). The calibration scan consists of the acquisition of $N_{z,shim}$ volumes of data; ζ_z is one (for every slice) for the first volume and is then incremented by one between each volume, such that data are acquired over the range of $\delta k_{z,sh}$ given by Equation 5.7.

Z-shim FMRI Data Acquisition

Using the method described later, the calibration scan is used to determine, on a slice by slice basis, the optimal pair of k-space offsets to be produced by the z-shim gradients to correct signal dropout. The shim numbers $\zeta_{z,1}$ and $\zeta_{z,2}$ are calculated from the optimal k-space offsets for each slice using Equation 5.8. When acquiring the FMRI data $N_{z,shim}$ and β are set to the same values as the calibration scan. The volumes are acquired in pairs; the slice specific values of $\zeta_{z,1}$ are used for the first volume of each pair and the slice specific values of $\zeta_{z,2}$ are used for the second volume of each pair.

5.4.3 Producing Grey Matter Masks with Double Inversion-Recovery Echo Planar Imaging

Introduction

The optimisation process used to select the pair of z-shims to recover signal dropout was restricted to grey matter using a mask. This was produced by thresholding images acquired with a double inversion recovery (DIR) sequence with a SE-EPI readout. This can produce images of the grey matter by nulling the signal from cerebrospinal fluid (CSF) and white matter[281–283].

Implementation on the 3 T

DIR-EPI combined with the OIL (optimised interleaved inversion) scheme (which is used to increase the time efficiency by minimising the dead time in multi-slice acquisitions) [284] had previously been implemented on a 1.5 T GE Signa HDx system (at software release 12.0) within the Department of Neuroimaging by Dr Simon Meara [285]. This was upgraded for use on both a 3 T GE Signa HDx system (at software release 14.0M5) and a 3 T GE Discovery MR750 System (at software release 22.0).

Determining the Inversion Times Required to Null CSF and White Matter Signals at 3 T

Assuming that the inversion and refocusing pulses both have 180° flip angles, that the excitation pulse has a 90° flip angle and that the transverse magnetisation has either decayed away or is spoiled after the signal is readout the steady-state longitudinal magnetisation available immediately prior to the 90° excitation pulse for a DIR sequence with a spin-echo readout is [282]:

$$M_A = M_0 \left[1 + 2e^{-(TI_1+TI_2)/T_1} - 2e^{-TI_2/T_1} - e^{-TR/T_1}\left(2e^{TE/2T_1} - 1\right)\right] \tag{5.9}$$

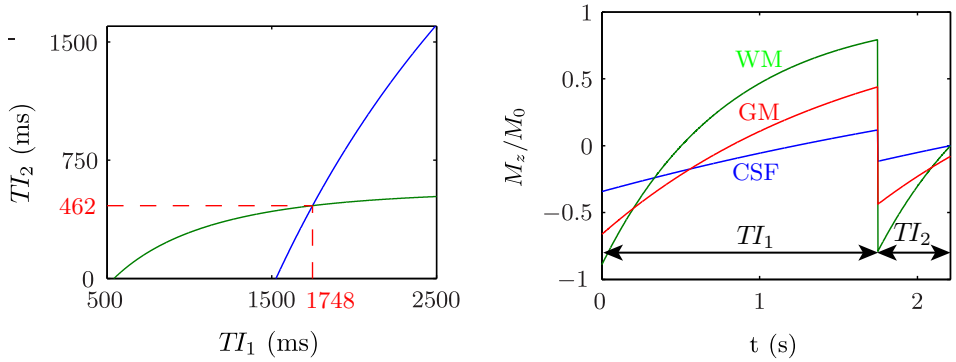

(a) Determing the Optimal inversion times to null white matter and CSF at 3 T

(b) Time evolution of white matter, CSF and grey matter signals

Figure 5.3: (a) A plot of TI_2 against TI_1 for white matter and CSF assuming $TR = 4$ s, $T_{1,WM} = 791$ ms and $T_{1,CSF} = 4163$ ms [286] used to determine the optimal inversion times, $TI_1 = 1748$ ms and $TI_2 = 462$ ms.(b) A graph showing the time evolution of the available steady-state longitudinal magnetisation of white matter, CSF and grey matter at the optimal inversion times (assuming $T_{1,GM} = 1607$ ms [287]). This demonstrates the ability of the DIR sequence to null the signals from CSF and white matter.

Here TI_1 is the time between the first and second inversion pulses, TI_2 is the time between the second inversion pulse and the 90° excitation pulse and $TE/2$ is the time between the 90° excitation pulse and 180° refocusing pulse. For a given relaxation time, T_1 and first inversion time, TI_1, the signal from a specific tissue is nulled ($M_A = 0$) when [282]:

$$TI_2 = T_1 \ln \left[\frac{2\left(e^{-TI_1/T_1} - 1\right)}{\left(2e^{TE/2T_1} - 1\right) e^{-TR/T_1} - 1} \right] \tag{5.10}$$

The values of TI_1 and TI_2 that simultaneously null both CSF and white matter can be found graphically. TI_2 is plotted as a function of TI_1 for both CSF and white matter; the point of intersection of the two curves gives the required inversion times. Following previous work, in which the optimal inversion times were determined at 1.5 T [285], TI_1 and TI_2 were found graphically for an acquisition at 3 T with a repetition time of 4 s and an echo time of 40 ms assuming that $T_{1,WM} = 791$ ms and $T_{1,CSF} = 4163$ ms at 3 T [286]. As shown in Figure 5.3(a) the optimal inversion times are $TI_1 = 1748$ ms and $TI_2 = 462$ ms. The time evolution of grey matter, white matter and CSF are shown in Figure 5.3(b) to demonstrate graphically how a DIR sequence nulls the signal from two different tissues.

A set of in-vivo experiments were performed to determine if a single pair of inversion times, TI_1 and TI_2, could be found to sufficiently null white matter and CSF in a range of subjects. The optimal inversion times derived from the theory

above were used to guide the range of inversion times investigated. Twenty-five different DIR-EPI images were acquired in three healthy male subjects on a 3 T GE Signa HDx system; i.e. all combinations of $TI_1 = 1740, 1750, 1760, 1770, 1780$ ms and $TI_2 = 400, 410, 420, 430, 440$ ms. A quadrature head coil was used for signal transmission and reception. For each image twenty 5 mm slices with a 0.5 mm spacing were acquired in two acquisitions[1] with two averages. The $TR = 4$ s and $TE = 40$ ms, and the flip angle was 90°. The field-of-view was 24 cm with a 128×128 acquisition matrix. To allow the signal to reach a steady state the data acquisition was preceded by two dummy scans, so that the total time to form an image was 48s.

The mean signals from manually traced regions of interest in areas of white matter and CSF were extracted using tools from FSL. The values of TI_1 and TI_2 at which these signals were minimised are shown in Table 5.1. There is a relatively small difference in the optimal inversion times across subjects. Representative slices from the DIR images acquired with the average value of $TI_1 = 1740$ ms and $TI_2 = 410$ ms (the mean of the optimal values given in Table 5.1 rounded to the nearest 10 ms) from the three subjects are shown in Figure 5.4. The mean signal intensities from regions of interest in grey matter, white matter, CSF and air outside of the head are shown in Table 5.2. From Figure 5.4 and Table 5.2 it can be seen that when the average values of $TI_1 = 1740$ ms and $TI_2 = 410$ ms are used, the CSF and white matter signals are suppressed to levels close to the background noise in all subjects. The mean signal in the grey matter is approximately five times the mean background signal. These results suggest that a single pair of inversion times, $TI_1 = 1740$ ms and $TI_2 = 410$ ms, can be used across subjects to produce grey matter images. Grey matter masks can be produced by thresholding and binarising the DIR-EPI image. A threshold of 50 % of the maximum image intensity (which in this case was defined as the 98^{th} percentile of the intensity distribution in the image to reduce the impact of intensity spikes in the images that would affect the thresholding procedure) was found empirically to produce acceptable grey matter masks.

5.4.4 Determining the Optimal Z-shim Spacing

As described in Section 5.2, a z-shim gradient displaces the signal in k-space in the direction of slice selection. The z-shim spacing, Δk_z, defined as the difference in

[1]In this context the term acquisition means that sets of slices are collected separately as they would not all fit within a single TR. Specifically odd numbered slices were collected first, and then the process was repeated for collection of the even numbered slices. On Siemens MR systems this is known as 'concatenations' and on Philips MR systems as 'packages'.

Subject	TI_1 (ms)	TI_2 (ms)
A	1740	410
B	1750	430
C	1740	400
Mean	1743	413

Table 5.1: Optimal inversion times to null white matter and CSF at 3 T in three healthy male subjects

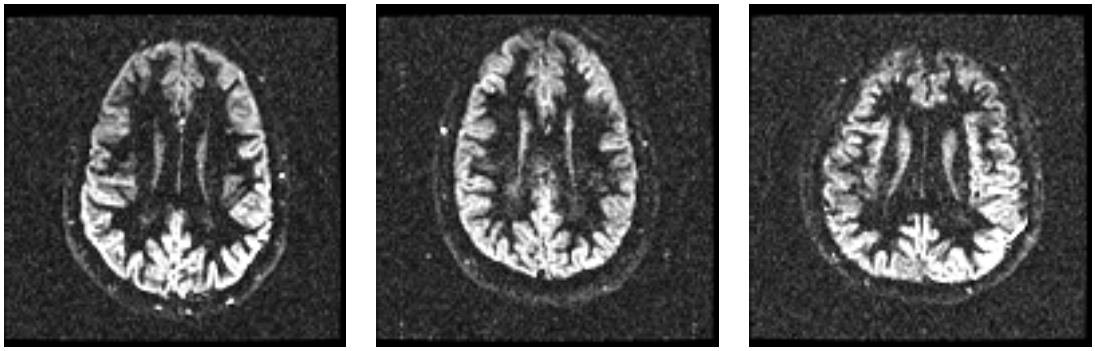

(a) Subject A (b) Subject B (c) Subject C

Figure 5.4: Representative slices from the DIR-EPI images acquired with $TI_1 = 1740$ ms and $TI_2 = 410$ ms demonstrating the suppression of CSF and white matter signals. As for all subsequent images, the data above is shown using the radiological convention, with the right hand side of the subjects head displayed on the left of the images.

Subject	Grey Matter	White Matter	CSF	Air
A	165.5	36.7	32.8	32.3
B	162.3	39.3	34.5	33.2
C	136.4	36.8	34.1	31.9

Table 5.2: Mean signal intensities from regions of interest in grey matter, white matter, CSF and air outside of the head when $TI_1 = 1740$ ms and $TI_2 = 410$ ms

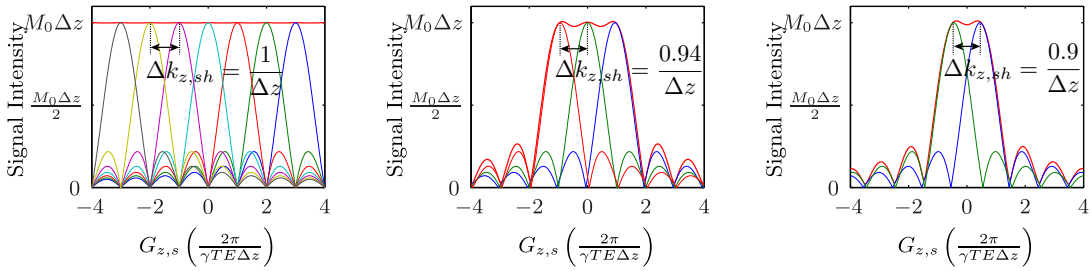

(a) Ordidge et al. [74] (b) Wild et al. [288] (c) Marshall et al. [274]

Figure 5.5: The square root of the sum of squares combination of (a) and infinite number of images with z-shim spacing of $\Delta k_{z,sh} = 1/\Delta z$ [74] (b) three images with z-shim spacing of $\Delta k_{z,sh} = 0.94/\Delta z$ and (c) two images with z-shim spacing of $\Delta k_{z,sh} = 0.9/\Delta z$ is plotted (thick red line) as function of through slice susceptibility gradient $G_{z,s}$. The thin lines show the signal as a function of $G_{z,s}$ for each underlying image used to form the final composite image. The range of gradients shown in both plots $-4\left(\frac{2\pi}{\gamma TE\Delta z}\right) < G_{z,s} < 4\left(\frac{2\pi}{\gamma TE\Delta z}\right)$ corresponds to $-1044 < G_{z,s} < 1044$ μTm^{-1} when $\Delta z = 3$ mm and $TE = 30$ ms.

offsets produced by two z-shim gradients, is:

$$\Delta k_{z,sh} = \delta k_{z,sh,2} - \delta k_{z,sh,1} \tag{5.11}$$

where $\delta k_{z,sh,1}$ and $\delta k_{z,sh,2}$ are the k-space offsets produced by the first and second z-shim gradients respectively. The optimal z-shim spacing ensures that signals from regions with different susceptibility gradients have equal weighting in the final composite image [74]; i.e. the signal from identical tissues would be the same regardless of the strength of the susceptibility gradient.

Previous Work

Several previous studies have determined the optimal z-shim spacing, $\Delta k_{z,sh}$ for a number of different cases. Ordidge et al. [74] showed theoretically that when an infinite set of images, acquired with z-shim gradients spaced by $\Delta k_{z,sh} = 1/\Delta z$, were combined by SSQ the signals from regions with an infinite range of susceptibility gradients were equal in the resulting composite image; Figure 5.5(a). Their derivation assumed that the excited slices were perfectly rectangular such that the signal as a function of the susceptibility gradient was given by Equation 5.3. More practically, Wild et al. [288] went on to show, by numerical simulation assuming perfectly rectangular slices, that the optimal spacing of three z-shims was $\Delta k_{z,sh} = 0.94/\Delta z$; Figure 5.5(b). This ensured that the signals were as uniform as possible from regions with a range of different susceptibility gradients. Finally Marshall et al. [274] showed that the optimal spacing of two z-shims was $\Delta k_{z,sh} = 0.9/\Delta z$; Figure 5.5(c).

Numerical Simulation of the Bloch Equations to Determine the Optimal Z-shim Spacing

In practice, the slice selection process does not produce perfectly rectangular slices. Therefore, the z-shim spacing needed to ensure that the signals from areas with a range of susceptibility gradients are as uniform as possible was determined by numerical simulation of the Bloch Equations in MATLAB, using the SLR RF pulse (described Section 2.5) and gradient waveform used by the scanner. The steady state voxel signal for grey matter (at $TE = 30$ ms and $TR = 2$ s assuming $T_1 = 1.6$ s [287] and $T_2^* = 66$ ms [289]) was determined as a function of the z-shim spacing ($-1/\Delta z < \Delta k_{z,sh} < 1/\Delta z$) and the through-plane linear susceptibility gradient $G_{z,s}$. The slice-selection gradient and RF excitation pulse (with a 73° flip angle - the Ernst angle[290] for grey-matter at 3 T for TR=2 s assuming $T_1 = 1.6$ s [287]) used in the simulation were recorded directly from the GE Discovery MR750 system. For each combination of $\delta k_{z,sh}$ and $G_{z,s}$ the transverse magnetisation in the x- and y-directions, $M_x(z)$ and $M_y(z)$, were found by Bloch simulation for $-\Delta z < z < \Delta z$ (i.e. including the regions either side of the prescribed slice to incorporate the effect of the non-rectangular slice profile). The total signal magnitude was calculated numerically using:

$$S = \sqrt{\left[\int_{-\Delta z}^{\Delta z} M_x(z)\mathrm{d}z\right]^2 + \left[\int_{-\Delta z}^{\Delta z} M_y(z)\mathrm{d}z\right]^2} \tag{5.12}$$

This was normalised to the steady state signal when $\delta k_{z,sh} = 0$ and $G_{z,s} = 0$, i.e. when there was was no susceptibility gradient and no z-shimming. The square root of the sum of squares of the signal was then calculated from two acquisitions as a function of the z-shim spacing, $\Delta k_{z,sh}$, and through plane susceptibility gradient and is plotted in Figure 5.6(a). The z-shim spacing that gave the SSQ signal closest to one across a range of susceptibility gradients was $\Delta k_{z,sh} = 0.68/\Delta z$. The SSQ signal as a function of through plane susceptibility gradient is shown for the optimal z-shim spacing in Figure 5.6(b). The spacing is considerably smaller than $0.9/\Delta z$ used by Marshall et al. [274]. The difference arises as a result of the asymmetric side lobes of the signal response as a function of $G_{z,s}$, Figure 5.6(b).

Experimental Validation of the Bloch Simulation

To confirm that the asymmetries observed in the side lobes of the signal response as a function of $G_{z,s}$ were a real effect and not an artefact of the simulation, a series of images were obtained of uniform spherical phantom[2]. All data were acquired

[2]Containing silicone oil (dimethylpolysiloxanes) doped with a gadolinium compound (tris(2,2,6,6-tetramethyl-3,5-heptanedionate) gadolinium (III)). The longitudinal relaxation time

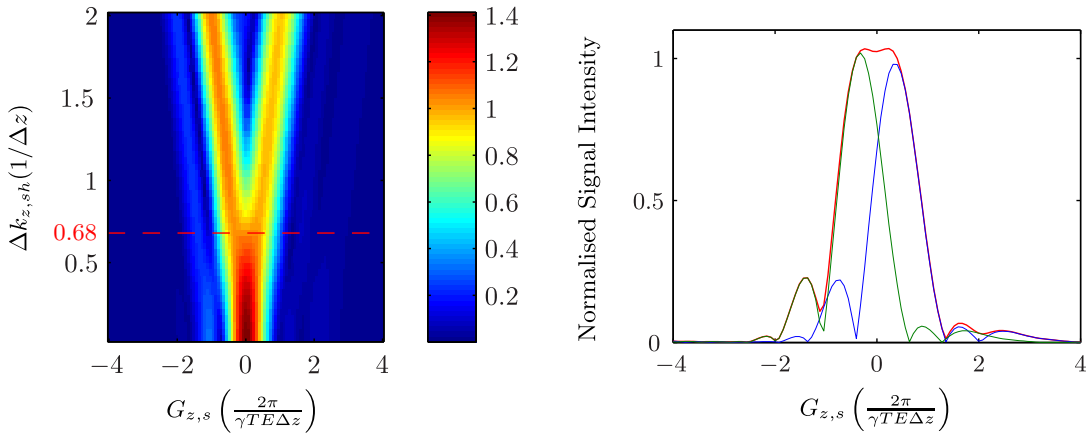

Figure 5.6: Numerical solutions of the Bloch equations showing (a) The SSQ signal in the composite image as a function of z-shim spacing and through-plane susceptibility gradient, $G_{z,s}$ when $\Delta z = 3$ mm and $TE = 30$ ms for the excitation pulse from the GE Discovery MR750 system. The dashed red line shows the optimal z-shim spacing $\Delta k_{z,sh} = 0.68/\Delta z$. (b) Profile through (a) showing the SSQ signal from two acquisitions with the optimal z-shim spacing of $\Delta k_{z,sh} = 0.68/\Delta z$ (thick red line) as function of through slice susceptibility gradient $G_{z,s}$. The thin blue and green lines show the signal as a function of $G_{z,s}$ for the two separate acquisitions. The range of gradients shown in both plots $-4\left(\frac{2\pi}{\gamma TE\Delta z}\right) < G_{z,s} < 4\left(\frac{2\pi}{\gamma TE\Delta z}\right)$ corresponds to $-1044 < G_{z,s} < 1044$ μTm^{-1} when $\Delta z = 3$ mm and $TE = 30$ ms.

using the standard GE-EPI sequence on a 3 T GE Discovery MR750 system. A quadrature head coil was used for signal transmission and reception. Initially the scanner was shimmed using the in-built automatic procedure. To model the effects of different through-plane linear susceptibility gradients, the shim gradient in the slice-selection direction was then deliberately miss-set. At each different setting of the shim gradient, a single 3 mm axial slice with a field-of-view of 32 cm and a 64×64 acquisition matrix was acquired with a $TR = 5$ s and $TE = 30$ ms and a 90° flip angle. Signal excitation and fat suppression were carried using a CHESS and SLR pulse combination described in Section 2.5. The repetition time of 5 s and the 90° flip angle were chosen to avoid differences in steady-state signal resulting from the difference between the T_1 of grey matter and the phantom. The quadrature coil and large field-of-view were selected to enable straightforward measurements of the signal and background noise. The signal from a region-of-interest in the centre of the phantom as a function of the 'susceptibility' gradient (induced by miss-setting the shim) was calculated using FSL tools. The experimental results, shown in Figure 5.7, confirm that the asymmetries observed in the side lobes of the signal response as a function of $G_{z,s}$ seen in the Bloch simulations were a real effect.

$T_1 = 170$ ms and the transverse relaxation time $T_2 = 25$ ms. (Part Number: 2359877, General Electric, Waukesha, WI, USA)

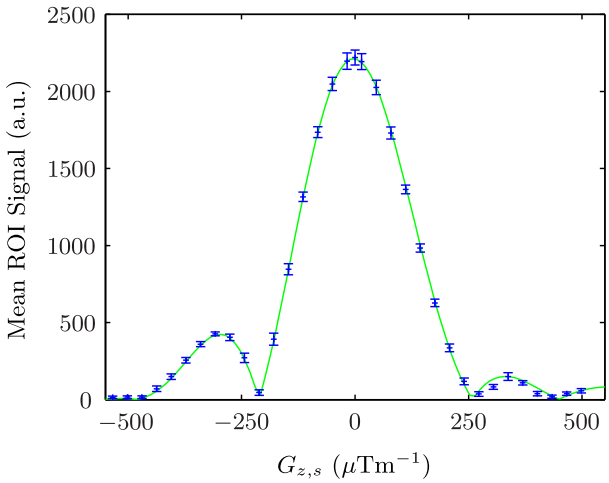

Figure 5.7: Variation in the mean signal from a region-of-interest in the centre of the phantom as a function of 'susceptibility' gradient (induced by mis-setting the scanner's shim gradient in the slice-selection direction) for the SLR excitation pulse. The error bars represent the standard deviation of the signal in the ROI. The voxel signal calculated by Bloch simulation (green line) is shown for comparison. The Bloch simulation was scaled such that the signal at $G_{z,s} = 0$ was equal to the signal in the acquired data at the same susceptibility gradient.

5.4.5 Determining the Optimal Pair of Z-shims to Recover Signal in Grey Matter

MATLAB Prototype

An algorithm was developed in MATLAB to determine the optimal pair of slice specific z-shim gradients to recover signal in grey matter using z-shim calibration scan and DIR-EPI image data. To ensure the DIR-EPI and z-shim calibration scans were co-registered and distortion matched, they were acquired with the same slice positioning, thickness and gap, as well as the same matrix size, ASSET acceleration factor and field-of-view.

Firstly the DIR-EPI data was thresholded and binarised as described above to produce a grey matter mask. The z-shim calibration data were then multiplied by this mask to ensure that the later optimisation stages were restricted to grey matter only. An exhaustive search was then performed to determine the pair of z-shim gradients for each slice (with the restriction that the z-shim spacing was $\Delta k_{z,sh} = 0.68/\Delta z$) which resulted in an SSQ signal greater than 50 % of the robust maximum of the GE-EPI image with no z-shimming in the greatest number of voxels.

The algorithm was tested using DIR-EPI and z-shim calibration data from a single healthy male volunteer using the acquisition parameters given in Section 5.5.1. As shown in Figure 5.8, combining the images acquired with the optimal pair of slice specific z-shims by SSQ results in increased signal in the majority of grey matter

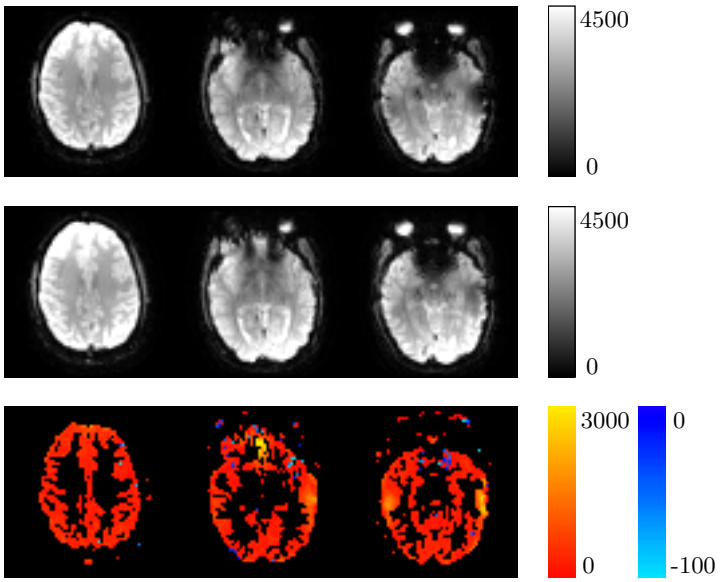

Figure 5.8: A comparison of conventional GE-EPI images (top-row) with SSQ images formed from the pair of z-shim images which recovered signal in the greatest number of *grey matter* voxels in a slice (second-row). The difference between the images is shown in the third-row. Representative slices are shown for a region free from signal dropout (left-column) through the orbitofrontal cortex (middle-column) and through the inferior temporal lobes (right-column). The difference maps are masked to show only grey matter voxels.

voxels. Signal was recovered in a significant proportion of the areas of dropout in the orbitofrontal and inferior temporal regions.

As a comparison with previous methods, which determine the z-shim gradients based on the signal in all brain voxels in a particular slice [272, 274], the algorithm was re-run using the same calibration scan but without the grey matter mask. In this case the images were simply thresholded to exclude voxels outside of the head. For each slice, the pair of z-shim images which recovered the signal in the most voxels, where combined by SSQ. In Figure 5.9 the resulting images were compared to the SSQ images formed from the pair of z-shim images which recovered the signal in the most *grey matter* voxels. In the slice free from susceptibility gradients, the same optimal pair of z-shim gradients are found using both algorithms. However, in the slices through the orbitofrontal and inferior temporal regions, different pairs of z-shim gradients were deemed optimal. The grey matter mask resulted in improved signal recovery in the orbitofrontal and inferior temporal regions.

Implementation on the 3 T GE Discovery MR750 System

Following prototyping in MATLAB, the algorithm was implemented in C++ such that the optimal pair of z-shim gradients could be calculated on the 3 T GE Discovery MR750 System itself. An open source DICOM library (DCMTK version 3.5.4

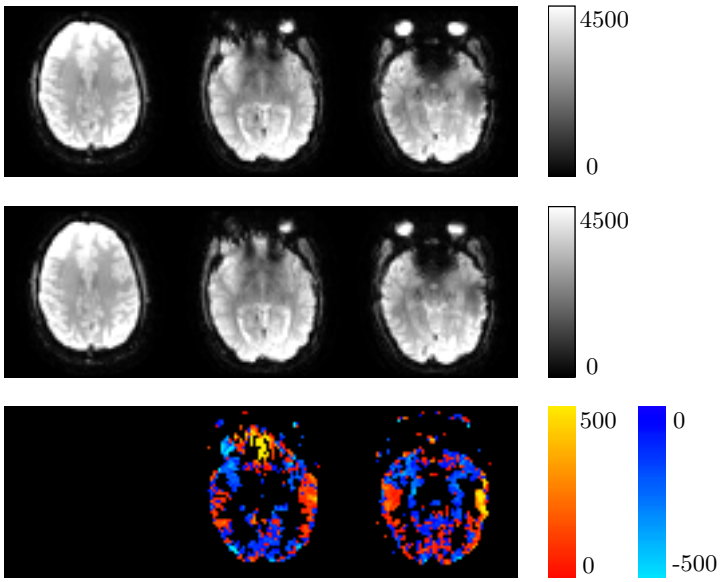

Figure 5.9: A comparison of SSQ images formed from the pair of z-shim images which recovered signal in the greatest number of voxels in a slice (top-row) with SSQ images formed from the pair of z-shim images which recovered signal in the greatest number of *grey matter* voxels in a slice (second-row). The difference between the images is shown in the third-row. Representative slices are shown for a region free from signal dropout (left-column) through the orbitofrontal cortex (middle-column) and through the inferior temporal lobes (right-column). The difference maps are masked to show only grey matter voxels.

available from dicom.offis.de/dcmtk.php.en) was used to read the image data. The resulting program took approximately 5 s to determine, and then generate a text file containing, the optimal pairs of slice specific z-shim values ($\zeta_{z,1}$ and $\zeta_{z,2}$).

5.5 Evaluating the Impact of the Grey Matter Optimised Two-Step Z-Shimming In-vivo

A series of scans were performed on six healthy male volunteers (five right handed, one left handed) on the 3 T GE Discovery MR750 system to assess the impact of using grey matter specific z-shimming in FMRI experiments. The data were used to measure the changes in the temporal signal-to-noise ratio and the ability to detect both task-induced and resting-state BOLD signal changes.

5.5.1 Data Acquisition

The subjects' breathing pattern was tracked using a respiratory bellows and a pulse oximeter was used to monitor cardiac activity throughout. Their hearing was protected using a combination of earplugs and headphones. Foam pads were used to

minimise subject motion throughout data acquisition. FMRI paradigms were presented using a projector and screen at the rear of the scanner bore. This was viewed by the subject using a mirror attached to the head coil. The paradigms were triggered by the scanner to start with the first RF pulse of data acquisition.

All data were acquired with an eight-channel phased array head coil for signal reception and the body coil for RF transmission. With the exception of the localiser and ASSET calibration scans, all imaging data were acquired with a 21.2 cm field-of-view and a 64×64 acquisition matrix. Thirty-six 3 mm slices with 0.3 mm slice gaps were prescribed parallel to the line intersecting the anterior and posterior commissure. The slices were placed in identical locations for all scans. As described in Section 2.5, signal excitation and fat suppression were carried using a CHESS and SLR pulse combination.

Spin-echo EPI

A single volume, preceded by six dummy acquisitions, was acquired using a SE-EPI pulse sequence with a repetition time of two seconds and an echo time of 30 ms. The flip angle of the SLR excitation pulse was 90°. The ASSET acceleration factor was two. Slices were collected sequentially from the top to the bottom of the head. These data were collected to provide a "gold-standard" image, free from susceptibility induced signal dropouts for comparison with the GE-EPI images.

DIR-EPI

A single volume DIR image, with a spin-echo EPI readout, was acquired in two acquisitions with two averages at a repetition time of four seconds and an echo time of 40 ms. To supress the white-matter and CSF signals the first inversion time, $TI_1 = 1740$ ms and the second inversion time, $TI_1 = 410$ ms (the optimal inversion times were determined in Section 5.4.3). To allow the signal to reach a steady state the data acquisition was preceded by two dummy scans; the total time acquisition time was therefore 48 s.

Z-Shim Calibration

A z-shim calibration scan was performed. One hundred and one volumes, preceded by four dummy acquisitions (without a z-shim gradient), of data were acquired with the GE-EPI pulse sequence that had been modified to enable z-shimming. The repetition time was 2 s, the echo time was 30 ms, the flip angle was 73° and the ASSET acceleration factor was 2. Slices were collected top-down sequentially. $N_{shim} = 101$, $\beta = 25$ and ζ was incremented from 1 to 101 such that $\delta k_{z,sh} = -2/\Delta z$ for the first volume, $\delta k_{z,sh} = -1.96/\Delta z$ for second volume, etc..., up to $\delta k_{z,sh} = 2/\Delta z$

for the final volume. This range of $\delta k_{z,sh}$ corresponds to k-space offsets caused by susceptibility gradients in the range $-522 < G_{z,s} < 522$ μTm^{-1} for $\Delta z = 3$ mm and $TE = 30$ ms.

Using the z-shim calibration and DIR-EPI, scans the optimal pair of z-shim gradients needed to recover signal in the greatest number of grey matter voxels for each slice were then calculated on the scanner with the algorithm described above.

Resting State Functional MRI

A pair of resting-state functional MRI scans were acquired using a conventional GE-EPI sequence and GE-EPI with z-shimming (using optimal pair of z-shim gradients for each slice calculated above). For both scans the repetition time was 2 s, the echo time was 30 ms, the flip angle was 73° and the ASSET acceleration factor was 2. Slices were collected top-down sequentially. The order of the two scans was counter balanced across the six subjects. For each acquisition four hundred and fifty volumes of data (15 minutes) were acquired, preceded by four dummy acquisitions, whilst the subject was at rest. Subjects were instructed to keep their eyes open and to look at a cross hair projected onto the screen. In the environment of the scanner this is relatively difficult to maintain; several subjects reported falling asleep during the data acquisition. Because there is evidence that the effects of task-based FMRI experiments persist for several minutes after the task has ended[291, 292] the resting-state data were acquired before the motor and breath-hold FMRI data described below. These data were used in several ways, firstly to measure the changes in the temporal signal-to-noise ratio resulting from z-shimming, and secondly to determine if z-shimming caused any changes in the detectability of resting-state networks.

Functional MRI with a Motor Task

A pair of functional MRI scans were then acquired with the same parameters as the resting-state FMRI whilst the subject performed a motor task. As before, one dataset was acquired with conventional GE-EPI, and the other with z-shimming. Again, the order of the two scans counter balanced across the six subjects, to avoid bias due to habituation effects or fatigue. For each scan one hundred and thirty five volumes of data (4 minutes and 30 seconds) were acquired, preceded by four dummy acquisitions, whilst the subjects performed a block-design motor task consisting of five 30 s blocks of rest interleaved with four 30 s blocks of motor activity. During the task periods the subjects were visually cued to squeeze a ball with their right hand every two seconds. During the rest periods the word 'Rest' was projected onto the screen at the same frequency. The squeeze ball was connected to a pressure actuator, allowing task compliance to be monitored throughout. Prior to each acquisition of

Figure 5.10: Instructions presented to the subjects during the breath-hold FMRI scans

FMRI data the pressure actuator was calibrated by measuring the pressure as the subject squeezed the ball as hard as they could. The pressure recorded during subsequent squeezes was then expressed as a percentage of this, subject specific, maximum. The FMRI data were used to assess changes in the ability to detect task-based FMRI activations resulting from the use of two-step z-shimming.

Functional MRI with a Breath-hold Paradigm

Finally a pair of functional MRI scans were acquired during which the subjects performed a breath-hold task. The same parameters as the resting-state FMRI acquisition were used. As for the other functional tasks one was acquired using conventional GE-EPI, and the other with two-step z-shimming, again with the order counter balanced across subjects. For each breath-hold experiment one hundred and fifty eight volumes of data (5 minutes and 16 seconds) were acquired. The subject was visually cued to perform paced breathing for 60 s, followed by interleaved blocks of paced breathing (48 s) and breath holding on expiration (16 s) finishing with a 48 s block of paced breathing; the instructions presented to the subjects are shown in Figure 5.10. The first six volumes of data were discarded such that the signal in all of the data used in the analysis were acquired in a steady state condition. This specific paradigm design was used as it has been shown to produce reliable BOLD signal increases across grey matter (in a previous study carried out in the Department of Neuroimaging)[293].

Following previous work, in which alternative methods were presented to reduce signal dropout [29, 115, 279], the breath-hold data were used to assess changes in the BOLD sensitivity [28] caused by two-step z-shimming. The task causes a hypercapnic stress, similar to carbon dioxide inhalation[294], and reliably increases cerebral blood flow (CBF), and hence causes increases in the BOLD signal across grey matter.

5.5.2 Data Analysis

Following acquisition, all imaging data were converted into the NIfTI-1 data format[3] using dcm2nii[4]. All the data processing described below was carried out using tools from FSL (FMRIB's Software Library[5]).

The FMRI data acquired using the two-step z-shimming approach were combined pairwise by the square root of the sum of squares (SSQ). Specifically, the first volume of combined data was the SSQ of volumes one and two of the acquired data, the second volume of the combined data was the SSQ of volumes two and three of the acquired data and so on.

Z-shim Calibration

To test the earlier finding in Section 5.4.5, that optimising the pair of z-shim gradients based on the signal in grey matter voxels only in each slice was superior to optimising over all voxels in each slice, the calibration data were also processed offline in MATLAB. As in Section 5.4.5, the algorithm was re-run without the grey matter mask. For each slice, the pair of z-shim images which recovered the signal in the most voxels, where combined by SSQ. Maps of the difference between the between these and the SSQ images formed from the pair of z-shim images which recovered the signal in the most *grey matter* voxels were calculated.

Qualitative Comparison of Signal In Regions of Through-Slice Susceptibility Gradient

Representative slices through the orbitofrontal and inferior temporal regions from data acquired with SE-EPI, GE-EPI and GE-EPI with z-shimming were visually compared to determine if signal was recovered in regions with through-slice susceptibility gradients when z-shimming was used.

Temporal Signal-to-Noise Ratio

The temporal signal-to-noise ratio was calculated from the resting-state FMRI data sets acquired using both conventional GE-EPI and GE-EPI with z-shimming. For each subject, all of the volumes from both datasets were registered to the first volume of the conventional GE-EPI data set using FSL MCFLIRT (Motion Correction using FMRIB's Linear Image Registration Tool)[205]. This corrected for motion throughout the data acquisition and enabled a voxel-wise comparison of the TSNR

[3]See nifti.nimh.nih.gov/nifti-1 for details

[4]A program written by Chris Rorden and distributed as part of MRIcron, see: www.mccauslandcenter.sc.edu/mricro/mricron/dcm2nii.html for details

[5]See www.fmrib.ox.ac.uk/fsl for details

of the data acquired with the two acquisition methods. The brain was extracted using FSL BET (Brain Extraction Tool) [267] and the resulting data were high pass filtered using a Gaussian weighted least-squares line fit, with a cut-off $\sigma = 50$ s (0.01 Hz), to remove signal drifts [295]. The TSNR was calculated voxel-wise as the ratio of the temporal mean to the temporal standard deviation. Maps of the percentage change in TSNR between the data acquired with the z-shimmed and conventional GE-EPI sequences for each subject using:

$$\text{Percentage Difference} = 100 \left(\frac{TSNR_{z-shim} - TSNR_{GE-EPI}}{TSNR_{GE-EPI}} \right) \tag{5.13}$$

In addition, the percentages of grey matter voxels showing either increases or decreases in TSNR were calculated. The grey matter mask needed for this was produced by thresholding[6] and binarising the DIR-EPI image.

The degree of subject motion between the z-shim calibration scan and the FMRI data acquired with z-shimming was determined by registering the central volume of the z-shimmed data to the central volume of the calibration data using FLIRT (FMRIB's Linear Image Registration Tool)[205, 296] (with six degrees of freedom and the correlation ratio cost function). The translations and rotations of the head were extracted from the transformation matrix using *avscale* (an FSL tool).

Detectability of Motor Activations

Firstly, to check that each subject performed the task, the pressure measured in the squeeze ball (as a percentage of the pressure measured during calibration) was plotted as a function of time for both acquisition types.

The FMRI data sets acquired whilst the subject performed the motor task were analysed using FEAT. To correct for subject motion, each volume in the FMRI timeseries was registered to the central volume using MCFLIRT [205]. The brain was extracted using BET [267] and the resulting data were spatially smoothed using a Gaussian kernel with a 5 mm FWHM. The data were then scaled, by a single multiplicative factor, such that the overall mean signal was 10000. Finally the timeseries from each voxel was temporally high pass filtered using a Gaussian weighted least-squares line fit, with a cut-off $\sigma = 30$ s (equivalent to 0.0167 Hz).

The regions of the brain showing significant changes in BOLD signal in response to the motor stimulus were found by fitting eight explanatory variables to the preprocessed time series signals using the General Linear Model (GLM). This was carried out with local autocorrelation correction using FILM [224]. An example of the

[6]The threshold, determined empirically, was 50 % of the maximum image intensity (which in this case was defined as the 98^{th} percentile. This is referred to as the '*robust maximum*' within FSL as it reduces the impact of outliers in the intensity distribution.)

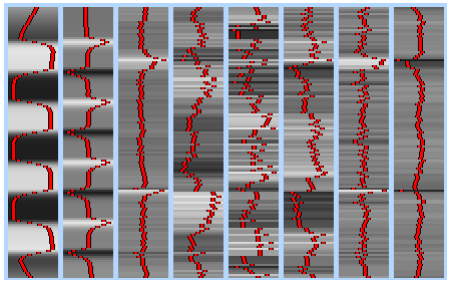

Figure 5.11: An example of the design matrix, generated in FEAT, used to determine the regions of the brain showing significant changes in BOLD signal in response to the motor stimulus. The first explanatory variable contains the stimulus design convolved with a Gamma function. The second explanatory variable is the temporal derivative of the first. The last six explanatory variables are subject specific motion parameters estimated by the motion correction procedure.

design matrix for one of the subjects is shown in Figure 5.11. The first explanatory variable contained the stimulus design convolved with a Gamma function (phase of 0 s, standard deviation of 3 s and mean lag of 6 s) to model the haemodynamic response function. The second explanatory variable was the temporal derivative of the first to account for small variations in the timing of the HRF and therefore reduce the level of unexplained variance. The last six explanatory variables were subject specific; they contained the estimated motion parameters (three translations and three rotations) from the motion correction procedure. The t-statistic maps for each subject and acquisition method, calculated using the contrast $\boldsymbol{c}' = (1, 0, 0, 0, 0, 0, 0, 0)$, were converted to maps of the z-statistic. These maps were then thresholded using clusters determined areas of contiguous voxels with $z > 2.3$ and a (corrected) cluster significance threshold of $p = 0.05$ [263].

As above, the degree of subject motion between the z-shim calibration scan and the z-shimmed FMRI data was determined by registering the central volume of the z-shimmed data to the central volume of the calibration data using FLIRT.

Measuring BOLD sensitivity via Breath-hold BOLD Signal Changes

Firstly, to check each subject performed the task, the normalised signal from the respiratory bellows was plotted as a function of time for both acquisition types.

The FMRI data sets acquired whilst the subject performed the breath-hold task were analysed using FSL FEAT. The same preprocessing steps as used for the analysis of the motor task were carried out, with the exception that high pass filter cut-off $\sigma = 50$ s in this case.

The regions of the brain showing significant changes in BOLD signal in response to the breath-hold stimulus were found by fitting eight explanatory variables to the pre-processed time series signals using the General Linear Model (GLM). This

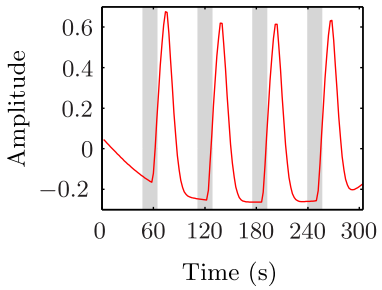

Figure 5.12: The first explanatory variable used to model the haemodynamic response to the breath-hold task. The shaded grey regions illustrate the periods when the subjects held their breath after expiration.

was carried out with local autocorrelation correction using FILM [224]. The first explanatory variable contained the stimulus design, with a delay of 8 s, convolved with a Gaussian function (phase of 0 s, standard deviation of 7.48 s and peak lag of 5 s); Figure 5.12. These parameters were chosen based on the analysis in previous studies using a similar breath-hold paradigm [29, 115] and the observed mean percentage change in BOLD signal, in voxels containing grey matter[7], for all six subjects; Figure 5.13. As in the motor task analysis, the second explanatory variable contained the temporal derivative of the first and the last six explanatory variables were subject specific estimated motion parameters.

The t-statistic maps for each subject and acquisition method, calculated using the contrast $\boldsymbol{c}' = (1, 0, 0, 0, 0, 0, 0, 0)$, were converted to maps of the z-statistic. These maps were then thresholded using clusters determined by $z > 2.3$ and a (corrected) cluster significance threshold of $p = 0.05$. The thresholded z-statistic maps were used to determine if increases in signal produced by z-shimming were matched by increases in BOLD sensitivity.

As above, the degree of subject motion between the z-shim calibration scan and the z-shimmed FMRI data was determined by registering the central volume of the z-shimmed data to the central volume of the calibration data using FLIRT.

Detectability of Resting-State FMRI Networks with PICA

Both sets of resting-state FMRI data were preprocessed using FEAT. To correct for subject motion, each volume in the FMRI timeseries was registered to the central volume using MCFLIRT [205]. The brain was extracted using BET [267] and the resulting data were spatially smoothed using a Gaussian kernel with a 6 mm FWHM. The data were temporally high pass filtered using a Gaussian weighted least-squares line fit, with a cut-off $\sigma = 50$ s (0.01 Hz). The data were then scaled, by a single

[7]The subject specific grey matter masks produced, as described above, by thresholding and binarising the DIR-EPI data were used as a mask.

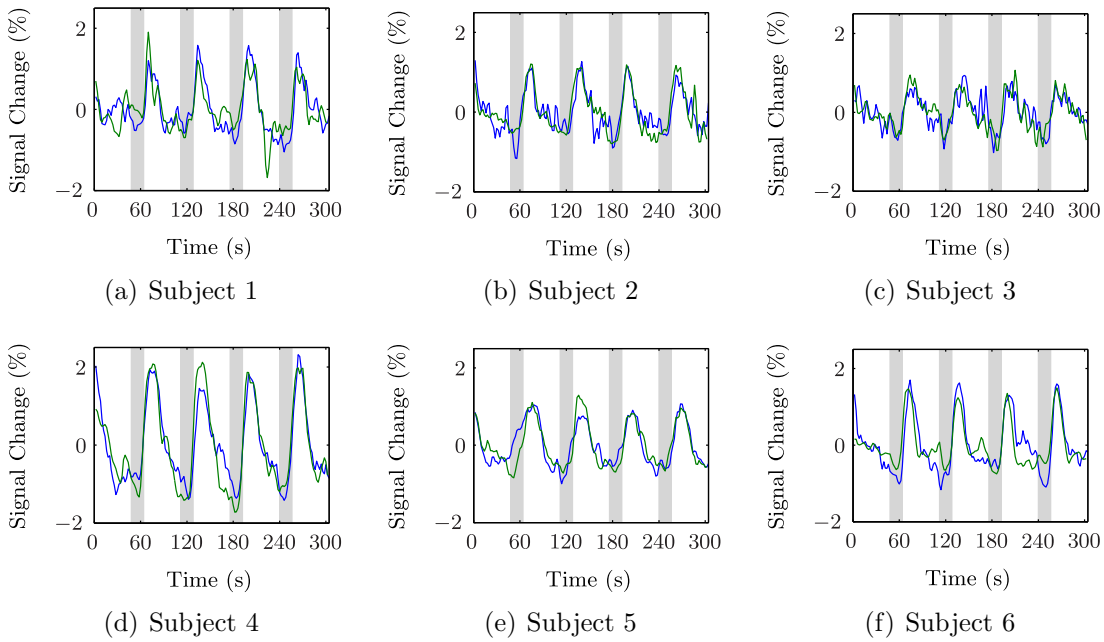

(a) Subject 1 (b) Subject 2 (c) Subject 3

(d) Subject 4 (e) Subject 5 (f) Subject 6

Figure 5.13: The mean percentage change in BOLD signal for grey matter voxels, in response to the breath-hold task for all six subjects for data acquired with conventional GE-EPI (blue-line) and GE-EPI with z-shimming (green-line). The shaded grey regions illustrate the periods in which the subject was instructed to hold their breath.

multiplicative factor, such that the overall mean signal was 10000. The 12 degrees of freedom transformations needed to register both sets of functional data into MNI152 standard-space were calculated using FLIRT [205, 296] with the correlation ratio cost function. The inverse transformation was calculated using *convert_xfm* (an FSL tool).

Probabilistic Independent Component Analysis (PICA) [220] as implemented in MELODIC, was performed to determine if the ten resting-state networks described in Smith et al. [169] were detectable in data acquired with GE-EPI and z-shimmed GE-EPI. Firstly, each data set was registered into MNI152 standard-space using the transformations determined during preprocessing and resampled to 4 mm isotropic voxels to reduce the required computational effort. The data in each voxel were then demeaned and the variance normalised. The data acquired from all six subjects with conventional GE-EPI were temporally concatenated. (Specifically, following preprocessing the data from each subject was in MNI152 space that had been resampled to 4mm isotropic voxels, i.e. $45 \times 54 \times 45$ voxels at 450 time points. This was reshaped to form a 2D matrix with 109350 columns (voxels) and 450 rows (time points) (i.e. 109350 observations of 450 variables). The 2D matrices from each subject were concatenated in the time dimension to produce a single larger 2D matrix with 109350 columns (voxels) and 2700 rows (time points)). Using Principal Component Analysis this data was whitened and projected into a 20-dimensional subspace (20 variables).

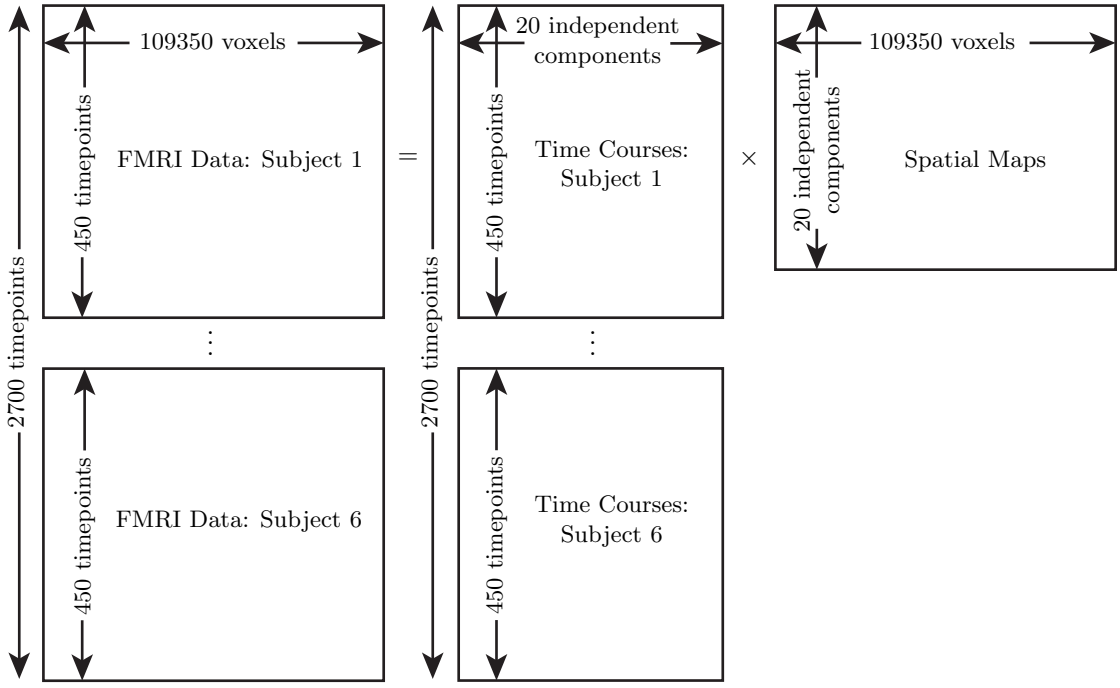

Figure 5.14: A pictorial illustration of temporal concatenation PICA. The temporally concatenated FMRI data sets are decomposed into a set of statistically independent spatial maps and their associated time courses. Adapted from fsl.fmrib.ox.ac.uk/fsl/fslwiki/MELODIC

By optimising for non-Gaussian spatial source distributions using a fixed-point iteration technique [243] this was decomposed into sets of vectors containing the 20 estimated independent spatial components and their associated time courses. This process is shown schematically in Figure 5.14. The vectors of estimated independent spatial components were reshaped into three-dimensional volumes, divided by the standard deviation of the residual noise and thresholded by fitting a mixture model to the histogram of intensity values. As explained in [166] this process is an example of alternative, rather than null, hypothesis testing. Two Gamma and one Gaussian function, to model positive and negative activations and noise respectively, are fitted to the histogram of intensity values. The posterior probability of an activation is calculated as the ratio of the probability of the intensity value under the Gaussian relative to the sum of probabilities of the value under the Gamma distributions. This is thresholded at a probability of 0.5. (i.e. an equal loss is placed on false positives and false negatives [255]). The same analysis was carried out on the data acquired with z-shimming pulse sequence.

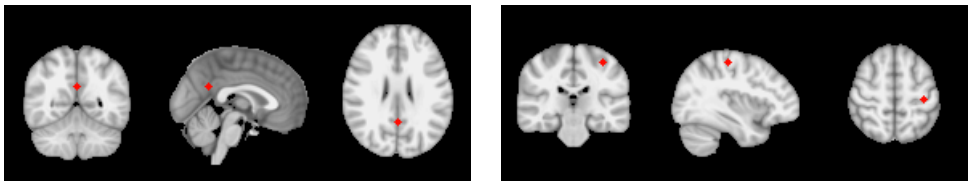

(a) Posterior cingulate seed ROI (b) Left motor cortex seed ROI

Figure 5.15: Size and position of the default mode and motor network seed regions of interest overlaid on the MNI152 standard space template.

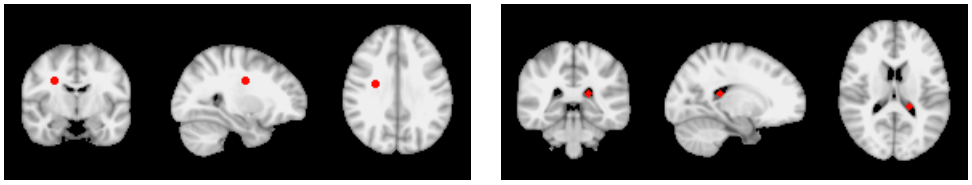

(a) White matter ROI (b) CSF ROI

Figure 5.16: Size and position of the white matter and CSF regions of interest overlaid on the MNI152 standard space template.

Detectability of Resting-State FMRI Networks Using Seed Based Analysis

Both sets of resting-state FMRI data were preprocessed as in the previous section, with the exception that the data were band-pass (rather than high-pass) filtered (0.01 to 0.08Hz).

Seed-based regression analyses were then performed to determine if the fluctuations in the resting-state signals in the regions of recovered signal in the orbitofrontal and inferior temporal regions were correlated with fluctuations from seed regions in the default mode and sensorimotor networks. Two spherical seed regions with 4 mm radiuses were defined in MNI space. The first was in the posterior cingulate ($x = 0$, $y = -53$ and $z = 26$ mm), a node of the default mode network, and the second in the left motor cortex ($x = -36$, $y = 25$ and $z = 57$ mm) [297]; Figure 5.15. A further two regions of interest were defined in MNI space, the first in the lateral ventricle ($x = 27$, $y = -8$ and $z = 32$ mm) and the second in the white matter ($x = -19$, $y = -36$ and $z = 17$ mm); Figure 5.16. These were used to produce confound regressors to reduce the contribution of motion and physiological noise in the following analyses[297]. The analyses for each subject, acquisition method and seed region of interest were carried out separately in the native space of each set of functional data. The seed and confound regions of interest were registered from MNI standard-space into each subject's native space using the inverse transformations calculated in the preprocessing stage. The mean time courses from each of these regions were then extracted. In addition, the global mean time course was

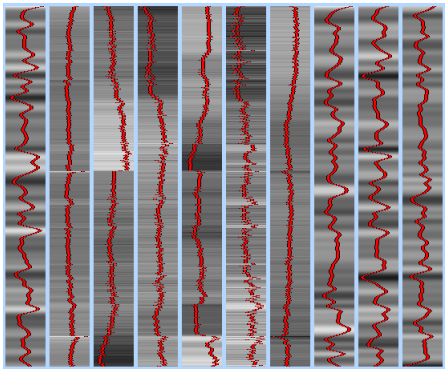

Figure 5.17: An example of the design matrix, generated in FEAT, used to determine the regions of the brain showing significant changes in BOLD signal that were correlated with the resting-state signal in the left motor cortex. All the explanatory variables are subject specific. The first contains the mean time course from the seed in the left motor cortex. Explanatory variables two to seven are the motion parameters estimated by the motion correction procedure. The eighth, ninth and tenth explanatory variables contain the mean CSF, global and white matter signals.

calculated. The regions of the brain showing significant changes in BOLD signal that were correlated with the BOLD signal changes in each seed region were found by fitting ten explanatory variables to the pre-processed time series signals using the General Linear Model as implemented in FILM [224]. An example of the design matrix for one of the subjects is shown in Figure 5.17. All the explanatory variables were subject specific. The first contained the mean time course from the seed in the left motor cortex. Explanatory variables two to seven are the motion parameters estimated by the motion correction procedure. The eighth, ninth and tenth explanatory variables contained the mean CSF, global and white matter signals (which has been shown to be the optimal combination of nuisance regressors [298]). The t-statistic maps for each subject, acquisition method and seed region, calculated using the contrast $\boldsymbol{c}' = (1, 0, 0, 0, 0, 0, 0, 0, 0, 0)$, were converted to maps of the z-statistic. These maps were then thresholded using clusters determined by $z > 2.3$ and a (corrected) cluster significance threshold of $p = 0.05$.

5.5.3 Results

Optimal Z-shims

The optimal pairs of subject and slice specific shifts in k-space, $\delta k_{z,sh}$, produced by the z-shim gradient lobe, to reduce signal dropout are shown in Figure 5.18. The large negative k-space shift for slice one in subjects two, three, five and six is a result of the algorithm attempting to determine the optimal shims from a very small number of voxels containing grey matter in the most superior slice. With the exception of subject four, in the inferior regions (slices 30 to 36) the optimal pair of z-

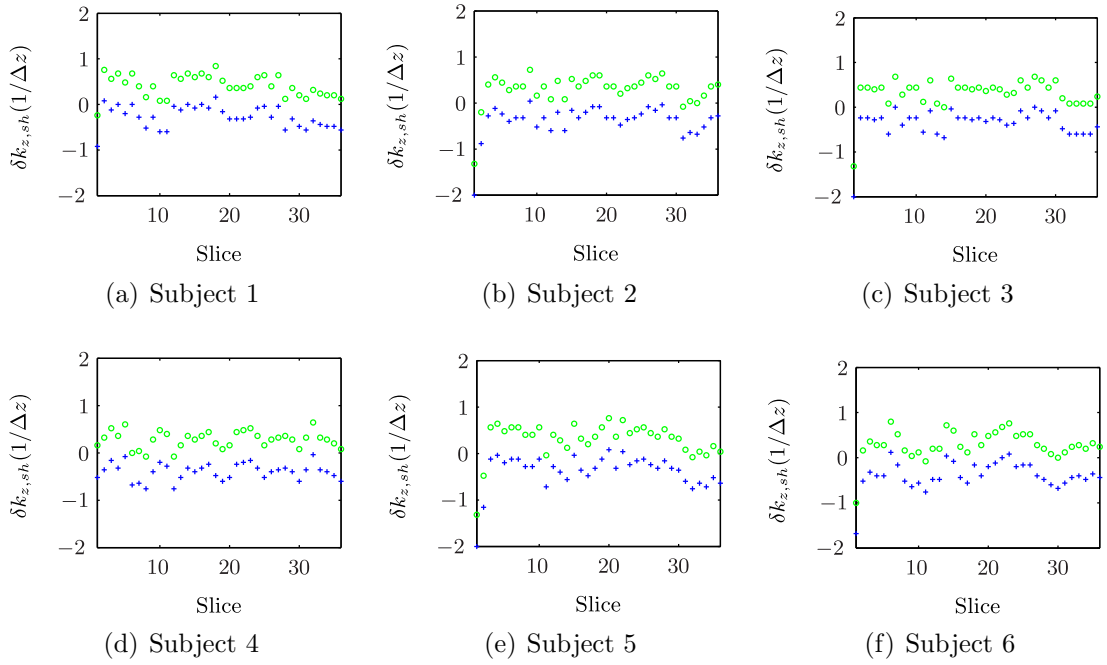

(a) Subject 1 (b) Subject 2 (c) Subject 3

(d) Subject 4 (e) Subject 5 (f) Subject 6

Figure 5.18: The optimal pairs of slice and subject specific shifts in k-space, $\delta k_{z,sh}$, produced by the z-shim gradient lobe. As the slices were acquired from top to bottom slice one is at the top of the head.

shim gradients produce shifts in k-space that are more negative than in the superior slices. In all six subjects, excluding the most superior slice, the optimal k-space offsets produced by the z-shim gradient are in the range $-1/\Delta z < \delta k_{z,sh} < 1/\Delta z$.

Maps of the difference between the SSQ images produced using the pairs of z-shim images which recovered signal in the most *grey matter* voxels and the SSQ images calculated, offline in MATLAB, using the pairs of z-shim images which recovered signal in the most voxels (regardless of the type of tissue they contained) are shown, for all six subjects for representative slices through the orbitofrontal and inferior temporal regions in Figure 5.19. For all six subjects, improved signal recovery in the orbitofrontal and inferior temporal regions was achieved when the grey matter masking was included in the algorithm to determine the optimal slice specific pair of z-shim gradients.

Qualitative Comparison of Signal In Regions of Through-Slice Susceptibility Gradient

Representative slices through the orbitofrontal and inferior temporal regions from data acquired with SE-EPI, conventional GE-EPI and z-shimming pulse sequences are shown for each subject in Figures 5.20 and 5.21. Comparing the images acquired with SE-EPI and conventional GE-EPI, signal dropout is observed in both the orbitofrontal and inferior temporal regions for all six subjects. The signal in

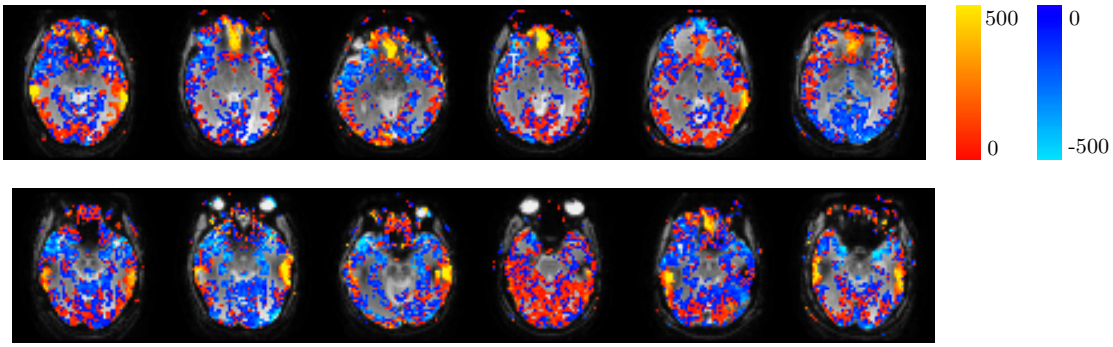

Figure 5.19: Maps showing the difference in SSQ signal when the optimal pair of z-shim gradients was calculated for grey matter voxels versus all voxels in the head. The top row shows representative slices through the orbitofrontal cortex and the bottom row slices through the inferior temporal lobes for the six subjects.

the large areas of these two regions is recovered when z-shimming is used. However, some residual regions of signal dropout remain. The asymmetries observed in the signal recovered in subject five are a result of the slices being poorly prescribed; the imaging plane was rotated slightly downwards on the subject's left hand side.

Temporal Signal-to-Noise Ratio

Maps of the temporal signal-to-noise ratio for each subject for data acquired with conventional GE-EPI and z-shimmed GE-EPI are shown through the orbitofrontal and inferior temporal regions in Figures 5.22 and 5.23. The percentage change in the temporal signal-to-noise ratio between data acquired with conventional GE-EPI and z-shimmed GE-EPI is shown in Figure 5.24.

As detailed in Table 5.3 the TSNR increased in, on average, 80.7 % of grey matter voxels increased. TSNR increases were observed consistently across the six subjects in the regions of recovered signal in the orbitofrontal and inferior temporal regions as well as a large proportion of the other voxels. The origin of the band of reduced TSNR anterior to the orbitofrontal region in subject one is currently not understood.

The estimated movement of the subjects between the z-shim calibration scan and the data used to calculate the TSNR are shown in Table 5.4. Subject one moved by approximately half a voxel in the superior-inferior direction and subject five moved by approximately one voxel in the same direction.

Comparing the Detectability of BOLD Signal Changes Resulting From the Motor Task

The pressure recorded in the squeeze ball for all six subjects throughout the motor-task FMRI scans are shown in Figure 5.25. These plots demonstrate that in the

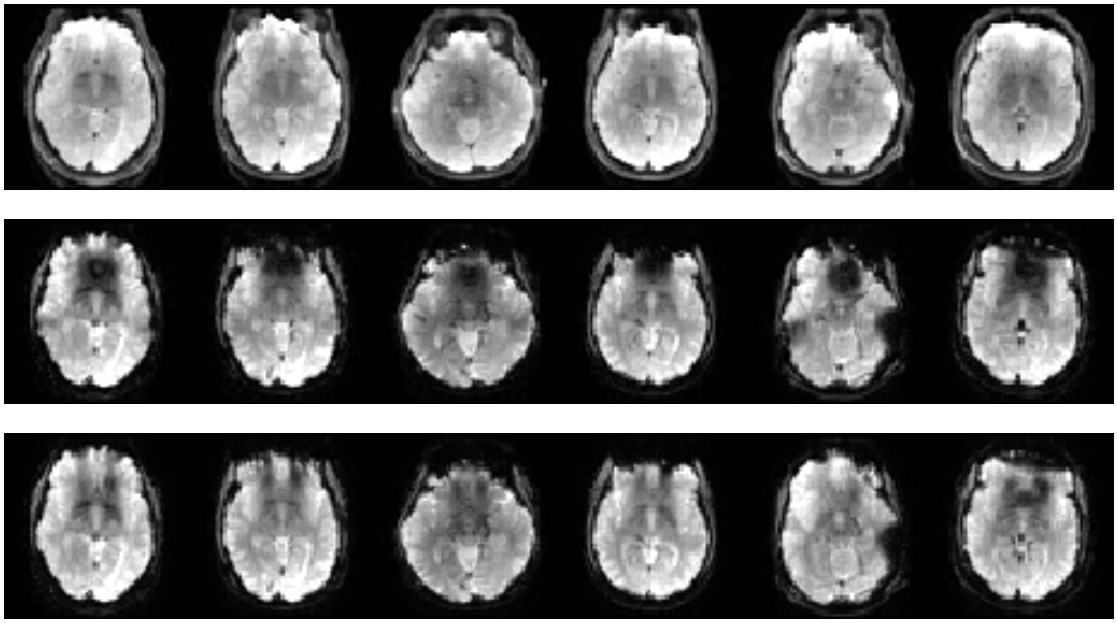

Figure 5.20: Representative slices through the orbitofrontal cortex of the six subjects from images acquired with SE-EPI (top-row), GE-EPI (middle-row) and z-shimmed GE-EPI (bottom-row). The intensity range used to display each image was chosen so that the areas of signal dropout and recovery could be easily seen. The slices shown are in the native space of each subject.

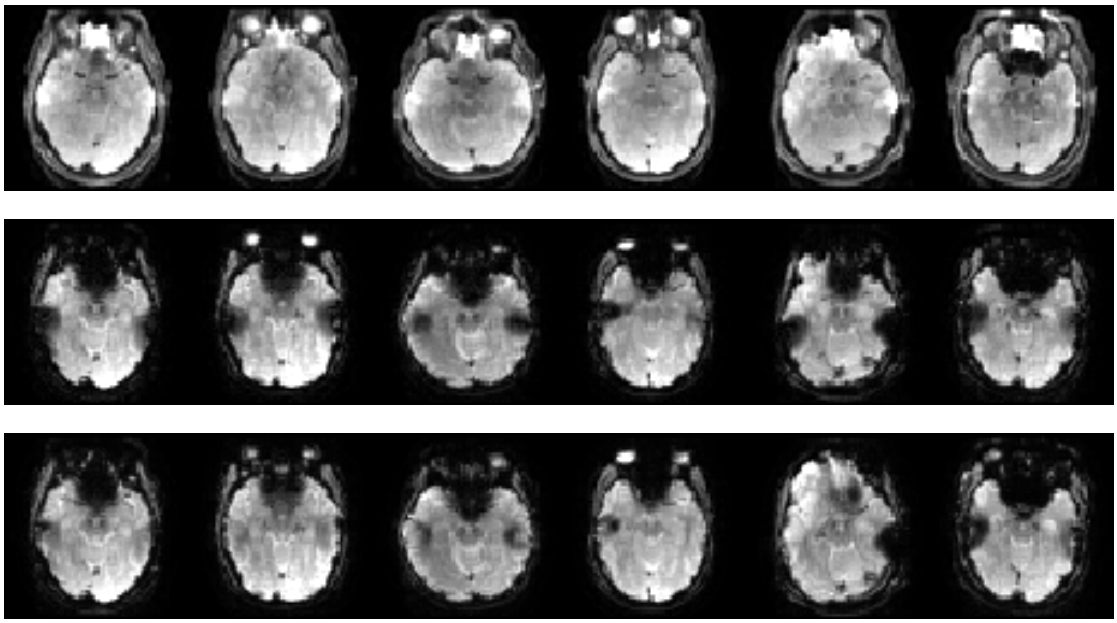

Figure 5.21: Representative slices through the inferior temporal lobes of the six subjects from images acquired with SE-EPI (top-row), GE-EPI (middle-row) and z-shimmed GE-EPI (bottom-row). The intensity range used to display each image was chosen so that the areas of signal dropout and recovery could be easily seen.

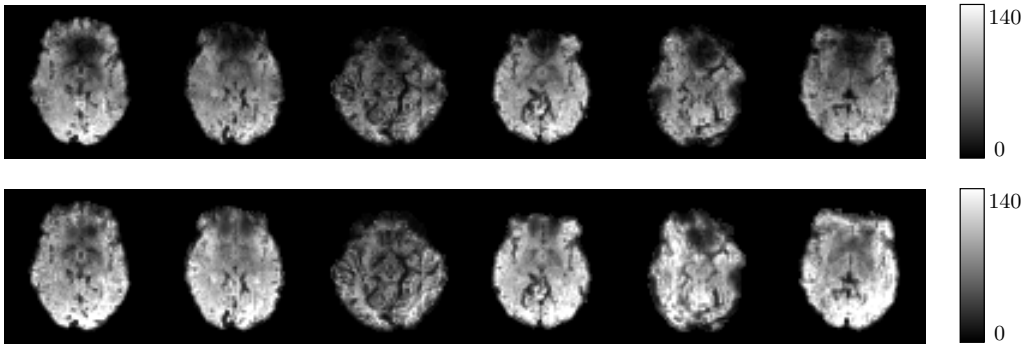

Figure 5.22: TSNR maps for representative slices through the orbitofrontal cortex of the six subjects calculated from data acquired with conventional GE-EPI (top-row) and z-shimmed GE-EPI (bottom-row).

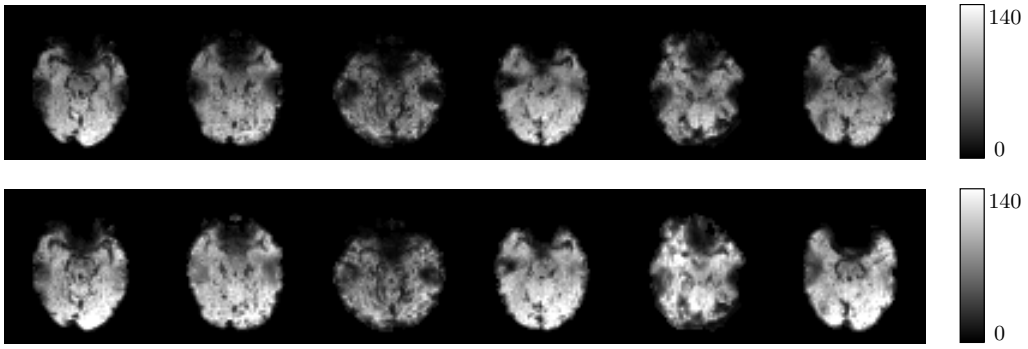

Figure 5.23: TSNR maps for representative slices through the inferior temporal lobes of the six subjects calculated from data acquired with conventional GE-EPI (top-row) and z-shimmed GE-EPI (bottom-row).

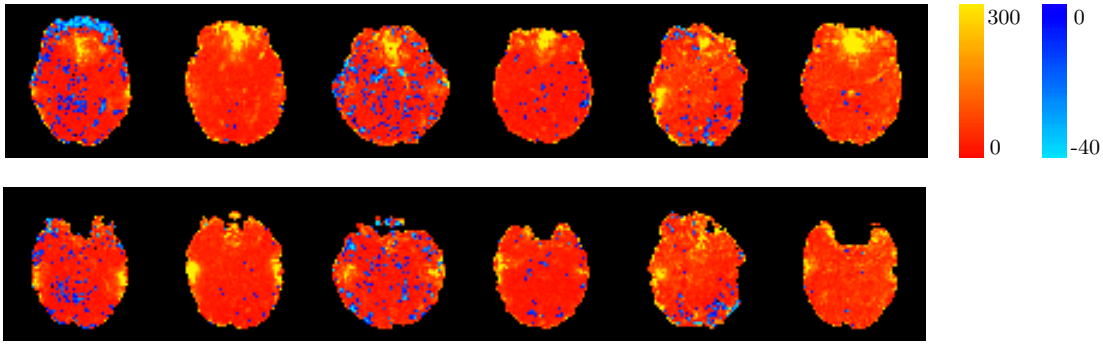

Figure 5.24: Maps showing the percentage change in the TSNR between data acquired using conventional GE-EPI and z-shimmed GE-EPI. The top row shows representative slices through the orbitofrontal cortex and the bottom row slices through the inferior temporal lobes for the six subjects.

Subject	Grey matter voxels with increased TSNR (%)	Grey matter voxels with decreased TSNR (%)
1	74.5	16.5
2	90.8	1.2
3	65.6	26.7
4	85.9	4.0
5	81.4	8.7
6	85.7	1.1
Mean	80.7	9.7

Table 5.3: The percentage of grey matter voxels showing increases or decreases in TSNR when z-shimmed GE-EPI is used in place of conventional GE-EPI.

	Translations (mm)			Rotation Angles (rad)		
Subject	x	y	z	x	y	z
1	0.03	0.50	-1.71	-0.010	0.008	-0.001
2	0.07	-0.21	-0.52	-0.004	0.003	-0.001
3	0.19	-0.20	0.35	-0.007	-0.002	-0.003
4	0.11	0.19	-0.65	-0.006	0.002	-0.001
5	-2.13	3.96	3.27	-0.008	-0.023	0.024
6	-0.37	-0.05	-0.66	-0.005	-0.003	0.002

Table 5.4: Estimated subject motion between the acquisition of the z-shim calibration scan and the resting-state FMRI data acquired with z-shimming. Translations greater than half the voxel size (1.65 mm) in any direction are highlighted in red.

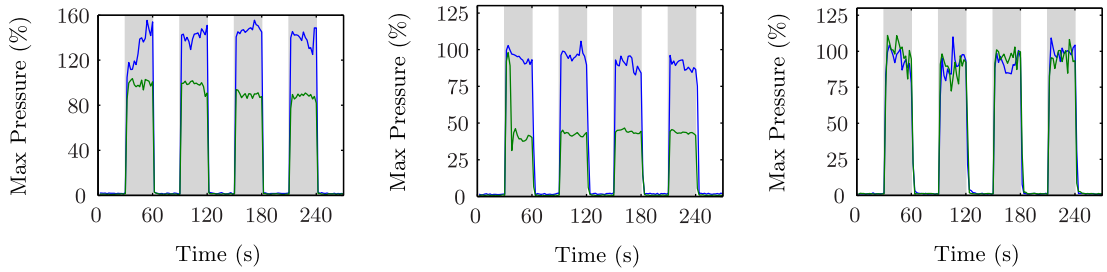

(a) Subject 1 (note y-axis scale is different to the other subjects)

(b) Subject 2

(c) Subject 3

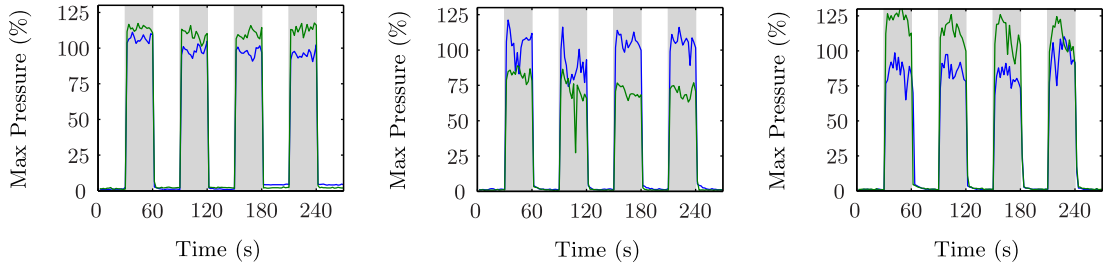

(d) Subject 4

(e) Subject 5

(f) Subject 6

Figure 5.25: The pressure recorded in the squeeze ball (as a percentage of the maximum pressure measured during calibration) for all six subjects for FMRI data acquired with conventional GE-EPI pulse (blue line) and z-shimmed GE-EPI (green line). The shaded grey regions illustrate the periods in which the subject was instructed to squeeze the ball in their right hand every 2 s.

majority of case the subjects performed the task consistently over the full duration of both FMRI data acquisitions. However, differences are observed in the maximum percentage pressure between FMRI runs. Unfortunately, as the squeeze ball pressure was re-calibrated prior to each FMRI data acquisition, it is not possible to determine if these differences were due to the subject squeezing the ball harder during calibration or the task itself. During the collection of the data acquired with the z-shim sequence, subject two reduced the pressure exerted on the squeeze ball close to the start of data acquisition, but after this step change squeezed the ball consistently hard. Subject five failed to squeeze the ball once during the second epoch of data acquired with the z-shim pulse sequence.

Thresholded z-statistic maps for each subject and acquisition method are shown in Figure 5.26. The motor paradigm resulted in statistically significant BOLD signal changes in the left motor cortex in all subject for both acquistion methods. With the exception of subject four, statistically significant BOLD signal changes were also observed in the supplementary motor area. As shown in Table 5.5 the peak z-statistic was greater for data acquired with z-shimming in five of the six subjects. The estimated movement of the subjects between the z-shim calibration scan and the

	Peak z-statistic	
Subject	GE-EPI	2-step z-shim GE-EPI
1	13.6	15.7
2	12.3	13.9
3	12.5	13.5
4	7.0	7.2
5	12.3	11.5
6	12.9	15.1
Mean	11.8	12.8

Table 5.5: Peak z-statistic from the GLM analysis of the motor task FMRI data acquired with conventional GE-EPI and GE-EPI with z-shimming.

	Translations (mm)			Rotation Angles (rad)		
Subject	x	y	z	x	y	z
1	0.18	1.06	-1.39	-0.017	0.008	-0.001
2	0.12	0.62	-0.89	-0.004	0.015	0.004
3	1.67	-1.13	-1.41	-0.005	0.008	-0.014
4	0.15	-0.27	1.08	0.004	0.006	-0.002
5	-4.39	7.46	5.56	-0.028	-0.050	0.0447
6	-0.02	-0.61	-0.87	-0.004	-0.004	-0.003

Table 5.6: Estimated subject motion between the acquisition of the z-shim calibration scan and the motor-task FMRI data acquired with z-shimming. Translations greater than half the voxel size (1.65 mm) in any direction are highlighted in red.

motor-task FMRI data acquired with z-shimming are shown in Table 5.6. Subject three moved by approximately half a voxel in the left-right direction and subject five moved by nearly two voxels in the superior-inferior direction.

Measuring BOLD sensitivity via Breath-hold BOLD Signal Changes

The variations in the subjects' breathing throughout the breath-hold FMRI scans, measured using the respiratory bellows, are shown in Figure 5.27 for all six subjects. These plots demonstrate that all subjects performed the paced breathing and breath-holding on expiration as instructed throughout both FMRI acquisitions.

Thresholded z-statistic maps showing voxels with significant changes in BOLD signal as a result of the breath-hold task for each subject and acquisition method are shown for representative slices through the orbitofrontal and inferior temporal regions in Figures 5.28 and 5.29. In all six subjects statistically significant BOLD signal changes in response to the breath-hold task are observed in the regions of recovered signal in the orbitofrontal and inferior temporal areas.

The estimated movement of the subjects between the z-shim calibration scan

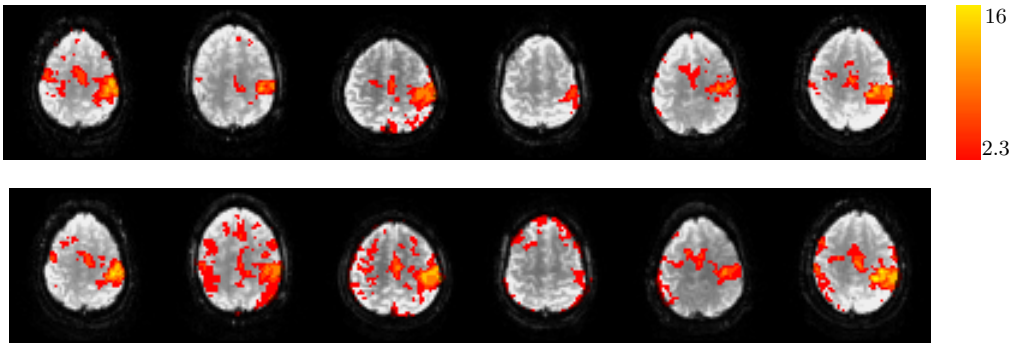

Figure 5.26: Thresholded z-statistic maps, showing voxels with significant changes in BOLD signal in response to the motor task, overlaid on the GE-EPI data from which they were derived, for each subject acquired with the conventional GE-EPI (top-row) and GE-EPI with 2-step z-shimming (bottom-row) for representative slices though the motor cortex and supplementary motor area.

	Translations (mm)			Rotation Angles (rad)		
Subject	x	y	z	x	y	z
1	0.46	-0.43	0.23	0.003	0.005	-0.008
2	0.95	0.38	-1.57	-0.011	0.023	-0.001
3	2.77	-2.62	-2.09	0.002	0.015	-0.023
4	0.36	-0.03	2.60	-0.002	0.017	-0.004
5	-4.77	7.47	6.26	-0.027	-0.047	0.045
6	0.42	-0.88	-0.99	0.004	0.004	-0.001

Table 5.7: Estimated subject motion between the acquisition of the z-shim calibration scan and the breath-hold FMRI data acquired with z-shimming. Translations greater than half the voxel size (1.65 mm) in any direction are highlighted in red.

and the breath-hold FMRI data acquired with z-shimming are shown in Table 5.7. Subjects two and three moved by more than half a voxel in the superior-inferior direction, subject five moved by nearly two voxels in the same direction.

Detectability of Resting-State FMRI Networks with PICA

The ten independent components from the probabilistic independent component analyses which visually matched the resting-state networks described in Smith et al. [169] are shown in Figure 5.30. The ten networks were readily identified from the set of twenty independent components resulting from the analysis of the data acquired with conventional GE-EPI. In the remaining ten components artefacts such as subject motion and blood flow in the sagittal sinus were observed, in agreement with previous findings [169]. The task of identifying the ten networks from the independent components of the z-shim datasets proved only slightly more difficult. The medial and occipital visual networks were observed as a single component (Figures

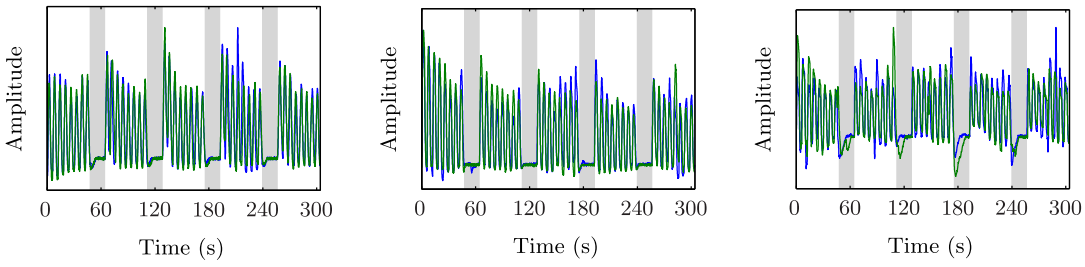

(a) Subject 1 (b) Subject 2 (c) Subject 3

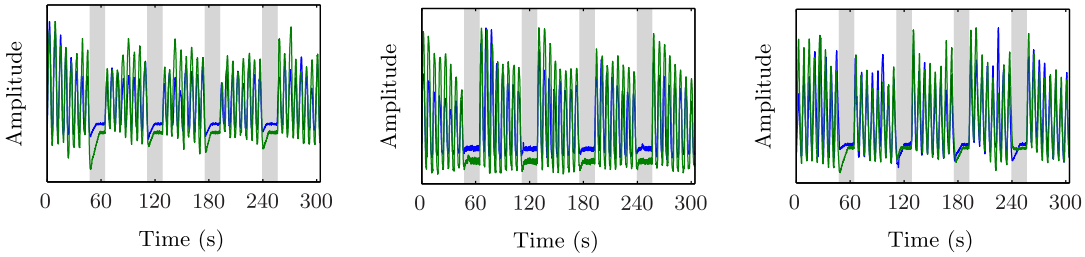

(d) Subject 4 (e) Subject 5 (f) Subject 6

Figure 5.27: Variations in the subjects breathing during acquisition of the breath-hold FMRI data with both conventional GE-EPI (blue line) and GE-EPI with z-shimming (green line). The shaded grey regions illustrate the periods in which the subject was instructed to hold their breath.

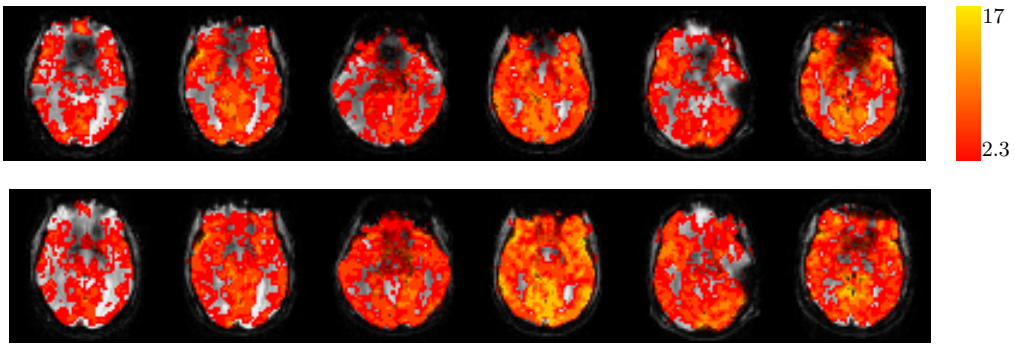

Figure 5.28: Thresholded z-statistic maps, showing voxels with significant changes in BOLD signal as a result of the breath-hold task overlaid on the GE-EPI data from which they were derived for each subject acquired with conventional GE-EPI (top-row) and GE-EPI with z-shimming (bottom-row) for representative slices though the orbitofrontal cortex.

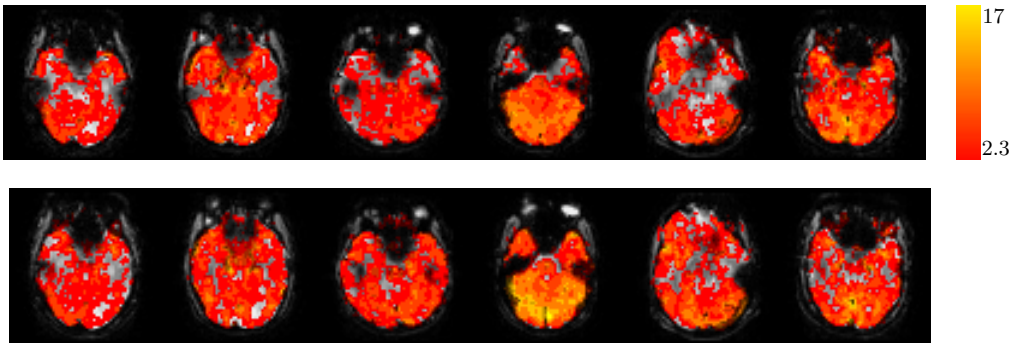

Figure 5.29: Thresholded z-statistic maps, showing voxels with significant changes in BOLD signal as a result of the breath-hold task overlaid on the GE-EPI data from which they were derived for each subject acquired with conventional GE-EPI (top-row) and GE-EPI with z-shimming (bottom-row) for representative slices though the inferior temporal regions.

5.30(a) and 5.30(b)) however, the remaining networks were identified as separate, spatially independent, components.

Detectability of Resting-State FMRI Networks Using Seed Based Analysis

In all six subjects, for data acquired with conventional GE-EPI, the BOLD signal fluctuations in the left and right lateral parietal cortex as well as in the medial prefrontal cortex were significantly correlated with the mean BOLD signal from a seed in the posterior cingulate; Figure 5.31. These brain regions are the main areas involved in the default mode network. For data acquired with z-shimming a similar spatial pattern of correlation was observed. In subjects one, two, three and five the BOLD signal variations in the areas of recovered signal in the orbitofrontal cortex were significantly correlated with the posterior cingulate seed, Figure 5.32. The BOLD signal variations in the areas of recovered signal in the inferior temporal regions were also significantly correlated with the posterior cingulate seed in subjects three and four. However, a large number of other voxels with similar z-statistics were also observed. The regions where the BOLD signal variations were significantly correlated with resting-state signal changes from a seed in the left motor cortex are shown in Figures 5.34 to 5.36. The supplementary motor area and right motor cortex were significantly correlated with the left motor cortex in data acquired with both aquisition techniques. For subjects one and two the thresholded z-statistic maps, calculated from data acquired with z-shimming, also showed significant correlations in the orbitofrontal and inferior temporal regions. Again, since a large number of other voxels have a similar z-statistic it is difficult to determine if this is an artifact or indicative of a functional connection to the other nodes of the motor network.

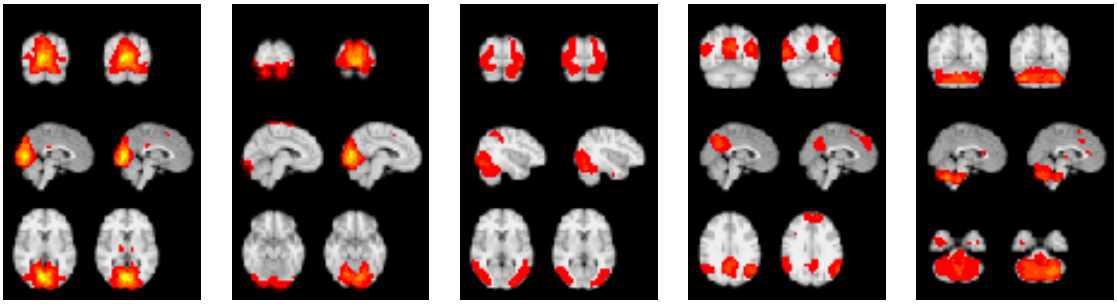

(a) Medial Visual† (b) Occipital Pole Visual† (c) Lateral Visual (d) Default Mode (e) Cerebellar

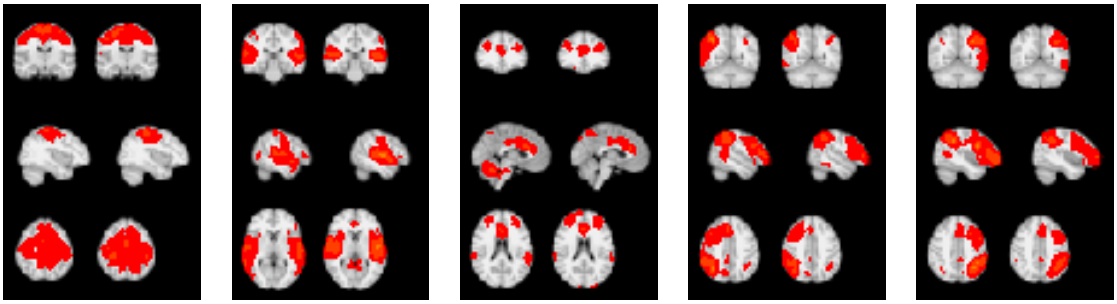

(f) Sensoriomotor (g) Auditory (h) Executive Control (i) Right Fronto-Parietal (j) Left Fronto-Parietal

Figure 5.30: Thresholded z-statistic maps ($3 < z < 22$) for the ten independent components from the probabilistic independent component analyses which visually matched those described in Smith et al. [169]. The three most informative orthogonal slices are shown for each network. The left column in each sub-figure contains independent components from the data acquired using conventional GE-EPI and the right column the components from the z-shim data. The components are shown overlaid on the MNI152 standard space template (re-sampled to 4 mm isotropic voxel size). †The medial and occipital-pole lateral visual networks were observed as a single component in the z-shim data.

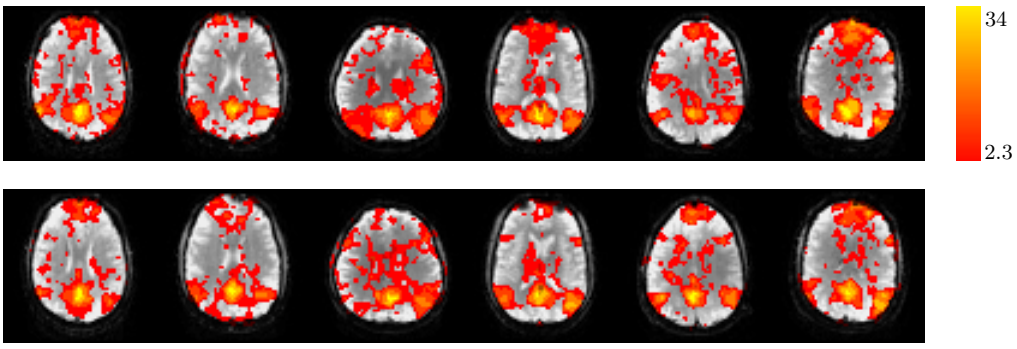

Figure 5.31: Thresholded z-statistic maps, showing voxels in which the resting-state BOLD signal changes are significantly correlated with the signal variation from a seed in the posterior cingulate, for data acquired with conventional GE-EPI (top-row) and z-shimming (bottom-row). Representative axial slices though posterior cingulate regions are shown for each subject.

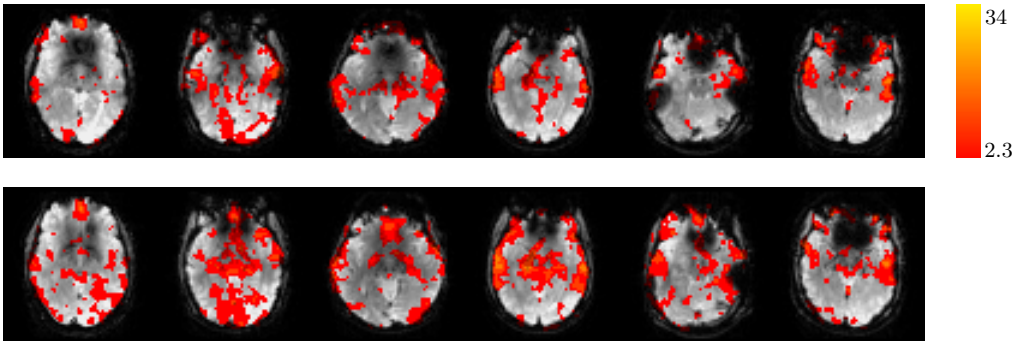

Figure 5.32: Thresholded z-statistic maps, showing voxels in which the resting-state BOLD signal changes are significantly correlated with the signal variation from a seed in the posterior cingulate, for data acquired with conventional GE-EPI (top-row) and z-shimming (bottom-row). Representative axial slices though the orbitofrontal regions are shown for each subject.

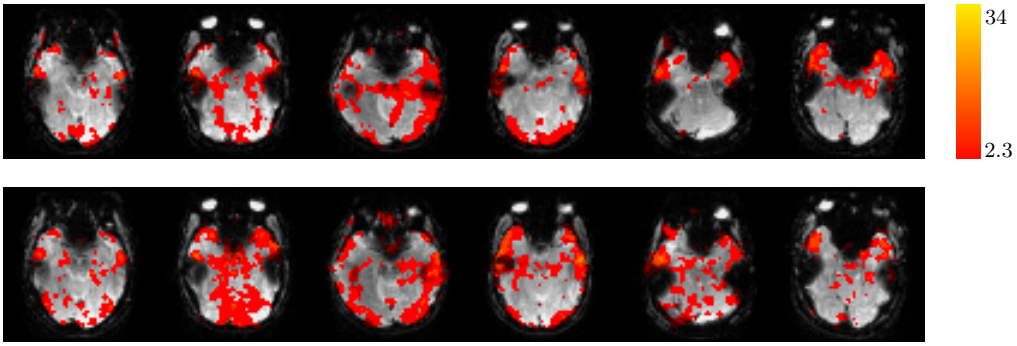

Figure 5.33: Thresholded z-statistic maps, showing voxels in which the resting-state BOLD signal changes are significantly correlated with the signal variation from a seed in the posterior cingulate, for data acquired with conventional GE-EPI (top-row) and z-shimming (bottom-row). Representative axial slices though inferior temporal regions are shown for each subject.

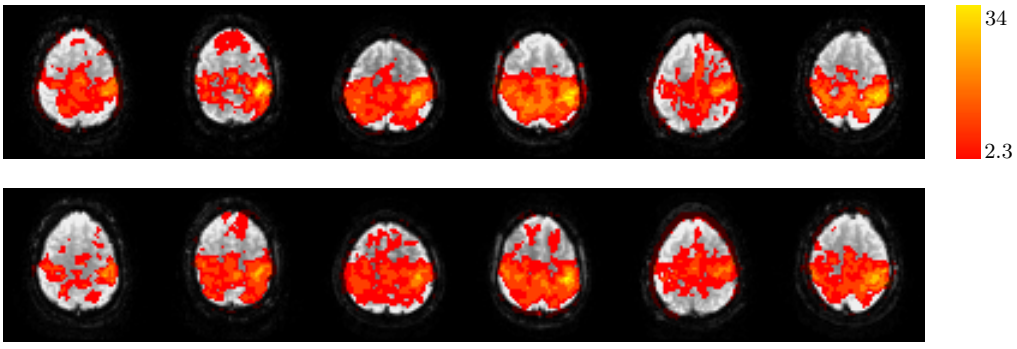

Figure 5.34: Thresholded z-statistic maps, showing voxels in which the resting-state BOLD signal changes are significantly correlated with the signal variation from a seed in the left motor cortex, for data acquired with conventional GE-EPI (top-row) and z-shimming (bottom-row). Representative axial slices though left and right motor cortex and supplementary motor area are shown for each subject.

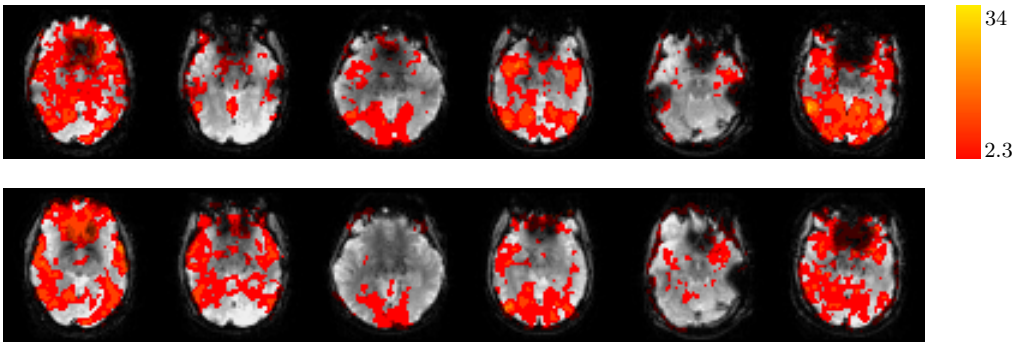

Figure 5.35: Thresholded z-statistic maps, showing voxels in which the resting-state BOLD signal changes are significantly correlated with the signal variation from a seed in the left motor cortex, for data acquired with conventional GE-EPI (top-row) and z-shimming (bottom-row). Representative axial slices though orbitofrontal regions are shown for each subject.

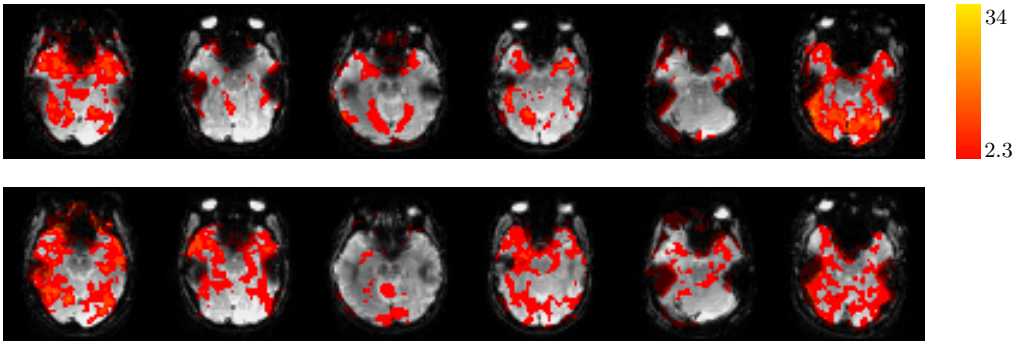

Figure 5.36: Thresholded z-statistic maps, showing voxels in which the resting-state BOLD signal changes are significantly correlated with the signal variation from a seed in the left motor cortex, for data acquired with conventional GE-EPI (top-row) and z-shimming (bottom-row). Representative axial slices though inferior temporal regions are shown for each subject.

5.5.4 Discussion and Conclusions

From the results of the experiments performed on the six healthy volunteers a number of conclusions may be drawn about the usefulness of the two-step z-shimming approach in task-based and resting-state FMRI experiments.

For each of the six subjects the pair of slice specific z-shim gradients were calculated on the scanner, in five seconds, from a calibration scan (with an acquisition time of 3 minutes and 30 seconds) masked to include only voxels containing grey matter (using a DIR-EPI scan with an acquisition time of 48 s). The range of k-space offsets required to recover signal was $-1/\Delta z < \delta k_{z,sh} < 1/\Delta z$, which is half that spanned by the calibration scan. Therefore it would be possible to improve the technique by halving the number of steps in the calibration scan ($N_{shim} = 51$); this would save 1 minute and 40 seconds.

It is encouraging that compared to the conventional GE-EPI images, signal was recovered in large parts of the orbitofrontal and inferior temporal regions in the SSQ z-shimmed images. Additionally, the recovery of signal was greater in these regions compared to when the pairs of z-shim gradients were determined using all voxels in a slice (regardless of the type of tissue they contained). However some areas of signal dropout remained; this remaining signal loss may have been caused by susceptibility gradients in the frequency and phase encoding directions, which is not recoverable by z-shimming.

Importantly the recovery of signal was accompanied by increases in the TSNR in the same areas of the orbitofrontal and inferior temporal regions. Moderate increases in TSNR were also observed across the majority of grey matter voxels. This general increase can be explained by reference to the Bloch simulations shown in Figure 5.6(b); the normalised signal intensity from the SSQ combination of two z-shim images at the optimal shim spacing $\Delta k = 0.68/\Delta z$ is greater than one for $-0.4 < G_{z,s} < 0.4$ in units of $\frac{2\pi}{\gamma TE\,\Delta z}$ (which corresponds to $-105 < G_{z,s} < 105$ $\mu\mathrm{Tm}^{-1}$ for $TE = 30$ ms and $\Delta z = 3$ mm).

The results of the motor task FMRI experiment shows that, despite the loss of temporal resolution caused by two-step z-shimming, statistically significant activations were detected in all six subjects in the left motor cortex. In five out of the six subjects the peak z-statistic was greater for the data acquired with z-shimming; i.e. for this specific task increases in TSNR translated into an increased sensitivity to detect BOLD signal changes. However, these increases may not be achievable in event-related FMRI experiments because of the loss of temporal resolution.

Statistically significant BOLD signal changes were observed in the breath-hold FMRI data, acquired with z-shimming, in those in the regions with improved signal and TSNR. This suggests that the BOLD sensitivity had increased in these regions.

In addition, the pattern of statistically significant BOLD signal changes in the rest of the brain was similar to that from the conventional GE-EPI data. This implies that improvements in the BOLD sensitivity in the regions affected dropout does not come at the cost of reduced sensitivity elsewhere. That said, because the breath-hold task has a block-design, the impact of the loss of temporal resolution may not be accounted for in these observations.

The probabilistic independent component analyses of the resting-state data showed that it was slightly more difficult to identify the common resting-state functional networks described in Smith et al. [169] in the z-shimming data as in one case two brain networks were combined into a single independent component. This may be a result of the changes in the temporal resolution and temporal smoothness of the data caused by the combination of pairs of images by SSQ. However, more work is needed to determine if this is the case.

In agreement with the very recent findings of Dalwani et al. [299] the seed-based analysis suggests that the regions of the orbitofrontal cortex, previously obscured by signal dropout, may potentially be functionally connected to the default mode network. However this correlation was not consistently observed in all six subjects. In addition, in those subjects where it was observed, a large number of other voxels, distributed across the brain, had similar z-statistics. Furthermore, in two out of the six subjects significant correlations between the orbitofrontal region and the motor network were seen. These results may imply the correlations are artifactual, potentially as a result of residual physiological noise unaccounted for by the white matter, CSF and global signal regressors. Further work is required to determine the true source of these correlations.

Given that the optimal z-shims were determined for each slice, the z-shimming technique as described in this chapter could be sensitive to subject motion at a number of points. Subject motion during the calibration scan could result in a sub-optimal choice of the pairs of slice specific z-shim gradients. Motion between the calibration scan and DIR-EPI acquisition would result in the algorithm determining the optimal z-shims based on a set of voxels that may not necessarily contain grey matter. Finally, motion between that calibration scan and the volume of FMRI data being acquired may result in a suboptimal choice of z-shim gradients for the location of the slices that are actually being acquired. This may hinder the signal recovery in areas of dropout. The six healthy subjects scanned in this experiment were all experienced and therefore were able to keep still. The largest movement observed relative to the calibration scan was approximately two voxels in the direction of slice selection. This did not appear to significantly impact the efficacy of the technique however, further studies in patient cohorts are needed to determine how robust the technique is to subject motion.

5.6 Summary

A number of different implementations of z-shimming have previously been shown to increase the detectability of task induced BOLD signal changes in the regions of signal dropout such as the orbitofrontal cortex, inferior temporal and parahippocampal-amygdala regions [72, 271, 273–275]. In the last year Dalwani et al. [299] have demonstrated that when resting-state FMRI data were acquired with z-shimming, regions of the orbitofrontal cortex, which are affected by signal dropout in conventional GE-EPI images, may be functionally connected to the default mode network.

I developed an algorithm to determine, on a slice specific basis, the optimal pair of z-shim gradients to recover signal in the grey matter in the regions of dropout whilst preserving the signal in grey matter in regions of homogeneous B_0. This used data acquired in a calibration scan, as well a grey matter mask produced from a DIR-EPI acquisition. This was tailored to null the signal from white matter and CSF. Rather than using a theoretical model that assumed perfectly rectangular slice profiles, Bloch simulations were used to determine the optimal spacing, $\Delta k_{z,sh} = 0.68/\Delta z$, of the two z-shim gradients for the specific RF pulse and slice selection gradient used on the GE Discovery MR750 system. This procedure would be straightforward to replicate for the RF pulses used on other scanners as programs to perform Bloch simulations are widely available. The algorithm was implemented in C++; it took five seconds to run on the scanner. Therefore, in total, the acquisition of the calibration scan and DIR-EPI image and the calculation of the optimal z-shim gradients required 4 minutes and 23 seconds (however, as noted above, this could be reduced by halving the number of steps in the calibration scan).

A set of experiments were carried out on six healthy volunteers to determine if grey matter optimised z-shimming improved the sensitivity to BOLD signal changes in the regions affected by signal dropout. The technique resulted in increases in both the signal and TSNR in significant areas of the orbitofrontal and inferior temporal regions. In addition increases in the BOLD sensitivity were observed in the same regions. Seed based analysis of the resting state data suggested that parts of the orbitofrontal cortex, affected by signal dropout in conventional GE-EPI images, were functionally connected to the default mode network in agreement with previous work [299]. Further work is needed, in a greater number of subjects, to determine if this is a genuine effect rather than a false positive finding however.

Further work is also needed to determine the impact of the loss of temporal resolution, resulting from the need to acquire two volumes of data with different z-shim gradients, on resting-state and event-related FMRI experiments. The PICA analysis of the z-shimmed resting-state FMRI data showed that two of the expected resting state networks were combined into a single independent component which

could be a result of the loss in temporal resolution or changes in the temporal smoothness of the data caused by the SSQ combination of pairs of images.

Chapter 6

Reducing Signal Dropout with Quadratic Phase Radiofrequency Pulses

6.1 Introduction

Cho and Ro [126] were the first to demonstrate that RF excitation pulses could be designed to reduce the signal loss caused by susceptibility gradients in the human head. They created a tailored radiofrequency (TRF) pulse which induced a quadratic variation in the phase of the transverse magnetisation in the direction of slice-selection. This partially cancelled the phase dispersion resulting from linear through-slice susceptibility gradients, leading to signal recovery. More recently Chung et al. [132] modified the original TRF pulse and, with an FMRI task involving the processing of facial attractiveness, found statistically significant BOLD signal changes in the orbitofrontal and inferior temporal areas which were not detected using a conventional GE-EPI acquisition. Unfortunately neither Cho and Ro [126] nor Chung et al. [132] gave sufficient details of the functional form of their pulses to allow their work to be replicated [30, 300]. 3D TRF pulses which completely cancel out the phase changes induced by the susceptibility gradients have also been developed [128–130]. They have the advantage that the signal in the regions of homogeneous field is conserved, however, the RF design procedure is computationally intensive, and hence it is not practical at present to produce subject specific 3D TRF pulses during the scanning session [131]. Therefore I extend the work of Shmueli [30], using full-passage scaled-down complex hyperbolic secant (HS) pulses for signal excitation. These pulses produce an approximately quadratic variation in the phase of the transverse magnetisation in the slice-selection direction [301–303] so they can be used to reduce signal dropout [30]. I describe a systematic approach

to designing HS pulses for signal recovery. Bloch simulations are used to determine the HS pulse parameters required to produce a uniform signal response across the range of susceptibility gradients typically observed in the head. The limitations imposed on the RF pulse amplitude and imaging gradient parameters by the MRI scanner hardware are accounted for and an expression for the bandwidth of a HS pulse (when used for signal excitation) is derived and used for the first time. The ability of this optimised HS pulse to recover signal is investigated in six healthy male subjects using both task and resting-state FMRI experiments at 3 T.

6.2 Theoretical Background

6.2.1 Theory of Signal Recovery using Quadratic Phase RF Pulses

A linear susceptibility gradient in the direction of slice selection, $G_{z,s}$, induces a linear variation in the phase, ϕ, of the transverse magnetisation, M_{xy}, across the slice:

$$\phi = \gamma \, TE \, G_{z,s} z \tag{6.1}$$

As first shown by Cho and Ro [126] this phase dispersion can be cancelled out, at least in part of the slice, using a radiofrequency pulses that induces a quadratic variation in the phase of M_{xy}:

$$\phi = az^2 \tag{6.2}$$

such that the overall variation in the phase is given by:

$$\phi = az^2 + \gamma \, TE \, G_{z,s} z \tag{6.3}$$

Here a is a design parameter that can be used to tailor degree of quadratic phase variation. The phase as a function of position within the slice, calculated using Equation 6.3 for four illustrative cases, is shown in Figure 6.1. Firstly with a conventional RF excitation pulse ($a = 0$ rad mm^{-2}) and in the absence of a susceptibility gradient the phase is constant and equal to zero across the whole slice; Figure 6.1(a). Secondly, if the same conventional RF pulse is used in a region of linear through-plane susceptibility gradient, the phase of the transverse magnetisation also varies linearly across the slice. When $G_{z,s} = \frac{2\pi}{\gamma TE \Delta z}$ the isochromats are distributed evenly in the transverse plane and thus cancel out, Figure 6.1(b), leading to a complete loss of signal. Thirdly, using an RF pulse that produces a quadratic phase variation in M_{xy} ($a = 1.67$ rad mm^{-2}) leads to a purely quadratic phase distribution in regions without a susceptibility gradient. From the distribution of isochromats it can be seen

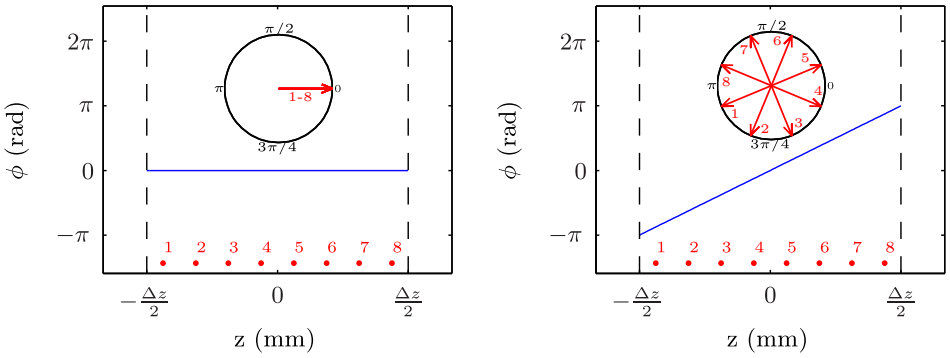

(a) $G_{z,s} = 0$ and $a = 0$ rad mm^{-2} (b) $G_{z,s} = \frac{2\pi}{\gamma TE\Delta z}$ and $a = 0$ rad mm^{-2}

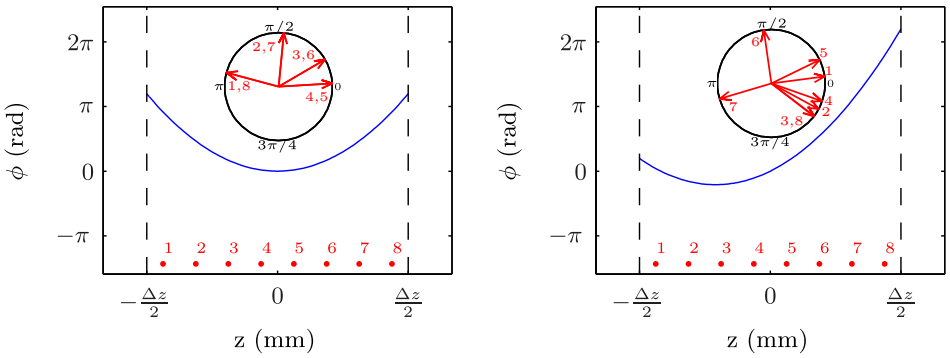

(c) $G_{z,s} = 0$ and $a = 1.67$ rad mm^{-2} (d) $G_{z,s} = \frac{2\pi}{\gamma TE\Delta z}$ and $a = 1.67$ rad mm^{-2}

Figure 6.1: An illustration of the phase distribution across a 3 mm thick slice in four representative cases; a conventional RF pulse with a uniform phase variation through the slice both with (b) and without (a) a linear through-slice susceptibility gradient, a quadratic phase RF pulse when $G_{z,s} = 0$ (c) and when $G_{z,s} = \frac{2\pi}{\gamma TE\Delta z}$ (d). The polar plots show the phases of eight isochromats distributed evenly across the slice in the positions shown at the base of each plot. This figure is a modified version of Figure 1 from Cho and Ro [126] with the addition, for clarity, of a scale on the y-axis.

that this will result in a reduction of the signal. Fourthly, and importantly, when a quadratic phase RF pulse is used in regions with linear through-plane susceptibility gradients signal is recovered. The phase distribution produced by the RF pulse cancels, in a section of the slice, the linear phase resulting from the through-plane susceptibility gradient; Figure 6.1(d).

Based on the assumption that the slice profile is perfectly rectangular, Cho and Ro [126] showed that the signal, S, acquired at an echo time TE, in the presence of a linear susceptibility gradient $G_{z,s}$, from a voxel with thickness Δz, using an RF pulse that produces a quadratic phase variation in the transverse magnetisation

across the slice is:

$$S = \sqrt{\left[\int_{-\Delta z/2}^{\Delta z/2} M_0 \cos\left[az^2 + \gamma\, TE\, G_{z,s} z\right] \mathrm{d}z\right]^2 + \left[\int_{-\Delta z/2}^{\Delta z/2} M_0 \sin\left[az^2 + \gamma\, TE\, G_{z,s} z\right] \mathrm{d}z\right]^2} \tag{6.4}$$

The signal, S, calculated numerically using Equation 6.4, is plotted as a function the design parameter, a, and the susceptibility gradient, $G_{z,s}$, in Figure 6.2. Profiles at three specific choices of the design parameter a ($a = 0$ rad mm^{-2} representing a conventional RF pulse, $a = 0.89$ rad mm^{-2} equivalent to the pulse used in Chung et al. [132] and $a = 1.67$ rad mm^{-2} to match the pulse used in Cho and Ro [126]) are shown in Figure 6.3. It is important to note that Cho and Ro [126] did not specify the value of a for their TRF pulse, Shmueli et al. [300] showed that by setting $a = 1.67$ rad mm^{-2} (for 3 mm thick slices) they could match the results of Cho and Ro [126]. This choice of a implies that the phase at the edge of the slice $\phi_{RF}(\Delta z/2)$ due to the RF pulse is:

$$\begin{aligned} \phi_{RF}\left(\frac{\Delta z}{2}\right) &= a\left(\frac{\Delta z}{2}\right)^2 \\ &= 1.67 \times 1.5^2 \\ &= 3.76\,\mathrm{rad} \end{aligned} \tag{6.5}$$

However, confusingly Chung et al. [132] stated that the phase at the edge of the slice was 2π for the TRF pulse of Cho and Ro [126]. Numerical calculations of Equation 6.4 in MATLAB support the results of Shmueli et al. [300].

When $a = 0$ rad mm^{-2} , the signal is described by Equation 6.6:

$$S = M_0 \Delta z \left|\mathrm{sinc}\left(\frac{\gamma\, TE\, G_{z,s} \Delta z}{2}\right)\right| \tag{6.6}$$

As the magnitude of the through-plane susceptibility gradient increases the signal intensity is reduced. Complete signal loss occurs when the through-plane susceptibility gradient is an integer multiple of $2\pi/\gamma TE\Delta z$, Figure 6.3(a). When $TE = 30$ ms and $\Delta z = 3$ mm the first zeros fall at $G_{z,s} = \pm 261$ μTm^{-1}. As the echo time or slice thickness are increased signal dropout occurs at smaller values of $G_{z,s}$. Susceptibility gradients in the range $-250 < G_{z,s} < 250$ μTm^{-1} have been measured at 3 T in the human head [28, 29]. As described previously [126, 132], and from Figures 6.2 and 6.3(a) it can be seen that as the degree of quadratic phase, a, is increased increasing amounts of signal are recovered in regions with susceptibility gradients, however signal is reduced in regions where $G_{z,s} = 0$. Hence there is a trade-off, controlled by a, between signal recovery in regions currently affected by signal dropout

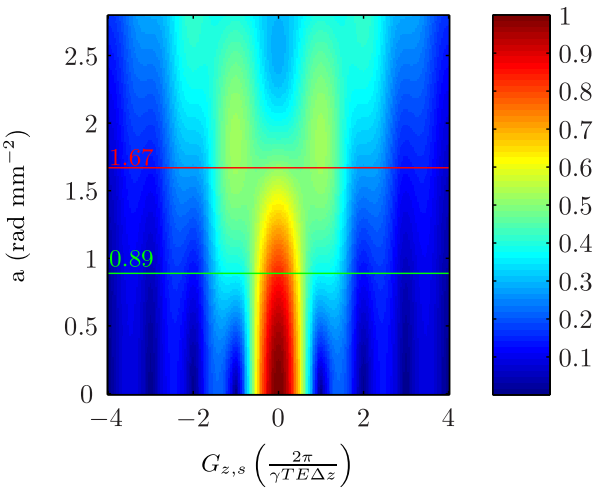

Figure 6.2: Signal intensity plotted as a function of the susceptibility gradient $G_{z,s}$ and RF pulse design parameter a. The highlighted values of $a = 0.89$ and 1.67 rad mm^{-2} match the pulses used in Chung et al. [132] and Cho and Ro [126] respectively. These specific cases are shown in more detail in Figure 6.3. For slices with $\Delta z = 3$ mm and at an echo time $TE = 30$ ms the range of gradients shown in the plot $-4\left(\frac{2\pi}{\gamma TE\Delta z}\right) < G_{z,s} < 4\left(\frac{2\pi}{\gamma TE\Delta z}\right)$ correspond to $-1044 < G_{z,s} < 1044$ μTm^{-1}

and loss of signal caused by the RF pulse in regions unaffected by through-plane susceptibility gradients. Cho and Ro [126] chose, by setting $a = 1.67$ rad mm^{-2}, to recover the greatest amount of signal. For example at $G_{z,s} = 2\pi/\gamma TE\Delta z$ the signal is $0.52\, M_0\Delta z$ compared to zero when a conventional RF pulse is used. However, at $G_{z,s} = 0$ the signal is reduced to $0.51\, M_0\Delta z$. In contrast, Chung et al. [132] set $a = 0.89$ rad mm^{-2} in an attempt to recover some signal whilst causing less signal loss of regions free of through-plane susceptibility gradients.

Whilst the signal model given by Equation 6.4 [126] highlights the tradeoff, controlled by a, between signal recovery in regions affected by signal dropout and loss of signal in areas unaffected by susceptibility gradients, the assumption that slices are perfectly rectangular is not possible to satisfy in practice. This assumption has been made elsewhere, for example by Ordidge et al. [74] when deriving the effect of z-shim compensatory gradients, and by others when correcting for the effect of through-plane susceptibility gradients in T_2^* maps [289, 304, 305]. One telling example is the slice profile of the RF pulse designed by Cho and Ro [126] shown in Figure 6.4; this is evidently not rectangular and as such does not satisfy the assumptions of their own theoretical model. Therefore, rather than using Equation 6.4, the signal as a function of the susceptibility gradient, $G_{z,s}$, and the degree of quadratic phase, a, is calculated by numerical simulation of the Bloch equations for the remainder of this chapter.

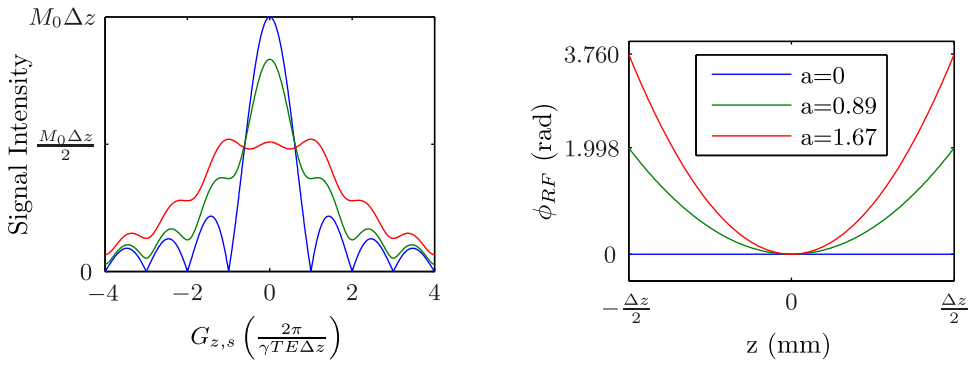

(a) Signal as a function of the susceptibility gradient

(b) Phase profiles of the RF pulses shown in (a)

Figure 6.3: Signal intensity plotted as a function of the susceptibility gradient $G_{z,s}$ for three specific choices of the design parameter a; $a = 0$ rad mm^{-2} corresponds to an RF pulse with a uniform variation in phase across the slice (blue line), the signal as a function of $G_{z,s}$ for the pulse with $a = 0.89$ rad mm^{-2} visually matches that used in Chung et al. [132] (green line) and the pulse with $a = 1.67$ rad mm^{-2} matches that used in Cho and Ro [126] (red line).

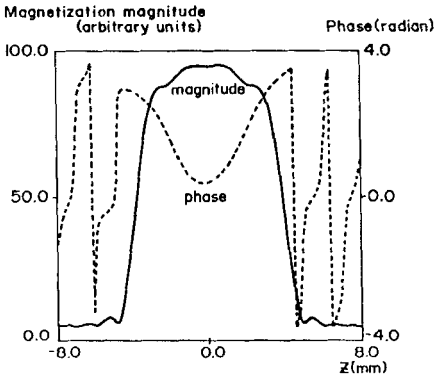

Figure 6.4: Reproduction of Figure 3 from Cho and Ro [126] showing that their RF pulse produces slices with non-rectangular profiles.

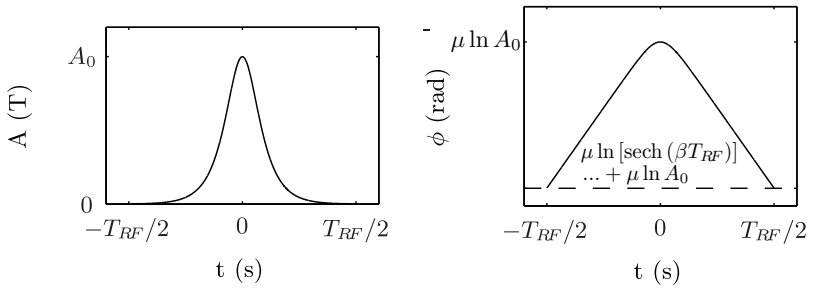

(a) Amplitude modulation (b) Phase modulation

Figure 6.5: Plots showing the amplitude and phase modulation of a complex hyperbolic secant pulse

6.2.2 Complex Hyperbolic Secant Pulses

Since neither Cho and Ro [126] nor Chung et al. [132] gave details of the functional form of their RF pulses I extend the work of Shmueli [30] who showed that complex hyperbolic secant (HS) RF excitation pulses could be used to recover signal in GE-EPI images.

Introduction

HS pulses [306, 307] were first introduced as the analytical solution to the Bloch equations in the absence of T_1 and T_2 relaxation. They are most commonly used for adiabatic inversion [39], however, throughout this chapter they are used for signal excitation[302, 303, 308]. An HS pulse with duration T_{RF} has a B_1 field [39]:

$$B_1(t) = [A_0 \,\mathrm{sech}\,(\beta t)]^{1+i\mu} \tag{6.7}$$

for $-T_{RF}/2 < t < T_{RF}/2$. Here A_0 is the maximum amplitude of the pulse, β is the modulation angular frequency and μ is a dimensionless parameter that determines both the sharpness of the slice profile [307] and controls the degree of quadratic phase [30]. Using Equation 6.7 it can be deduced that the pulse has both an amplitude $A(t)$ and a phase $\phi(t)$ modulation:

$$A(t) = A_0 \,\mathrm{sech}\,(\beta t) \tag{6.8}$$

$$\phi(t) = \mu \ln [\mathrm{sech}\,(\beta t)] + \mu \ln A_0 \tag{6.9}$$

The amplitude and phase modulation are shown in Figure 6.5.

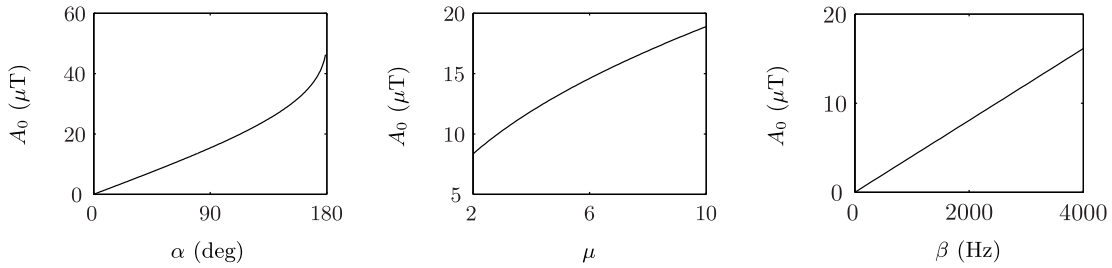

(a) Variation with flip angle for $\mu = 4.25$ and $\beta = 3040$ Hz

(b) Variation with μ for $\alpha = 73°$ and $\beta = 3040$ Hz

(c) Variation with β for $\alpha = 73°$ and $\mu = 4.25$

Figure 6.6: Plots showing the dependence of A_0 on the flip angle, α, the modulation frequency, β and μ.

Pulse Amplitude for Signal Excitation

The maximum amplitude[1], A_0, of an HS pulse used for signal excitation is a function of the flip angle, α, modulation angular frequency, β, and μ:

$$A_0 = \frac{\beta}{\gamma}\sqrt{\left(\frac{\cos^{-1}\left[\cosh^2\left(\frac{\pi\mu}{2}\right)\cos\alpha + \sinh^2\left(\frac{\pi\mu}{2}\right)\right]}{\pi}\right)^2 + \mu^2} \tag{6.10}$$

A derivation of Equation 6.10 is given in Appendix B. The dependence of A_0 on the flip angle, modulation angular frequency, β, and μ is shown in Figure 6.6. As might be expected, higher flip angles require greater pulse amplitudes. Increasing μ to produce sharper slice profiles or increased degrees of quadratic phase also requires a greater pulse amplitude. Finally, a linear increase in β, for example to reduce the stop-band ripple in the slice profile, necessitates a linear increase in the maximum pulse amplitude.

Excitation Pulse Bandwidth

In the previous work [30, 300] using HS pulses for signal excitation it was assumed that the pulse bandwidth, Δf, is:

$$\Delta f_{inv} = \frac{\mu\beta}{\pi} \tag{6.11}$$

i.e. the same as when the pulses are used for adiabatic inversion[307]. However, the bandwidth of an excitation pulse is defined as the full-width at half-maximum (FWHM) of the magnitude of the transverse magnetisation, $|M_{x,y}|$, which as shown

[1]This expression is equivalent to Equation 7 of Warnking and Pike [309].

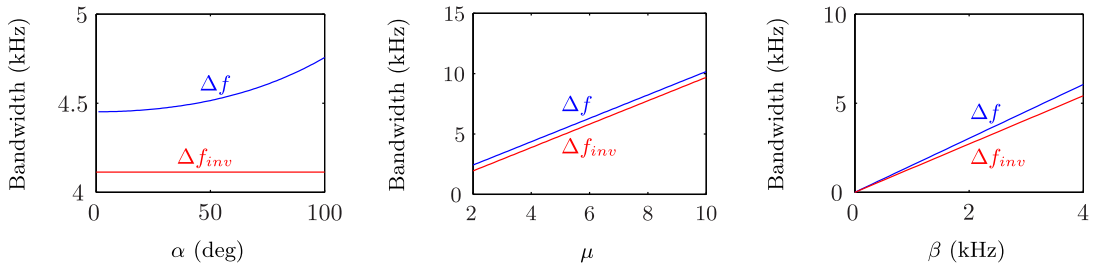

(a) Variation in bandwidth with flip angle for $\mu = 4.25$ and $\beta = 3040$ Hz

(b) Variation in bandwidth with μ for $\alpha = 73°$ and $\beta = 3040$ Hz

(c) Variation in bandwidth with β for $\alpha = 73°$ and $\mu = 4.25$

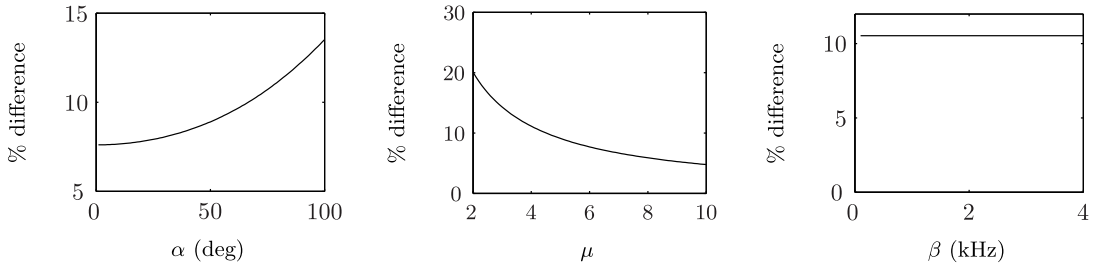

(d) Percentage difference in resulting slice thickness as a function of flip angle for $\mu = 4.25$ and $\beta = 3040$ Hz

(e) Percentage difference in resulting slice thickness as a function of μ for $\alpha = 73°$ and $\beta = 3040$ Hz

(f) Percentage difference in resulting slice thickness as a function of β for $\alpha = 73°$ and $\mu = 4.25$

Figure 6.7: Plots (a)-(c) show the effect of the flip angle, α, μ and β on the bandwidth derived for HS excitation pulses, Δf and the bandwidth, Δf_{inv}, derived previously for HS inversion pulses [307]. Plots (d)-(e) show the resulting percentage change in slice thickness if it is wrongly assumed that the inversion pulse bandwidth is valid for excitation pulses.

for the first time in Appendix C is:

$$\Delta f = \frac{\beta}{\pi^2}\cosh^{-1}\left[\frac{\cosh(\pi\mu)\left(\cos(\alpha) - \frac{1}{2}\sqrt{3+\cos^2(\alpha)}\right) + \cos(\alpha) - 1}{\frac{1}{2}\sqrt{3+\cos^2(\alpha)} - 1}\right] \tag{6.12}$$

When $\mu \geq 2$ this simplifies to (again see Appendix C for details):

$$\Delta f = \frac{\beta\mu}{\pi} + \frac{\beta}{\pi^2}\ln\left(\frac{\cos(\alpha) - \frac{1}{2}\sqrt{3+\cos^2(\alpha)}}{\frac{1}{2}\sqrt{3+\cos^2(\alpha)} - 1}\right) \tag{6.13}$$

Therefore, as shown in Figures 6.7(a) to 6.7(c), the bandwidth is a function of μ, β and the flip angle. Given that:

$$\ln\left(\frac{\cos(\alpha) - \frac{1}{2}\sqrt{3+\cos^2(\alpha)}}{\frac{1}{2}\sqrt{3+\cos^2(\alpha)} - 1}\right) > 0 \tag{6.14}$$

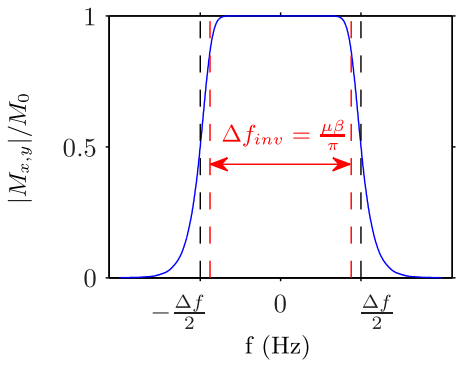

Figure 6.8: A numerical simulation of the Bloch equations showing the frequency response of an HS pulse ($\alpha = 90°$, $\mu = 4.25$ and $\beta = 2040$ Hz) to highlight the difference between the two definitions of bandwidth, Δf_{inv}, from Silver et al. [307] and Δf, given by Equation 6.12

for $0 < \alpha < \pi$, Δf_{inv} is less than the true bandwidth of a hyperbolic secant excitation pulse. As shown in Figures 6.7(d) to 6.7(f) this results in slices that are thicker than prescribed. This is further highlighted in Figure 6.8 where the two different definitions of the bandwidth are overlaid on a plot of the frequency response of a HS pulse (calculated by numerically solving the Bloch equations in MATLAB).

Tailoring the Phase Variation Produced by a Complex Hyperbolic Secant Pulse

Shmueli [30] found that a quadratic function (az^2) accurately described the variation in the phase of the transverse magnetisation, resulting from a HS pulse, over the central 75% of the slice. In addition they showed by simulation that the degree of quadratic phase, a, was proportional to μ. They did not, however, investigate the dependence of the phase variation on the pulse duration, T_{RF}, modulation frequency, β, or the flip angle, α. These dependencies can be determined from the analytic expression for the variation of the phase of the transverse magnetisation through the slice, $\phi(z)$, resulting from an HS pulse [302, 303]:

$$\phi(z) = -\mu \ln\left(\frac{-\mu\beta \,\mathrm{sech}\,(\beta T_{RF}/2)}{\sqrt{(\mu\beta)^2 - (\gamma G_z z)^2}}\right) + \frac{\gamma G_z z}{2\beta} \ln\left(\frac{\mu\beta + \gamma G_z z}{\mu\beta - \gamma G_z z}\right) \tag{6.15}$$

where G_z is the amplitude of the slice selection gradient. As shown in Appendix D the phase variation described in Equation 6.15 can be rearranged to give:

$$\phi(z) = -\mu \ln\left(\frac{1}{\sqrt{1 - z^2\left(\frac{2}{\Delta z} + \frac{2h(\alpha)}{\pi\mu\Delta z}\right)^2}}\right) - \mu z\left(\frac{1}{\Delta z} + \frac{h(\alpha)}{\pi\mu\Delta z}\right)\ln\left(\frac{1 + z\left(\frac{2}{\Delta z} + \frac{h(\alpha)}{\pi\mu\Delta z}\right)}{1 - z\left(\frac{2}{\Delta z} + \frac{h(\alpha)}{\pi\mu\Delta z}\right)}\right) \quad (6.16)$$

where Δz is the slice thickness and:

$$h(\alpha) = \ln\left(\frac{\cos(\alpha) - \frac{1}{2}\sqrt{3 + \cos^2(\alpha)}}{\frac{1}{2}\sqrt{3 + \cos^2(\alpha)} - 1}\right) \quad (6.17)$$

A Taylor expansion[2] of both terms makes it clear that the first order variation of the phase is quadratic in z. It is also clear that the phase variation depends on μ and α, however, it is independent of β and T_{RF}. Therefore the degree of quadratic variation in the phase of the transverse magnetisation produced by the pulse can be tailored using μ. It is important to note, however, that if the flip angle is changed then, to maintain the same degree of quadratic phase, μ must be modified accordingly. This effect was not accounted for in previous studies [30].

In addition to controlling the phase variation, μ determines the sharpness of the slice profile [307]. The dependence of the phase variation and slice profile on μ are clear from the Bloch simulations of HS pulses with $\mu = 2$, 5 and 8 shown in Figure 6.9.

Addendum: During the write up of this chapter a slight asymmetry in the phase variation was noticed for $\mu = 2$. This suggests that the pulse isodelay (used to set the area of the slice-selection refocussing gradient) is not exactly $T_{RF}/2$, for all μ, as had been assumed. Further Bloch simulations for the optimal HS pulse (μ=4.25, β=3040 Hz, T_{RF}=5ms and $\alpha = 73°$) designed and used in the later parts of this chapter suggest that the isodelay for these particular parameters is $0.5035\,T_{RF}$. Further simulations showed that using a value of $0.5\,T_{RF}$ rather than the more precise $0.5035\,T_{RF}$ did not significantly affect the dependence of the voxel signal on the sus-

[2]As explained by Park et al. [302] the phase profile is approximately quadratic as the Taylor expansion of both terms in Equation 6.15 are:

$$\ln\left(\frac{1}{\sqrt{1 - x^2}}\right) = \frac{1}{2}x^2 + \frac{1}{4}x^4 + \frac{1}{6}x^6 + \frac{1}{8}x^8 + \ldots \quad (6.18)$$

$$x\ln\left(\frac{1 + x}{1 - x}\right) = 2x^2 + \frac{2}{3}x^4 + \frac{2}{5}x^6 + \frac{2}{7}x^8 + \ldots \quad (6.19)$$

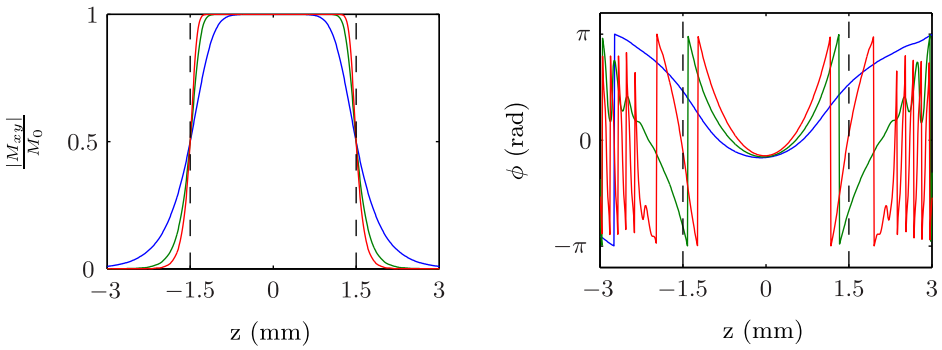

(a) Slice profile (b) Phase variation

Figure 6.9: Bloch simulations of the magnitude and phase across a 3mm slice excited using a scaled-down full passage hyperbolic secant pulse ($\alpha = 90°$ and $\beta = 3040$ Hz) for a representative range of $\mu = 2$ (blue), 5 (green) and 8 (red), demonstrating the dependence of the slice profile and degree of quadratic phase on μ.

ceptibility gradient, and as such the optimisation of the pulse parameters described below (with an isodelay of $0.5035\,T_{RF}$*) remains valid.*

The Effect of β on the Slice Profile

As described above, the value of β does not affect the variation of the phase across the slice, however for a pulse with a finite duration, T_{RF}, it does impact upon the degree of stop-band ripple in the slice profile. As shown in Figure 6.10(a) the finite duration of the HS pulse means that its amplitude has a discontinuity at the start and end, this truncation leads to ripples in the stop-band, Figure 6.10(b) and (c). For comparison with previous work, this truncation is measured using the cut-off, c, is defined as the ratio of the amplitude at the start or end of the RF pulse to the peak amplitude [30]:

$$\begin{aligned} c &= \frac{A_0 \operatorname{sech}\left(\frac{\beta T_{RF}}{2}\right)}{A_0 \operatorname{sech}(0)} \\ &= \operatorname{sech}\left(\frac{\beta T_{RF}}{2}\right) \end{aligned} \tag{6.20}$$

The cut-off, and consequently the size of stop-band ripple, are reduced as β is increased.

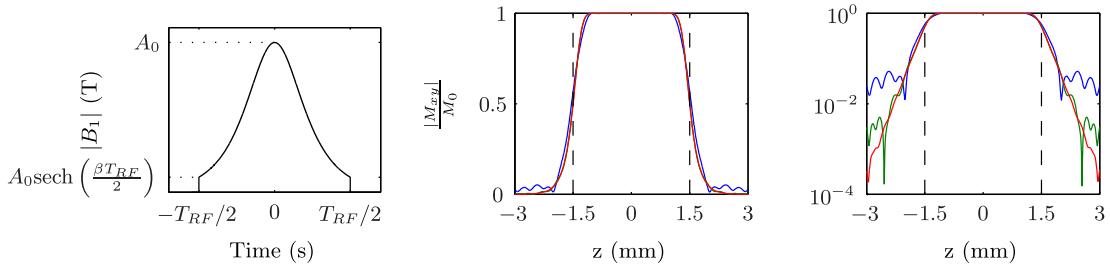

(a) Discontinuities at the start and end of the HS pulse

(b) Slice profile on a linear scale

(c) Slice profile on a logarithmic scale

Figure 6.10: Graphs illustrating the discontinuities at the start and end of the HS pulse (a), and Bloch simulations demonstrating the effect of the cut-off (10% (blue), 1% (green) and 0.1% (red)) on the stop-band ripple in the resulting slice profile displayed with a linear (b) and logarithmic (c) scale. The cut-off shown in (a) is 10%; this is purely for illustrative purposes and is an order of magnitude greater than is typically used in practice

μ	a (rad mm^{-2})	Bandwidth (kHz)	T_{RF} (ms)	Cut-off (%)	TE (ms)	α (°)	Δz (mm)
1.0	0.25	1.5	4.0	0.02	18	90	3
5.0	1.22	1.5	20.0	0.02	34	90	3
6.8	1.67	3.0	6.6	2.02	21	90	3
10.0	2.45	1.5	20.0	1.80	34	90	3
15.3	3.75	3.0	14.9	2.02	29	90	3

Table 6.1: HS pulse parameters used by Shmueli [30] to reduce signal dropout caused by through-plane susceptibility gradients in GE-EPI images

6.3 Designing Complex Hyperbolic Secant Pulse for Slice Selection with Dropout Recovery

6.3.1 Previous Work

In the only previous work in which HS pulses were used to reduce signal dropout in GE-EPI images [30, 300] the choice of the pulse parameters was based on the theory of signal recovery for ideal quadratic phase RF pulses described in Section 6.2.1 along with an element of trial and error. The parameters of the five HS pulses previously tested are shown in Table 6.1. Shmueli [30] assumed that the pulse bandwidth was given by $\mu\beta/\pi$ which as shown in Section 6.2.2 is an underestimate of the true bandwidth and results in thicker than expected slices being excited. The degree of quadratic phase, a, was found by fitting a quadratic function to the central 75% of the phase profile of the pulse (which was determined by Bloch simulation) such that the theoretical dependence of the signal on a and $G_{z,s}$ given by Equation 6.4 could be used to guide the pulse design. Apart from the pulse with $a = 1.67$ rad mm^{-2},

clearly chosen to match the pulse used by Cho and Ro [126], it is not obvious how the values of μ were chosen and in addition no justification was given for the choice of the bandwidth, pulse duration, cut-off and echo time. After testing these HS pulses on an anthropomorphic head phantom Shmueli [30] concluded that "*It seems that a HS90° pulse with a C between 1.22 and 2.45 rad mm^{-2} would result in the best compromise between overall signal reduction in areas of homogenous field and signal recovery in inhomogeneous regions*[3]*. Certainly a quadratic phase coefficient of 0.25 rad mm^{-2} was insufficient for signal recovery in this phantom with a voxel size of 3 mm.*". This suggests that more work is required to determine the optimal pulse parameters in a systematic manner for a given echo time and slice thickness.

6.3.2 Optimising the Parameters of an HS Pulse for Uniform Signal Recovery

When FMRI data are acquired using GE-EPI with a conventional RF pulse, the ability to detect brain activations of equal magnitude varies across the brain. This is because susceptibility gradients cause signal loss and reductions in the BOLD sensitivity [28, 71]. To reduce this variability the aim of the current work was to set the parameters of the HS pulse such that the signal response across the range of through-plane susceptibility gradients, which have been measured at 3 T in the human head, ($-250 < G_{z,s} < 250$ μTm^{-1}) [28, 29], was as uniform as possible.

A HS pulse was designed for an FMRI data acquisition at 3 T which could be used for both the task-based and resting-state experiments previously described in Chapter 3. It therefore needed to be compatible with a GE-EPI sequence with a repetition time of 2 s during which thirty-six 3 mm slices (with 0.3 mm gaps) could be acquired at an echo time of 30 ms, a field-of-view of 21.2 cm, a 64×64 matrix and a flip angle, $\alpha = 73°$ (the Ernst angle[290] for grey-matter at 3 T for TR=2 s assuming $T_1 = 1.6$ s [287]). In addition the pulse parameters were required to be within the hardware limits, on the gradient and RF amplitudes, set by the 3 T GE Discovery MR750 system (General Electric, Waukesha, WI, USA). The pulse duration was therefore set to 5 ms to match the excitation pulse (designed using the SLR algorithm), provided as standard by the manufacturer and shown in Figure 6.11. This ensured that the spatial coverage could be maintained, since the same number of slices could be collected during each repetition time.

[3]Shmueli [30] use C to represent the degree of quadratic phase, whereas I use a to avoid confusion with the cut-off.

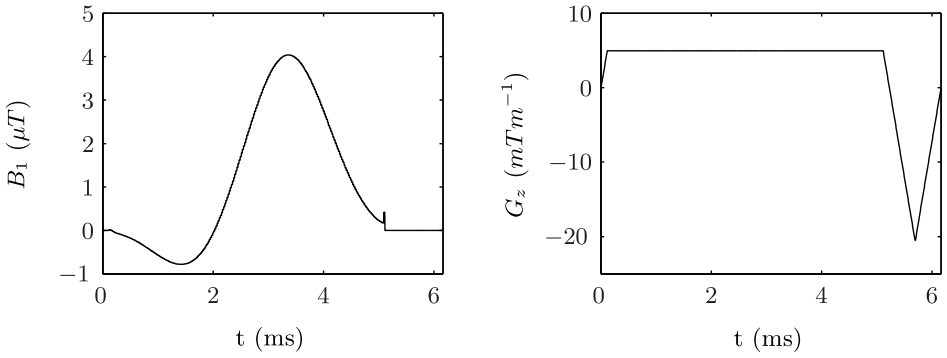

(a) SLR pulse (b) Slice-selection gradient

Figure 6.11: Plots showing the SLR pulse and gradient provided by the manufacturer for slice selection in the GE-EPI sequence on a 3 T GE Discovery MR750 system. In this example $\Delta z = 3$ mm and $\alpha = 90°$.

Determining the Optimal Values of μ and β

Given the choice of pulse duration and flip angle the optimal values of μ and β were determined by Bloch simulations such that the signal as a function of through-plane susceptibility gradient was as uniform as possible over the range $-250 < G_{z,s} < 250$ μTm^{-1}. From initial simulations, and previous studies [30, 126, 300], the search space of μ was set to $2 < \mu < 8$.

To minimise the stop-band ripple the value of β was set close to its maximum possible value over this range of μ. Depending on the scanner hardware limits β can be limited by either the maximum gradient or the maximum RF amplitudes. By rearranging Equation 6.12, and given that $\Delta f_{max} = \frac{\gamma G_{z,max} \Delta z}{2\pi}$, it can be seen that the limit imposed by the maximum gradient amplitude ($G_{z,max} = 50$ mTm^{-1}) is:

$$\beta_{max} = \frac{\pi \gamma G_{z,max} \Delta z}{2 \cosh^{-1}\left[\frac{\cosh(\pi\mu)\left(\cos(\alpha) - \frac{1}{2}\sqrt{3+\cos^2(\alpha)}\right) + \cos(\alpha) - 1}{\frac{1}{2}\sqrt{3+\cos^2(\alpha)} - 1}\right]} \tag{6.21}$$

Additionally β could by constrained by the maximum RF amplitude ($A_{0,max} = 25$ μT), as shown by rearranging of Equation 6.10:

$$\beta_{max} = \frac{\gamma A_{0,max}}{\sqrt{\left[\frac{\cos^{-1}\left(\cosh^2\left(\frac{\pi\mu}{2}\right)\cos\alpha + \sinh^2\left(\frac{\pi\mu}{2}\right)\right)}{\pi}\right]^2 + \mu^2}} \tag{6.22}$$

Both the gradient and RF contraints on β are plotted as a function of μ, for a slice thickness of 3 mm and a flip angle of 73°, in Figure 6.12. This shows that for all values of μ tested, β is limited by the maximum gradient amplitude. β was therefore set to 2.12 kHz (corresponding to $c = 1\%$), close to its maximum possible value for

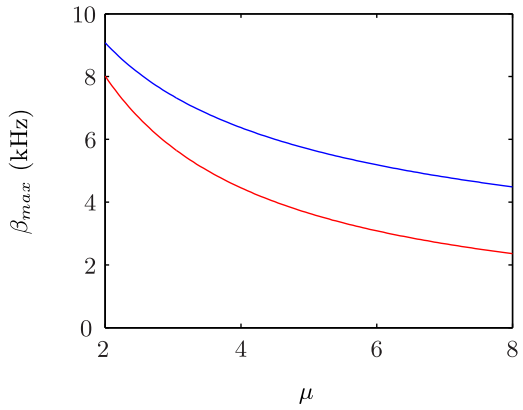

Figure 6.12: Limitations on β imposed by the maximum gradient (red line) and RF amplitudes (blue line) on a GE Discovery MR750 system for a slice thickness of 3 mm and a flip angle of 73°. For all values of μ tested, β is limited by the maximum gradient amplitude.

$2 < \mu < 8$.

The steady state voxel signal for grey matter (at $TE = 30$ ms and $TR = 2$ s assuming $T_1 = 1.6$ s [287] and $T_2^* = 66$ ms [289]) was determined as a function of μ and a through-plane linear susceptibility gradient, $G_{z,s}$. For each combination of μ and $G_{z,s}$ the transverse magnetisation in the x- and y-directions, $M_x(z)$ and $M_y(z)$, were found by Bloch simulation for $-\Delta z < z < \Delta z$ (i.e. including the regions either side of the prescribed slice to incorporate the effect of the stopband ripple and non-rectangular slice profile). The total signal magnitude was calculated numerically using:

$$S = \sqrt{\left[\int_{-\Delta z}^{\Delta z} M_x(z)\mathrm{d}z\right]^2 + \left[\int_{-\Delta z}^{\Delta z} M_y(z)\mathrm{d}z\right]^2} \tag{6.23}$$

This was normalised relative to the signal[4] from a perfectly rectangular slice, of thickness Δz. A comparison of the steady-state slice profile at the echo time from a perfectly rectangular slice and the slice profile from a HS pulse is shown in Figure 6.13.

The normalised signal as a function of μ and $G_{z,s}$ is shown in Figure 6.14(a). For comparison this is displayed next to the theoretical predictions of Cho and Ro

[4]In the steady state, using Equation 18.14 from Haacke et al. [51], the transverse magnetisation is:

$$\begin{aligned}\frac{|M_{xy}|}{M_0} &= \frac{\left(1 - e^{-TR/T_1}\right)\sin\alpha}{1 - \cos(\alpha)e^{-TE/T_2^*}} e^{-TE/T_2^*} \\ &= 0.472\end{aligned} \tag{6.24}$$

for the parameters given above. Therefore the signal from a voxel in a perfectly rectangular slice is:

$$S_{ideal} = 0.472\, M_0 \Delta z \tag{6.25}$$

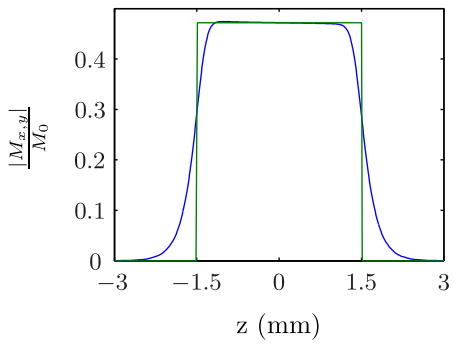

Figure 6.13: A comparison of the steady-state slice profile from an HS pulse (blue line) with the steady-state slice profile from an ideal rectangular slice (green line). $\mu = 4.25$, $\beta = 3040$ Hz, $T_{RF} = 5$ ms, and $\alpha = 73°$ for grey-matter ($T_1 = 1.6$ s and $T_2^* = 66$ ms) when $TR = 2$ s and $TE = 30$ ms

[126] given by Equation 6.4; Figure 6.14(b). The ranges covered by the y-axes of both plots are scaled to match each other using the linear relationship between μ and a shown in Figure 6.15. As in Shmueli [30], this relationship between μ and a was determined by fitting a quadratic function to the phase variation (determined by Bloch simulation) over the central 75% of slice. As mentioned briefly in Section 6.2.1, the discrepancy between the normalised signal predicted by Equation 6.4 and the Bloch simulations of HS pulses with varying μ is a result of the slice profiles of the HS pulses being non-rectangular, and thus violating the assumptions required for Equation 6.4 to be valid. From Figure 6.14(a) it can be seen that a trade-off between the signal at $G_{z,s} = 0$ and the signal at non-zero susceptibility gradients occurs with increasing μ (i.e. an increasing the degree of quadratic phase). Although quantitatively different, this trade-off is qualitatively similar to that predicted by Equation 6.4 and described in Section 6.2.1.

The optimal value of μ was determined by finding the most uniform signal profile as function of $G_{z,s}$. The uniformity was quantified as the ratio of the standard deviation of the signal, std(S), in the range $-250 < G_{z,s} < 250$ μTm^{-1} to the mean signal over the same range, $\overline{S}$. This ratio is plotted as a function of μ in Figure 6.16. The optimal value of μ is found to be 4.25.

Given this choice of μ, it is possible to further refine the value of β in an effort to reduce ripple in the stop-band of the slice profile. For $\mu = 4.25$, $\Delta z = 3$ mm and $\alpha = 73°$ the maximum value of β, given by Equation 6.21, is 4.2 kHz. During initial testing, this resulted in uncomfortable levels of acoustic noise and vibration as a result of the switching of the slice-selection gradient. Therefore β was only increased to 3040 Hz (equivalent to $c = 0.1\%$); this still reduced the stop-band ripple, whilst keeping the levels of vibration and acoustic noise within acceptable limits.

The amplitude and phase modulation of the optimised HS pulse, as well as the

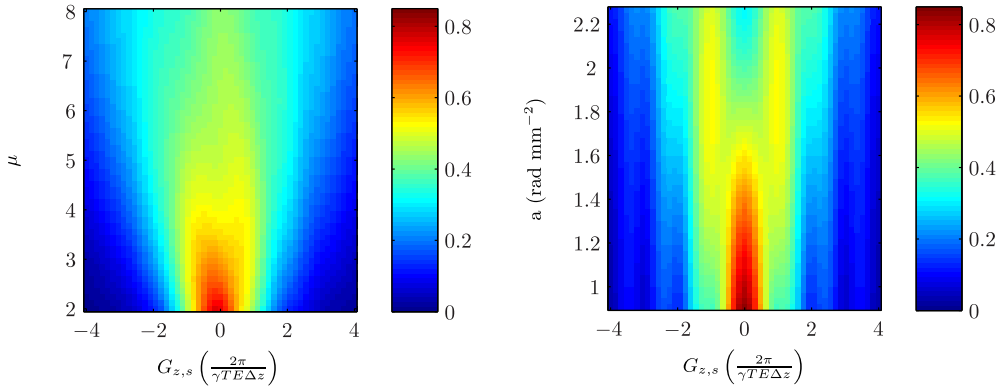

(a) Normalised signal from complex hyperbolic secant pulses

(b) Theoretical signal from ideal quadratic phase pulses

Figure 6.14: (a) The normalised steady-state signal as a function of μ and the through-plane susceptibility gradient, $G_{z,s}$, for HS pulses with $T_{RF} = 5$ ms and $\beta = 2.12$ kHz when $\Delta z = 3$ mm and $TE = 30$ ms. (b) The signal predicted by the theory of Cho and Ro [126] given in Equation 6.4. The range of gradients shown in both plots $-4\left(\frac{2\pi}{\gamma TE\Delta z}\right) < G_{z,s} < 4\left(\frac{2\pi}{\gamma TE\Delta z}\right)$ corresponds to $-1044 < G_{z,s} < 1044$ μTm^{-1}

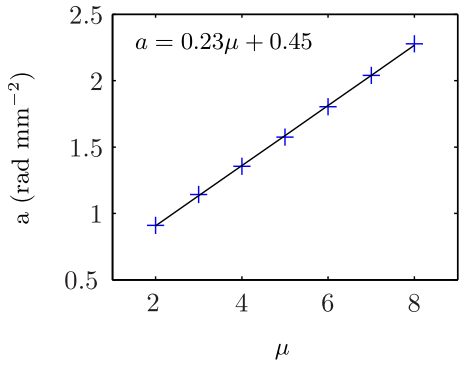

Figure 6.15: A plot of the linear relationship between the μ and the degree of quadratic phase a for HS pulses with $\beta = 2.12$ kHz, $T_{RF} = 5$ ms and $\alpha = 73°$

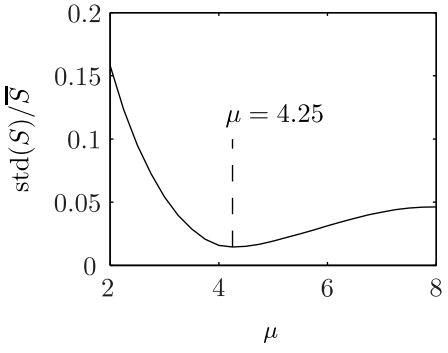

Figure 6.16: A plot of the ratio std$(S)/\overline{S}$ as a function of μ. The minimum of this ratio corresponds to the value of μ with the most uniform signal response for $-250 < G_{z,s} < 250$ μTm^{-1}

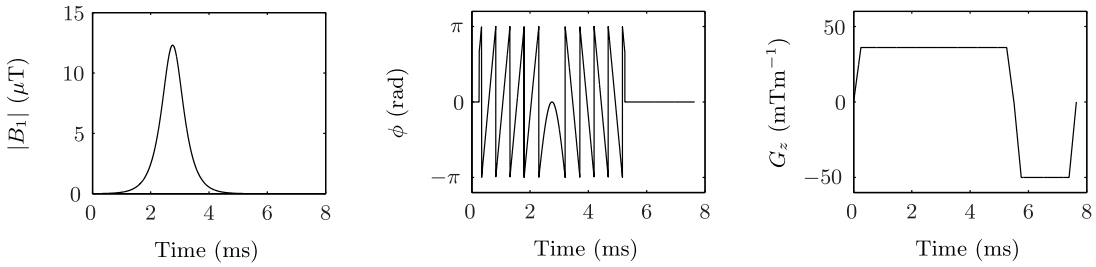

(a) Amplitude modulation (b) Phase modulation (c) Slice-section gradient

Figure 6.17: Plots showing the amplitude and phase modulation of the optimised HS pulse in addition to the accompanying slice-selection gradient. The pulse has the following parameters; $T_{RF} = 5$ ms, $\alpha = 73°$, $\mu = 4.25$, $\beta = 3040$Hz, A_0=12.3 μT and $\Delta f = 4598$ Hz.

accompanying slice-selection gradient, are shown in Figure 6.17. To summarise, the pulse was optimised for a 3 T GE Discovery MR750 system with a maximum gradient amplitude of 50 mTm^{-1} and a maximum RF amplitude of 25 μT. The RF pulse duration was set to 5 ms to match the product SLR pulse[5] it was replacing such that the same number of slices could be acquired per TR. The flip angle is 73° to maximise the steady-state signal from grey matter. μ is 4.25 such that the signal as a function of susceptibility gradient is as uniform as possible over $-250 < G_{z,s} < 250$ μTm^{-1} when the *TE* is 30 ms and the slice thickness is 3 mm. β is 3040 Hz to minimise the stop-band ripple in the slice profile. Using Equation 6.10 the maximum pulse amplitude, A_0, is 12.3 μT and the bandwidth, Δf, calculated using Equation 6.12 is 4598 Hz. At this bandwidth the slice-selection gradient amplitude needed to excite 3 mm thick slices is 31.2 mTm^{-1}.

The steady-state slice profile and phase variation for grey matter (at $TE = 30$ ms and $TR = 2$ s assuming $T_1 = 1.6$ s [287] and $T_2^* = 66$ ms [289]) using the optimised HS pulse are shown in Figure 6.18. The normalised steady-state voxel signal as a function of the through-plane susceptibility gradient is shown in Figure 6.19. As before, the signal for each value of $G_{z,s}$ was calculated numerically using Equation 6.23 from the transverse magnetisation in the x- and y-directions, $M_x(z)$ and $M_y(z)$, found by Bloch simulation in the range $-\Delta z < z < \Delta z$. This was normalised relative to the steady-state signal from a perfectly rectangular slice, of thickness Δz. From Figure 6.19 it can be seen that for $-250 < G_{z,s} < 250$ μTm^{-1} the normalised voxel signal is highly uniform, however it is reduced to between 48.2 and 51.8% of the signal from a conventional RF pulse without quadratic phase

[5]When the slice-selection refocusing lobe is taken into account the total duration of the slice-selection process for the optimised HS is 7.65 ms compared to 6.16 ms for the SLR pulse. This moderate difference is a result of the longer isodelay of the HS pulse. This did not affect other pulse sequence parameters. In particular, the thirty six slices could still be collected within the 2 s TR.

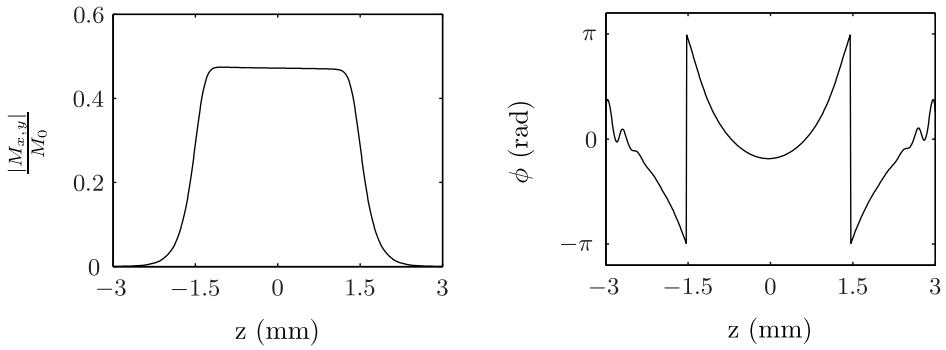

(a) Slice profile (b) Phase variation

Figure 6.18: Plots showing the steady-state slice profile and phase variation for the optimised HS pulse in grey matter at $TE = 30$ ms and $TR = 2$ s (assuming $T_1 = 1.6$ s [287] and $T_2^* = 66$ ms [289])

variation. Signal is recovered (i.e. the signal is greater than when a conventional RF pulse is used) for through-plane susceptibility gradients more extreme than ± 154 μTm^{-1}, as indicated by the dashed lines in Figure 6.19.

Implementation on a 3 T GE Discovery MR750 System

Separate files containing the amplitude and phase modulation of optimised pulse were generated in MATLAB. Following the addition of a header, using proprietary software provided by General Electric, these could be played out by the scanner's soft- and hardware. The echo-planar imaging pulse sequence provided with the 3 T GE Discovery MR750 system (at software release 22.0) was modified in EPIC (Extended Programming Environment in C) such that the optimised HS pulse could be used for signal excitation. An option was added to the user interface, enabling the user to select the HS pulse in place of the standard SLR pulse. The pulse parameters required by the scanner's specific absorption rate (SAR) and gradient amplitude calculation routines, calculated in MATLAB, were included in the relevant sections of the pulse sequence code.

Initial Pulse Testing

To validate the simulations used to optimise the parameters of the HS pulse and to demonstrate the ability of HS pulses to reduce the signal loss resulting from through-plane susceptibility gradients a series of images were obtained of uniform spherical phantom[6]. All data were acquired using the modified GE-EPI sequence on a 3 T GE

[6]Containing silicone oil (dimethylpolysiloxanes) doped with a gadolinium compound (tris(2,2,6,6-tetramethyl-3,5-heptanedionate) gadolinium (III)). The longitudinal relaxation time $T_1 = 170$ ms and the transverse relaxation time $T_2 = 25$ ms. (Part Number: 2359877, General Electric, Waukesha, WI, USA)

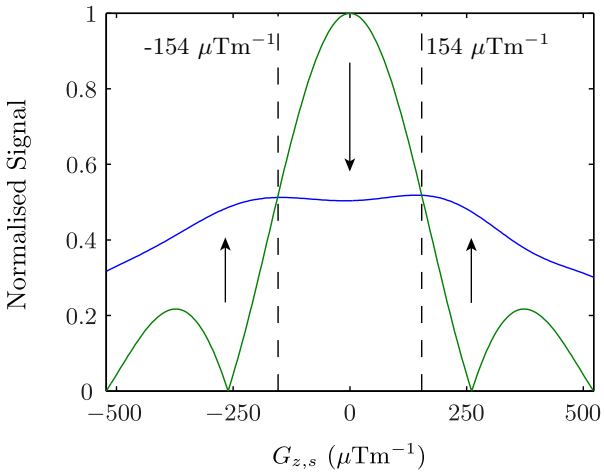

Figure 6.19: A plot of the normalised steady-state voxel signal as a function of the through-plane susceptibility gradient for the optimised HS pulse (blue line) compared to a conventional RF pulse without quadratic phase variation (green line) in grey matter at $TE = 30$ ms and $TR = 2$ s (assuming $T_1 = 1.6$ s [287] and $T_2^* = 66$ ms [289]).

Discovery MR750 system. A quadrature head coil was used for signal transmission and reception. Initially the scanner was shimmed using the in-built automatic procedure. To model the effects of different through-plane linear susceptibility gradients, the shim gradient in the slice-selection direction was then deliberately mis-set. At each different setting of the shim gradient a single 3 mm axial slice with a field-of-view of 32 cm and a 64×64 acquisition matrix was acquired with a $TR = 5$ s and $TE = 30$ ms using a HS pulse with $T_{RF} = 5$ ms, $\alpha = 90°$, $\mu = 4.25$, $\beta = 3040$Hz. The 5 s repetition time of and 90° flip angle we chosen to avoid the differences in steady-state signal resulting from the difference between the T_1 of grey matter and the phantom. The quadrature coil and large field-of-view were selected to enable straightforward measurements of the signal and background noise.

The signal from a region-of-interest in the centre of the phantom as a function of the 'susceptibility' gradient (induced by mis-setting the shim) was calculated using tools from FSL (FMRIB's Software Library); Figure 6.20. It is clear that the pulse produces a near uniform signal for susceptibility gradients in the range $-250 < G_{z,s} < 250$ μTm^{-1}. Using the same method described earlier, the voxel signal as a function of the through-plane susceptibility gradient was determined by Bloch simulation, this was scaled by a constant such that it could be easily compared to the measured data. It is clear that the variations in signal from the phantom experiments and simulations closely match, validating the optimisation procedure performed above.

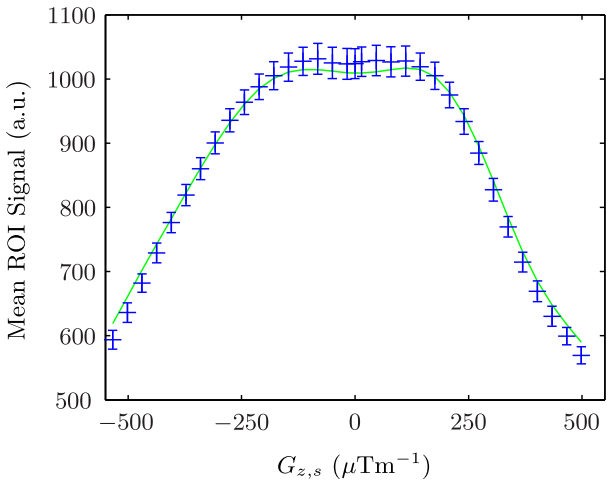

Figure 6.20: Variation in the mean signal from a region-of-interest in the centre of the phantom as a function of 'susceptibility' gradient (induced by mis-setting the scanner's shim gradient in the slice-selection direction) for a HS pulse. The error bars represent the standard deviation of the signal in the ROI. The voxel signal calculated by Bloch simulation (green line) is shown for comparison

6.4 Evaluating the Impact of the Optimised HS Pulse In-vivo

To assess the impact of using the optimal HS pulse in FMRI experiments the same battery of tests described in Section 5.5 were performed using the 3 T GE Discovery MR750 system on the same six healthy male subjects.

6.4.1 Data Acquisition

Using the methods described in Section 5.5.1 a series of scans were performed on each of the six subjects. Following localiser and ASSET calibration scans, a single volume was acquired using a spin-echo EPI (SE-EPI) sequence. A single volume DIR image, with a SE-EPI readout was then acquired. This was used to produce a subject specific grey matter mask that was used to restrict later analyses of the efficacy of the optimised HS pulse to grey matter, the origin of the effects of interest in FMRI experiments. This was used in preference to segmented high-resolution structural images because it is distortion matched with the FMRI data. As in Section 5.5.1 three pairs of functional MRI scans were then acquired. The first pair used the resting state paradigm, the second pair the motor-task and the third pair the breath-hold paradigm. One scan of each pair was acquired using a GE-EPI sequence with the conventional SLR excitation pulse and the other with the optimised HS pulse. As before, the ordering of the acquisition method (conventional SLR or optimised HS pulse) within each pair of scans was counter balanced across

the six subjects.

6.4.2 Data Analysis

As described in Section 5.5.2 all imaging data were converted into the NIfTI-1 data format, and then processed using tools from FSL. In contrast to the z-shim data acquired in the previous chapter there was no need combine volumes by SSQ. In addition to the preprocessing steps performed on the FMRI data described in Section 5.5.2 slice-timing correction was carried out between motion correction and brain extraction. This accounts for the different acquisition times of each slice within each volume of data by phase-shifting the Fourier transformed timeseries.

Qualitative Comparison of Signal In Regions with Through-Slice Susceptibility Gradients

Representative slices through the orbitofrontal and inferior temporal regions from data acquired with SE-EPI, GE-EPI with the SLR excitation pulse and GE-EPI with the HS pulse were visually compared to determine if signal was recovered from regions affected by susceptibility gradient induced signal dropout by the HS pulse.

Temporal Signal-to-Noise Ratio

Using the methods described in Section 5.5.2 maps of the temporal signal-to-noise ratio (TSNR) were calculated from the resting-state FMRI data sets. Maps of the percentage change in TSNR between the data acquired with the optimised HS and SLR RF pulses were also calculated for each subject.

Detectability of Motor Activations

The same set of analyses as previously described in Section 5.5.2 were carried out on the FMRI data acquired whilst the subject performed the motor task. The pressure measured in the squeeze ball was plotted as a function of time for both acquisition types to check that each subject performed the task. The regions of the brain showing significant changes in BOLD signal in response to the motor stimulus were determined using data acquired with the SLR and HS RF pulses. T-statistic maps for each subject and acquisition method were calculated and converted to maps of the thresholded z-statistic. In addition to the analyses described in the previous chapter, a map of the percentage change in the unthresholded t-statistic (masked to show results in only those voxels with significant activation from both FMRI acquisitions) between the data acquired using SLR and HS RF pulses was calculated for each subject. Finally the mean percentage change in the unthresholded t-statistic

and TSNR in regions of significant activation (common to the data acquired using both methods) was calculated for each subject.

Measuring BOLD sensitivity via Breath-hold BOLD Signal Changes

The set of analyses described in Section 5.5.2 were performed on the data acquired whilst the subject performed the breath-hold task. To confirm that each subject adhered to the task, the normalised signal from the respiratory bellows was plotted as a function of time for both acquisition types. In addition the variation in the mean percentage change in BOLD signal, from voxels containing grey matter, was calculated as a function of time for all six subjects separately. The regions of the brain showing significant changes in BOLD signal in response to the breath-hold stimulus were calculated from the data acquired with both the SLR and HS RF pulses. The t-statistic maps for each subject and acquisition method were converted to maps of the thresholded z-statistic. In addition to the analyses described in the previous chapter, maps of the change in unthresholded t-statistic when the HS pulse was used in place of the SLR pulse were calculated. To aid interpretation these maps were masked to show only those voxels whose signal increased when the HS pulse was used. Both the thresholded z-statistic and masked t-statistic difference maps were used to determine if increases in signal were matched by increases in BOLD sensitivity.

Detectability of Resting-State FMRI Networks

Finally the set of analyses outlined in Section 5.5.2 were performed on the resting-state FMRI data. Probabilistic Independent Component Analysis [220] as implemented in MELODIC was performed to determine if the ten resting-state networks described in Smith et al. [169] were detectable from data acquired with the SLR and HS RF pulses. Seed based analyses were also carried out to determine whether resting-state fluctuations in the regions of recovered signal in the orbitofrontal and inferior temporal lobes were correlated with fluctuations in the default-mode and sensorimotor networks.

6.4.3 Results

Qualitative Comparison of Signal In Regions of Through-Slice Susceptibility Gradient

Representative slices through the orbitofrontal and inferior temporal regions from data acquired with SE-EPI, GE-EPI with the SLR excitation pulse and GE-EPI with the HS pulse are shown for each subject in Figures 6.21 and 6.22. Comparing

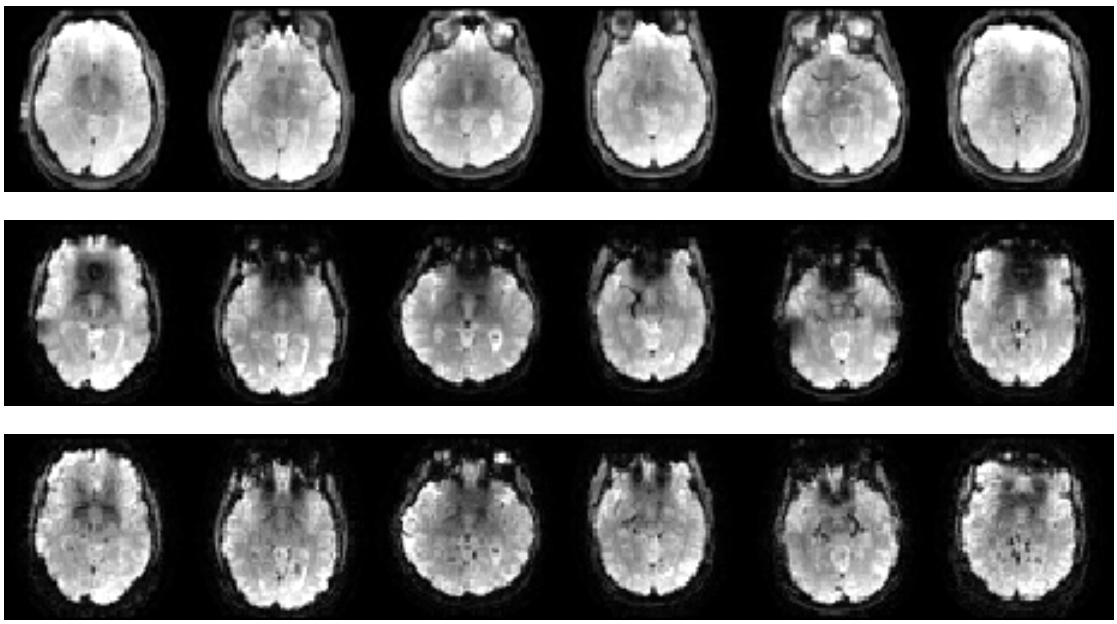

Figure 6.21: Representative slices through the orbitofrontal cortex of the six subjects from images acquired with SE-EPI (top-row), GE-EPI with the conventional SLR excitation pulse (middle-row) and GE-EPI with the HS pulse (bottom-row). The intensity range was chosen on a per subject and per acquisition basis such that the areas of signal dropout and recovery could be readily appreciated.

the images acquired with SE-EPI and GE-EPI using the conventional SLR pulse, signal dropout is observed in both the orbitofrontal and temporal regions for all six subjects. Using the HS pulse signal is recovered in some, but not all, voxels in these regions. The reduction in signal in regions free from susceptibility gradients, caused by the HS pulse, causes a visible reduction in the signal-to-noise ratio.

Temporal Signal-to-Noise Ratio

Maps of the temporal signal-to-noise ratio for each subject for data acquired with the SLR pulse and the HS pulse are shown for slices through the orbitofrontal and inferior temporal regions in Figures 6.23 and 6.24. The percentage change in the temporal signal-to-noise ratio between data acquired with SLR and HS pulses is shown in Figure 6.25.

The TSNR increases to a level comparable with voxels unaffected by through plane susceptibility gradients when the HS pulse is used. However, from Figure 6.25, the HS pulse results in decreases in TSNR of up to 60% in large areas of the brain[7]. Focussing specifically on grey matter, on average across all subjects the TSNR increased in 10.4% of voxels containing grey matter although it was reduced

[7]Inspection of the TSNR maps in Figure 6.24 shows that the very large percentage increases in TSNR observed in regions affected by signal dropout in Figure 6.25 are a result of very small TSNR in these regions when data is acquired using the SLR pulse (rather than a very large TSNR in these regions when the HS pulse is used).

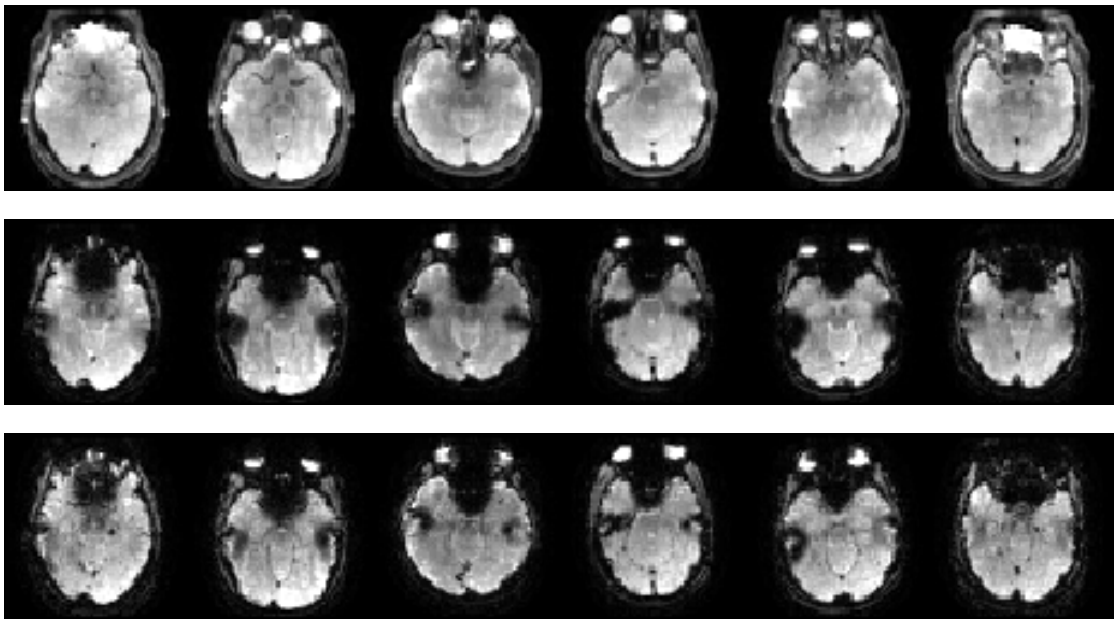

Figure 6.22: Representative slices through the inferior temporal lobes of the six subjects from images acquired with SE-EPI (top-row), GE-EPI with the conventional SLR excitation pulse (middle-row) and GE-EPI with the HS pulse (bottom-row). The intensity range was chosen on a per subject and per acquisition basis such that the areas of signal dropout and recovery could be readily appreciated.

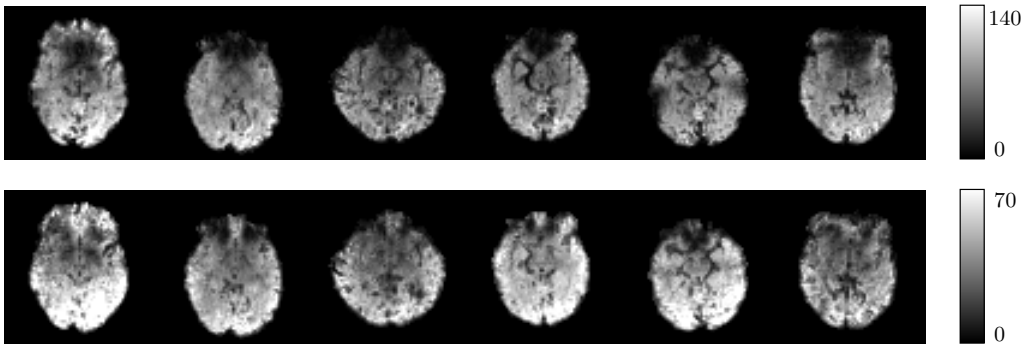

Figure 6.23: TSNR maps for representative slices through the orbitofrontal cortex of the six subjects calculated from data acquired with GE-EPI using the conventional SLR pulse (top-row) and with the HS pulse (bottom-row).

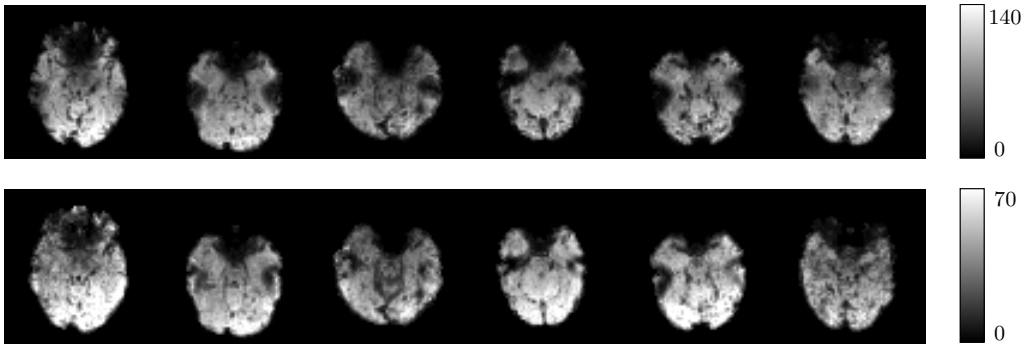

Figure 6.24: TSNR maps for representative slices through the inferior temporal lobes of the six subjects calculated from data acquired with GE-EPI using the conventional SLR pulse (top-row) and with the HS pulse (bottom-row).

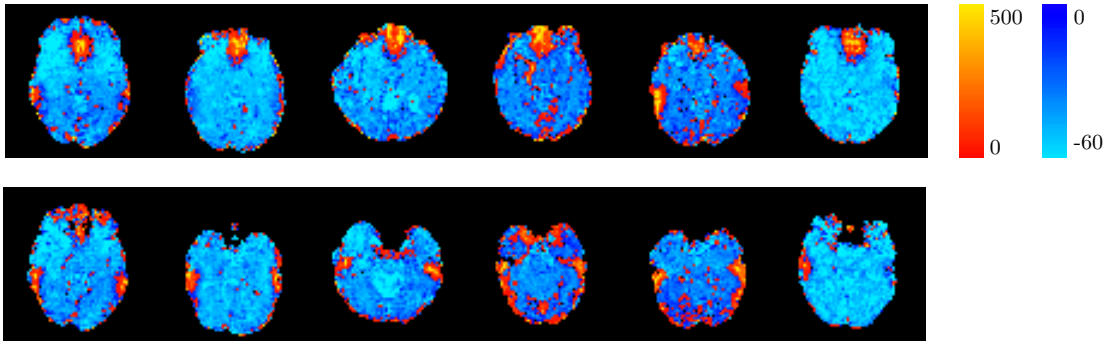

Figure 6.25: Maps showing the percentage change in the TSNR between data acquired using the SLR and optimised HS RF pulses. The top row shows representative slices through the orbitofrontal cortex, and the bottom row, slices through the inferior temporal lobes for the six subjects.

Subject	Grey matter voxels with increased TSNR (%)	Grey matter voxels with decreased TSNR (%)
1	8.5	85.0
2	6.6	86.2
3	5.7	86.1
4	22.1	68.9
5	15.6	72.0
6	3.6	83.9
Mean	10.4	80.4

Table 6.2: The percentage of grey matter voxels showing differences in TSNR when the optimised HS pulse is used in place of the conventional SLR RF pulse.

in 80.4%. Subject specific changes are detailed in Table 6.2.

Comparing the Detectability of BOLD Signal Changes Resulting From the Motor Task

The pressure recorded in the squeeze ball throughout the FMRI scans whilst the subjects performed the motor task are shown in Figure 6.26. These confirm that all subjects performed the task over the full duration of both FMRI data acquisitions. As described in the previous chapter, because the pressure in the squeeze ball was calibrated prior to each FMRI scan, it is not possible to determine if the differences in maximum percentage pressure observed in the data from subject four are due to them either squeezing the ball harder during the calibration or squeezing the ball less hard during the task itself.

Thresholded z-statistic maps for each subject and acquisition method are shown in Figure 6.27. From these maps, it can be seen that the motor paradigm results in statistically significant BOLD signal changes in the left motor cortex and the supplementary motor area in all six subjects in data acquired using both the conventional SLR and HS RF pulses. As shown in Table 6.3 the peak z-statistic was lower for data acquired with the HS pulse in four of the six subjects.

Maps of the percentage change in the unthresholded t-statistic between the data acquired using SLR and HS RF pulses (masked to show results in only those voxels with significant activation from both FMRI acquisitions) are shown in Figure 6.28. The mean percentage change in the unthresholded t-statistic for these voxels is shown for each subject in Table 6.4. On average, across the six subjects, the mean reduction in the TSNR in the same region of was 21.3 %. Using Equation 4.1 from Chapter 4 the same percentage reduction would be expected in the t-statistic. A reduction of 17.2 % in the unthresholded t-statistic was observed which is moderately less than expected. However, at the individual subject level this proportionality is much less clear, for example a reduction of 0.5% in the TSNR is accompanied by a

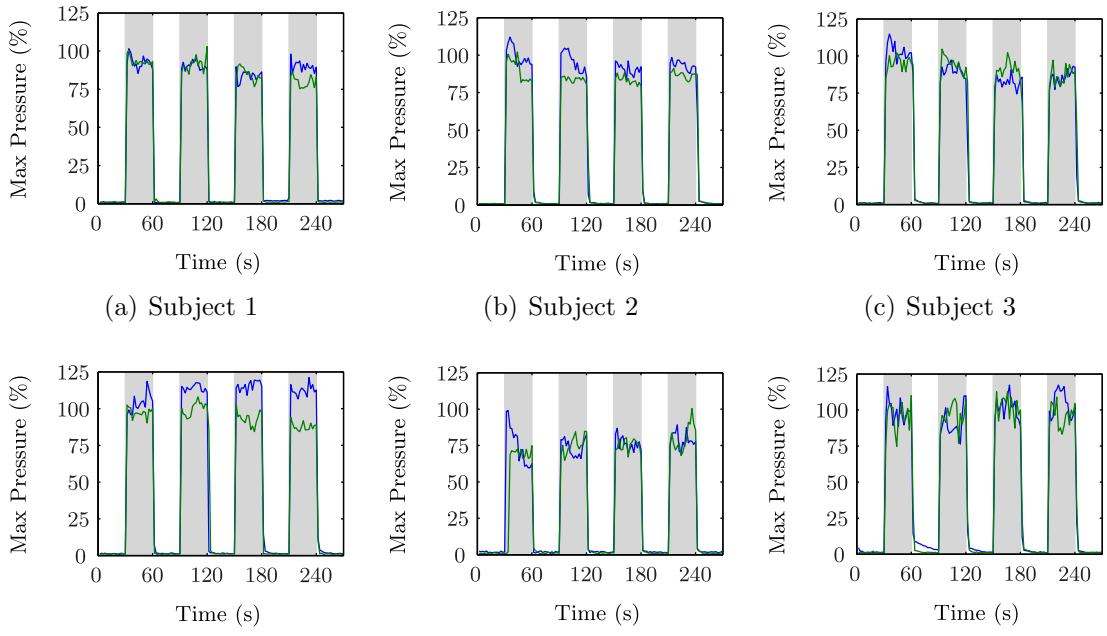

(a) Subject 1 (b) Subject 2 (c) Subject 3

(d) Subject 4 (e) Subject 5 (f) Subject 6

Figure 6.26: The pressure recorded in the squeeze ball (as a percentage of the maximum pressure measured during calibration) for all six subjects for FMRI data acquired with the SLR RF pulse (blue line) and HS pulse (green line). The shaded grey regions illustrate the periods in which the subject was instructed every 2 s to squeeze the ball in their right hand.

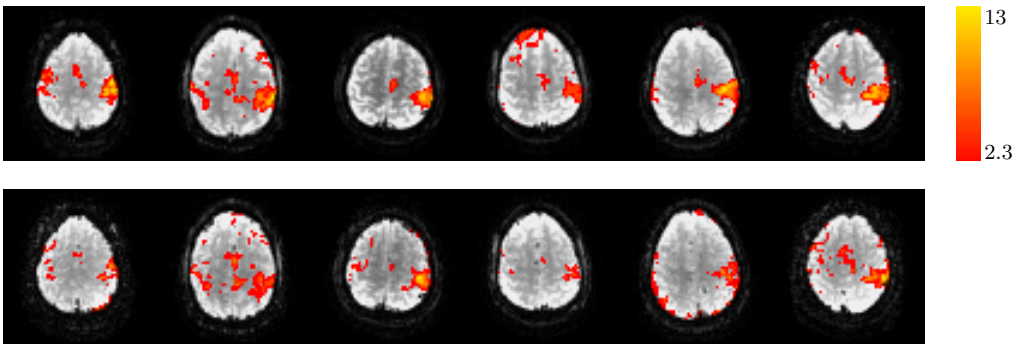

Figure 6.27: Thresholded z-statistic maps, showing voxels with significant changes in BOLD signal in response to the motor task, overlaid on the GE-EPI data from which they were calculated. Maps are shown for each subject acquired with the SLR (top-row) and HS pulse (bottom-row) for representative slices though the motor cortex and supplementary motor area.

	Peak z-statistic	
Subject	GE-EPI	GE-EPI with HS pulse
1	13.2	9.3
2	12.9	11.3
3	10.9	11.2
4	9.8	8.3
5	12.1	8.8
6	11.1	11.2
Mean	11.7	10.0

Table 6.3: Peak z-statistic from the GLM analysis of the motor task FMRI data acquired with conventional GE-EPI and GE-EPI with the HS pulse.

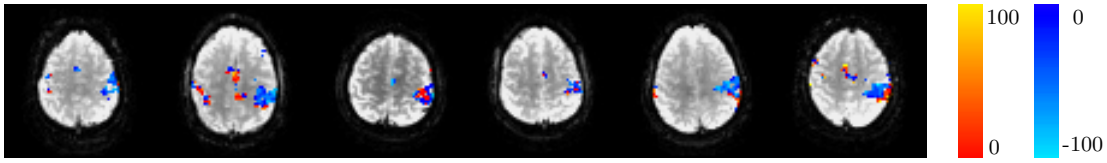

Figure 6.28: Maps of the percentage change in the unthresholded t-statistic between the motor-task FMRI data acquired using SLR and HS RF pulses overlaid on the GE-EPI data acquired with the SLR pulse. The maps were masked to only show changes in the area with significant BOLD activations in data acquired with both the SLR and HS pulses.

reduction of -23.1% for subject five. This may be due to difficulties calculating the change in TSNR in areas near the edge of the brain, it would be artifactually large if motion correction and registration of the two data sets during data preprocessing was imperfect.

Subject	Mean change in t-statistic (%)	Mean Change in TSNR (%)
1	-20.8	-23.3
2	-25.2	-33.6
3	-5.7	-31.2
4	-15.6	2.4
5	-23.1	-0.5
6	-12.7	-41.4
Mean	-17.2	-21.3

Table 6.4: Mean percentage change in t-statistic for the motor task and TSNR in the regions of significant BOLD signal change that were common to both data acquired with the SLR and HS pulses.

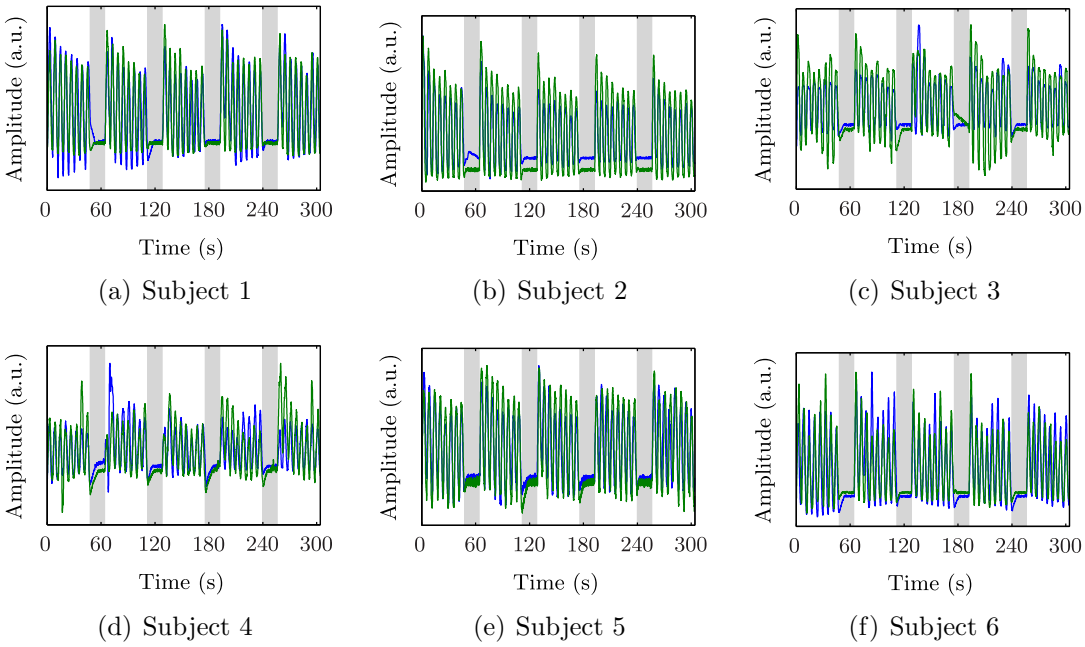

(a) Subject 1 (b) Subject 2 (c) Subject 3

(d) Subject 4 (e) Subject 5 (f) Subject 6

Figure 6.29: Variations in the subjects breathing during acquisition of the breath-hold FMRI data with both the SLR (blue line) and HS (green line) RF pulses. The shaded grey regions illustrate the periods in which the subject was instructed to hold their breath.

Measuring BOLD sensitivity via Breath-hold BOLD Signal Changes

The variations in the subjects' breathing, measured using the respiratory bellows throughout the breath-hold FMRI scans, are shown in Figure 6.29 for all six subjects. These demonstrate that all subjects performed the paced breathing and breath-holding on expiration as instructed throughout both FMRI acquisitions. The mean percentage changes in BOLD signal are shown, for all voxels containing grey matter as a function of time, for all six subjects are shown in Figure 6.30. Subject specific grey matter masks were produced, as described previously, by thresholding and binarising the DIR-EPI data. These plots show that the same percentage changes in BOLD signal are observed with the SLR and HS pulses (i.e. reductions in the signal, S, caused by the HS pulse are matched by proportional reductions in the BOLD signal change ΔS).

Thresholded z-statistic maps showing voxels with significant changes in BOLD signal as a result of the breath-hold task for each subject and acquisition method are shown for representative slices through the orbitofrontal and inferior temporal regions in Figures 6.31 and 6.33. In addition, maps of the change in the unthresholded t-statistic (masked to show only regions where the GE-EPI signal increased when the HS pulse was used in place of the SLR pulse) are shown in Figure 6.32. Visual inspection of both thresholded z-statistic and unthresholded t-statistic maps shows that the effect of the HS pulse is not consistent across subjects. For the first subject

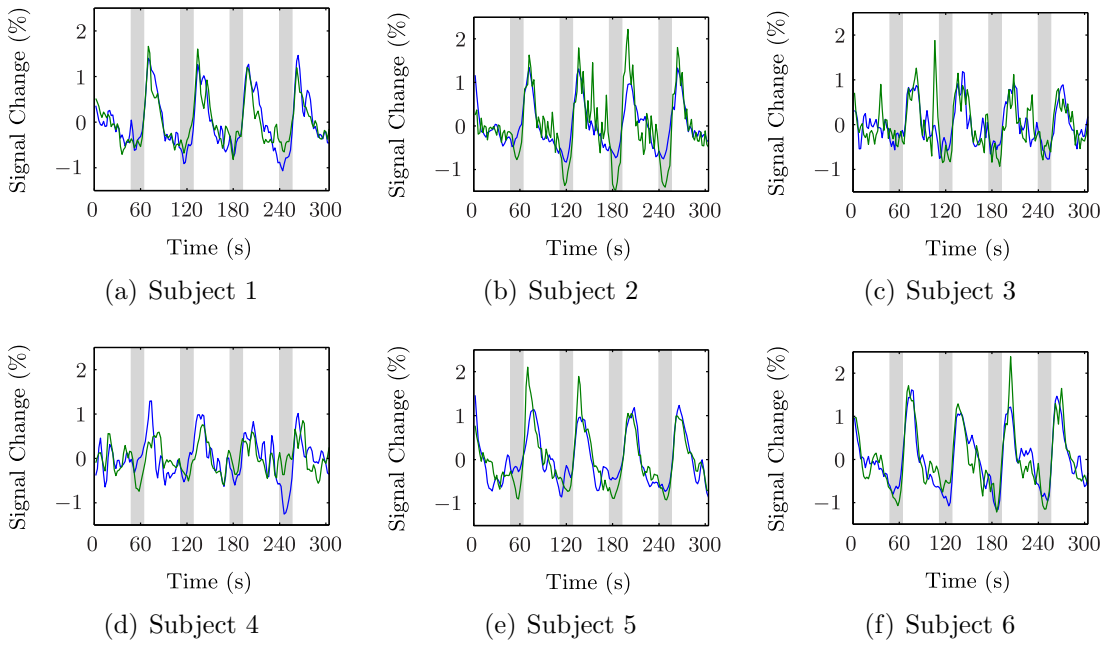

Figure 6.30: The mean percentage change in BOLD signal for grey matter voxels, in response to the breath-hold task, for all six subjects for data acquired with the SLR RF pulse (blue-line) and HS pulse (green-line). The shaded grey regions illustrate the periods in which the subject was instructed to hold their breath.

there is an overall reduction in the number of grey matter voxels with statistically significant changes in the BOLD signal when the HS pulse is used. In addition the thresholded z-statistic is generally reduced. Furthermore, from the GE-EPI images on which the z-statistic maps are overlaid, even though signal is recovered in the orbitofrontal and inferior temporal regions matching increases in statistically significant BOLD signal changes are not seen. However increases in the unthresholded t-statistic are observed, Figure 6.32. For subject two the number of grey matter voxels with statistically significant changes in the BOLD signal is again reduced when the HS pulse is used, although to a much smaller extent. From the underlying GE-EPI images signal is recovered in the orbitofrontal and left inferior temporal lobe, but the BOLD sensitivity, as measured by the thresholded z-statistic, is not increased. However increases in the unthesholded t-statistic are again observed in these regions. The picture is different again for the third and fourth subjects; the overall number of grey matter voxels with statistically significant changes in the BOLD signal is reduced when the HS pulse is used, but for both subjects signal and BOLD sensitivity is increased in the inferior temporal and orbitofrontal regions when the HS pulse is used. For subjects five and six the reduction in the number of grey matter voxels with statistically significant changes in the BOLD signal with the HS pulse is, like subject two, small. Like subjects three and four both the GE-EPI signal and BOLD sensitivity are increased in the inferior temporal and orbitofrontal

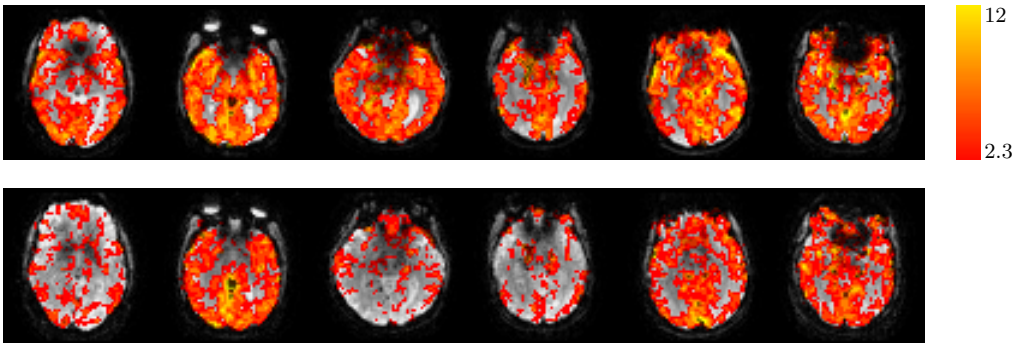

Figure 6.31: Thresholded z-statistic maps, showing voxels with significant changes in BOLD signal in response to the breath-hold task, overlaid on the GE-EPI data from which they were calculated. Maps are shown for each subject acquired with the SLR (top-row) and HS pulse (bottom-row) for representative slices though the orbitofrontal cortex.

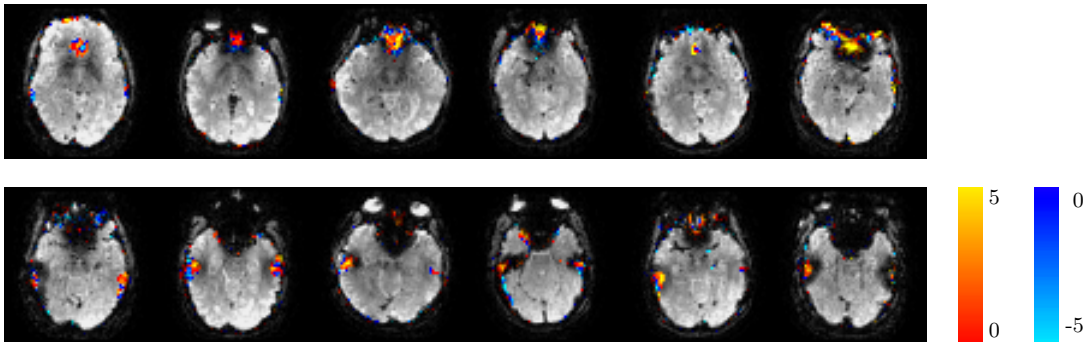

Figure 6.32: Maps of the change in the unthresholded t-statistic masked to show only regions where the GE-EPI signal increased when the HS pulse was used in place of the SLR pulse, for all six subjects for representative slices through the orbitofrontal (top-row) and inferior temporal regions (bottom-row).

regions when the HS pulse was used.

Detectability of Resting-State FMRI Networks with PICA

The ten independent components from the probabilistic independent component analyses which visually matched the resting-state networks described in Smith et al. [169] are shown in Figure 6.34. The ten networks were readily identified from the set of twenty independent components resulting from the analysis of the data acquired with the SLR pulse. The remaining ten components were artifactual, resulting from, for example, subject motion and blood flow in sagittal sinus. However, the ten distinct networks were more difficult to identify in the independent components of the data acquired with the HS pulse. As seen in the right-hand columns of Figures 6.34(a) to 6.34(c) the medial, occipital and lateral visual networks were observed as a single component. The components identified as the default mode and cerebellar networks, Figures 6.34(d) and 6.34(e), are very similar between the SLR and HS

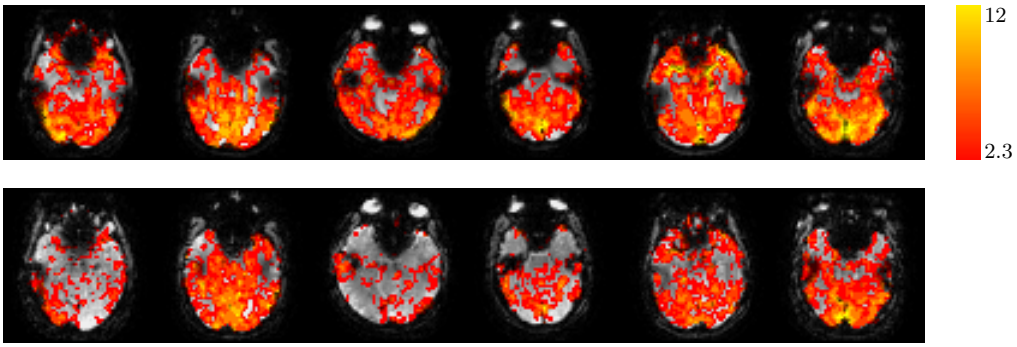

Figure 6.33: Thresholded z-statistic maps, showing voxels with significant changes in BOLD signal in response to the breath-hold task, overlaid on the GE-EPI data from which they were calculated. Maps are shown for each subject acquired with the SLR (top-row) and HS pulse (bottom-row) for representative slices though the inferior temporal regions.

pulse data. The auditory and sensorimotor networks are again combined into a single component (Figures 6.34(f) and 6.34(g)) as are the left and right fronto-parietal networks (Figures 6.34(i) and 6.34(j)). The spatial extent of the executive control network is reduced in the component identified from the HS pulse data; Figure 6.34(h).

Detectability of Resting-State FMRI Networks Using Seed Based Analysis

In all six subjects, for data acquired with the conventional SLR pulse regions with significant correlation of the resting-state BOLD signal from a seed in the posterior cingulate are observed in the left and right lateral parietal cortex as well as in the medial prefrontal cortex, Figure 6.35. These areas are the main regions involved in the default mode network. For data acquired with the HS pulse a similar pattern of correlation is observed, however in general the z-statistics are lower. Interestingly, in all six subjects, in the region of signal recovery in the orbitofrontal cortex the BOLD signal variations are significantly correlated with the posterior cingulate seed, suggesting it may be a part of the default mode network, Figure 6.36. Apart from subjects five and six, significant correlations with the posterior cingulate seed are not observed in the regions of recovered signal in the inferior temporal regions. The regions where the BOLD signal variations are significantly correlated with resting-state signal changes from a seed in the left motor cortex are shown in Figures 6.38 to 6.40. As expected, since they form a functional network, the supplementary motor area and right motor cortex are significantly correlated with the left motor cortex in data acquired with both the SLR and HS pulses. The thresholded z-statistic maps, calculated from data acquired with the HS pulse, also show significant correlations

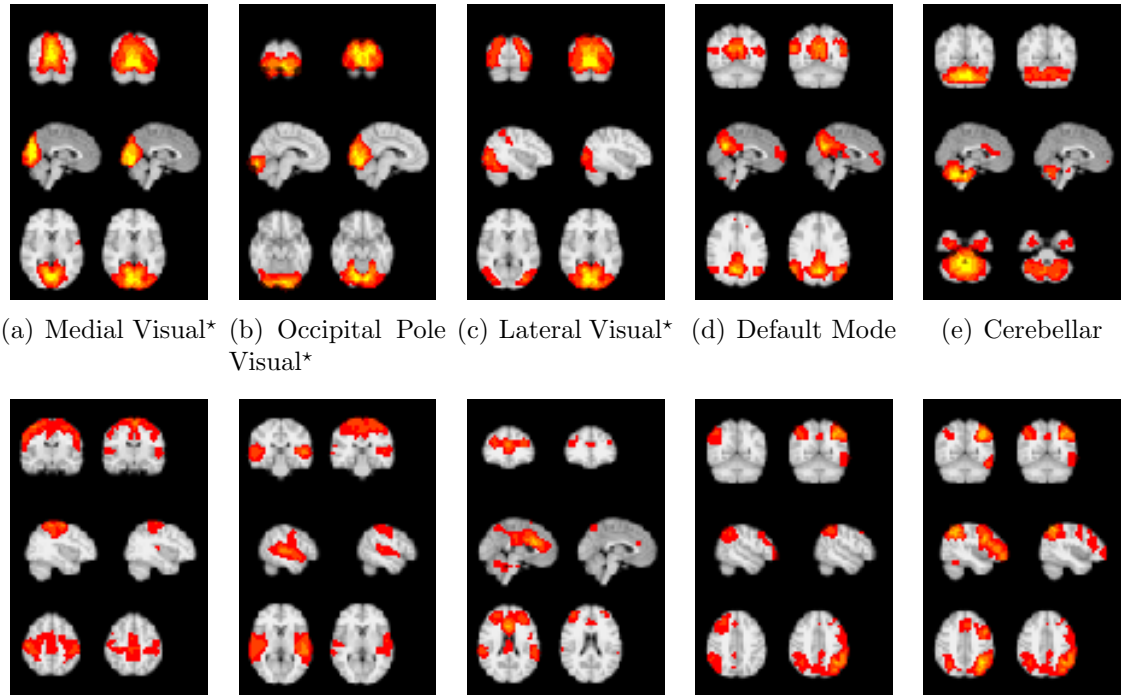

(a) Medial Visual* (b) Occipital Pole Visual* (c) Lateral Visual* (d) Default Mode (e) Cerebellar

(f) Sensoriomotor† (g) Auditory† (h) Executive Control (i) Right Fronto-Parietal‡ (j) Left Fronto-Parietal‡

Figure 6.34: Thresholded z-statistic maps ($3 < z < 15$) for the ten independent components from the probabilistic independent component analyses which visually matched those described in Smith et al. [169]. The three most informative orthogonal slices are shown for each network. The left column in each sub-figure contains independent components from the data acquired using the SLR pulse and the right column the components from the HS pulse data. The components are shown overlaid on the MNI152 standard space template (re-sampled to 4 mm isotropic voxel size).*The medial occipital pole and lateral visual networks were observed as a single component in the HS data. †The auditory and sensoriomotor networks were observed as a single component in the HS data. ‡The left and right fronto-parietal networks were observed as a single component in the HS data.

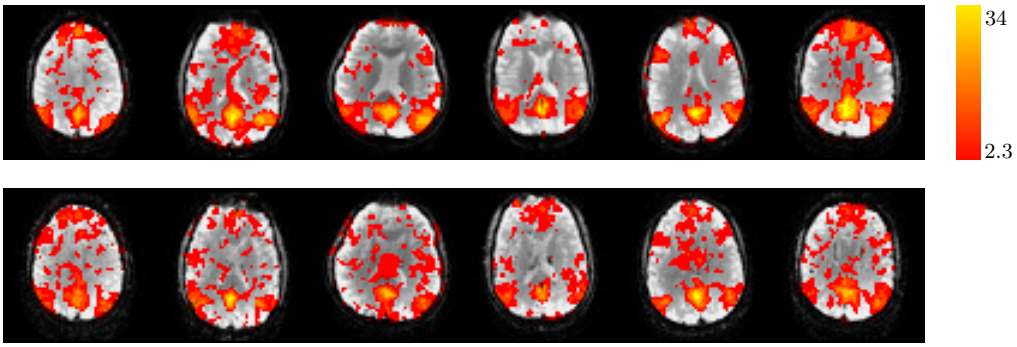

Figure 6.35: Thresholded z-statistic maps, showing voxels in which the resting-state BOLD signal changes were significantly correlated with the signal variation from a seed in the posterior cingulate, for data acquired with the SLR pulse (top-row) and HS pulse (bottom-row). Representative axial slices though posterior cingulate regions are shown for each subject.

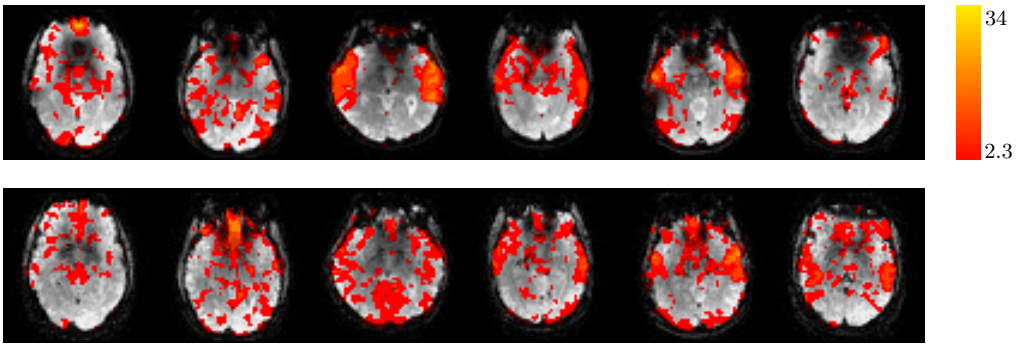

Figure 6.36: Thresholded z-statistic maps, showing voxels in which the resting-state BOLD signal changes were significantly correlated with the signal variation from a seed in the posterior cingulate, for data acquired with the SLR pulse (top-row) and HS pulse (bottom-row). Representative axial slices though the orbitofrontal region are shown for each subject.

in the orbitofrontal and temporal regions for subjects two and four; whether this is artifactual or indicating that these regions are functionally connected to the rest of the motor network is unclear.

6.4.4 Discussion and Conclusions

The results of the experiments performed on the six volunteers demonstrate the potential benefits of the using HS pulses for signal excitation in FMRI experiments. MR signal was recovered in parts of the orbitofrontal and inferior temporal regions, whilst maintaining the temporal resolution and spatial coverage of the images. The areas of unrecovered signal may be caused by susceptibility gradients in the frequency and phase encoding directions and through slice susceptibility gradients greater than those recoverable with the HS pulse. As predicted by Bloch simulations of the pulse, the localised signal recovery comes at the cost of approximately

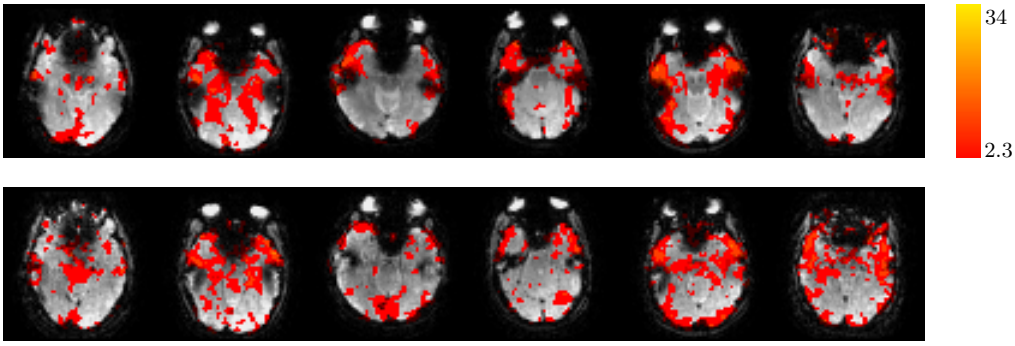

Figure 6.37: Thresholded z-statistic maps, showing voxels in which the resting-state BOLD signal changes were significantly correlated with the signal variation from a seed in the posterior cingulate, for data acquired with the SLR pulse (top-row) and HS pulse (bottom-row). Representative axial slices though inferior temporal regions are shown for each subject.

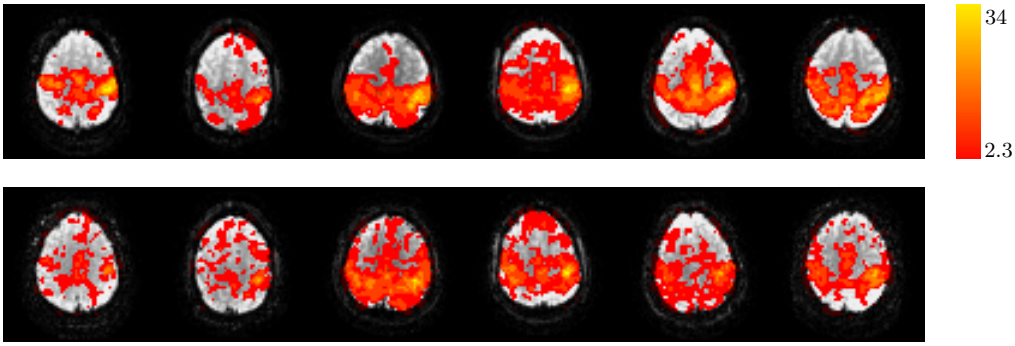

Figure 6.38: Thresholded z-statistic maps, showing voxels in which the resting-state BOLD signal changes were significantly correlated with the signal variation from a seed in the left motor cortex, for data acquired with the SLR pulse (top-row) and HS pulse (bottom-row). Representative axial slices though the left and right motor cortex and supplementary motor area are shown for each subject.

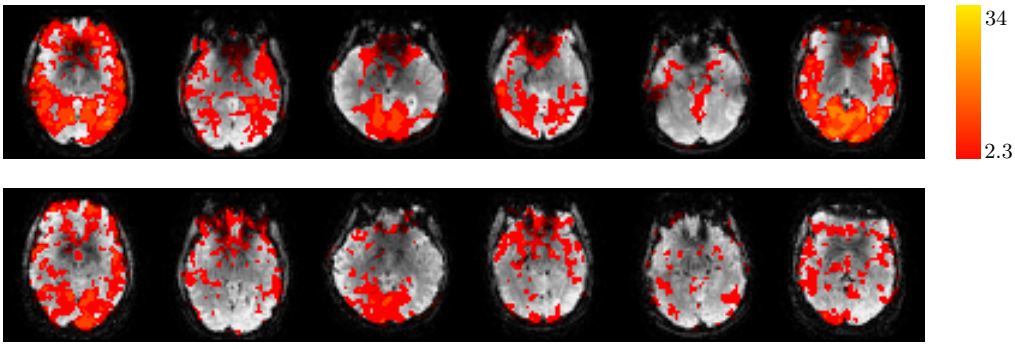

Figure 6.39: Thresholded z-statistic maps, showing voxels in which the resting-state BOLD signal changes were significantly correlated with the signal variation from a seed in the in the left motor area, for data acquired with the SLR pulse (top-row) and HS pulse (bottom-row). Representative axial slices though orbitofrontal region are shown for each subject.

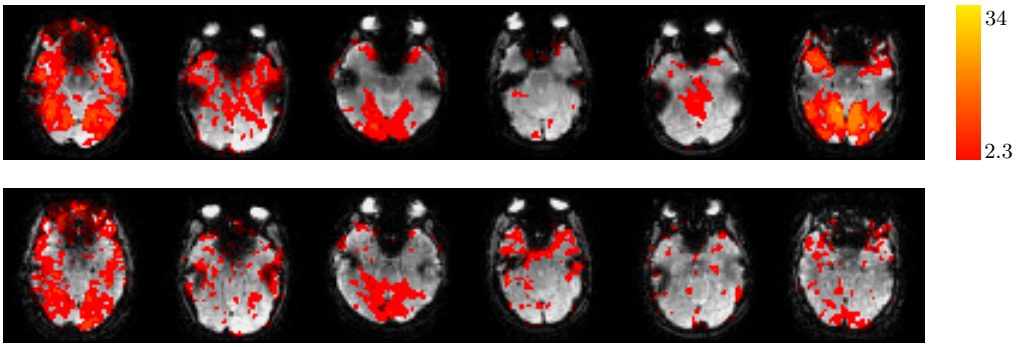

Figure 6.40: Thresholded z-statistic maps, showing voxels in which the resting-state BOLD signal changes were significantly correlated with the signal variation from a seed in the left motor area, for data acquired with the SLR pulse (top-row) and HS pulse (bottom-row). Representative axial slices though inferior temporal regions are shown for each subject.

50% loss of signal in regions of the brain unaffected by through-slice susceptibility gradients. These changes in signal translate to increases in temporal signal-to-noise in the orbitofrontal and inferior temporal regions, although these are accompanied by losses of up to 60% in TSNR elsewhere. The changes in TSNR do not translate in a straightforward way into BOLD sensitivity changes.

The results of the analysis of the FMRI data acquired whilst the subject performed the motor task show that, despite the reduction in TSNR, statistically significant changes in the BOLD signal could still be detected in the motor cortex and supplementary motor area. However, the unthesholded t-statistic in the areas of significant BOLD signal change were reduced. These results are in line with the findings of Chapter 4; specifically that the t-statistic resulting from a GLM analysis is proportional to the TSNR and percentage BOLD signal change. Whilst the detection of activations in the motor cortex is promising, it does not necessarily imply that BOLD signal changes induced by other FMRI paradigms will be detectable when the HS pulse is used. Specifically, if a paradigm induces smaller changes in BOLD signal than the motor task, as shown in Chapter 4, the t-statistic may fall below the level deemed to be statistical significant because of the reduction in TSNR when the HS pulse is used.

The changes BOLD sensitivity in voxels containing grey matter were assessed with a breath-hold paradigm. The results were inconsistent across the six subjects scanned. Inspection of the changes in unthresholded t-statistic when the HS pulse was used in place of the conventional SLR pulse show increases in the regions of recovered MR signal. However, statistically significant breath-hold induced BOLD signal changes in these regions were only detected in four out of the six subjects. In addition, in three of the subjects large reductions were observed in the number of voxels with statistically significant activations in regions unaffected by susceptibility

gradients.

The cause of the variations in significant BOLD signal changes between subjects is not clear; as shown earlier task compliance and mean grey matter BOLD signal changes were similar across subjects. The variation could arise from the order in which the data were acquired, however no direct correlation is obvious. FMRI data was acquired first with the conventional SLR pulse for subjects one, four and five and second for subjects two, three and six. Further work is required to understand the causes of this subject-to-subject variability; to determine if it is a result of the breath-hold task or variability in the efficacy of the HS pulse across subjects. For example the breath-hold paradigm could be replaced by a more technically challenging experiment in which the subject breathes carbon dioxide [310], as this would remove the variability in the execution of the breath-hold task. Alternatively breath-hold data from a larger group of subjects could be acquired to see if the variability in BOLD signal changes is present in a bigger sample.

The probabilisitic independent component analyses of the resting-state data show that the reductions in TSNR caused by the HS pulse make it more difficult to identify the common resting-state functional networks described in Smith et al. [169]. In data acquired with the conventional SLR pulse, each independent component contains a single resting-state network, however when the HS pulse was used several networks were combined into a single component. This could lead to problems when trying to determine the functional connections in the brain.

The results of the seed-based analysis suggest that the regions of the orbitofrontal cortex, previously obscured by signal dropout, may potentially be functionally connected to the default mode network. As noted in Chapter 5 this result is in agreement with the very recent findings of Dalwani et al. [299]. Using a GE-EPI pulse sequence modified to enable z-shimming they found similar significant correlations to the default mode network in the orbitofrontal cortex. In two out of the six subjects significant correlations between the orbitofrontal region and the motor network were also found. Without further experiments it is not possible to determine whether these correlations imply functional connections that were previously not seen because of signal dropout.

6.5 Discussion and Conclusions

Building on the previous experiments using tailored RF pulses [30, 126, 132] I have optimised the parameters of a full-passage scaled-down complex hyperbolic secant pulse to recover signal in regions of the brain affected by susceptibility induced dropout. I describe a systematic approach that can be used to design HS pulses based on the slice thickness and echo time required for an FMRI experiment, as

well as the hardware constraints of the MRI system. Bloch simulations were used to determine the HS pulse parameters required to produce a uniform signal response across the range of susceptibility gradients typically present in the head, as the previous theoretical model [126] was shown to be inaccurate. An expression for the bandwidth of a HS pulse (when used for signal excitation) was derived for the first time. This enabled the amplitude of the slice selection gradient to be calculated correctly, meaning that slices with the prescribed slice thickness were excited. Experiments in a phantom demonstrated the ability of the HS pulse to recover susceptibility gradient induced signal losses. A series of experiments were then performed in six healthy volunteers to assess whether these improvements in signal translated to improvements in the detectability of task-based and resting-state BOLD signal changes. Reductions in the signal dropout were observed in parts of the orbitofrontal and inferior temporal regions and the TSNR increased in the same areas. However, this was not without cost; reductions of up to 60% in the TSNR were measured in regions unaffected by susceptibility gradients. The changes in BOLD sensitivity across the grey matter, assessed using a breath-hold task, were inconsistent across the six subjects; in several subjects the improvements in signal and TSNR were not matched by increases in BOLD sensitivity. However in the remaining four subjects promising improvements were observed. The impact of the HS pulse on resting-state FMRI data differed depending on the method of data analysis. With a seed based approach significant correlations were observed between the region of recovered signal in the orbitofrontal cortex and the default mode network in all six subjects, suggesting it could form part of the default mode network. However, when analysed with independent component analysis it became harder to identify common resting-state networks from amongst the independent components.

Chapter 7

Combining Gradient and Radiofrequency Pulse Based Methods to Reduce Signal Dropout

7.1 Introduction

In the previous two chapters it was shown that signal dropout caused by through-plane susceptibility gradients can be reduced using either z-shimming or quadratic phase RF pulses. However, even with these techniques some areas of signal dropout remain caused by susceptibility gradients in both the frequency and phase encoding directions [28, 29]. As described in Chapter 2 and Appendix A, in-plane susceptibility gradients cause image distortion and shifts of the signal in k-space. These shifts modify the echo time and, if they are large enough, cause the echo to fall outside the window of signal acquisition leading to signal dropout [70, 71]. A number of methods have been proposed to recover the signal from these areas. Deichmann et al. [28] corrected for susceptibility gradients in the phase encoding direction by the addition of a compensatory gradient pulse in the phase encoding direction. Specifically, they demonstrated signal recovery in composite images formed (by weighted square-root sum-of-squares) from three images acquired with different z-shim and phase-encode compensatory gradients. A single step method was then developed; optimising the slice angle, the direction of k-space traversal and the areas of the z-shim and phase-encode compensatory gradients to maximise the BOLD sensitivity for a region of interest or across the whole brain [70, 71, 124]. Even with compensation for susceptibility gradients in the phase encoding direction, some areas of signal dropout remain. Weiskopf et al. [29] demonstrated that the signal in these areas could be

recovered using compensatory gradient pulses in the frequency encoding direction. Recently, Rick et al. [125] combined z-shimming with compensatory gradient pulses in both the frequency and phase encoding directions with the aim of maximising BOLD sensitivity in amygdala and orbitofrontal regions. They acquired data in a single step after determining the optimal slice-specific compensatory gradients from a field map.

In this chapter I investigate the potential of combining the quadratic phase RF pulse, described in Chapter 6, with compensation gradients in frequency and/or phase encoding directions to further reduce the areas of signal dropout.

7.2 Pulse Sequence Programming

The modified echo-planar imaging pulse sequences using hyperbolic secant excitation pulses and z-shimming, described in the previous two chapters, were combined and extended (at software release 22.0). The option to play out a slice specific compensatory gradients in both the frequency and phase encoding directions was added. The shift of the signal in k-space produced by the compensatory gradients in the frequency ($\delta k_{x,sh}$) and phase encoding ($\delta k_{y,sh}$) directions were controlled using three, direction specific, parameters; the number of shim steps ($N_{x,shim}$ and $N_{y,shim}$), a parameter to allow the shift to be set in units of the voxel size (β_x and β_y) and the shim number (ζ_x and ζ_y). The k-space offset in the frequency encoding direction is given by:

$$\delta k_{x,sh} = \frac{1}{\Delta x \beta_x}\left(\zeta_x - \frac{N_{x,shim}+1}{2}\right) \tag{7.1}$$

In the phase encoding direction the k-space offset is:

$$\delta k_{y,sh} = \frac{1}{\Delta y \beta_y}\left(\zeta_y - \frac{N_{y,shim}+1}{2}\right) \tag{7.2}$$

Here Δx and Δy are the the voxel sizes in the frequency and phase encoding directions respectively. The values of $N_{x,shim}$, $N_{y,shim}$, $N_{z,shim}$, β_x, β_y, β_z, ζ_x, ζ_y, and ζ_z are supplied to the pulse sequence via a text file. The position of the compensatory gradient pulses within the modified GE-EPI pulse sequence are shown in Figure 7.1.

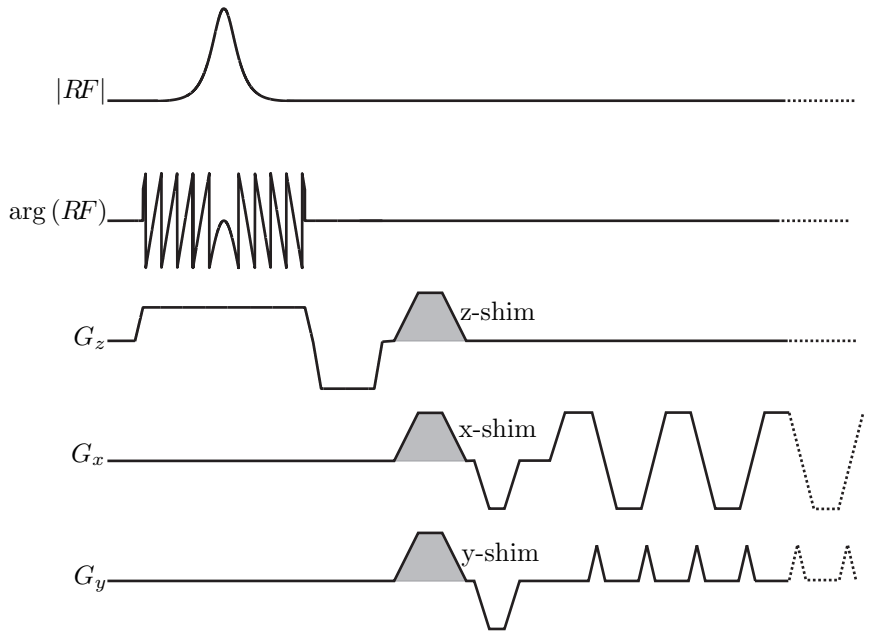

Figure 7.1: Schematic of the GE-EPI pulse sequence, modified to include the optimised hyperbolic secant RF pulse and to enable compensatory gradient pulses in the slice selection (z-shim), phase encoding (y-shim) and frequency encoding (x-shim) directions. Fat suppression was carried out with the CHESS pulse (not shown), described in Chapter 2, played out prior to the hyperbolic secant excitation pulse.

7.3 Determing the Impact of Compensatory Gradients in the Frequency and Phase Encoding Directions on Signal Dropout

7.3.1 Introduction

The modified GE-EPI pulse sequence was used to determine the impact on signal dropout of using the optimised hyperbolic secant pulse with compensatory gradients in the frequency and phase encoding directions.

7.3.2 Methods

A single volume, preceded by four dummy acquisitions, was acquired of a healthy male volunteer using the conventional GE-EPI pulse sequence on the a 3 T GE Discovery MR750 system. The volunteer's head was aligned so that the line intersecting the anterior and posterior commissure was in the axial plane of the scanner. An eight-channel phased array head coil was used for signal reception and the body coil for RF transmission. Thirty-six 3 mm slices with 0.3 mm slice gaps were acquired with a 21.2 cm field-of-view and a 64×64 acquisition matrix in a sequential manner from the top to the bottom of the head. The view order in k-space was bottom-up

(i.e. positive phase encode gradient blips) as shown in Figure A.1(c). The repetition time was 2 s and the echo time was 30 ms. The ASSET acceleration factor was two. The CHESS pulse was used for fat suppression and the signal was excited using a 73° SLR pulse, as described in Chapter 2.

Twenty five volumes, preceded by four dummy acquisitions, were then acquired using the modified GE-EPI pulse sequence for all combinations of $\delta k_{x,sh} = \frac{-1}{\Delta x}$, $\frac{-1}{2\Delta x}$, 0, $\frac{1}{2\Delta x}$, $\frac{1}{\Delta x}$ and $\delta k_{y,sh} = \frac{-1}{\Delta y}$, $\frac{-1}{2\Delta y}$, 0, $\frac{1}{2\Delta y}$, $\frac{1}{\Delta y}$. The same compensatory gradients were used for all slices and the z-shim gradient was not used. All other imaging parameters were the same as for the data acquired with the conventional GE-EPI sequence.

To determine the overall signal recovery when images were acquired with different compensatory gradients a total of ten maximum intensity projection (MIP) images were produced. These included a MIP of all 25 volumes, a MIP of the five volumes acquired with $\delta k_{y,sh} = \frac{1}{\Delta y}$ and $\delta k_{x,sh} = \frac{-1}{\Delta x}, \frac{-1}{2\Delta x}, 0, \frac{1}{2\Delta x}, \frac{1}{\Delta x}$, a MIP of the five volumes acquired with $\delta k_{y,sh} = \frac{1}{2\Delta y}$ and $\delta k_{x,sh} = \frac{-1}{\Delta x}, \frac{-1}{2\Delta x}, 0, \frac{1}{2\Delta x}, \frac{1}{\Delta x}$ and so on, for all combinations of images shown in Figure 7.2.

7.3.3 Results

Representative slices through the orbitofrontal and inferior temporal regions of data acquired with conventional GE-EPI are shown in Figure 7.3. As expected from the previous chapters, significant signal dropout can be seen. Representative slices from all twenty volumes of data acquired with the modified GE-EPI acquisition and all ten MIPs, described above, are shown for the orbitofrontal cortex in Figure 7.4 and inferior temporal regions in Figure 7.5.

Firstly, focussing on the slice through the orbitofrontal region, shown in Figures 7.3(a) and 7.4, it can be seen that when the HS pulse is used in the absence of any compensatory gradients ($\delta k_{x,sh} = 0$ and $\delta k_{y,sh} = 0$ highlighted in Figure 7.4 with a yellow outline) signal is recovered in the medial anterior part of the orbitofrontal cortex. For the largest compensatory gradients ($\delta k_{x,sh} = -1/\Delta x$, $\delta k_{x,sh} = 1/\Delta x$, $\delta k_{y,sh} = -1/\Delta y$ and $\delta k_{y,sh} = 1/\Delta y$) some signal is recovered in a small number of voxels, however signal is lost from the majority of remaining voxels. The voxels showing increased signal with these large compensation gradients also show signal recovery with smaller compensation gradients ($\delta k_{x,sh} = -1/2\Delta x$, $\delta k_{x,sh} = 1/2\Delta x$, $\delta k_{y,sh} = -1/2\Delta y$ and $\delta k_{y,sh} = 1/2\Delta y$), although signal is again reduced in a large number of other voxels. This suggests that most susceptibility gradients present in the had result in shifts of the signal in k-space in the ranges $-1/\Delta x < \delta k_{x,s} < 1/\Delta x$ and $-1/\Delta y < \delta k_{y,s} < 1/\Delta y$. When all twenty five images are combined using a maximum intensity projection no signal dropout is observed (blue outline in Figure

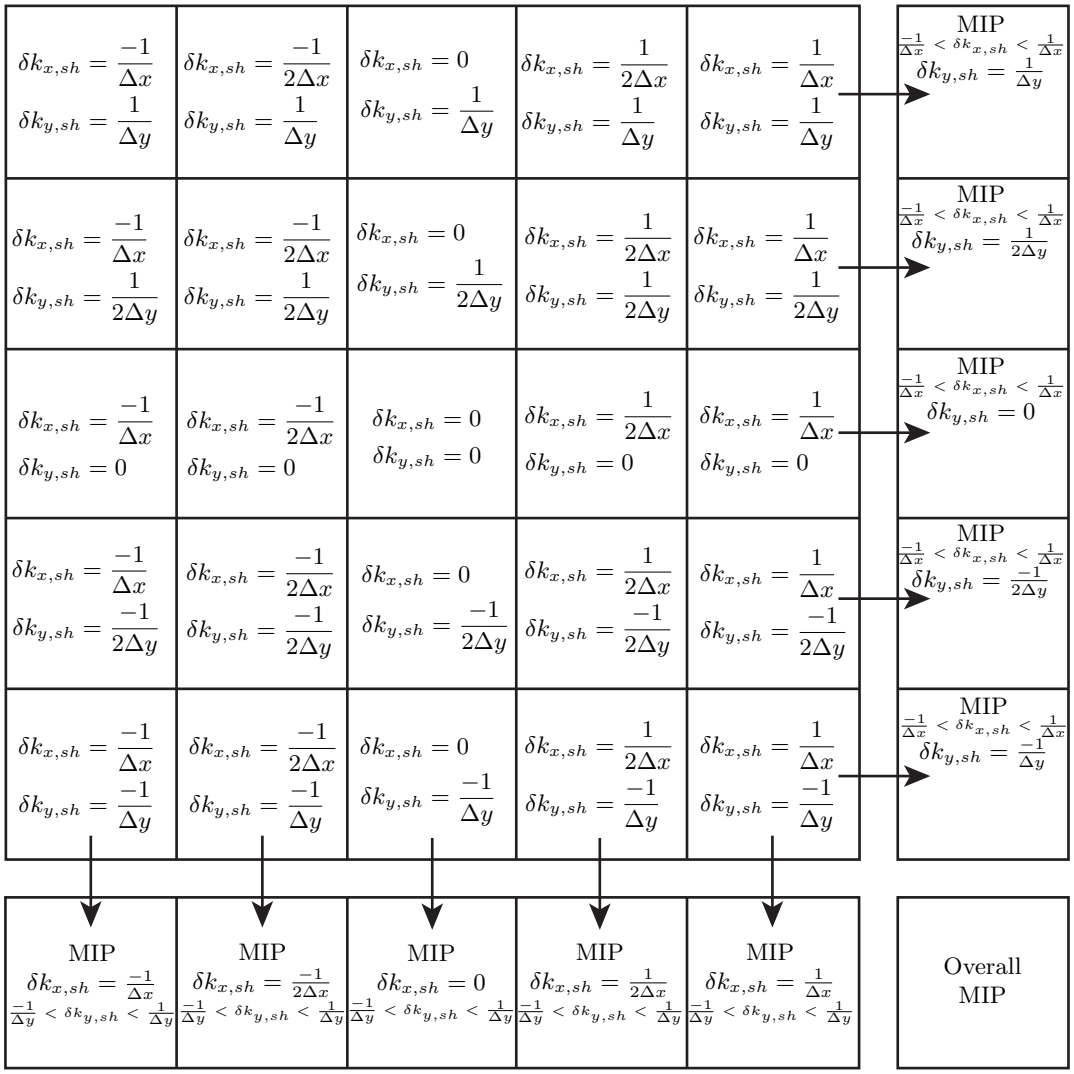

Figure 7.2: A schematic showing the ten maximum intensity projections calculated from the twenty five volumes of data acquired with all combinations of $\delta k_{x,sh} = \frac{-1}{\Delta x}, \frac{-1}{2\Delta x}, 0, \frac{1}{2\Delta x}, \frac{1}{\Delta x}$ and $\delta k_{y,sh} = \frac{-1}{\Delta y}, \frac{-1}{2\Delta y}, 0, \frac{1}{2\Delta y}, \frac{1}{\Delta y}$.

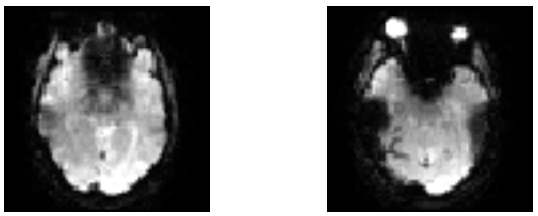

(a) Orbitofrontal region

(b) Inferior temporal region

Figure 7.3: Representative slices through the orbitofrontal and inferior temporal regions of an image acquired with the conventional GE-EPI pulse sequence.

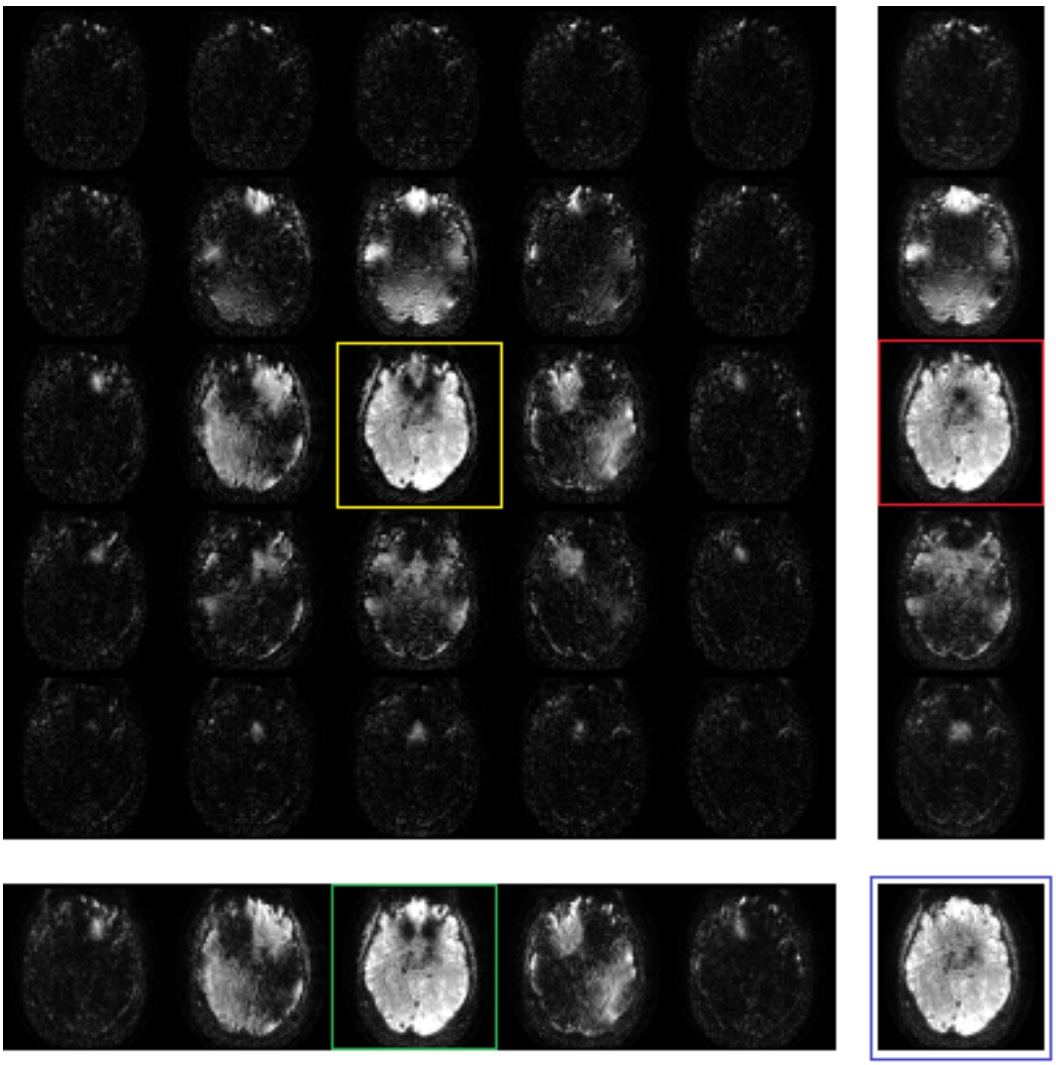

Figure 7.4: Images demonstrating the impact of using the HS pulse and twenty-five combinations of $\delta k_{x,sh} = \frac{-1}{\Delta x}, \frac{-1}{2\Delta x}, 0, \frac{1}{2\Delta x}, \frac{1}{\Delta x}$ and $\delta k_{y,sh} = \frac{-1}{\Delta y}, \frac{-1}{2\Delta y}, 0, \frac{1}{2\Delta y}, \frac{1}{\Delta y}$ for a single representative slice through the orbitofrontal cortex. MIPs are shown in the separate column on the right and separate row at bottom of the figure. The acquired images and MIPs are arranged in an identical manner to the schematic shown in Figure 7.2. They are all displayed using the same colour scale.

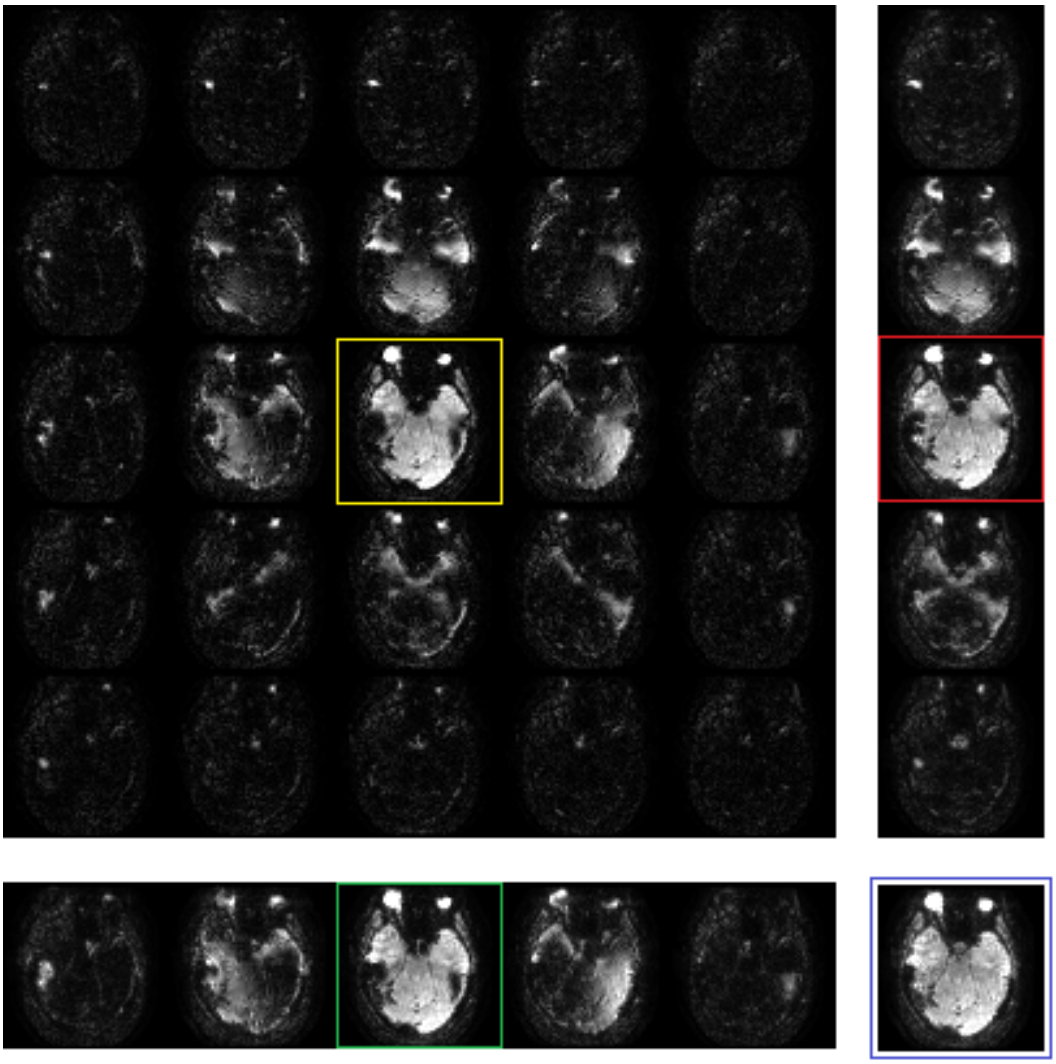

Figure 7.5: Images demonstrating the impact of using the HS pulse and twenty-five combinations of $\delta k_{x,sh} = \frac{-1}{\Delta x}, \frac{-1}{2\Delta x}, 0, \frac{1}{2\Delta x}, \frac{1}{\Delta x}$ and $\delta k_{y,sh} = \frac{-1}{\Delta y}, \frac{-1}{2\Delta y}, 0, \frac{1}{2\Delta y}, \frac{1}{\Delta y}$ for a single representative slice through the inferior temporal regions. MIPs are shown in the separate column on the right and separate row at bottom of the figure. The acquired images and MIPs are arranged in an identical manner to the schematic shown in Figure 7.2. They are all displayed using the same colour scale.

7.4). When the five images acquired with compensation gradients in the frequency encoding direction $\delta k_{x,sh} = \frac{-1}{\Delta x}, \frac{-1}{2\Delta x}, 0, \frac{1}{2\Delta x}, \frac{1}{\Delta x}$ but without any compensation gradient in the phase encoding direction ($\delta k_{y,sh} = 0$) are combined only a small region of dropout remains in the central anterior portion of the orbitofrontal cortex (red outline in Figure 7.4). In contrast, when the five images acquired with compensation gradients in the phase encoding direction $\delta k_{y,sh} = \frac{-1}{\Delta y}, \frac{-1}{2\Delta y}, 0, \frac{1}{2\Delta y}, \frac{1}{\Delta y}$ and without any compensation gradient in the frequency encoding direction ($\delta k_{x,sh} = 0$) are combined two larger regions of dropout remain in the more lateral portions of the orbitofrontal cortex (green outline in Figure 7.4).

Secondly, focussing on the slice through the inferior temporal region, Figures 7.3(b) and 7.5, signal is recovered in the a part of the left inferior temporal lobe when the HS pulse is used in the absence of any compensatory gradients. Combining all twenty five images using a MIP (blue outline in Figure 7.5) only one small area of dropout remains in the right inferior temporal region. As above, the shift of the signal in k-space as a result of susceptibility gradients appear to all be in the ranges $-1/\Delta x < \delta k_{x,s} < 1/\Delta x$ and $-1/\Delta y < \delta k_{y,s} < 1/\Delta y$. In addition, signal is recovered in a greater number of voxels when the compensation gradients are only in the frequency encoding direction (red outline in Figure 7.5) compared to when they are only in the phase encoding direction (green outline in Figure 7.5).

7.3.4 Discussion and Conclusion

The results above show that the areas of unrecovered signal in images acquired with the HS pulse can be reduced with the addition of compensatory gradients in the frequency and phase encoding directions. The maximum intensity projection of the data acquired with all twenty five combinations of compensatory gradients had only one small area of remaining dropout in the right inferior temporal region. Acquiring FMRI data with twenty five shim combinations would however be impractical because of the twenty five fold decrease in the temporal resolution. To reduce this loss of temporal resolution compensation gradients could be limited to either the frequency or phase encoding direction. For compensation gradients in the phase encoding direction only, the MIP has two residual areas of dropout in the lateral portions of the orbitofrontal cortex as well as areas of dropout in the more posterior regions of the temporal lobes. In contrast, with compensation gradients only in the frequency encoding direction the MIP shows signal dropout is reduced in a greater number of voxels. Given these observations and because the component of a susceptibility gradient in the phase encoding direction (and by extension the signal dropout it causes) can potentially be reduced by tilting the slices [70, 71, 124], the combination of the HS pulse and compensatory gradients in the frequency encoding

direction appears the most promising method for signal recovery.

7.4 Investigating the Impact of Slice Orientation on Signal Dropout

7.4.1 Introduction

Given the results of the previous experiment, the effect of the angle of the slice on the amount of signal dropout was investigated for data acquired with the HS pulse and compensatory gradients in the frequency encoding direction only.

7.4.2 Methods

A two-step approach was investigated, with compensatory gradients in the frequency encoding direction. In the previous experiment it was shown that the k-space signal offsets resulting from susceptibility gradients were in the range $-1/\Delta x < \delta k_{x,s} < 1/\Delta x$. Signal recovery from this range of susceptibility gradients can be achieved if two images were acquired; the first with $\delta k_{x,sh} = \frac{-1}{2\Delta x}$ and the second with $\delta k_{x,sh} = \frac{1}{2\Delta x}$. However, this would result in large reductions in signal in the regions unaffected by susceptibility gradients because of the effect of the low pass filtering of the k-space data[1]; the compensation gradients would mean that the largest signal from these homogeneous regions would occur very close to the edge of the k-space acquisition window and would therefore by attenuated by the filter. It was therefore decided to investigate the use of $\delta k_{x,sh} = \frac{-3}{10\Delta x}$ and $\frac{3}{10\Delta x}$, because the signal from regions of homogeneous field is then not shifted to the very edge of the data acquisition window. The total k-space coverage in the frequency encoding (x) direction when these two steps are acquired is $\frac{-4}{5\Delta x} < k_x < \frac{4}{5\Delta x}$; Figure 7.7.

Nineteen data sets were acquired of a healthy male volunteer using the modified GE-EPI pulse sequence for slices at $\theta = 45°$, $50°$, $55°$ ..., $125°$ and $130°$; the definition of θ relative to the z-axis is shown in Figure 7.8. For each data set two volumes were acquired with $\delta k_{x,sh} = \frac{-3}{10\Delta x}$ and $\frac{3}{10\Delta x}$, preceded by four dummy acquisitions. All

[1]On GE systems k-space data are low-pass filtered using a Fermi filter to reduce Gibbs ringing artefact caused by abrupt signal changes at the edges of k-space. For an acquisition with $N_x \times N_y$ matrix, such that there are N_y phase encoding steps and N_x samples in the frequency encoding direction the value of the fermi filter for the m^{th} sample ($-N_x/2 \leq m < N_x/2$) on the n^{th} phase encoding step ($-N_y/2 \leq n < N_y/2$) is:

$$\frac{1}{1 + e^{(r-F_c)/F_w}} \tag{7.3}$$

Here $r = \sqrt{n^2 + m^2}$, F_c is the cut-off of the filter, and F_w is the transition width. A Fermi filter is shown in Figure 7.6, with the default cut-off $F_c = 32$ and transition width $F_w = 10$ for a GE-EPI acquisition with a 64×64 matrix size on the 3T GE Discovery MR750 system.

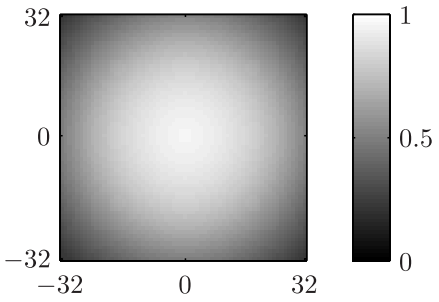

Figure 7.6: The Fermi filter used as standard by the 3T GE Discovery MR750 system to low-pass filter the raw k-space data prior to image reconstruction.

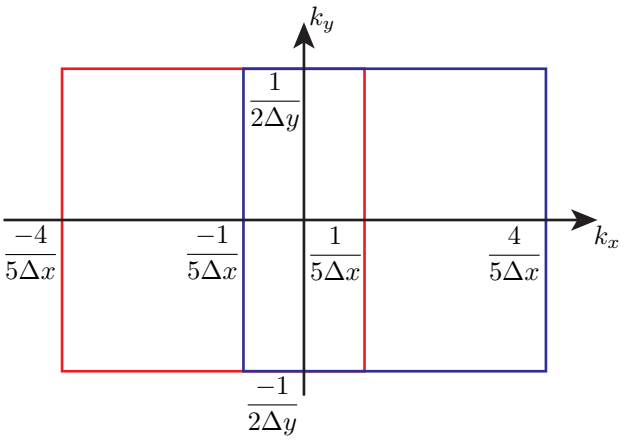

Figure 7.7: The total k-space coverage of the two images acquired with compensatory gradients in the frequency encoding direction with $\delta k_{x,sh} = \frac{-3}{10\Delta x}$ (red) and $\frac{3}{10\Delta x}$ (blue).

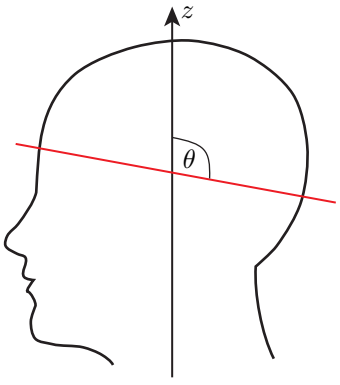

Figure 7.8: A schematic showing the definition of the slice angle, θ. For a true axial slice $\theta = 90°$. (The brain outline in this figure was adapted from a freely available image from all-free-download.com)

other pulse sequence parameters were the same as in the previous experiment. As before, the volunteer's head was aligned so that the line intersecting the anterior and posterior commissure was in the axial plane of the scanner. In addition, a DIR-EPI image was acquired with slices at $\theta = 90°$. This was thresholded to produce a grey matter mask as described in Section 5.5.1.

Following the method used in a previous study (and matching the approach in Chapter 5) which utilised in-plane compensatory gradients, composite images were produced using the square root of the sum of squares (SSQ) combination [71]. All SSQ images were aligned into the space of the data acquired at $\theta = 90°$ using MCFLIRT [205]. Maps of the signal differences between the data acquired at each slice angle (after realignment) and the data acquired at $\theta = 90°$ were calculated, and masked to show only voxels containing grey matter using the thresholded DIR-EPI data.

7.4.3 Results

The images combined by SSQ and the maps showing signal differences between the data acquired at each slice angle (after realignment) and the data acquired at $\theta = 90°$ are shown for representative slices through the orbitofrontal and inferior temporal regions in Figures 7.9 and 7.10.

From Figure 7.9 it can be seen that size of the region of signal dropout in the orbitofrontal cortex is minimised when the slices were in the axial plane of the scanner (at $\theta = 90°$). When the slices were tilted forward ($\theta < 90°$) the signal increased in the anterior parts of the orbitofrontal cortex, however dropout increased in the more posterior parts. As the slices were tilted backward ($\theta > 90°$) the converse was true; signal increased in the posterior parts of the orbitofrontal cortex and dropout increased in the more anterior regions.

From Figure 7.10 it can be seen that size of the region of signal dropout in the inferior temporal regions is minimised when the slices were tilted forward by 10° from the axial plane of the scanner (at $\theta = 80°$). When the slices were tilted forward by larger angles ($\theta < 70°$) slightly more signal was recovered but the field of view was not sufficient to cover the whole of the brain. As the slices were tilted backward ($\theta > 90°$) dropout increased in the more posterior regions of the temporal lobes.

7.4.4 Discussion and Conclusion

From the results presented above it can be seen that large areas of signal are recovered in SSQ images formed from two images acquired using the hyperbolic secant pulse and different compensatory gradients in the frequency encoding direction

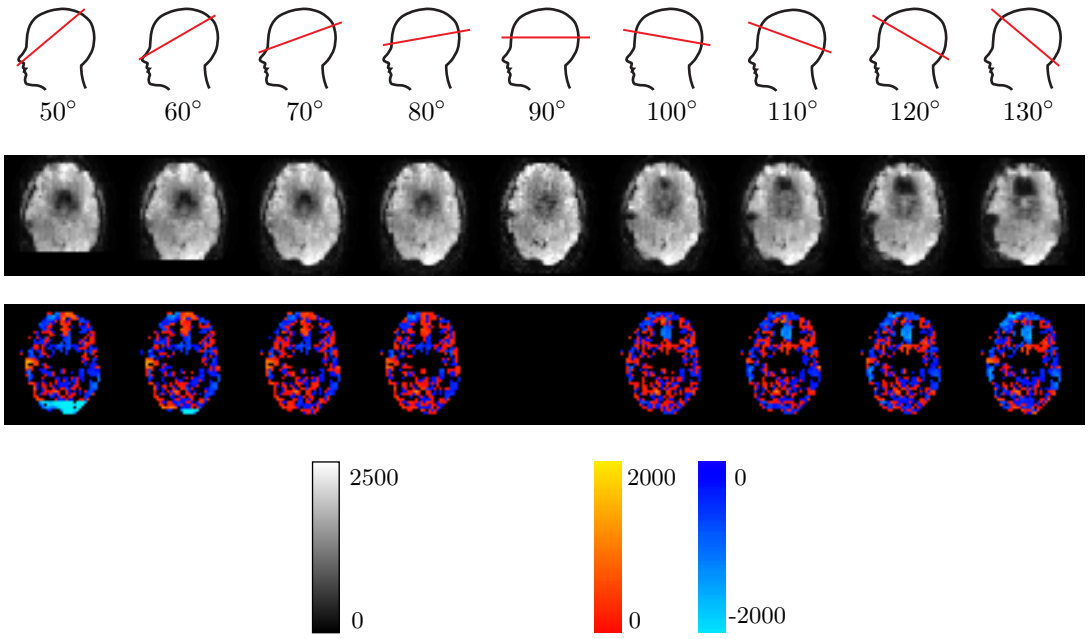

Figure 7.9: Images demonstrating the impact of slice orientation on the degree of signal dropout in data acquired using the HS pulse and compensatory gradients in the frequency encoding direction for a representative slice through the orbitofrontal region. The first row of images shows schematically the angle of the slices for the data shown in the lower two rows. The second row shows the realigned SSQ images and the third row the signal differences between the data acquired at each slice angle (after realignment) and the data acquired at $\theta = 90°$.

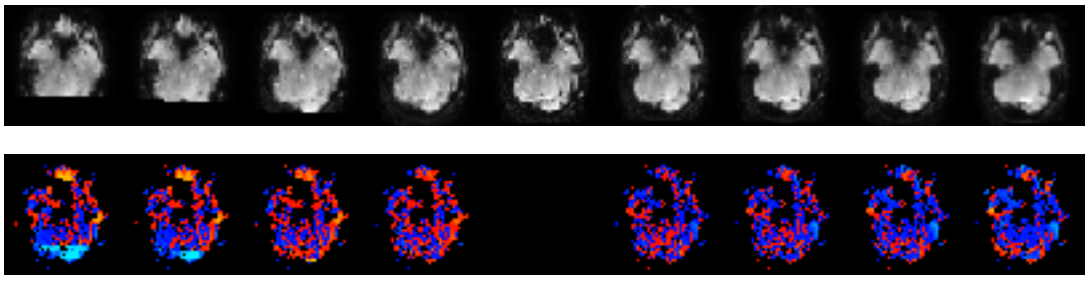

Figure 7.10: Images demonstrating the impact of slice orientation on the degree of signal dropout in data acquired using the HS pulse and compensatory gradients in the frequency encoding direction for a representative slice through the inferior temporal region. The first row shows the realigned SSQ images and the second row the signal differences between the data acquired at each slice angle (after realignment) and the data acquired at $\theta = 90°$. The slice orientations and colour scales are the same as shown in Figure 7.9.

($\delta k_{x,sh} = \frac{-3}{10\Delta x}$ and $\frac{3}{10\Delta x}$). This means that FMRI data with reduced signal dropout can be acquired with only a factor of two reduction in the temporal resolution. However, there were some areas of remaining signal dropout, especially in the left inferior temporal lobe. In conclusion, for a subject aligned so that the line intersecting the anterior and posterior commissure was in the axial plane of the scanner, the optimal slice angle for maximum signal recovery was (for the protocol described here) 90° for the orbitofrontal cortex and 80° for the inferior temporal regions.

7.5 Evaluating the Impact of the Optimised HS Pulses and Two-Step Gradient Based Compensation In-vivo

As in the previous two chapters a series of experiments were carried out to assess the impact of using a modified GE-EPI acquisition with a combination of x-shimming (a compensation gradient in the frequency encoding direction) and an HS pulse (GE-EPI-XHS) to reduce signal dropout in FMRI experiments. These were performed on the same set of six healthy male subjects as in the previous two chapters.

7.5.1 Data Acquisition

Using the methods described in Section 5.5.1, the following set of scans were acquired of each subject: a localiser, ASSET calibration, SE-EPI, DIR-EPI, a pair of resting-state FMRI scans, a pair of FMRI scans with a motor task and a pair of FMRI scans with a breath-hold paradigm. As in previous chapters, one scan of each pair was acquired using a conventional GE-EPI sequence and the other with GE-EPI-XHS (with $\delta k_{x,sh} = \frac{-3}{10\Delta x}$ and $\frac{3}{10\Delta x}$). The ordering of the acquisition method within each pair of FMRI scans was counter balanced across the six subjects. The subjects' heads were aligned so that the line intersecting the anterior and posterior commissure was in the axial plane of the scanner. Based on the results of the previous experiment, the slices were aligned in the axial plane of the scanner ($\theta = 90°$).

7.5.2 Data Analysis

All imaging data were converted into the NIfTI-1 data format, and then processed using tools from FSL. The FMRI data acquired using GE-EPI-XHS were combined pairwise by the square root of the sum of squares (SSQ) in the same manner as in Section 5.5.2.

Qualitative Comparison of Signal In Regions of Through-Slice Susceptibility Gradient

The data acquired with the SE-EPI, conventional GE-EPI and GE-EPI-XHS pulse sequences were visually compared to determine the extent of signal recovery in the orbitofrontal and inferior temporal regions when the GE-EPI-XHS sequence was used.

Temporal Signal-to-Noise Ratio

Maps of the temporal signal-to-noise ratio (TSNR) were calculated from the resting-state FMRI data sets using the method outlined in Section 5.5.2. As in previous chapters, maps of the percentage change in TSNR between the data acquired with the conventional GE-EPI and GE-EPI-XHS pulse sequences were also calculated for each subject.

Detectability of Motor Activations

The FMRI data acquired whilst the subject performed the motor task were analysed using the method described in Section 5.5.2: To confirm the subjects performed the task as instructed, the pressure measured in the squeeze ball was plotted as a function of time for both image acquisition methods. The areas of the brain showing significant changes in BOLD signal in response to the motor stimulus were determined for the conventional GE-EPI and GE-EPI-XHS datasets. Maps of the percentage change in the unthresholded t-statistic between the GE-EPI and GE-EPI-XHS data were calculated for each subject. In addition, for each subject, the mean percentage change in the unthresholded t-statistic and TSNR in regions of significant activation (common to the data acquired using both methods) were calculated.

Measuring BOLD sensitivity via Breath-hold BOLD Signal Changes

The breath-hold FMRI data were analysed using the method described in Section 5.5.2; the normalised signal from the respiratory bellows was plotted as a function of time for both acquisition types to check whether the subjects adhered to the task. Additionally, for each subject, the variation in the mean percentage change in BOLD signal was calculated as a function of time from voxels containing grey matter. The regions of the brain showing significant changes in BOLD signal in response to the breath-hold stimulus were calculated from the data acquired with both the GE-EPI and GE-EPI-XHS pulse sequences. Maps of the change in unthresholded t-statistic between the GE-EPI and GE-EPI-XHS datasets were calculated. As in Chapter 6, these maps were masked so that only those voxels with increased signal in the

GE-EPI-XHS data were shown. Both the thresholded z-statistic and masked t-statistic difference maps were used to determine if increases in signal were matched by increases in BOLD sensitivity.

Detectability of Resting-State FMRI Networks

The resting-state FMRI data were analysed using the techniques outlined in Section 5.5.2. PICA as implemented in MELODIC was performed to determine if the ten resting-state networks described in Smith et al. [169] were detectable in the GE-EPI and GE-EPI-XHS data. In addition, seed based analyses were performed to determine whether resting-state fluctuations in the regions of recovered signal in the orbitofrontal and inferior temporal lobes were correlated with fluctuations in the default-mode and sensorimotor networks.

7.5.3 Results

Qualitative Comparison of Signal In Regions of Through-Slice Susceptibility Gradient

Representative slices through the orbitofrontal and inferior temporal regions from data acquired with SE-EPI, conventional GE-EPI and GE-EPI-XHS are shown for each subject in Figures 7.11 and 7.12. As in the previous two chapters, signal dropout is observed in both the orbitofrontal and temporal regions for all six subjects in the conventional GE-EPI images. With the exception of subject five, the signal in the region of dropout in the orbitofrontal cortex is recovered in nearly all voxels in the GE-EPI-XHS images. For subject five, a small region of dropout remains in the posterior part of the orbitofrontal region. In addition large areas of signal are recovered in the inferior temporal regions in the images acquired with GE-EPI-XHS. However, in all six subjects signal dropout is still evident in the more medial and anterior parts of the inferior temporal lobes.

Temporal Signal-to-Noise Ratio

Maps of the TSNR for each subject for data acquired with conventional GE-EPI and GE-EPI-XHS are shown through the orbitofrontal and inferior temporal regions in Figures 7.13 and 7.14. Maps of the percentage change in the TSNR between data acquired with conventional GE-EPI and GE-EPI-XHS, for each subject, for representative slices through the orbitofrontal cortex and inferior temporal regions are shown in Figure 7.15. In the regions of dropout, where signal was recovered with the GE-EPI-XHS sequence, it can be seen that the TSNR increases from close to zero to a level that is close to that observed in voxels in regions of homogeneous

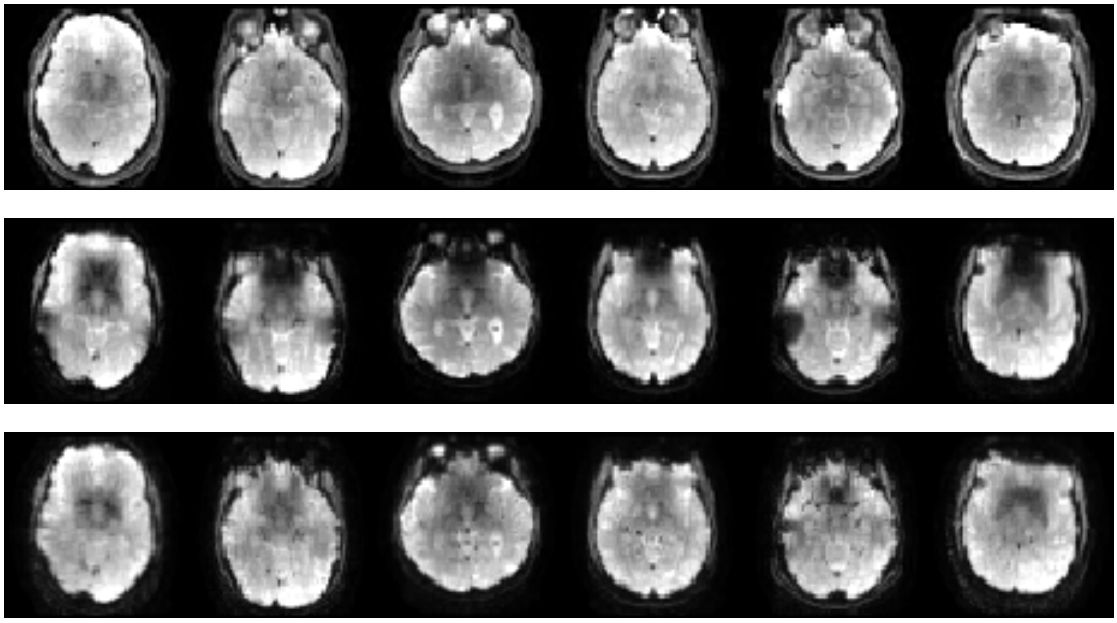

Figure 7.11: Representative slices through the orbitofrontal cortex of the six subjects from images acquired with SE-EPI (top-row), conventional GE-EPI (middle-row) and GE-EPI-XHS (bottom-row). The intensity range was chosen on a per subject and per acquisition basis such that the areas of signal dropout and recovery could be readily appreciated.

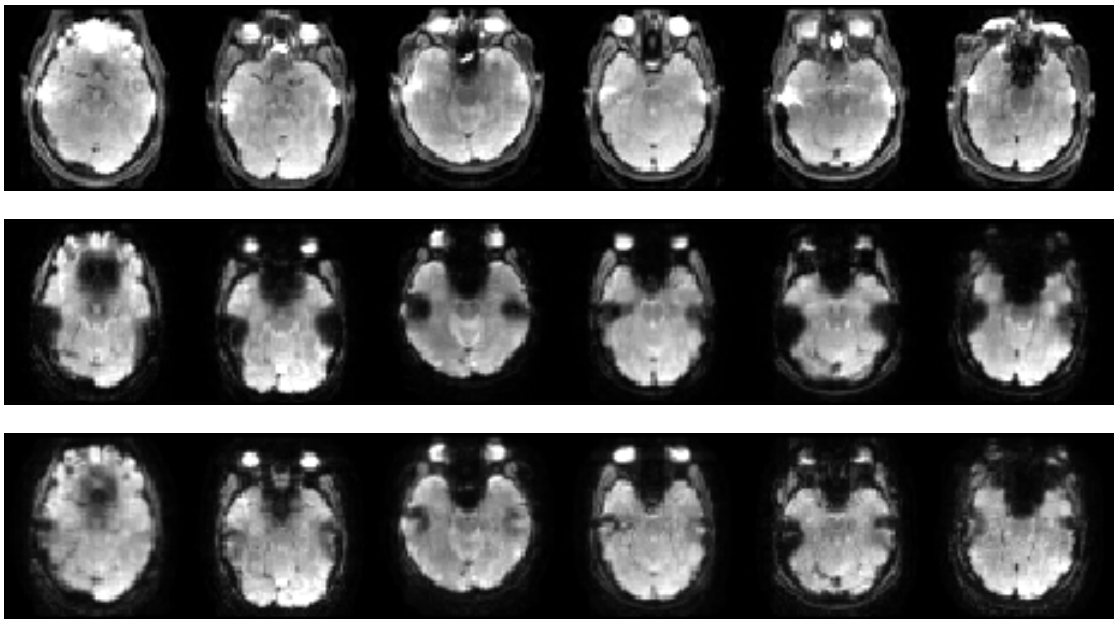

Figure 7.12: Representative slices through the inferior temporal lobes of the six subjects from images acquired with SE-EPI (top-row), conventional GE-EPI (middle-row) and GE-EPI-XHS (bottom-row). The intensity range was chosen on a per subject and per acquisition basis such that the areas of signal dropout and recovery could be readily appreciated.

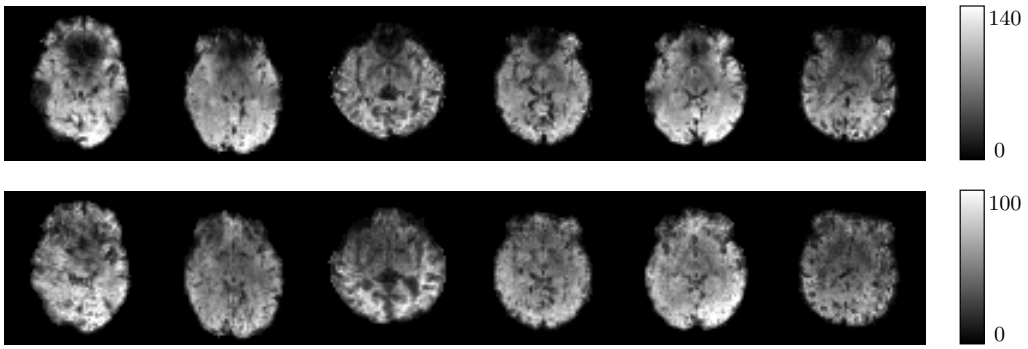

Figure 7.13: TSNR maps for representative slices through the orbitofrontal cortex of the six subjects calculated from data acquired with conventional GE-EPI (top-row) and with GE-EPI-XHS (bottom-row).

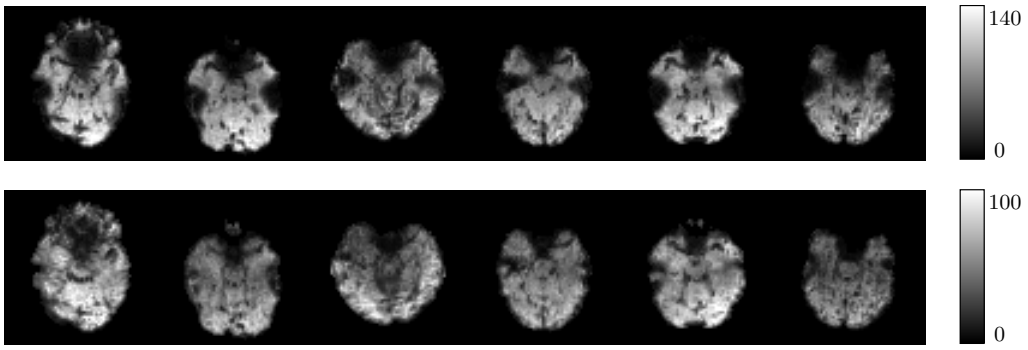

Figure 7.14: TSNR maps for representative slices through the inferior temporal lobes of the six subjects calculated from data acquired with conventional GE-EPI (top-row) and with GE-EPI-XHS (bottom-row).

field. Because of the properties of the HS pulse, however, decreases in TSNR of up to 60% are seen in regions unaffected by susceptibility gradients. In grey matter, on average across all subjects, the TSNR increased in 13.5% of voxels but was reduced in 77.8%. The subject specific changes are detailed in Table 7.1.

Comparing the Detectability of BOLD Signal Changes Resulting From the Motor Task

The pressure recorded in the squeeze ball throughout the motor-task FMRI scans are shown in Figure 7.16, for all six subjects, and both image acquisition methods. These plots demonstrate that all subjects performed the task over the full duration of both FMRI data acquisitions. The force with which subject one squeezed the ball reduced by 25% during the final task period in the acquisition with the GE-EPI-XHS pulse sequence. The force with which subject six squeezed the ball reduced by approximately 40% throughout the experiment when imaging data was acquired with conventional GE-EPI.

Thresholded z-statistic maps for each subject and acquisition method are shown

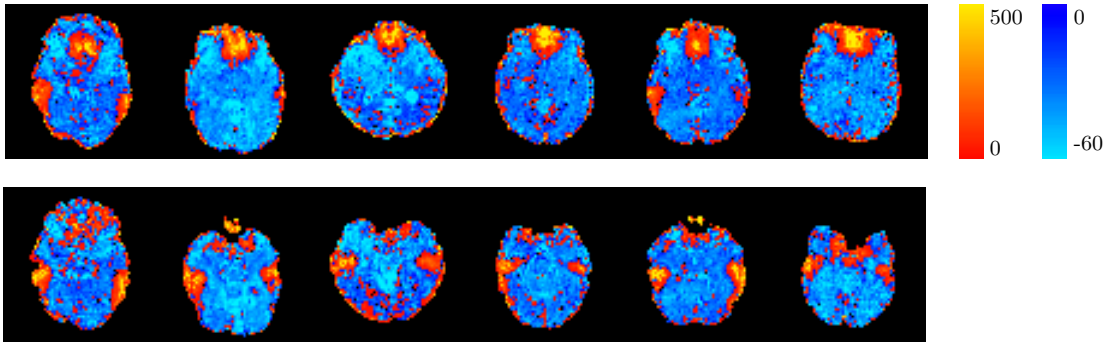

Figure 7.15: Maps showing the percentage change in the TSNR between data acquired using conventional GE-EPI and GE-EPI-XHS. The top row shows representative slices through the orbitofrontal cortex, and the bottom row, slices through the inferior temporal lobes for the six subjects.

Subject	Grey matter voxels with increased TSNR (%)	Grey matter voxels with decreased TSNR (%)
1	17.5	77.0
2	7.4	87.6
3	13.4	77.2
4	14.7	77.5
5	13.1	74.7
6	14.6	72.6
Mean	13.5	77.8

Table 7.1: The percentage of grey matter voxels showing increases or decreases in TSNR when GE-EPI-XHS is used in place of conventional GE-EPI.

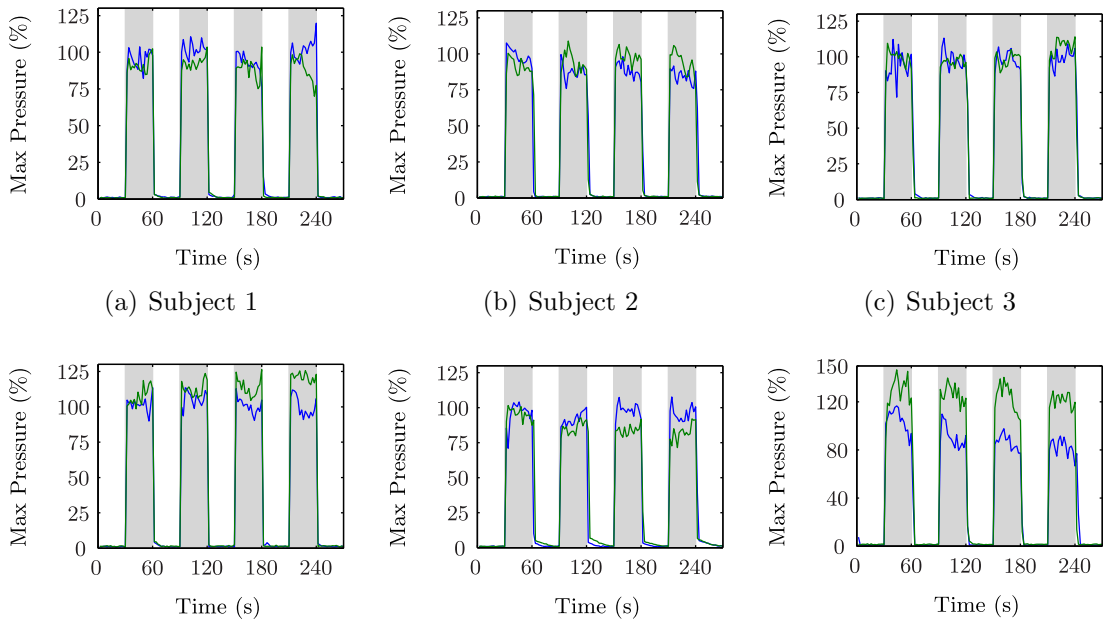

(a) Subject 1 (b) Subject 2 (c) Subject 3

(d) Subject 4 (e) Subject 5 (f) Subject 6

Figure 7.16: The pressure recorded in the squeeze ball (as a percentage of the maximum pressure measured during calibration) for all six subjects for FMRI data acquired with conventional GE-EPI (blue line) and GE-EPI-XHS (green line). The shaded grey regions illustrate the periods in which the subject was instructed to squeeze the ball in their right hand every 2 s.

in Figure 7.17. The motor task resulted in statistically significant activations of the left motor cortex in all six subjects for both methods of data acquisition. With the exception of subject four the same is true of the supplementary motor area. For subject five there is a more diffuse pattern of significant activations seen in the data acquired with GE-EPI, the origin of this is unclear. As shown in Table 7.2, the peak z-statistic was lower for data acquired with GE-EPI-XHS in five of the six subjects. Maps of the percentage change in the unthresholded t-statistic between data acquired with conventional GE-EPI and GE-EPI-XHS are shown in Figure 7.18. The maps for each subject are masked to show only those voxels with significant activations in both the data acquired with GE-EPI and GE-EPI-XHS. The average percentage change in the t-statistic within the mask for each subject are detailed in Table 7.3. From the maps and the table of results it can be seen that the t-statistic is reduced in data acquired with the GE-EPI-XHS pulse sequence, on average across all the subjects, by 20.8%. As also shown in Table 7.3, the TSNR in the same regions is reduced by on average 10.5%.

	Peak z-statistic	
Subject	GE-EPI	GE-EPI-XHS
1	15.4	13.0
2	15.3	14.7
3	11.4	9.9
4	9.5	8.2
5	12.6	9.9
6	12.0	12.6
Mean	12.7	11.4

Table 7.2: Peak z-statistic from the GLM analysis of the motor task FMRI data acquired with conventional GE-EPI and GE-EPI-XHS.

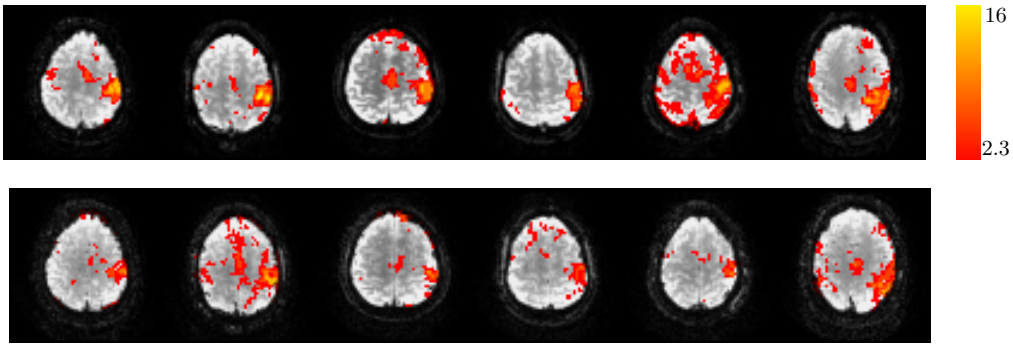

Figure 7.17: Thresholded z-statistic maps, showing voxels with significant changes in BOLD signal in response to the motor task, overlaid on the GE-EPI data from which they were calculated. Maps are shown for each subject acquired with the conventional GE-EPI (top-row) and GE-EPI-XHS (bottom-row) for representative slices though the motor cortex and supplementary motor area.

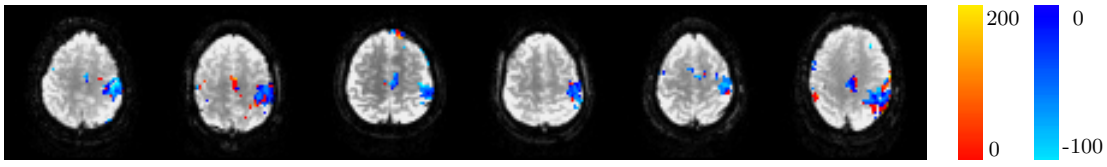

Figure 7.18: Maps of the percentage change in the unthresholded t-statistic between the motor-task FMRI data acquired using conventional GE-EPI and GE-EPI-XHS overlaid on the conventional GE-EPI images. The maps were masked to only show changes in the area with significant BOLD activations in data acquired with both acquisition techniques.

Subject	Mean Change in t-statistic (%)	Mean Change in TSNR (%)
1	-26.4	-12.9
2	-21.5	-29.2
3	-23.6	-10.3
4	-24.6	-13.5
5	-20.7	12.9
6	-8.2	-20.2
Mean	-20.8	-10.5

Table 7.3: Mean percentage change in t-statistic for the motor task and TSNR in the regions of significant BOLD signal change that were common to both data acquired with conventional GE-EPI and GE-EPI-XHS

Measuring BOLD sensitivity via Breath-hold BOLD Signal Changes

The variations in the subjects breathing, throughout the breath-hold FMRI scans, measured using the respiratory bellows, are shown for all six subjects in Figure 7.19. These plots demonstrate that, in general, all subjects performed the breath-hold task as instructed throughout both FMRI acquisitions. The one exception is that subject six appeared to take two small breaths during the penultimate and final breath-hold periods when imaging data were being acquired with the GE-EPI-XHS pulse sequence. The average percentage changes in the grey matter signal as a function of time are shown for each subject in Figure 7.20. These are similar across subjects, however appear noisier for subjects two, three and four. The reason for the differences is unclear, as all subjects appeared to perform the task equally well.

Thresholded z-statistic maps showing voxels with significant changes in BOLD signal as a result of the breath-hold task, for each subject and acquisition method, are shown, for representative slices through the orbitofrontal and inferior temporal regions, in Figures 7.21 and 7.22. Maps of the change in the unthresholded t-statistic (masked to show only regions where the signal increased when GE-EPI-XHS pulse sequence was used) are shown in Figure 7.23. The effect of the GE-EPI-XHS acquisition method is not consistent across the subjects. For subject one, use of GE-EPI-XHS results in a reduction, across the brain, in the number of voxels with statistically significant changes in the BOLD signal in response to the breath-hold task. The unthresholded t-statistic does increase in the orbitofrontal and left inferior temporal regions, however, from the thresholded z-statistic maps, it can be seen that this increase is insufficient for the signal changes to be deemed significant. The maps for subject two show significant BOLD signal changes in the anterior part of the orbitofrontal region, however in the right inferior temporal lobe, where clear recovery of signal is observed statistically significant BOLD signal changes are not seen. For subject three, like subject one, use of GE-EPI-XHS results in a reduction,

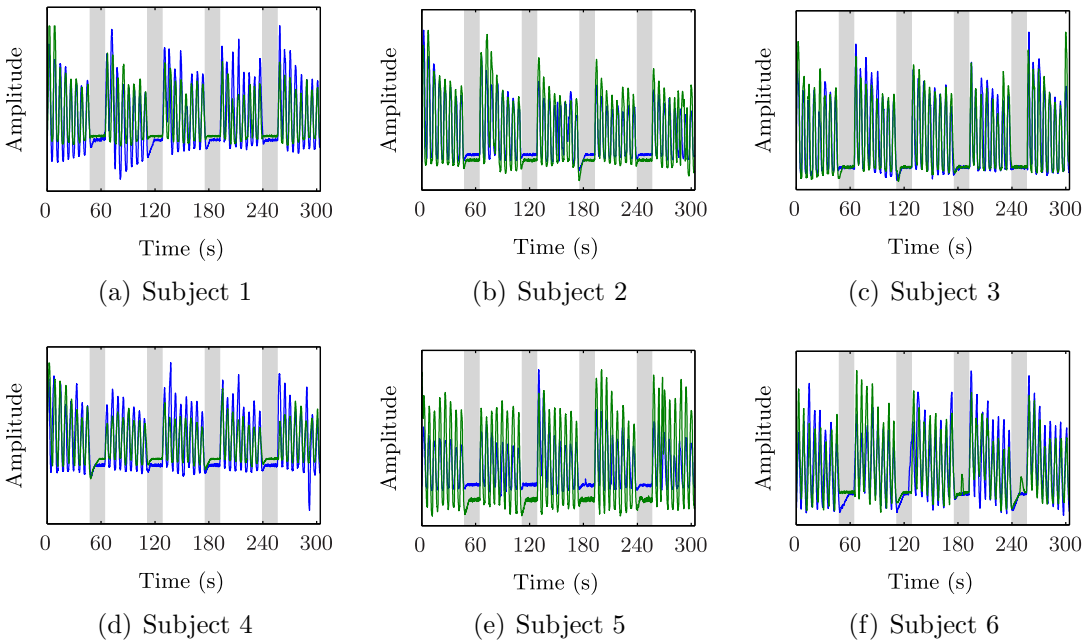

(a) Subject 1 (b) Subject 2 (c) Subject 3

(d) Subject 4 (e) Subject 5 (f) Subject 6

Figure 7.19: Variations in the subjects breathing during acquisition of the breath-hold FMRI data with both conventional GE-EPI (blue line) and GE-EPI-XHS (green line). The shaded grey regions illustrate the periods in which the subject was instructed to hold their breath.

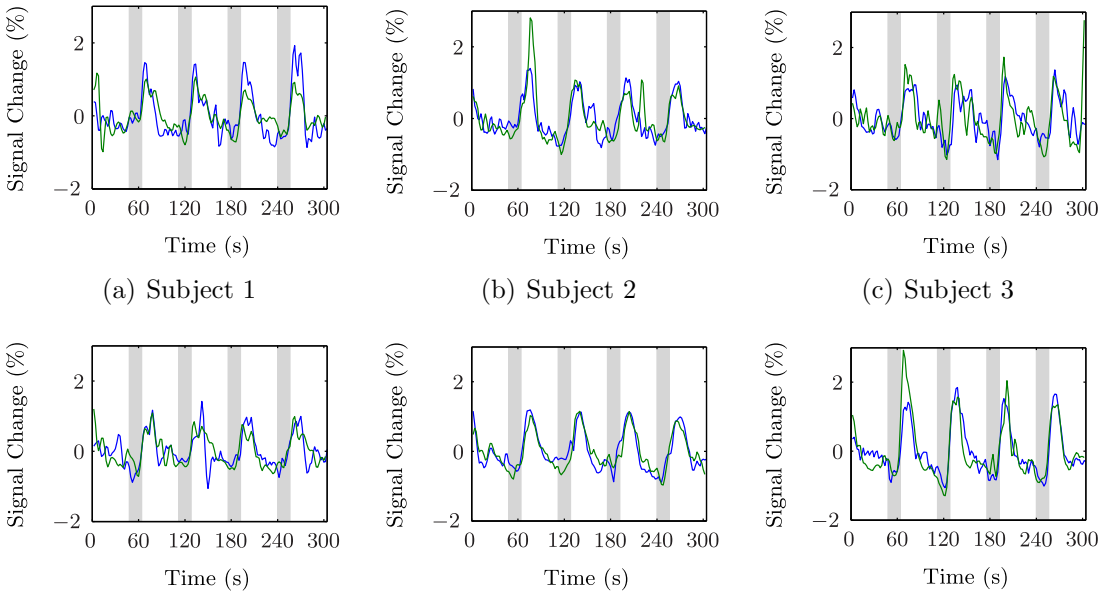

(a) Subject 1 (b) Subject 2 (c) Subject 3

(d) Subject 4 (e) Subject 5 (f) Subject 6

Figure 7.20: The mean percentage change in BOLD signal for grey matter voxels, in response to the breath-hold task for all six subjects for data acquired with conventional GE-EPI (blue-line) and GE-EPI-XHS (green-line). The shaded grey regions illustrate the periods in which the subject was instructed to hold their breath.

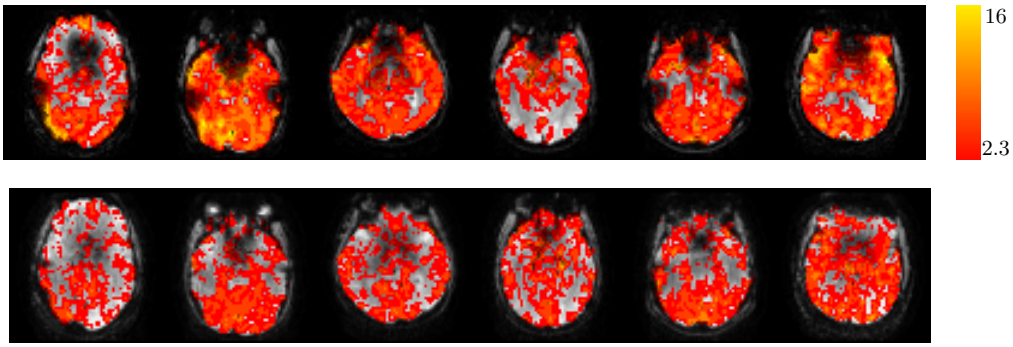

Figure 7.21: Thresholded z-statistic maps, showing voxels with significant changes in BOLD signal in response to the breath-hold task, overlaid on the GE-EPI data from which they were calculated. Maps are shown for each subject acquired with the conventional GE-EPI (top-row) and GE-EPI-XHS (bottom-row) for representative slices though the orbitofrontal cortex.

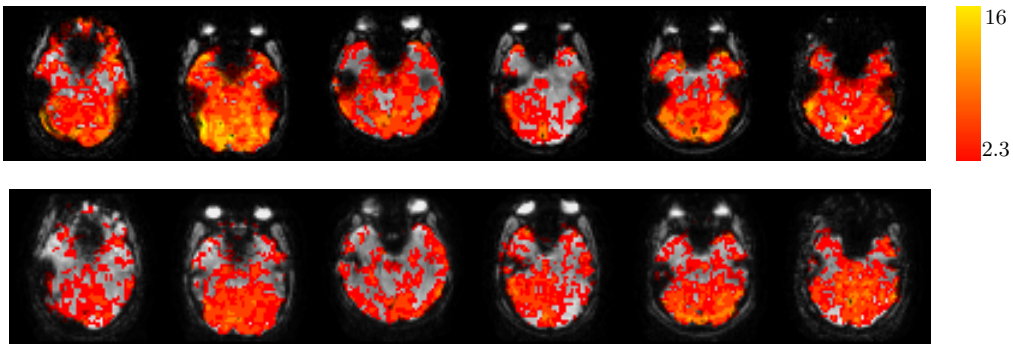

Figure 7.22: Thresholded z-statistic maps, showing voxels with significant changes in BOLD signal in response to the breath-hold task, overlaid on the GE-EPI data from which they were calculated. Maps are shown for each subject acquired with the conventional GE-EPI (top-row) and GE-EPI-XHS (bottom-row) for representative slices though the inferior temporal regions.

across the brain, in the number of voxels with statistically significant changes in the BOLD signal. However, in the regions of signal recovery in the orbitofrontal and inferior temporal regions, statistically significant changes in the BOLD signal in response to the breath-hold task are observed; i.e. the signal increases are matched by increased BOLD sensitivity. For subjects four, five and six, improvements of the signal in the regions of dropout in the orbitofrontal and inferior temporal regions are matched, to a large extent, by increases in the number of voxels in these regions with statistically significant changes in the BOLD signal in response to the breath-hold task.

Detectability of Resting-State FMRI Networks with PICA

The independent components from the probabilistic independent component analyses which visually matched the resting-state networks described in Smith et al. [169]

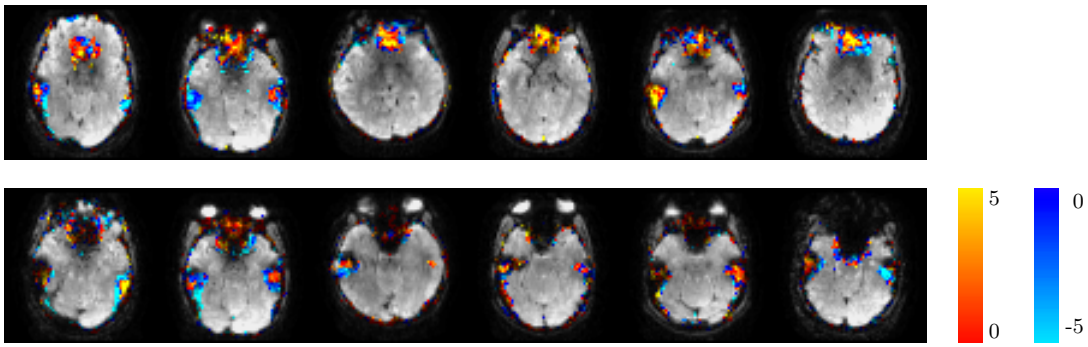

Figure 7.23: Maps of the change in unthresholded t-statistic masked to show only regions where the signal increased when GE-EPI-XHS was used in place of conventional GE-EPI, for all six subjects for representative slices through the orbitofrontal cortex (top row) and the inferior temporal lobes (bottom row).

are shown in Figure 7.24. From the data acquired with conventional GE-EPI only eight of the networks were clearly identified; no component matched the occipital pole visual network and the component that most closely matched the right fronto-parietal network also has nodes in the left frontal and parietal regions. From the data acquired with GE-EPI-XHS the medial and occipital visual networks were combined into a single independent component (Figures 7.24(a) and 7.24(b)). The lateral visual, cerebellar, auditory, executive control and left fronto-parietal networks were observed as separate components from the data acquired with GE-EPI-XHS. None of the independent components from the data acquired with GE-EPI-XHS corresponded to the left fronto-parietal network. The spatial extent of the sensorimotor network was greater in the data acquired with GE-EPI-XHS than with conventional GE-EPI. The default mode network was split into two components, one of which is shown in 7.24(d) and the second of which is shown separately in Figure 7.25.

Detectability of Resting-State FMRI Networks Using Seed Based Analysis

As shown in Figure 7.26, for five of the six subjects, for data acquired with both conventional GE-EPI and GE-EPI-XHS there are significant correlations of the resting-state BOLD signal from a seed in the posterior cingulate with the BOLD signal in the medial prefrontal cortex and the left and right lateral parietal cortex. No significant correlations are observed in the medial prefrontal cortex for data acquired with conventional GE-EPI for subject three. In addition to these significant correlation, which are expected for the default mode network, there are, especially for subjects two, three and four, large numbers of other statistically significant correlations distributed across the brain in the data acquired with GE-EPI-XHS. In subjects one, two, four and six in the region of signal recovery in the orbitofrontal cortex the BOLD

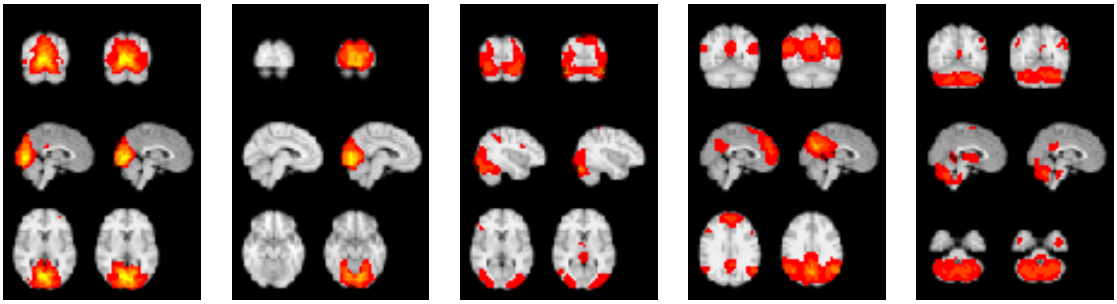

(a) Medial Visual* (b) Occipital Pole Visual* (c) Lateral Visual (d) Default Mode (e) Cerebellar

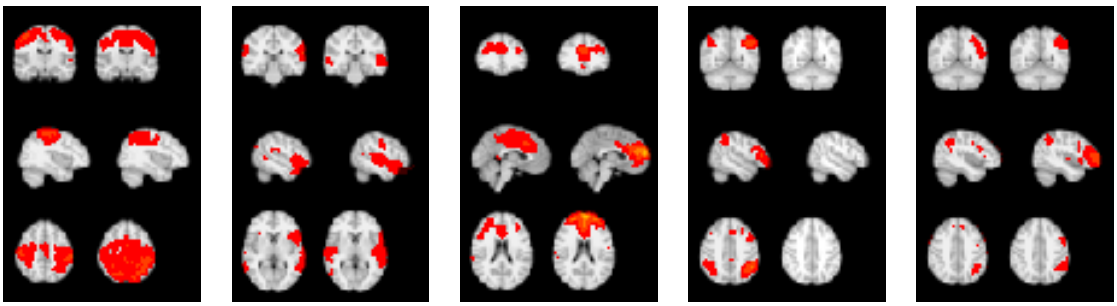

(f) Sensoriomotor (g) Auditory (h) Executive Control (i) Right Fronto-Parietal (j) Left Fronto-Parietal

Figure 7.24: Thresholded z-statistic maps ($3 < z < 22$) for the ten independent components from the probabilistic independent component analyses which visually matched those described in Smith et al. [169]. The three most informative orthogonal slices are shown for each network. The left column in each sub-figure contains independent components from the data acquired using conventional GE-EPI and the right column the components from the GE-EPI-XHS data. The components are shown overlaid on the MNI152 standard space template (re-sampled to 4 mm isotropic voxel size).*The medial and occipital pole visual networks were observed as a single component in the GE-EPI-XHS data.

Figure 7.25: Thresholded z-statistic map showing the second independent component that corresponds to the default mode network in the data acquired with GE-EPI-XHS. The first component corresponding to the default mode network is shown in Figure 7.24(d).

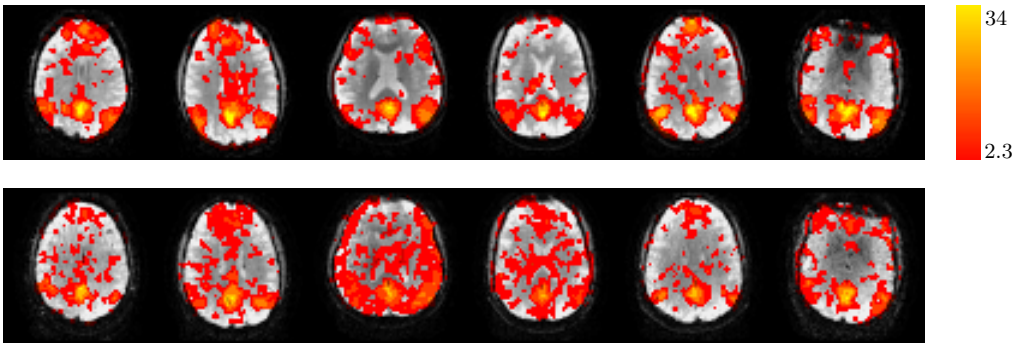

Figure 7.26: Thresholded z-statistic maps, showing voxels in which the resting-state BOLD signal changes were significantly correlated with the signal variation from a seed in the posterior cingulate, for data acquired with the SLR pulse (top-row) and HS pulse (bottom-row). Representative axial slices though posterior cingulate regions are shown for each subject.

signal variations are significantly correlated with the posterior cingulate seed; Figure 7.27. Such significant correlation are not observed in the areas of recovered signal in the inferior temporal lobes; Figure 7.28. Those voxels in which the BOLD signal variations are significantly correlated with resting-state signal changes from a seed in the left motor cortex are shown in Figures 7.29 to 7.31. In all six subjects, in the data acquired with conventional GE-EPI, significant correlations are observed with the right motor cortex and the supplementary motor area. The areas of activation for subjects three, four and five however are large and encompass voxels not in the areas recognised as belonging to the canonical resting state motor network. The patterns of significant correlation are similar for data acquired with GE-EPI-XHS, although for subjects three, four and six the majority of voxels in the slice through the motor cortex are significantly correlated with the seed in the left motor cortex. Significant correlations with the areas of signal recovery in the orbitofrontal and inferior temporal regions are not observed.

7.5.4 Discussion and Conclusions

The experimental results described above highlight the benefits of using the HS secant pulse which was optimised in Chapter 6, in combination with compensatory gradients in the frequency encoding direction. Signal was recovered in the vast majority of voxels in the orbitofrontal region. In the inferior temporal regions, some signal was recovered, however areas of dropout remained in the more medial and anterior regions of the inferior temporal lobes. As well as showing increased signal, the areas with reduced signal dropout also showed increases in TSNR to levels comparable with the rest of the brain. The reduction in signal dropout achieved with GE-EPI-XHS however comes at a cost, firstly it results in a reduction in the

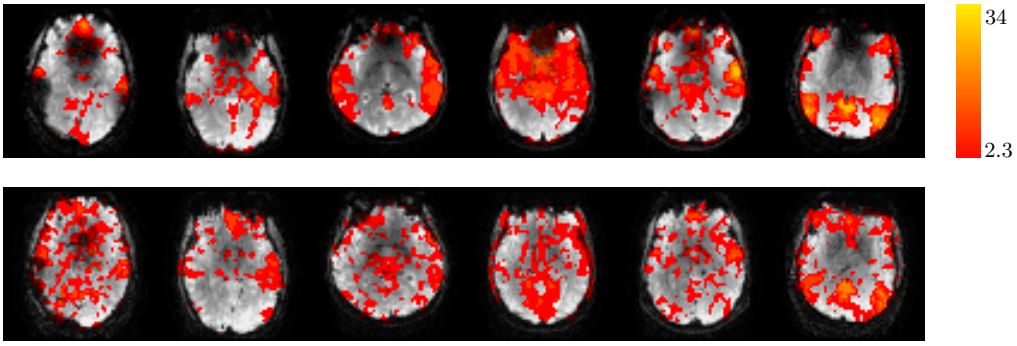

Figure 7.27: Thresholded z-statistic maps, showing voxels in which the resting-state BOLD signal changes were significantly correlated with the signal variation from a seed in the posterior cingulate, for data acquired with the SLR pulse (top-row) and HS pulse (bottom-row). Representative axial slices though the orbitofrontal region are shown for each subject.

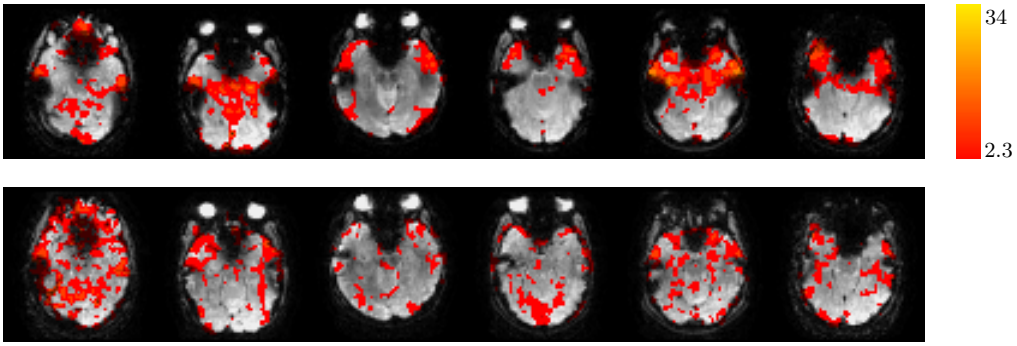

Figure 7.28: Thresholded z-statistic maps, showing voxels in which the resting-state BOLD signal changes were significantly correlated with the signal variation from a seed in the posterior cingulate, for data acquired with the SLR pulse (top-row) and HS pulse (bottom-row). Representative axial slices though inferior temporal regions are shown for each subject.

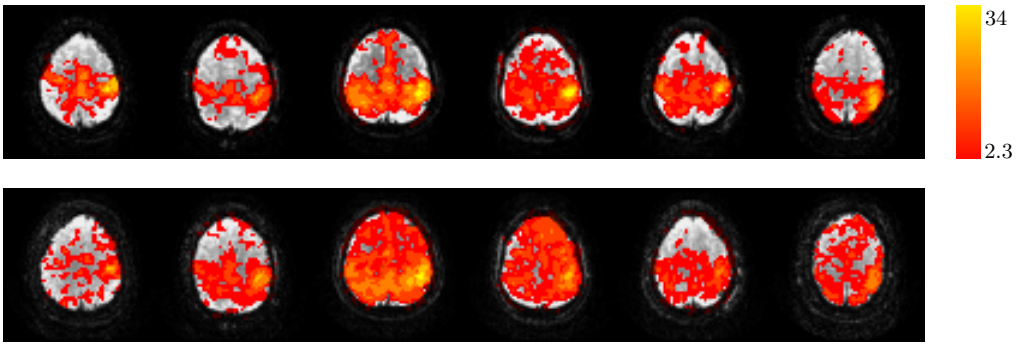

Figure 7.29: Thresholded z-statistic maps, showing voxels in which the resting-state BOLD signal changes were significantly correlated with the signal variation from a seed in the left motor cortex, for data acquired with the SLR pulse (top-row) and HS pulse (bottom-row). Representative axial slices though the left and right motor cortex and supplementary motor area are shown for each subject.

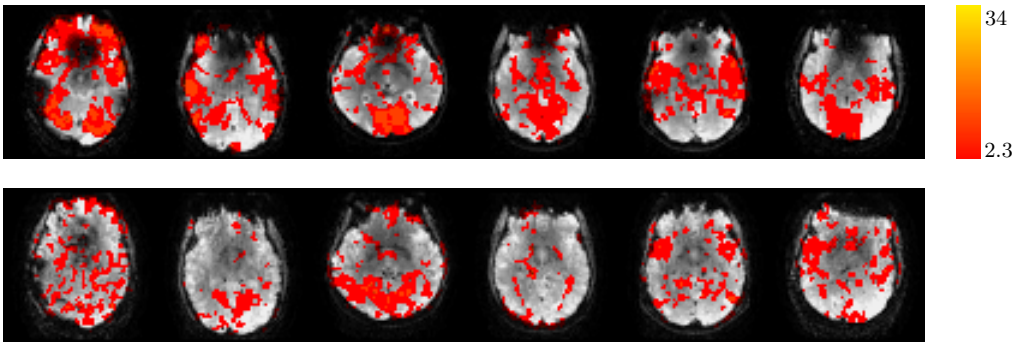

Figure 7.30: Thresholded z-statistic maps, showing voxels in which the resting-state BOLD signal changes were significantly correlated with the signal variation from a seed in the in the left motor area, for data acquired with the SLR pulse (top-row) and HS pulse (bottom-row). Representative axial slices though orbitofrontal region are shown for each subject.

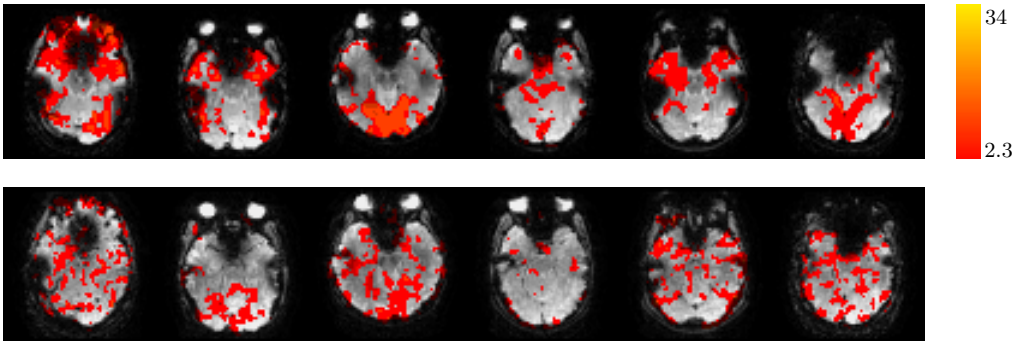

Figure 7.31: Thresholded z-statistic maps, showing voxels in which the resting-state BOLD signal changes were significantly correlated with the signal variation from a seed in the left motor area, for data acquired with the SLR pulse (top-row) and HS pulse (bottom-row). Representative axial slices though inferior temporal regions are shown for each subject.

temporal resolution, and secondly it leads to reductions in the TSNR of up to 60% in the regions unaffected by susceptibility gradients.

The detectability of BOLD signal changes as a result of the motor-task were similar for the two methods of data acquisition. The reduction in TSNR using GE-EPI-XHS, was accompanied by reductions in the unthresholded t-statistic, however these reductions did not mean that activations were no longer statistically significant. This result suggests that the sensitivity to robust BOLD signal changes from a block-design experiment is only moderately reduced. However, as noted previously, it is unclear from this experiment alone whether for other paradigms with smaller BOLD signal changes the TSNR reductions would mean that significant activations would no longer be detected.

The results of the BOLD sensitivity measurements using the breath-hold FMRI experiments are inconsistent across the six subjects tested. In only three of the six subjects were the increases in signal and TSNR, in the regions affected by dropout in conventional GE-EPI images, matched by increases in BOLD sensitivity. In two of the subjects (one and three) a large reduction in the number of voxels with statistically significant BOLD signal changes was observed when the GE-EPI-XHS acquisition method was used. As was the case in Chapter 6, the cause of these inter-subject inconsistencies is currently not understood.

The results of the probabilistic independent component analysis of the data acquired with conventional GE-EPI are not consistent with the previous two chapters. It was previously shown that individual independent components corresponded to the ten networks described in Smith et al. [169], however in this case only eight of the networks were readily identified from amongst the independent components. It is unclear why this would be the case as the same imaging protocol was used on the same six subjects. It is however recognised that when PICA is constrained to find only twenty components it may not converge to a stable solution [169], so the analysis was repeated three times (the results of which were not shown above), in each case only eight networks could be identified from the independent components. For the data acquired with GE-EPI-XHS it was also difficult to identify all ten resting state networks; the medial and occipital pole visual networks were observed as a single component, the default mode network was split across two components and the right fronto-parietal network did not correspond to any of the components. This suggests that the reductions in TSNR may have reduced the ability to detect resting state networks with PICA, however the inconsistent results from the conventional GE-EPI data mean that more work is necessary to confirm and quantify this.

As seen in the previous two chapters, the results of the seed based analyses of the resting state FMRI data suggest that, in four out of the six subjects, the areas of signal recovery in the orbitofrontal cortex may be functionally connected to the

default mode network. It is unclear why this potential functional connection was not observed in the PICA analysis. It would be interesting to repeat the resting state FMRI experiments using GE-EPI-XHS in a larger group of subjects to determine if this is real functional connection and not the result of subject motion or physiological noise.

7.6 Discussion and Conclusions

The effect of combining the optimised hyperbolic secant pulse, described in Chapter 6, with compensation gradients in the phase and frequency encoding directions was investigated for the first time. It was shown that the areas of remaining signal dropout when the HS pulse was used alone could be corrected by combining images acquired with twenty five combinations of in-plane compensatory gradients. Because this would cause a large reduction in the temporal resolution, and thus make the technique unusable for FMRI experiments, combinations of smaller number of images were investigated. It was found that combining five images with varying compensation gradients in the frequency encoding direction recovered a large amount of the signal dropout.

Further to this, it was shown that by combining only two images acquired with $\delta k_{x,sh} = \frac{-3}{10\Delta x}$ and $\frac{3}{10\Delta x}$ the signal dropout was reduced compared to using the optimised HS pulse alone. In the case that the subject's head is positioned such that the line intersecting the anterior and posterior commissure is in the axial plane of the scanner, the optimal slice angle for signal recovery (for the protocol described earlier) in the orbitofrontal cortex was shown to be 90° (i.e. in the axial plane of the scanner). The optimal angle for recovery in the inferior temporal lobes was 80° (i.e. tilted forward by 10° from the axial plane).

The series of experiments performed on the six healthy volunteers showed that the improvements in signal in the regions of dropout translated to improvements in TSNR when the GE-EPI-XHS acquisition method was used. However, this was accompanied by reductions of up to 60% in the TSNR in regions of homogeneous field. In areas unaffected by susceptibility gradients, such as the motor cortex, this TSNR reduction caused a small decrease in the sensitivity to task induced BOLD signal changes. The changes in BOLD sensitivity across all grey matter voxels as measured using breath-hold FMRI were inconsistent. In half the subjects, the BOLD sensitivity increased in the areas of recovered signal in the orbitofrontal and inferior temporal regions. Repeating these experiments, in a larger group of subjects may help to clarify if GE-EPI-XHS can reliably improve BOLD sensitivity in regions obscured by dropout in conventional GE-EPI datasets.

The results of the PICA and seed based analyses of the resting state FMRI

data were inconsistent. The PICA analysis suggested that it was more difficult to detect resting state networks from data acquired with GE-EPI-XHS, however, the seed based analysis showed an additional functional connection between the area of recovered signal in the orbitofrontal cortex and the default mode network. Again, it would be useful to extend the current experiments, acquiring data from a greater number of subjects to confirm the effect of GE-EPI-XHS on the detectability of resting state networks.

It would be interesting to extend this work by altering the compensatory gradients on a slice by slice basis as in a recent previous study[125]. This would require the acquisition of a field map such that the gradients could be optimised for each slice. It would offer the potential to recover signal in a single step, thus not affecting the temporal resolution. This could be beneficial for both resting state and event related studies where the rapid sampling of the signal is important.

Chapter 8

Conclusions and Further Work

Functional magnetic resonance imaging (FMRI) data acquired using gradient-echo echo-planar imaging (GE-EPI) suffer from signal dropout in the orbitofrontal cortex (OFC) and inferior temporal lobes (ITL) caused by susceptibility induced magnetic field gradients in the slice-selection, phase and frequency encoding directions. A number of different techniques have been developed to correct this problem, all of which have different pros and cons. The work presented in this thesis aimed to build on several of these existing approaches. Three techniques were developed to increase the sensitivity of GE-EPI to blood oxygen level dependent (BOLD) signal changes in the regions affected by signal dropout whilst retaining as much sensitivity as possible in other parts of the brain.

Initially, a theoretical model and numerical simulations were used to determine the improvements in signal to noise ratio (SNR) necessary to increase the detectability of BOLD signal changes in low signal regions. By combining the model of Smith et al. [256] with the physiological noise model of Kruger and Glover [261], it was shown that the t-statistic resulting from a GLM analysis of task-based FMRI data does not linearly increase with the SNR. Rather, the rate of increase reduces until the t-statistic reaches a plateau. In addition, for a given FMRI paradigm, the model implies that there is a minimum percentage BOLD signal change below which, irrespective of the SNR, activations will never be deemed statistically significant at the voxel level. Numerical simulations of both task-based and resting-state FMRI data showed that the dependence of the observed power on the SNR followed a sigmoid shaped curve. This suggested that moderate increases in SNR could lead to large increases in the detectability of resting-state and task-induced BOLD signal changes, motivating the development of techniques which reduce signal dropout.

Three different techniques were then developed, the first, described in Chapter 5, built on the z-shimming technique [27] which reduces the dropout caused by *through-plane* susceptibility gradients. In a number of different implementations, it has been shown to increase the detectability of task-induced [72, 271, 273–275]

and resting-state [299] BOLD signal changes in the regions of signal dropout. The second, described in Chapter 6, was an optimised implementation of the tailored radiofrequency (TRF) pulse [30, 126] approach which, like z-shimming, reduces the dropout caused by *through-plane* susceptibility gradients. The third, described in Chapter 7, combined the TRF pulse from Chapter 6 with compensatory gradients in the frequency encoding direction to correct much of the dropout caused by both *in-plane* and *through-plane* susceptibility gradients.

The z-shimming approach was based on the acquisition of two images with different compensatory gradients in the slice-selection direction which were then combined by SSQ [271, 274]. A novel aspect of this work was that in contrast to previous methods, the algorithm to determine the slice specific pairs of z-shims aimed to recover signal in only those voxels containing *grey matter* - the origin of BOLD signal changes. This modification required the acquisition of a DIR-EPI image, which was thresholded and binarised to produce a grey matter mask. A second difference from previous studies [74, 274, 288] was that the optimal difference between the z-shim gradients was determined by numerical simulations of the Bloch equations for the specific RF pulse and slice-selection gradient used by the MR system. This modification was needed because theoretical predictions of the dependence of the signal on the through-plane susceptibility gradient assume that the slice profile is perfectly rectangular [74] which is not true in practice. Programs to perform Bloch simulations are widely available so it would be straightforward to replicate this optimisation for the RF pulses and gradients used for slice selection by other MR scanners. The algorithm to determine the slice specific pairs of z-shim gradients was implemented in C++ so it could be run on the scanner itself. In total, the acquisition of the calibration scan and DIR-EPI image and the calculation of the optimal z-shim gradients took 4 minutes and 23 seconds. The impact of two-step grey matter optimised z-shimming was then assessed in a group of six healthy male volunteers. The technique resulted in increases in both the signal and temporal signal to noise ratio (TSNR) in large parts of the orbitofrontal and inferior temporal regions that are obscured by dropout in conventional GE-EPI images. For all six subjects, greater signal recovery was achieved when grey matter masking was included in the algorithm to determine the optimal slice specific pair of z-shim gradients. In addition, the improvements in TSNR were accompanied by increases in the BOLD sensitivity. In agreement with a previous finding [299], a seed based analysis of the resting state data suggested that parts of the orbitofrontal cortex, which are obscured by signal dropout in conventional GE-EPI images, were functionally connected to the default mode network. However, additional work is needed, in a greater number of subjects, to determine if this is a genuine effect as this connection was not seen in the probabilistic independent component analysis (PICA) of the

same data. In addition, the PICA analysis showed that two of the resting state networks described by Smith et al. [169] were combined into a single independent component. This could be a result of a loss in temporal resolution or changes in the temporal smoothness of the data caused by the SSQ combination of pairs of images, but further work is needed to understand this observation.

In an effort to avoid the loss of temporal resolution, a hyperbolic secant (HS) radiofrequency pulse was developed to correct dropout without the need to combine two volumes of data. This work built upon previous experiments using tailored RF pulses [30, 126, 132]. A systematic approach was developed that can be used to design HS pulses based on the desired slice thickness and echo time, as well as the hardware constraints of the MRI system. Bloch simulations were used to determine the HS pulse parameters required to produce a uniform signal response across the range of susceptibility gradients typically present in the head, as the previous theoretical model [126] was shown to be inaccurate. An expression was derived for the bandwidth of a HS pulse (when used for signal excitation), which enabled the amplitude of the slice selection gradient to be calculated correctly. Using the same battery of tests and the same six volunteers as above it was shown that signal was recovered in similar regions as with the z-shimming approach. However the improvements in TSNR were not as large and they came at the cost of up to 60% losses in TSNR in regions of homogeneous field. In addition, the changes in BOLD sensitivity were inconsistent across the six subjects; in two subjects the improvements in signal and TSNR were not matched by increases in BOLD sensitivity, however, in the remaining four subjects promising improvements were observed. The impact of the HS pulse on resting-state FMRI data differed with the method of data analysis. With PICA it became harder to identify the resting-state networks described by Smith et al. [169] from amongst the components. Promisingly, however the results of the seed based analysis were in agreement with those using z-shimmed data; significant correlations were observed between the region of recovered signal in the orbitofrontal cortex and the default mode network in all six subjects. In contrast to z-shimming, this approach was not subject specific and therefore it did not require the acquisition of either a calibration scan or DIR-EPI image. However, the pulse was designed specifically for a given slice thickness and flip angle (chosen to maximise the steady state signal based on the TR required and the T_1 of grey matter). As it stands, for this technique to be applied more widely a library of pulses would therefore need to be produced that could be used with different acquisition protocols. One potential extension of the current technique would be to use slice specific RF pulses. At its simplest this would mean using a conventional RF pulse in the more superior slices in the brain, since these are generally free from signal dropout, and the HS pulse in the inferior slices. A second possible improvement would be a HS pulse designed to

have a uniform, but greater, signal over a smaller range of susceptibility gradients. This would potentially reduce the losses in TSNR and BOLD sensitivity across the whole brain and could be achieved by using a smaller μ, as shown in Figure 6.14(a). On its own, this may reduce the signal recovery in the OFC and ITL, however when combined with a slice specific z-shim gradient, which would modify the range of susceptibility gradients over which signal is uniform, similar levels of signal recovery in regions affected by dropout may be possible.

Finally, the effects of combining the optimised hyperbolic secant pulse with compensation gradients in the phase [28] and frequency encoding directions [29] was explored for the first time. In a preliminary experiment it was shown that a combination of twenty five images acquired with different in-plane compensatory gradients could correct almost all the remaining areas of signal dropout. Since this would not be practical in FMRI, an approach combining just two images, acquired with different compensation gradients in the frequency encoding direction, was explored. For the imaging protocol described in Chapter 7, this increased signal recovery in a greater number of voxels than the optimised HS pulse alone. Using the same battery of tests, and the same six volunteers as previously, it was shown that the improvements in signal in the regions of dropout were translated to improvements in TSNR. However, this was again accompanied by reductions of up to 60% in the TSNR in regions of homogeneous field. In areas unaffected by susceptibility gradients, such as the motor cortex, this TSNR reduction caused a small decrease in the sensitivity to task induced BOLD signal changes. Similar to when the HS pulse was used without correction for in-plane susceptibility gradients, the changes in BOLD sensitivity were inconsistent across subjects; increases in the areas of recovered signal were only observed in half the subjects tested. In addition, the results of the PICA and seed based analyses of the resting state FMRI data were inconsistent. The PICA analysis suggested that it was more difficult to detect resting state networks. However, in agreement with the seed based analyses carried out on the data acquired with z-shimming and the HS pulse alone, a potential functional connection between the area of recovered signal in the orbitofrontal cortex and the default mode network was found. Given that susceptibility gradients in the frequency encoding direction vary across the brain it would be interesting to explore the potential benefits of altering the compensatory gradients on a slice-by-slice basis with the aim of recovering signal in a greater number of voxels. This would require the acquisition of a field map; however, it offers the potential to recover signal without the need to acquire and combine two images [125], which could widen its application to event related FMRI studies where temporal resolution is important.

One potential area that has not been explored previously would be to analyse data acquired in two steps (i.e. from the approaches using z-shimming or compen-

sation gradients in the frequency encoding direction) without combining the pairs of images by SSQ, which inherently affects the data's temporal smoothness. This could result in inappropriate statistical inferences depending on the analysis package and options used. Instead, it may be possible to analyse the raw data with an additional regressor in the design matrix to account for the alternating changes in signal between the images. This may improve the sensitivity of the analysis to BOLD signal changes.

In their current implementations, the techniques described above are suitable for different types of FMRI experiment. Z-shimming recovers signal, TSNR and BOLD sensitivity in the OFC and ITL without losses in the rest of the brain. It could therefore be used to investigate the functions of the OFC and ITL with block-design paradigms; however the lower temporal resolution makes it unsuitable for studies with event-related designs and may make the detection of resting state networks more problematic. The HS pulse approach, is more suited to event related designs as well as resting-state FMRI as it does not cause a loss of temporal resolution, however larger group sizes and/or longer acquisitions may be needed to overcome the resulting global reduction in signal. Finally, the combination of the HS pulse and compensation gradients in the frequency encoding direction recovers signal from the greatest number of voxels, so it would be useful tool for investigating the functions of the OFC and ITL with block-design paradigms; as with the HS pulse longer acquisitions and/or larger group sizes may be needed because of the signal reduction.

So that all three new acquisition approaches can be qualitatively compared, representative slices through the orbitofrontal and inferior temporal regions of images from all six subjects are shown together in Figures 8.1 and 8.2.

8.0.1 Summary of Main Contributions

In summary, the research presented in this thesis has contributed the following developments to the field:

- A theoretical model, explicitly incorporating the effect of physiological noise, to determine the improvements in the signal-to-noise ratio needed to detect BOLD signal changes in the areas of GE-EPI images affected by signal dropout.

- An automated method to determine the slice-specific pairs of z-shim gradients that recover signal in voxels containing grey matter that are affected by signal dropout, whilst maintaining signal in regions of homogeneous field.

- A method for optimising the parameters of a hyperbolic secant radiofrequency excitation pulse for the recovery of signal in brain regions affected by through-plane susceptibility gradients.

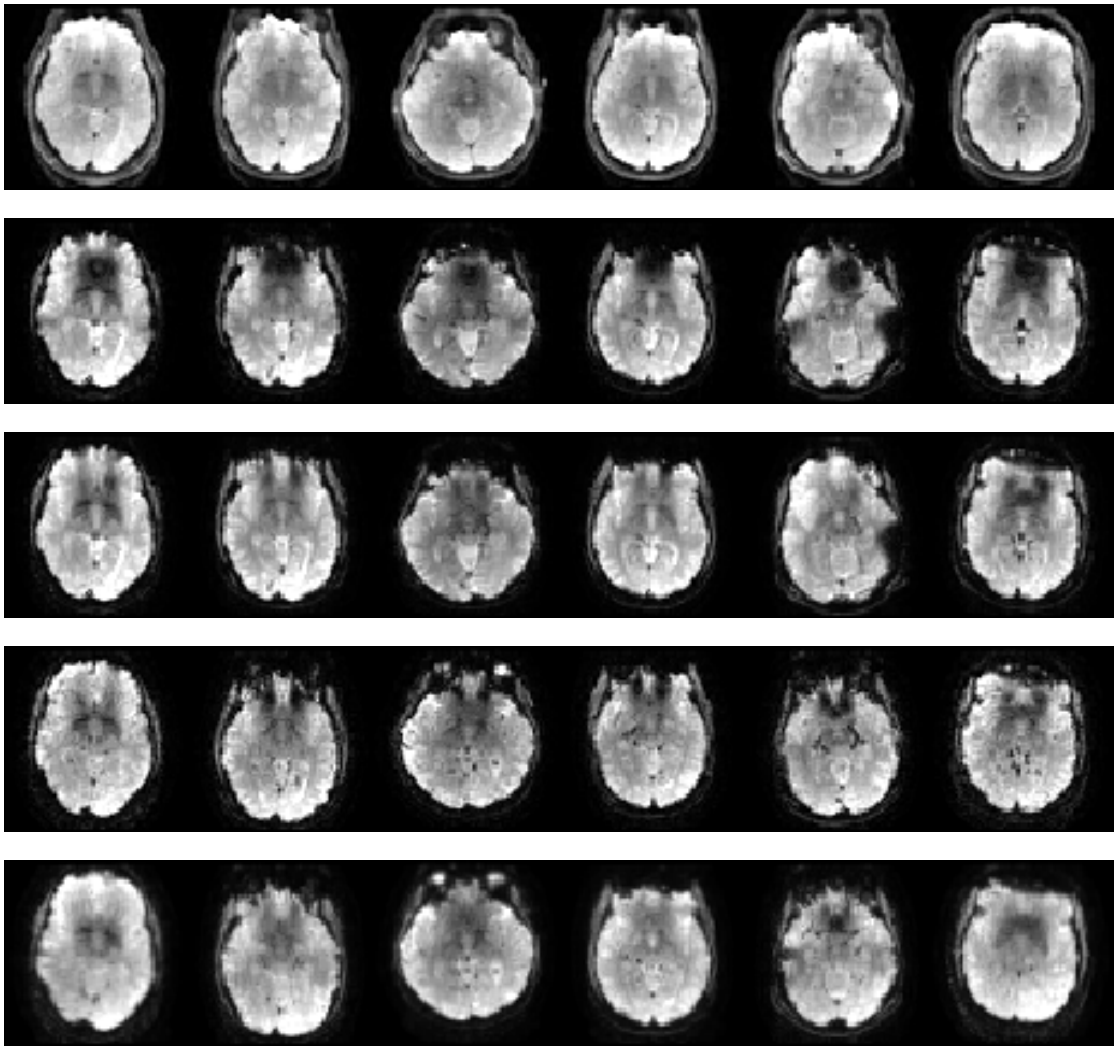

Figure 8.1: Representative slices through the orbitofrontal cortex of the six subjects from images acquired with SE-EPI (first-row), GE-EPI with the conventional SLR excitation pulse (second-row), z-shimmed GE-EPI (third-row), GE-EPI with the HS pulse (forth-row) and GE-EPI-XHS (fifth-row). The intensity range was chosen on a per subject and per acquisition basis such that the areas of signal dropout and recovery could be readily appreciated.

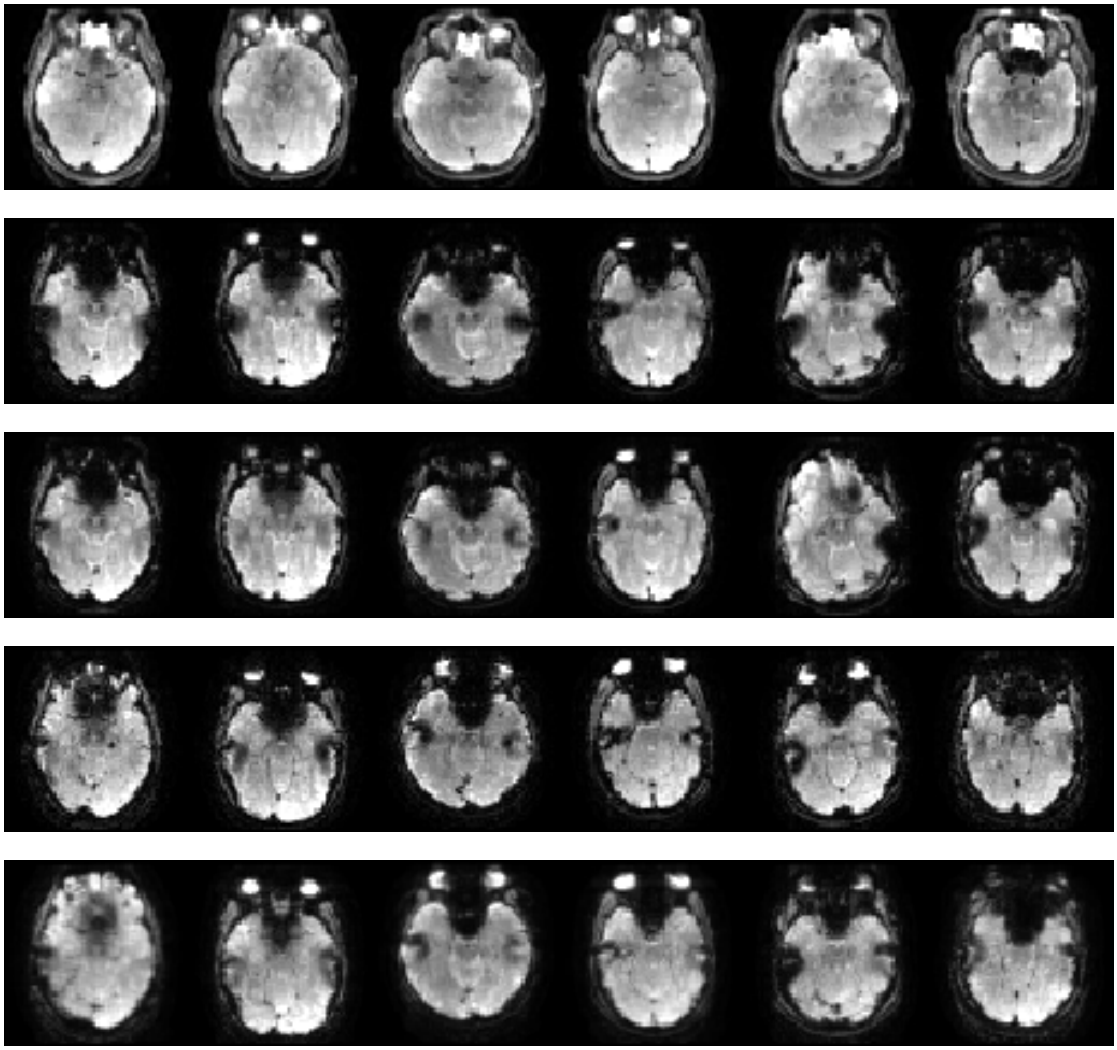

Figure 8.2: Representative slices through the inferior temporal lobes of the six subjects from images acquired with SE-EPI (first-row), GE-EPI with the conventional SLR excitation pulse (second-row), z-shimmed GE-EPI (third-row), GE-EPI with the HS pulse (forth-row) and GE-EPI-XHS (fifth-row). The intensity range was chosen on a per subject and per acquisition basis such that the areas of signal dropout and recovery could be readily appreciated.

- An approach for correcting dropout caused by both through-plane and in-plane susceptibility gradients by combining the hyperbolic secant radiofrequency excitation pulse with compensatory gradients in the frequency encoding direction.

Appendix A

A Derivation of the Artefacts in Gradient Echo EPI Images Caused by Magnetic Field Inhomogeneities

A.1 The GE-EPI Signal

Using the notation of Farzaneh et al. [68] the signal for the n^{th} phase encoding line measured during a GE-EPI acquisition of an object $\rho(x, y)$ with an $N_x \times N_y$ acquisition matrix, $L_x \times L_y$ field of view is:

$$s_n(t) = \int_{\frac{-L_y}{2}}^{\frac{L_y}{2}} \int_{\frac{-L_x}{2}}^{\frac{L_x}{2}} \rho(x, y) e^{-i\gamma G_x x t} e^{-i\gamma H_n y} \mathrm{d}x\mathrm{d}y \tag{A.1}$$

Here x corresponds to the frequency encoding (or readout) direction and y to the phase encoding direction. n is an integer in the range $-N_y/2 \leq n < N_y/2$, G_x is the amplitude of the readout gradient lobes, H_n is the total area of the gradients in the y-direction prior to the acquisition of the n^{th} phase encoding line and $-T_s/2 \leq t < T_s/2$. Rewriting the phase-encoding gradient area H_n as a function of the phase encoding line number n, i.e. $H_n = G_y n T'$ where T' is the inter-echo spacing ($T' = T_s + \tau_{pe}$) and G_y is the change in phase-encoding gradient between each phase encode line ($G_y = A_{pe}/T' = 2\pi/\gamma L_y T'$):

$$s_n(t) = \int_{\frac{-L_y}{2}}^{\frac{L_y}{2}} \int_{\frac{-L_x}{2}}^{\frac{L_x}{2}} \rho(x, y) e^{-i\gamma G_x x t} e^{-i\gamma G_y n T' y} \mathrm{d}x\mathrm{d}y \tag{A.2}$$

The signal is sampled at discrete time points $m\Delta t$ (where $-N_x/2 \leq m < N_x/2$) therefore the digitised signal is:

$$s_{nm} = \int_{\frac{-L_y}{2}}^{\frac{L_y}{2}} \int_{\frac{-L_x}{2}}^{\frac{L_x}{2}} \rho(x,y) e^{-i\gamma G_x x m\Delta t} e^{-i\gamma G_y n T' y} \mathrm{d}x\mathrm{d}y \tag{A.3}$$

Incorporating the effect of signal decay (assuming that T_2^* does not vary with position) :

$$s_{nm} = e^{-\left(TE+nT'+(-1)^{(n+N_y/2)}m\Delta t\right)/T_2^*} \int_{\frac{-L_y}{2}}^{\frac{L_y}{2}} \int_{\frac{-L_x}{2}}^{\frac{L_x}{2}} \rho(x,y) e^{-i\gamma G_x x m\Delta t} e^{-i\gamma G_y n T' y} \mathrm{d}x\mathrm{d}y \tag{A.4}$$

Where TE is the echo time as entered on the scanner console. Alternate phase encoding lines are traversed in opposite directions, accounted for by the term $(-1)^{(n+N_y/2)}$ which is positive for the odd phase encoding lines when k-space is sampled from bottom-left to top-right [68]. For compactness R_{nm} is defined as:

$$R_{nm} \equiv e^{-\left(TE+nT'+(-1)^{(n+N_y/2)}m\Delta t\right)/T_2^*} \tag{A.5}$$

Therefore:

$$s_{nm} = R_{nm} \int_{\frac{-L_y}{2}}^{\frac{L_y}{2}} \int_{\frac{-L_x}{2}}^{\frac{L_x}{2}} \rho(x,y) e^{-i\gamma G_x x m\Delta t} e^{-i\gamma G_y n T' y} \mathrm{d}x\mathrm{d}y \tag{A.6}$$

A.2 The Effect of Magnetic Field Inhomogeneities

In the presence of a magnetic field offset $\Delta B(x,y)$, the digitised signal becomes:

$$s_{nm} = R_{nm} \int_{\frac{-L_y}{2}}^{\frac{L_y}{2}} \int_{\frac{-L_x}{2}}^{\frac{L_x}{2}} \rho(x,y) e^{-i\gamma G_x x m\Delta t} e^{-i\gamma G_y n T' y} e^{-i\gamma \Delta B(x,y)(nT'+(-1)^{(n+N_y/2)}m\Delta t+TE)} \mathrm{d}x\mathrm{d}y \tag{A.7}$$

After collecting up like terms in the exponentials:

$$s_{nm} = R_{nm} \int_{\frac{-L_y}{2}}^{\frac{L_y}{2}} \int_{\frac{-L_x}{2}}^{\frac{L_x}{2}} \rho(x,y) e^{-i\gamma G_x m\Delta t\left(x+(-1)^{(n+N_y/2)}\frac{\Delta B(x,y)}{G_x}\right)} e^{-i\gamma G_y n T'\left(y+\frac{\Delta B(x,y)}{G_y}\right)} e^{-i\gamma \Delta B(x,y) TE} \mathrm{d}x\mathrm{d}y \tag{A.8}$$

Farzaneh et al. [68] showed that a magnetic field offset $\Delta B(x,y) = \alpha + \beta x$, which represents a constant field offset α from for example the chemical shift of lipids, and a magnetic field gradient from for example susceptibility differences across the

object results in images with shifts due to the constant field offset and geometric distortions due to the field gradient. Their derivation can be extended to account for susceptibility gradients in both the x- and y-directions $G_{x,s}$ and $G_{y,s}$ as well as a constant field offset α i.e. $\Delta B(x,y) = \alpha + G_{x,s}x + G_{y,s}y$ (assuming the gradients and field offset do not vary with position). In this case the digitised signal becomes:

$$s_{nm} = R_{nm} \int_{\frac{-L_y}{2}}^{\frac{L_y}{2}} \int_{\frac{-L_x}{2}}^{\frac{L_x}{2}} \rho(x,y) e^{-i\gamma G_x m \Delta t \left(x + (-1)^{(n+N_y/2)} \frac{\alpha + G_{x,s}x + G_{y,s}y}{G_x}\right)} e^{-i\gamma G_y n T' \left(y + \frac{\alpha + G_{x,s}x + G_{y,s}y}{G_y}\right)} e^{-i\gamma(\alpha + G_{x,s}x + G_{y,s}y)TE} \mathrm{d}x\mathrm{d}y \quad \text{(A.9)}$$

Performing a change of variables, from $x \to x'$ and $y \to y'$ using:

$$y' = y + \frac{\alpha + G_{x,s}x + G_{y,s}y}{G_y} \quad \text{(A.10)}$$

$$x' = x + (-1)^{(n+N_y/2)} \frac{\alpha + G_{x,s}x + G_{y,s}y}{G_x} = x \quad \text{(A.11)}$$

Where the approximation $x = x'$ is valid because α/G_x, $G_{x,s}/G_x$ and $G_{y,s}/G_x$ are typically small. The digitised signal is:

$$s_{nm} = \frac{R_{nm}}{\lambda_y} \int_{\frac{-L_y}{2}}^{\frac{L_y}{2}} \int_{\frac{-L_x}{2}}^{\frac{L_x}{2}} \rho\left(x', \frac{y'}{\lambda_y} - \frac{\alpha + G_{x,s}x'}{\lambda_y G_y}\right) e^{-i\gamma G_x m \Delta t x'} e^{-i\gamma G_y n T' y'} e^{-i\gamma \left(\alpha + G_{x,s}x' + \frac{G_{y,s}\left(y' - \frac{\alpha + G_{x,s}x'}{G_y}\right)}{\lambda_y}\right) TE} \mathrm{d}x'\mathrm{d}y' \quad \text{(A.12)}$$

Here $\lambda_y \equiv 1 + \frac{G_{y,s}}{G_y}$. To simply further the third exponential term can be expanded into terms in x', y' and α:

$$\begin{aligned} & e^{-i\gamma\alpha TE} e^{-i\gamma G_{x,s}x' TE} e^{-i\gamma \frac{G_{y,s}y'}{\lambda_y} TE} e^{i\gamma \frac{G_{y,s}\alpha}{G_y \lambda_y} TE} e^{i\gamma \frac{G_{y,s}G_{x,s}x'}{G_y \lambda_y} TE} \\ &= e^{-i\gamma G_{x,s}x' TE\left(1 - \frac{G_{y,s}}{G_y\lambda_y}\right)} e^{-i\gamma \frac{G_{y,s}y'}{\lambda_y} TE} e^{-i\gamma\alpha TE\left(1 - \frac{G_{y,s}}{G_y\lambda_y}\right)} \\ &= e^{-i\gamma \frac{G_{x,s}x' TE}{\lambda_y}} e^{-i\gamma \frac{G_{y,s}y'}{\lambda_y} TE} e^{-i\gamma \frac{\alpha TE}{\lambda_y}} \end{aligned} \quad \text{(A.13)}$$

When this is substituted in the equation for s_{nm} the digitised signal becomes:

$$s_{nm} = \frac{R_{nm} e^{-i\gamma \frac{\alpha TE}{\lambda_y}}}{\lambda_y} \int_{\frac{-L_y}{2}}^{\frac{L_y}{2}} \int_{\frac{-L_x}{2}}^{\frac{L_x}{2}} \rho\left(x', \frac{y'}{\lambda_y} - \frac{\alpha + G_{x,s}x'}{\lambda_y G_y}\right) e^{-i\left(\gamma G_x m \Delta t + \frac{\gamma G_{x,s} TE}{\lambda_y}\right)x'} e^{-i\left(\gamma G_y n T' + \frac{\gamma G_{y,s} TE}{\lambda_y}\right)y'} \mathrm{d}x'\mathrm{d}y' \quad \text{(A.14)}$$

The exponential terms can be re-expressed in terms of k_x and k_y by recognising that:

$$\gamma G_x m \Delta t = 2\pi k_{x,m} \tag{A.15}$$

$$\gamma G_y n T' = 2\pi k_{y,n} \tag{A.16}$$

It is then evident that the following terms represent shifts of the echo in k-space $\delta k_{x,s}$ and $\delta k_{y,s}$ caused by susceptibility gradients in the frequency and phase encoding directions:

$$\frac{\gamma G_{x,s} TE}{\lambda_y} = 2\pi \delta k_{x,s} \tag{A.17}$$

$$\frac{\gamma G_{y,s} TE}{\lambda_y} = 2\pi \delta k_{y,s} \tag{A.18}$$

The k-space shift of the signal in the frequency encoding direction, given by Equation A.17, agrees with the result previously shown by Weiskopf et al. [29]. Using these definitions the final expression for the digitised signal is:

$$s_{nm} = \frac{R_{nm} e^{-i\gamma \frac{\alpha TE}{\lambda_y}}}{\lambda_y} \int_{\frac{-L_y}{2}}^{\frac{L_y}{2}} \int_{\frac{-L_x}{2}}^{\frac{L_x}{2}} \rho\left(x', \frac{y'}{\lambda_y} - \frac{\alpha + G_{x,s} x'}{\lambda_y G_y}\right) e^{-2\pi i (k_{x,m} + \delta k_{x,s}) x'} e^{-2\pi i (k_{y,n} + \delta k_{y,s}) y'} \mathrm{d}x' \mathrm{d}y' \tag{A.19}$$

The consequences of each factor contributing to the B_0 inhomogeneity are most easily understood by considering each in turn, as described below.

A.2.1 The Effect of a Constant Magnetic Field Offset

If the B_0 inhomogeneity is a constant field offset, $\Delta B(x, y) = \alpha$, caused by the chemical shift of lipids then the signal is simply translated by α / G_y in the y-direction. For example, the chemical shift of fat relative to water is 3.5 ppm, at 3 T corresponds to a field offset $\alpha = 10.5$ μT. For an image with a 25 cm field of view acquired with an inter-echo spacing $T' = 700$ μs the translation of the lipid signal in the phase encoding direction is:

$$\frac{\alpha}{G_y} = \frac{\alpha}{\pm 2\pi / \gamma \left(25 \times 10^{-2}\right) \left(7 \times 10^{-4}\right)} = \pm 7.8\,\mathrm{cm} \tag{A.20}$$

The relationship between the phase encoding gradient G_y, the field of view L_y and the inter-echo spacing T' is:

$$G_y = \varepsilon \frac{2\pi}{\gamma L_y T'} \tag{A.21}$$

Here $\varepsilon = \pm 1$ is a factor to account for the polarity of G_y. It is negative if k-space is traversed from k_y to $-k_y$ and positive if from $-k_y$ to k_y, i.e. the direction

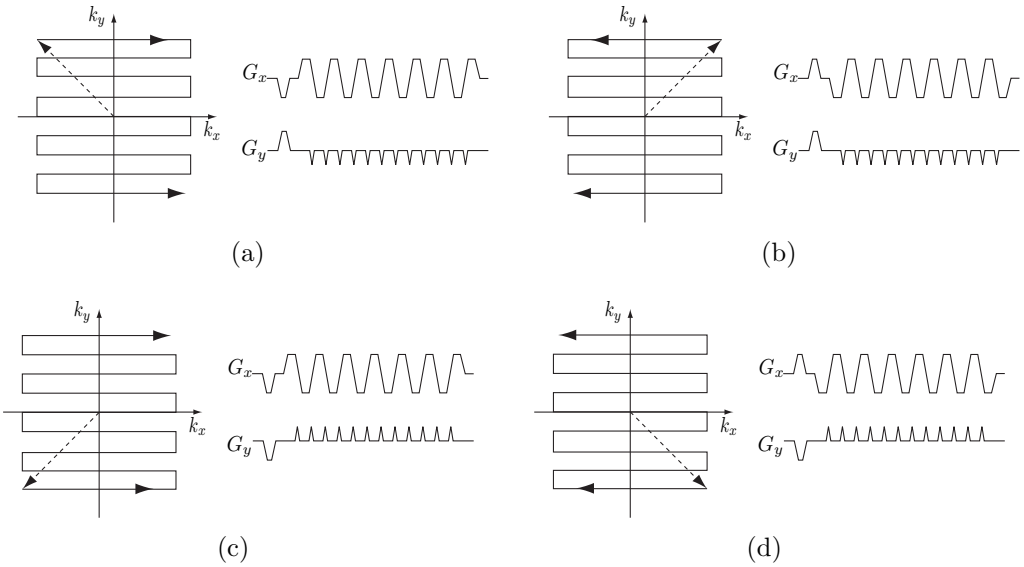

Figure A.1: Gradient-echo EPI k-space trajectories

of the shift depends upon the relative polarities of the field offset α and the phase encoding gradient G_y. The four possible directions in which k-space can be traversed are shown in Figure A.1.

A.2.2 The Effect of a Susceptibility Gradient in the Phase Encoding Direction

The impact of a susceptibility gradient in the y-direction has been previously investigated by Deichmann et al. [28]. The results below are in agreement with their findings. A susceptibility gradient in the y-direction, $\Delta B(x, y) = G_{y,s}y$ induces stretching or compressing of the object, depending on the sign of $G_{y,s}$ relative to the sign of G_y. In addition the signal magnitude is scaled by λ_y:

$$\frac{\rho\left(x', y'/\lambda_y\right)}{\lambda_y} \tag{A.22}$$

Echo Time Shifting

The shift of the echo in k-space $\delta k_{y,s}$ due to the susceptibility gradient changes the echo time from TE to TE' where:

$$\begin{aligned} TE' &= TE - \delta t \\ &= TE - \frac{\delta k_{y,s}}{\Delta k_y} T' \\ &= TE - \frac{\gamma G_{y,s} TE/\lambda_y}{\gamma G_y T'} T' \\ &= TE \left(\frac{G_y}{G_y + G_{y,s}} \right) \\ &= \frac{TE}{\lambda_y} \end{aligned} \tag{A.23}$$

Signal Attenuation Caused by Echo Time Shifting

This change in echo time causes a change in the T_2^* weighting of an image as s_{nm} is weighted by R_{nm}. The greatest contribution to the image intensity is from the point $k_x = 0$ and $k_y = 0$. The value of n and m at which this occurs are derived below. Firstly the value of m at which $k_x = 0$:

$$\begin{aligned} k_x &= k_{x,m} + \delta k_{x,s} \\ &= \frac{\gamma G_x m \Delta t}{2\pi} + \frac{\gamma G_{x,s} TE'}{2\pi} = 0 \end{aligned} \tag{A.24}$$

Rearranging:

$$m = -\frac{G_{x,s} TE'}{\lambda_y G_x \Delta t} \tag{A.25}$$

Given the earlier assumption that $G_{x,s}/G_x \ll 1$ then:

$$m = 0 \tag{A.26}$$

Secondly, the value of n at which $k_y = 0$:

$$\begin{aligned} k_y &= k_{y,n} + \delta k_{y,s} \\ &= \frac{\gamma G_y n T'}{2\pi} + \frac{\gamma G_{y,s} TE}{2\pi \lambda_y} = 0 \end{aligned} \tag{A.27}$$

Rearranging:

$$n = -\frac{G_{y,s} TE}{\lambda_y G_y T'} \tag{A.28}$$

Substituting m and n into R_{nm}:

$$\begin{aligned} R_{nm} &= e^{-\frac{\left(TE+nT'+(-1)^{(n+N_y/2)}m\Delta t\right)}{T_2^*}} \\ &= e^{-\frac{\left(TE+\left(-\frac{G_{y,s}TE}{\lambda_y G_y T'}\right)T'\right)}{T_2^*}} \\ &= e^{-\frac{\left(TE-\left(\frac{G_{y,s}TE}{\lambda_y G_y T'}\right)T'\right)}{T_2^*}} \\ &= e^{-\frac{TE'}{T_2^*}} \end{aligned} \tag{A.29}$$

Signal Dropout Caused by Echo Time Shifting

The change in echo time can lead to signal dropout if the echo is shifted to such an extent that it falls outside of the acquisition window [70, 71]. The range of susceptibility gradients $G_{y,s}$, over which signal dropout does not occur, is derived by considering the range of k-space that is sampled in the y-direction:

$$\frac{-N_y}{2L_y} \leq k_y \leq \frac{N_y}{2L_y} \tag{A.30}$$

This definition of $k_y = 1/\Delta y = N_y/L_y$ does not include a factor of 2π to ensure consistency with the definition $k = \frac{\gamma}{2\pi}\int \mathrm{d}t' G(t')$. Therefore the maximum k-space shift before signal dropout occurs is:

$$\frac{-N_y}{2L_y} \leq \delta k_{y,s} \leq \frac{N_y}{2L_y} \tag{A.31}$$

Given that $\delta k_{y,s} = \frac{\gamma G_{y,s} TE}{2\pi\lambda_y}$:

$$\frac{-N_y}{2L_y} \leq \frac{\gamma G_{y,s} TE}{2\pi\lambda_y} \leq \frac{N_y}{2L_y} \tag{A.32}$$

Rearranging:

$$\frac{-\pi N_y \lambda_y}{\gamma L_y TE} \leq G_{y,s} \leq \frac{\pi N_y \lambda_y}{\gamma L_y TE} \tag{A.33}$$

Focussing on the first inequality, i.e. the lower limit of k-space coverage, expanding λ_y and collecting terms in $G_{y,s}$:

$$\frac{-\pi N_y}{\gamma L_y TE} \leq G_{y,s}\left(1 + \frac{\pi N_y}{\gamma L_y TE G_y}\right) \tag{A.34}$$

Therefore:

$$\frac{-\pi N_y}{\gamma L_y TE\left(1 + \frac{\pi N_y}{\gamma L_y TE G_y}\right)} \leq G_{y,s} \tag{A.35}$$

Similarly for the upper limit:

$$G_{y,s} \leq \frac{\pi N_y}{\gamma L_y TE\left(1 - \frac{\pi N_y}{\gamma L_y TEG_y}\right)} \tag{A.36}$$

Hence the range of k-space shifts before signal dropout occurs is:

$$\frac{-\pi N_y}{\gamma L_y TE\left(1 + \frac{\pi N_y}{\gamma L_y TEG_y}\right)} \leq G_{y,s} \leq \frac{\pi N_y}{\gamma L_y TE\left(1 - \frac{\pi N_y}{\gamma L_y TEG_y}\right)} \tag{A.37}$$

Using $G_y = 2\pi\varepsilon/(\gamma L_y T')$ this expression can be written in terms of the matrix size, N_y, field of view, L_y, and the echo time (as entered on the scanner console), TE:

$$\frac{-N_y\pi}{\gamma L_y\left(TE + \varepsilon\frac{N_y T'}{2}\right)} \leq G_{y,s} \leq \frac{N_y\pi}{\gamma L_y\left(TE - \varepsilon\frac{N_y T'}{2}\right)} \tag{A.38}$$

A.2.3 The Effect of a Susceptibility Gradient in the Frequency Encoding Direction

Finally susceptibility gradients in the x-direction, $\Delta B(x, y) = G_{x,s}x$, result in shears in the resulting image since:

$$\rho\left(x', y' - \frac{G_{x,s}x'}{G_y}\right) \tag{A.39}$$

Echo Time Shifting

Unlike the case for susceptibility gradients in the y-direction the k-space shift caused by $G_{x,s}$ does not cause appreciable changes in the echo time because $G_{x,s}/G_x$ is small:

$$\begin{aligned} TE' &= TE - \delta t \\ &= TE - \frac{\delta k_{x,s}}{\Delta k_x}\Delta t \\ &= TE - \frac{\gamma G_{x,s} TE}{\gamma G_x \Delta t}\Delta t \\ &= TE\left(1 - \frac{G_{x,s}}{G_x}\right) \\ &\approx TE \end{aligned} \tag{A.40}$$

Signal Dropout Caused by Echo Time Shifting

As with susceptibility gradients in the y-direction the k-space shift caused by $G_{x,s}$ can lead to signal dropout if the echo is shifted to such an extent that it falls outside of the acquisition window[29]. The range of susceptibility gradients $G_{x,s}$ over which

signal dropout does not occur, when a susceptibility gradients $G_{y,s}$ is also present is derived by considering the range of k-space that is sampled in the x-direction:

$$\frac{-N_x}{2L_x} \leq k_x \leq \frac{N_x}{2L_x} \tag{A.41}$$

Therefore the maximum k-space shift before signal dropout occurs is:

$$\frac{-N_x}{2L_x} \leq \delta k_{x,s} \leq \frac{N_x}{2L_x} \tag{A.42}$$

Given that $\delta k_{x,s} = \frac{\gamma G_{x,s} TE}{2\pi\lambda_y}$:

$$\frac{-N_x}{2L_x} \leq \frac{\gamma G_{x,s} TE}{2\pi\lambda_y} \leq \frac{N_x}{2L_x} \tag{A.43}$$

Therefore:

$$-\frac{\pi N_x \lambda_y}{\gamma TE L_x} \leq G_{x,s} \leq \frac{\pi N_x \lambda_y}{\gamma TE L_x} \tag{A.44}$$

Substituting in λ_y

$$-\frac{\pi N_x}{\gamma TE L_x}\left(1 + \frac{G_{y,s}}{G_y}\right) \leq G_{x,s} \leq \frac{\pi N_x}{\gamma TE L_x}\left(1 + \frac{G_{y,s}}{G_y}\right) \tag{A.45}$$

Using $G_y = 2\pi\varepsilon/(\gamma L_y T')$ this expression can be written in terms of the matrix size, N_y, field of view, L_y, and the echo time (as entered on the scanner console) TE:

$$-\frac{N_x}{2\gamma L_x TE}\left(2\pi + \varepsilon\gamma L_y T' G_{y,s}\right) \leq G_{x,s} \leq \frac{N_x}{2\gamma L_x TE}\left(2\pi + \varepsilon\gamma L_y T' G_{y,s}\right) \tag{A.46}$$

A.3 Incorporating the Effects of Slice Selection

In a further extension the effects of slice-selection may then be incorporated by the addition of an integration over the z-direction (as shown in the general case of any image acquisition strategy by Haacke et al. [51]):

$$s_{nm} = \frac{e^{-i\gamma\frac{\alpha TE}{\lambda_y}} e^{-\frac{TE'}{T_2^*}}}{\lambda_y} \int_{\frac{-L_y}{2}}^{\frac{L_y}{2}} \int_{\frac{-L_x}{2}}^{\frac{L_x}{2}} \left[\int_{z_0 - \frac{\Delta z}{2}}^{z_0 + \frac{\Delta z}{2}} \rho\left(x', \frac{y'}{\lambda_y} - \frac{\alpha + G_{x,s} x'}{\lambda_y G_y}, z\right) \mathrm{d}z \right] e^{-2\pi i (k_{x,m} + \delta k_{x,s}) x'} e^{-2\pi i (k_{y,n} + \delta k_{y,s}) y'} \mathrm{d}x' \mathrm{d}y' \tag{A.47}$$

Where Δz is the slice thickness and z_0 is the position of the centre of the slice.

Slice Position, Thickness and Angle

Since $G_{z,s}$ causes a deviation from the prescribed slice thickness and position [51], the slice thickness Δz and position z_0 in the above expression are given by:

$$\Delta z = \frac{\Delta\omega}{\gamma\left(G_z + G_{z,s}\right)} \tag{A.48}$$

and:

$$z_0 = \frac{\omega_c - \omega_0}{\gamma\left(G_z + G_{z,s}\right)} \tag{A.49}$$

In addition in-plane susceptibility gradients can also impact the slice selection process, resulting in local rotations of the excited slice, [51]. This is because the slice select axis becomes $\boldsymbol{G} = G_{x,s}\hat{\boldsymbol{x}} + G_{y,s}\hat{\boldsymbol{y}} + \left(G_z + G_{z,s}\right)\hat{\boldsymbol{z}}$. The angle between the slice selection direction and the z-axis is:

$$\theta = \tan^{-1}\frac{\sqrt{G_{x,s}^2 + G_{y,s}^2}}{G_z + G_{z,s}} \tag{A.50}$$

and the angle between its projection into the x-y plane and the x-axis is:

$$\phi = \tan^{-1}\frac{G_{y,s}}{G_{x,s}} \tag{A.51}$$

Susceptibility Induced Signal Attenuation

A susceptibility gradient in the z-direction $G_{z,s}$ causes a phase variation $\phi(z,t) = \gamma G_{z,s} z t$ (where $t = TE \pm m\Delta t + nT'$) therefore the digitised signal is:

$$s_{nm} = \frac{e^{-i\gamma\frac{\alpha TE}{\lambda_y}} e^{-\frac{TE'}{T_2^*}}}{\lambda_y} \int_{\frac{-L_y}{2}}^{\frac{L_y}{2}} \int_{\frac{-L_x}{2}}^{\frac{L_x}{2}} \left[\int_{z_0-\frac{\Delta z}{2}}^{z_0+\frac{\Delta z}{2}} \rho\left(x', \frac{y'}{\lambda_y} - \frac{\alpha + G_{x,s}x'}{\lambda_y G_y}, z\right) e^{-i\gamma G_{z,s} z t} \mathrm{d}z \right] e^{-2\pi i(k_{x,m}+\delta k_{x,s})x'} e^{-2\pi i(k_{y,n}+\delta k_{y,s})y'} \mathrm{d}x'\mathrm{d}y' \tag{A.52}$$

With the simplifying assumption that the spin density $\rho(x,y,z)$ is constant across the slice, and that the RF pulse excites perfectly rectangular slices [74, 126] then:

$$s_{nm} = \frac{e^{-i\gamma\frac{\alpha TE}{\lambda_y}} e^{-\frac{TE'}{T_2^*}}}{\lambda_y} \int_{\frac{-L_y}{2}}^{\frac{L_y}{2}} \int_{\frac{-L_x}{2}}^{\frac{L_x}{2}} \left[\int_{z_0-\frac{\Delta z}{2}}^{z_0+\frac{\Delta z}{2}} e^{-i\gamma G_{z,s} z t} \mathrm{d}z \right] \rho\left(x', \frac{y'}{\lambda_y} - \frac{\alpha + G_{x,s}x'}{\lambda_y G_y}, z_0\right) e^{-2\pi i(k_{x,m}+\delta k_{x,s})x'} e^{-2\pi i(k_{y,n}+\delta k_{y,s})y'} \mathrm{d}x'\mathrm{d}y' \tag{A.53}$$

Performing the integral over z leads to:

$$s_{nm} = \Delta z \text{sinc}\left(\frac{\gamma G_{z,s}\Delta z(TE + (-1)^{(n+N_y/2)}m\Delta t + nT')}{2}\right) e^{-i\gamma G_{z,s}(TE \pm m\Delta t + nT')z_0}$$
$$\frac{e^{-i\gamma\frac{\alpha TE}{\lambda_y}} e^{-\frac{TE'}{T_2^*}}}{\lambda_y} \int_{\frac{-L_y}{2}}^{\frac{L_y}{2}} \int_{\frac{-L_x}{2}}^{\frac{L_x}{2}} \rho\left(x', \frac{y'}{\lambda_y} - \frac{\alpha + G_{x,s}x'}{\lambda_y G_y}, z_0\right) e^{-2\pi i(k_{x,m}+\delta k_{x,s})x'}$$
$$e^{-2\pi i(k_{y,n}+\delta k_{y,s})y'} \mathrm{d}x'\mathrm{d}y' \quad \text{(A.54)}$$

Where sinc(x) $\equiv \sin(\mathrm{x})/\mathrm{x}$. Therefore, in addition to the image stretching and shearing, intensity scaling and echo shifting caused by the x- and y- susceptibility gradients, if a susceptibility gradient is present in the z-direction then the signal is modulated by a sinc function. As before the greatest contribution to the image intensity is from the point $k_x = 0$ and $k_y = 0$, therefore substituting in the values of n and m at which this occurs:

$$s_{nm} = \Delta z \text{sinc}\left(\frac{\gamma G_{z,s}\Delta z TE'}{2}\right) \frac{e^{-\frac{TE'}{T_2^*}}}{\lambda_y} e^{-i\gamma G_{z,s}TE'z_0} e^{-i\gamma\frac{\alpha TE}{\lambda_y}}$$
$$\int_{\frac{-L_y}{2}}^{\frac{L_y}{2}} \int_{\frac{-L_x}{2}}^{\frac{L_x}{2}} \rho\left(x', \frac{y'}{\lambda_y} - \frac{\alpha + G_{x,s}x'}{\lambda_y G_y}, z_0\right) e^{-2\pi i(k_{x,m}+\delta k_{x,s})x'}$$
$$e^{-2\pi i(k_{y,n}+\delta k_{y,s})y'} \mathrm{d}x'\mathrm{d}y' \quad \text{(A.55)}$$

Appendix B

A Derivation of the Maximum Amplitude of a Complex Hyperbolic Secant Pulse Used for Signal Excitation

The maximum amplitude, A_0, of a complex hyperbolic secant pulse used for signal excitation, with a flip angle, α, can be derived from the expression for the longitudinal magnetisation given in Equation 17 in Silver et al. [307]:

$$\frac{M_z(\Delta\omega)}{M_0} = \tanh\left(\frac{\pi\Delta\omega}{2\beta} + \frac{\pi\mu}{2}\right)\tanh\left(\frac{\pi\Delta\omega}{2\beta} - \frac{\pi\mu}{2}\right) + \cos\left(\pi\sqrt{\left(\frac{\gamma A_0}{\beta}\right)^2 - \mu^2}\right)\operatorname{sech}\left(\frac{\pi\Delta\omega}{2\beta} + \frac{\pi\mu}{2}\right)\operatorname{sech}\left(\frac{\pi\Delta\omega}{2\beta} - \frac{\pi\mu}{2}\right) \quad \text{(B.1)}$$

Here $\Delta\omega$ is the offset frequency, which in the presence of a slice-selection gradient is equal to $\gamma G_z z$. At the centre of the slice ($\Delta\omega = 0$) and the z-magnetisation is:

$$\frac{M_z(\Delta\omega = 0)}{M_0} = \tanh\left(\frac{\pi\mu}{2}\right)\tanh\left(-\frac{\pi\mu}{2}\right) + \cos\left(\pi\sqrt{\left(\frac{\gamma A_0}{\beta}\right)^2 - \mu^2}\right)\operatorname{sech}\left(\frac{\pi\mu}{2}\right)\operatorname{sech}\left(-\frac{\pi\mu}{2}\right) \quad \text{(B.2)}$$

Given that hyperbolic tangent is an odd function and hyperbolic secant is an even function this expression simplifies to:

$$\frac{M_z(\Delta\omega = 0)}{M_0} = \cos\left(\pi\sqrt{\left(\frac{\gamma A_0}{\beta}\right)^2 - \mu^2}\right)\operatorname{sech}^2\left(\frac{\pi\mu}{2}\right) - \tanh^2\left(\frac{\pi\mu}{2}\right) \quad \text{(B.3)}$$

Then, recognising that the z-magnetisation at the slice centre can also be written in terms of the flip angle, α:

$$\frac{M_z(\Delta\omega = 0)}{M_0} = \cos\alpha \tag{B.4}$$

and by equating B.3 and B.4:

$$\cos\alpha = \cos\left(\pi\sqrt{\left(\frac{\gamma A_0}{\beta}\right)^2 - \mu^2}\right)\operatorname{sech}^2\left(\frac{\pi\mu}{2}\right) - \tanh^2\left(\frac{\pi\mu}{2}\right) \tag{B.5}$$

the RF amplitude as a function of β, μ and the flip angle α is after some straightforward rearrangement:

$$A_0 = \frac{\beta}{\gamma}\sqrt{\left[\frac{\cos^{-1}\left(\cosh^2\left(\frac{\pi\mu}{2}\right)\cos\alpha + \sinh^2\left(\frac{\pi\mu}{2}\right)\right)}{\pi}\right]^2 + \mu^2} \tag{B.6}$$

Appendix C

A Derivation of the Bandwidth of a Complex Hyperbolic Secant Pulse Used for Signal Excitation

The bandwidth of a complex hyperbolic secant pulse used for signal excitation is best defined as the full-width at half-maximum (FWHM) of the magnitude of the transverse magnetisation, $|M_{x,y}|$. This can be derived from Equation 17 in Silver et al. [307]:

$$\frac{M_z(\Delta\omega)}{M_0} = \tanh\left(\frac{\pi\Delta\omega}{2\beta} + \frac{\pi\mu}{2}\right)\tanh\left(\frac{\pi\Delta\omega}{2\beta} - \frac{\pi\mu}{2}\right) + \cos\left(\pi\sqrt{\left(\frac{\gamma A_0}{\beta}\right)^2 - \mu^2}\right)\operatorname{sech}\left(\frac{\pi\Delta\omega}{2\beta} + \frac{\pi\mu}{2}\right)\operatorname{sech}\left(\frac{\pi\Delta\omega}{2\beta} - \frac{\pi\mu}{2}\right) \quad \text{(C.1)}$$

The cosine term including the pulse amplitude, A_0, can then be written in terms involving the flip angle, α, and μ using Equation B.5:

$$\frac{M_z(\Delta\omega)}{M_0} = \tanh\left(\frac{\pi\Delta\omega}{2\beta} + \frac{\pi\mu}{2}\right)\tanh\left(\frac{\pi\Delta\omega}{2\beta} - \frac{\pi\mu}{2}\right) + \left(\frac{\cos\alpha + \tanh^2\left(\frac{\pi\mu}{2}\right)}{\operatorname{sech}^2\left(\frac{\pi\mu}{2}\right)}\right)\operatorname{sech}\left(\frac{\pi\Delta\omega}{2\beta} + \frac{\pi\mu}{2}\right)\operatorname{sech}\left(\frac{\pi\Delta\omega}{2\beta} - \frac{\pi\mu}{2}\right) \quad \text{(C.2)}$$

Using standard trigonometric identities[1], the term involving tanh can be simplified to:

$$\tanh\left(\frac{\pi\Delta\omega}{2\beta}+\frac{\pi\mu}{2}\right)\tanh\left(\frac{\pi\Delta\omega}{2\beta}-\frac{\pi\mu}{2}\right)=$$
$$\frac{\sinh^2\left(\frac{\pi\Delta\omega}{2\beta}\right)\cosh^2\left(\frac{\pi\mu}{2}\right)-\cosh^2\left(\frac{\pi\Delta\omega}{2\beta}\right)\sinh^2\left(\frac{\pi\mu}{2}\right)}{\cosh^2\left(\frac{\pi\Delta\omega}{2\beta}\right)\cosh^2\left(\frac{\pi\mu}{2}\right)-\sinh^2\left(\frac{\pi\Delta\omega}{2\beta}\right)\sinh^2\left(\frac{\pi\mu}{2}\right)}=\frac{\cosh(\frac{\pi\Delta\omega}{\beta})-\cosh(\pi\mu)}{\cosh(\frac{\pi\Delta\omega}{\beta})+\cosh(\pi\mu 2)} \tag{C.7}$$

and the term involving sech to:

$$\operatorname{sech}\left(\frac{\pi\Delta\omega}{2\beta}+\frac{\pi\mu}{2}\right)\operatorname{sech}\left(\frac{\pi\Delta\omega}{2\beta}-\frac{\pi\mu}{2}\right)=$$
$$\frac{1}{\cosh^2\left(\frac{\pi\Delta\omega}{2\beta}\right)\cosh^2\left(\frac{\pi\mu}{2}\right)-\sinh^2\left(\frac{\pi\Delta\omega}{2\beta}\right)\sinh^2\left(\frac{\pi\mu}{2}\right)}=\frac{2}{\cosh(\frac{\pi\Delta\omega}{\beta})+\cosh(\pi\mu)} \tag{C.8}$$

Substituting in these simplified expressions, the longitudinal magnetisation becomes:

$$\begin{aligned}\frac{M_z(\Delta\omega)}{M_0}&=\frac{\cosh(\frac{\pi\Delta\omega}{\beta})-\cosh(\pi\mu)}{\cosh(\frac{\pi\Delta\omega}{\beta})+\cosh(\pi\mu)}+\left(\frac{\cos\alpha+\tanh^2\left(\frac{\pi\mu}{2}\right)}{\operatorname{sech}^2\left(\frac{\pi\mu}{2}\right)}\right)\frac{2}{\cosh(\frac{\pi\Delta\omega}{\beta})+\cosh(\pi\mu)}\\&=\frac{\cosh(\frac{\pi\Delta\omega}{\beta})-\cosh(\pi\mu)+2\cosh^2\left(\frac{\pi\mu}{2}\right)\cos\alpha+2\sinh^2\left(\frac{\pi\mu}{2}\right)}{\cosh(\frac{\pi\Delta\omega}{\beta})+\cosh(\pi\mu)}\\&=\frac{\cosh(\frac{\pi\Delta\omega}{\beta})+\cosh(\pi\mu)\cos(\alpha)+\cos(\alpha)-1}{\cosh(\frac{\pi\Delta\omega}{\beta})+\cosh(\pi\mu)}\end{aligned} \tag{C.9}$$

To determine the FWHM this is first rearranged to make $\Delta\omega$ the subject:

$$\Delta\omega=\frac{\beta}{\pi}\cosh^{-1}\left[\frac{\cosh(\pi\mu)\left(\cos(\alpha)-\frac{M_z(\Delta\omega)}{M_0}\right)+\cos(\alpha)-1}{\frac{M_z(\Delta\omega)}{M_0}-1}\right] \tag{C.10}$$

[1]

$$\tanh(A+B)=\frac{\sinh A\cosh B+\cosh A\sinh B}{\cosh A\cosh B+\sinh A\sinh B} \tag{C.3}$$

$$\operatorname{sech}(A+B)=\frac{1}{\cosh A\cosh B+\sinh A\sinh B} \tag{C.4}$$

$$\cosh^2 A=\frac{1}{2}(\cosh(2A)+1) \tag{C.5}$$

$$\sinh^2 A=\frac{1}{2}(\cosh(2A)-1) \tag{C.6}$$

and then written in terms of the magnitude of the transverse magnetisation[2]:

$$\Delta\omega = \frac{\beta}{\pi}\cosh^{-1}\left[\frac{\cosh(\pi\mu)\left(\cos(\alpha)-\sqrt{1-\left(\frac{|M_{x,y}|}{M_0}\right)^2}\right)+\cos(\alpha)-1}{\sqrt{1-\left(\frac{|M_{x,y}|}{M_0}\right)^2}-1}\right] \tag{C.12}$$

At the centre of the excited slice, for a flip angle α, the magnitude of the transverse magnetisation is $|M_{x,y}|/M_0 = \sin(\alpha)$. The half-width at half-maximum (HWHM) is the value of $\Delta\omega$ when $|M_{x,y}|/M_0 = \sin(\alpha)/2$, i.e.:

$$\begin{aligned}\Delta\omega_{HWHM} &= \frac{\beta}{\pi}\cosh^{-1}\left[\frac{\cosh(\pi\mu)\left(\cos(\alpha)-\sqrt{1-\left(\frac{\sin\alpha}{2}\right)^2}\right)+\cos(\alpha)-1}{\sqrt{1-\left(\frac{\sin\alpha}{2}\right)^2}-1}\right] \\ &= \frac{\beta}{\pi}\cosh^{-1}\left[\frac{\cosh(\pi\mu)\left(\cos(\alpha)-\frac{1}{2}\sqrt{3+\cos^2(\alpha)}\right)+\cos(\alpha)-1}{\frac{1}{2}\sqrt{3+\cos^2(\alpha)}-1}\right]\end{aligned} \tag{C.13}$$

The bandwidth, defined as the FWHM (in Hz), $\Delta f = \Delta\omega_{HWHM}/\pi$ is therefore:

$$\Delta f = \frac{\beta}{\pi^2}\cosh^{-1}\left[\frac{\cosh(\pi\mu)\left(\cos(\alpha)-\frac{1}{2}\sqrt{3+\cos^2(\alpha)}\right)+\cos(\alpha)-1}{\frac{1}{2}\sqrt{3+\cos^2(\alpha)}-1}\right] \tag{C.14}$$

which, for $\mu \geq 2$, can be shown to be approximately proportional to both μ and β:

$$\Delta f \approx \frac{\beta\mu}{\pi} + \frac{\beta}{\pi^2}\ln\left(\frac{\cos(\alpha)-\frac{1}{2}\sqrt{3+\cos^2(\alpha)}}{\frac{1}{2}\sqrt{3+\cos^2(\alpha)}-1}\right) \tag{C.15}$$

The linear proportionality between the bandwidth and μ is not immediately evident by inspection of Equation C.14, however by rearranging:

$$\Delta f = \frac{\beta}{\pi^2}\cosh^{-1}\left[\frac{\cos(\alpha)-\frac{1}{2}\sqrt{3+\cos^2(\alpha)}}{\frac{1}{2}\sqrt{3+\cos^2(\alpha)}-1}\left(\cosh(\pi\mu)+\frac{\cos(\alpha)-1}{\cos(\alpha)-\frac{1}{2}\sqrt{3+\cos^2(\alpha)}}\right)\right] \tag{C.16}$$

[2]Using the following relationship:

$$M_0^2 = |M_{x,y}|^2 + M_z^2 \tag{C.11}$$

and making two substitutions to simplify the result:

$$\Delta f = \frac{\beta}{\pi^2} \cosh^{-1} \left[b \left(\cosh \left(\pi \mu \right) + c \right) \right] \tag{C.17}$$

Where:

$$b = \frac{\cos(\alpha) - \frac{1}{2}\sqrt{3 + \cos^2(\alpha)}}{\frac{1}{2}\sqrt{3 + \cos^2(\alpha)} - 1} \tag{C.18}$$

$$c = \frac{\cos(\alpha) - 1}{\cos(\alpha) - \frac{1}{2}\sqrt{3 + \cos^2(\alpha)}} \tag{C.19}$$

and by noting that for $0 < \alpha < \pi$ and $\mu \geq 2$ (c is a smoothly decreasing function of the flip angle; $c \to 4/3$ as $\alpha \to 0$, and $c \to 1$ as $\alpha \to \pi$):

$$\cosh \left(\pi \mu \right) \gg c \tag{C.20}$$

the bandwidth is approximately:

$$\Delta f \approx \frac{\beta}{\pi^2} \cosh^{-1} \left[b \cosh \left(\pi \mu \right) \right] \tag{C.21}$$

Then, given that inverse hyperbolic cosine can be written in terms of a natural logarithm:

$$\cosh^{-1} z = \ln \left[z + \sqrt{z^2 - 1} \right] \tag{C.22}$$

the bandwidth is:

$$\Delta f \approx \frac{\beta}{\pi^2} \ln \left[b \cosh \left(\pi \mu \right) + \sqrt{b^2 \cosh^2 \left(\pi \mu \right) - 1} \right] \tag{C.23}$$

and since $b \geq 3$ for $0 < \alpha < \pi$ this can be approximated as:

$$\Delta f \approx \frac{\beta}{\pi^2} \ln \left[2b \cosh(\pi \mu) \right] \tag{C.24}$$

Finally given that $\cosh(\pi\mu) \approx e^{\pi\mu}/2$ when $\mu \geq 2$ the bandwidth is approximately:

$$\begin{aligned} \Delta f &\approx \frac{\mu \beta}{\pi} + \frac{\beta}{\pi^2} \ln b \\ &\approx \frac{\beta \mu}{\pi} + \frac{\beta}{\pi^2} \ln \left(\frac{\cos(\alpha) - \frac{1}{2}\sqrt{3 + \cos^2(\alpha)}}{\frac{1}{2}\sqrt{3 + \cos^2(\alpha)} - 1} \right) \end{aligned} \tag{C.25}$$

i.e. the bandwidth is proportional to μ.

Appendix D

The Dependence of the Variation in the Phase of the Transverse Magnetisation on the Hyperbolic Secant Pulse Parameters

The dependence of the variation of the phase of the transverse magnetisation on the complex hyperbolic secant pulse parameters can be derived from the analytic expression for the phase, $\phi(z)$ given by Park and Garwood [303]:

$$\phi(z) = -\mu \ln\left(\frac{-\mu\beta \operatorname{sech}(\beta T_{RF}/2)}{\sqrt{(\mu\beta)^2 - (\gamma G_z z)^2}}\right) + \frac{\gamma G_z z}{2\beta} \ln\left(\frac{\mu\beta + \gamma G_z z}{\mu\beta - \gamma G_z z}\right) \tag{D.1}$$

where G_z is the amplitude of the slice selection gradient. Given that $\ln(AB) = \ln A + \ln B$ the first term can be written as:

$$-\mu \ln\left(-\mu\beta \operatorname{sech}(\beta T_{RF}/2)\right) - \mu \ln\left(\frac{1}{\sqrt{1 - \left(\frac{\gamma G_z z}{\mu\beta}\right)^2}}\right) \tag{D.2}$$

Then, since $-\mu \ln\left(-\mu\beta \operatorname{sech}(\beta T_{RF}/2)\right)$ does not depend on the spatial position, z, it can be ignored as it only contributes a constant offset to the phase. Therefore the phase is given by:

$$\phi(z) = -\mu \ln\left(\frac{1}{\sqrt{1 - \left(\frac{\gamma G_z z}{\mu\beta}\right)^2}}\right) + \frac{\gamma G_z z}{2\beta} \ln\left(\frac{1 + \frac{\gamma G_z z}{\mu\beta}}{1 - \frac{\gamma G_z z}{\mu\beta}}\right) \tag{D.3}$$

Recognising that slice selection gradient amplitude G_z can be written in terms of the HS pulse bandwidth ($G_z = 2\pi\Delta f/\gamma\Delta z$), the phase is:

$$\phi(z) = -\mu \ln\left(\frac{1}{\sqrt{1-\left(\frac{2\pi\Delta f z}{\mu\beta\Delta z}\right)^2}}\right) + \frac{\pi\Delta f z}{\beta\Delta z}\ln\left(\frac{1+\frac{2\pi\Delta f z}{\mu\beta\Delta z}}{1-\frac{2\pi\Delta f z}{\mu\beta\Delta z}}\right) \tag{D.4}$$

As shown in Appendix C, the bandwidth, Δf, for $\mu > 2$, is:

$$\Delta f = \frac{\beta\mu}{\pi} + \frac{\beta}{\pi^2}\ln\left(\frac{\cos(\alpha) - \frac{1}{2}\sqrt{3+\cos^2(\alpha)}}{\frac{1}{2}\sqrt{3+\cos^2(\alpha)} - 1}\right) \tag{D.5}$$

This can, for simplicity, be written as:

$$\Delta f = \beta\left(\frac{\mu}{\pi} + \frac{h(\alpha)}{\pi^2}\right) \tag{D.6}$$

Therefore the phase as a function of position is:

$$\begin{aligned}\phi(z) = -\mu \ln\left(\frac{1}{\sqrt{1-z^2\left(\frac{2}{\Delta z}+\frac{2h(\alpha)}{\pi\mu\Delta z}\right)^2}}\right) \\ - \mu z\left(\frac{1}{\Delta z}+\frac{h(\alpha)}{\pi\mu\Delta z}\right)\ln\left(\frac{1+z\left(\frac{2}{\Delta z}+\frac{h(\alpha)}{\pi\mu\Delta z}\right)}{1-z\left(\frac{2}{\Delta z}+\frac{h(\alpha)}{\pi\mu\Delta z}\right)}\right)\end{aligned} \tag{D.7}$$

Bibliography

[1] P. Lauterbur, "Image formation by induced local interactions - examples employing nuclear magnetic resonance," *Nature*, vol. 242, no. 5394, pp. 190–191, 1973.

[2] P. Mansfield and P. K. Grannell, "NMR 'diffraction' in solids?" *Journal of Physics C: Solid State Physics*, vol. 6, no. 22, pp. L422–L426, 1973.

[3] S. Ogawa and T. M. Lee, "Magnetic resonance imaging of blood vessels at high fields - in-vivo and in-vitro measurements and image simulation," *Magnetic Resonance in Medicine*, vol. 16, no. 1, pp. 9–18, 1990.

[4] S. Ogawa, T. M. Lee, A. R. Kay, and D. W. Tank, "Brain magnetic resonance imaging with contrast dependent on blood oxygenation," *Proceedings of the National Academy of Sciences of the United States of America*, vol. 87, no. 24, pp. 9868–9872, 1990.

[5] S. Ogawa, T. M. Lee, A. S. Nayak, and P. Glynn, "Oxygenation-sensitive contrast in magnetic resonance image of rodent brain at high magnetic fields," *Magnetic Resonance in Medicine*, vol. 14, no. 1, pp. 68–78, 1990.

[6] S. Ogawa, D. W. Tank, R. Menon, J. M. Ellermann, S. G. Kim, H. Merkle, and K. Ugurbil, "Intrinsic signal changes accompanying sensory stimulation: functional brain mapping with magnetic resonance imaging," *Proceedings of the National Academy of Sciences*, vol. 89, no. 13, pp. 5951–5955, 1992.

[7] K. K. Kwong, J. W. Belliveau, D. A. Chesler, I. E. Goldberg, R. M. Weisskoff, B. P. Poncelet, D. N. Kennedy, B. E. Hoppel, M. S. Cohen, R. Turner, H. M. Cheng, T. J. Brady, and B. R. Rosen, "Dynamic magnetic resonance imaging of human brain activity during primary sensory stimulation," *Proceedings of the National Academy of Sciences of the United States of America*, vol. 89, no. 12, pp. 5675–5679, 1992.

[8] P. A. Bandettini, E. C. Wong, R. S. Hinks, R. S. Tikofsky, and J. S. Hyde, "Time course EPI of human brain function during task activation," *Magnetic Resonance in Medicine*, vol. 25, no. 2, pp. 390–397, 1992.

[9] C. Weiller, A. May, M. Sach, C. Buhmann, and M. Rijntjes, "Role of functional imaging in neurological disorders," *Journal of Magnetic Resonance Imaging*, vol. 23, no. 6, pp. 840–850, 2006.

[10] M. T. Mitterschiffthaler, U. Ettinger, M. A. Mehta, D. Mataix-Cols, and S. C. R. Williams, "Applications of functional magnetic resonance imaging in psychiatry," *Journal of Magnetic Resonance Imaging*, vol. 23, no. 6, pp. 851–861, 2006.

[11] S. Sunaert, "Presurgical planning for tumor resectioning," *Journal of Magnetic Resonance Imaging*, vol. 23, no. 6, pp. 887–905, 2006.

[12] B. Biswal, F. Z. Yetkin, V. M. Haughton, and J. S. Hyde, "Functional connectivity in the motor cortex of the resting human brain using echo-planar MRI," *Magnetic Resonance in Medicine*, vol. 34, no. 4, pp. 537–541, 1995.

[13] M. D. Fox and M. E. Raichle, "Spontaneous fluctuations in brain activity observed with functional magnetic resonance imaging," *Nature Reviews Neuroscience*, vol. 8, no. 9, pp. 700–711, 2007.

[14] P. Mansfield, A. A. Maudsley, and T. Baines, "Fast scan proton density imaging by NMR," *Journal of Physics E - Scientific Instruments*, vol. 9, no. 4, pp. 271–278, 1976.

[15] P. Mansfield, "Multi-planar image formation using NMR spin echoes," *Journal of Physics C - Solid State Physics*, vol. 10, no. 3, pp. L55–L58, 1977.

[16] P. Mansfield, B. Chapman, R. Coxon, P. Glover, A. Howesman, R. Ordidge, M. Stehling, and R. Turner, "Advances in echo-planar imaging," *Proceedings of the Society of Magnetic Resonance in Medicine*, vol. 1988, no. S1, p. 237, 1988.

[17] R. Turner and R. J. Ordidge, "Technical challenges of functional magnetic resonance imaging," *IEEE Engineering in Medicine and Biology Magazine*, vol. 19, no. 5, pp. 42–54, 2000.

[18] J. G. Ojemann, E. Akbudak, A. Z. Snyder, R. C. McKinstry, M. E. Raichle, and T. E. Conturo, "Anatomic localization and quantitative analysis of gradient refocused echo-planar fMRI susceptibility artifacts," *NeuroImage*, vol. 6, no. 3, pp. 156–167, 1997.

[19] J. L. Wilson, M. Jenkinson, and P. Jezzard, "Optimization of static field homogeneity in human brain using diamagnetic passive shims," *Magnetic Resonance in Medicine*, vol. 48, no. 5, pp. 906–914, 2002.

[20] T. Tanabe, H. Yarita, M. Iino, Y. Ooshima, and S. F. Takagi, "An olfactory projection area in orbitofrontal cortex of the monkey," *Journal of Neurophysiology*, vol. 38, no. 5, pp. 1269–1283, 1975.

[21] S. T. Carmichael, M. C. Clugnet, and J. L. Price, "Central olfactory connections in the macaque monkey," *The Journal of Comparative Neurology*, vol. 346, no. 3, pp. 403–434, 1994.

[22] D. M. Small, R. J. Zatorre, A. Dagher, A. C. Evans, and M. Jones-Gotman, "Changes in brain activity related to eating chocolate: From pleasure to aversion," *Brain*, vol. 124, no. 9, pp. 1720–1733, 2001.

[23] A. Bechara, H. Damasio, and A. R. Damasio, "Emotion, decision making and the orbitofrontal cortex," *Cerebral Cortex*, vol. 10, no. 3, pp. 295–307, 2000.

[24] J. Hornak, E. T. Rolls, and D. Wade, "Face and voice expression identification in patients with emotional and behavioural changes following ventral frontal lobe damage," *Neuropsychologia*, vol. 34, no. 4, pp. 247–261, 1996.

[25] R. J. R. Blair, J. S. Morris, C. D. Frith, D. I. Perrett, and R. J. Dolan, "Dissociable neural responses to facial expressions of sadness and anger," *Brain*, vol. 122, no. 5, pp. 883–893, 1999.

[26] J. T. Devlin, R. P. Russell, M. H. Davis, C. J. Price, J. Wilson, H. E. Moss, P. M. Matthews, and L. K. Tyler, "Susceptibility-Induced Loss of Signal: Comparing PET and fMRI on a Semantic Task," *NeuroImage*, vol. 11, no. 6, pp. 589–600, 2000.

[27] J. Frahm, M. Klaus-Dietmar, and H. Wolfgang, "Direct FLASH MR imaging of magnetic field inhomogeneities by gradient compensation," *Magnetic Resonance in Medicine*, vol. 6, no. 4, pp. 474–480, 1988.

[28] R. Deichmann, O. Josephs, C. Hutton, D. R. Corfield, and R. Turner, "Compensation of susceptibility-induced BOLD sensitivity losses in echo-planar fMRI imaging," *NeuroImage*, vol. 15, no. 1, pp. 120–135, 2002.

[29] N. Weiskopf, C. Hutton, O. Josephs, R. Turner, and R. Deichmann, "Optimized EPI for fMRI studies of the orbitofrontal cortex: compensation of susceptibility-induced gradients in the readout direction," *Magnetic Resonance Materials in Physics Biology and Medicine*, vol. 20, no. 1, pp. 39–49, 2007.

[30] K. Shmueli, "Optimisation of magnetic resonance techniques for imaging the human brain at 4.7T," Ph.D. dissertation, 2005.

[31] F. Bloch, "Nuclear induction," *Physical Review*, vol. 70, no. 7-8, pp. 460–474, 1946.

[32] E. M. Purcell, H. C. Torrey, and R. V. Pound, "Resonance absorption by nuclear magnetic moments in a solid," *Physical Review*, vol. 69, no. 1-2, pp. 37–38, 1946.

[33] W. Gerlach and O. Stern, "Über die richtungsquantelung im magnetfeld," *Annalen der Physik*, vol. 379, no. 16, pp. 673–699, 1924.

[34] I. I. Rabi, J. R. Zacharias, S. Millman, and P. Kusch, "A new method of measuring nuclear magnetic moment," *Physical Review*, vol. 53, no. Copyright (C) 2009 The American Physical Society, p. 318, 1938.

[35] P. A. M. Dirac, "The quantum theory of the electron," *Proceedings of the Royal Society of London. Series A, Containing Papers of a Mathematical and Physical Character*, vol. 117, no. 778, pp. 610–624, 1928.

[36] ——, "The quantum theory of the electron. part II," *Proceedings of the Royal Society of London. Series A, Containing Papers of a Mathematical and Physical Character*, vol. 118, no. 779, pp. 351–361, 1928.

[37] R. Damadian, "Tumor detection by nuclear magnetic resonance," *Science*, vol. 171, no. 3976, pp. 1151–1153, 1971.

[38] I. I. Rabi, N. F. Ramsey, and J. Schwinger, "Use of rotating coordinates in magnetic resonance problems," *Reviews of Modern Physics*, vol. 26, no. 2, pp. 167–171, 1954.

[39] M. Bernstein, K. King, and X. Zhou, *Handbook of MRI Pulse Sequences*. Burlington, MA: Elsevier Academic Press, 2004.

[40] D. I. Hoult and R. E. Richards, "The signal-to-noise ratio of the nuclear magnetic resonance experiment," *Journal of Magnetic Resonance (1969)*, vol. 24, no. 1, pp. 71–85, 1976.

[41] S. Ljunggren, "A simple graphical representation of fourier-based imaging methods," *Journal of Magnetic Resonance*, vol. 54, no. 2, pp. 338–343, 1983.

[42] D. B. Twieg, "The k-trajectory formulation of the NMR imaging process with applications in analysis and synthesis of imaging methods," *Medical Physics*, vol. 10, no. 5, pp. 610–621, 1983.

[43] P. Joseph, L. Axel, and M. O'Donnell, "Potential problems with selective pulses in NMR imaging systems," *Medical Physics*, vol. 11, no. 6, pp. 772–777, 1984.

[44] P. Le Roux, Patent 8 610 179, 1986.

[45] M. Shinnar, L. Bolinger, and J. S. Leigh, "The synthesis of soft pulses with a specified frequency response," *Magnetic Resonance in Medicine*, vol. 12, no. 1, pp. 88–92, 1989.

[46] ——, "The use of finite impulse response filters in pulse design," *Magnetic Resonance in Medicine*, vol. 12, no. 1, pp. 81–87, 1989.

[47] M. Shinnar, S. Eleff, H. Subramanian, and J. S. Leigh, "The synthesis of pulse sequences yielding arbitrary magnetization vectors," *Magnetic Resonance in Medicine*, vol. 12, no. 1, pp. 74–80, 1989.

[48] M. Shinnar and J. S. Leigh, "The application of spinors to pulse synthesis and analysis," *Magnetic Resonance in Medicine*, vol. 12, no. 1, pp. 93–98, 1989.

[49] J. Pauly, P. Le Roux, D. Nishimura, and A. Macovski, "Parameter relations for the Shinnar-Le Roux selective excitation pulse design algorithm," *Medical Imaging, IEEE Transactions on*, vol. 10, no. 1, pp. 53–65, 1991.

[50] J. M. S. Hutchison, R. J. Sutherland, and J. R. Mallard, "NMR imaging: image recovery under magnetic fields with large non-uniformities," *Journal of Physics E-Scientific Instruments*, vol. 11, no. 3, pp. 217–221, 1978.

[51] E. Haacke, R. Brown, M. Thompson, and R. Venkatesan, *Magnetic Resonance Imaging Physical Principles and Sequence Design.* New York: Wiley-Liss, 1999.

[52] E. L. Hahn, "Spin echoes," *Physical Review*, vol. 80, no. 4, pp. 580–594, 1950.

[53] L. E. Crooks, D. A. Ortendahl, L. Kaufman, J. Hoenninger, M. Arakawa, J. Watts, C. R. Cannon, M. Brant-Zawadzki, P. L. Davis, and A. R. Margulis, "Clinical efficiency of nuclear magnetic resonance imaging," *Radiology*, vol. 146, no. 1, pp. 123–128, 1983.

[54] C. H. Meyer, J. M. Pauly, A. Macovskiand, and D. G. Nishimura, "Simultaneous spatial and spectral selective excitation," *Magnetic Resonance in Medicine*, vol. 15, no. 2, pp. 287–304, 1990.

[55] F. Schick, J. Forster, J. Machann, R. Kuntz, and C. D. Claussen, "Improved clinical echo-planar MRI using spatial-spectral excitation," *Journal of Magnetic Resonance Imaging*, vol. 8, no. 4, pp. 960–967, 1998.

[56] A. Haase, J. Frahm, W. Hanicke, and D. Matthaei, "^{1}H NMR chemical shift selective (CHESS) imaging," *Physics in Medicine and Biology*, vol. 30, no. 4, p. 341, 1985.

[57] D. Q. Chen, R. B. Marr, and P. C. Lauterbur, "Reconstruction from NMR data acquired with imaging gradients having arbitrary time dependance," *IEEE Transactions on Medical Imaging*, vol. 5, no. 3, pp. 162–164, 1986.

[58] J. A. de Zwart, P. van Gelderen, X. Golay, V. N. Ikonomidou, and J. H. Duyn, "Accelerated parallel imaging for functional imaging of the human brain," *NMR in Biomedicine*, vol. 19, no. 3, pp. 342–351, 2006.

[59] K. P. Pruessmann, M. Weiger, M. B. Scheidegger, and P. Boesiger, "SENSE: Sensitivity encoding for fast MRI," *Magnetic Resonance in Medicine*, vol. 42, no. 5, pp. 952–962, 1999.

[60] K. F. King, "ASSET - parallel imaging on the GE scanner," in *Second International Workshop on Parallel MRI*, 2004.

[61] ——, "SENSE image quality improvement using matrix regularization," in *Proceedings of the International Society for Magnetic Resonance in Medicine*, vol. 9, 2001.

[62] J. A. de Zwart, P. van Gelderen, P. A. Kellman, and J. H. Duyn, "Application of sensitivity-encoded echo-planar imaging for blood oxygen level-dependent functional brain imaging," *Magnetic Resonance in Medicine*, vol. 48, no. 6, pp. 1011–1020, 2002.

[63] H. Bruder, H. Fischer, H.-E. Reinfelder, and F. Schmitt, "Image reconstruction for echo planar imaging with nonequidistant k-space sampling," *Magnetic Resonance in Medicine*, vol. 23, no. 2, pp. 311–323, 1992.

[64] S. Huettel, A. Song, and G. McCarthy, *Functional Magnetic Resonance Imaging*, 2nd ed. Sunderland, MA: Sinauer Associates, 2009.

[65] J. F. Schenck, "The role of magnetic susceptibility in magnetic resonance imaging: MRI magnetic compatibility of the first and second kinds," *Medical Physics*, vol. 23, no. 6, pp. 815–850, 1996.

[66] H. W. Park, Y. M. Ro, and Z. H. Cho, "Measurement of the magnetic-susceptibilty effect in high-field NMR imaging," *Physics in Medicine and Biology*, vol. 33, no. 3, pp. 339–349, 1988.

[67] P. A. Bandettini, E. C. Wong, A. Jesmanowicz, R. S. Hinks, and J. S. Hyde, "Spin-echo and gradient-echo EPI of human brain activiation using BOLD contrast - a comparative study at 1.5T," *NMR in Biomedicine*, vol. 7, no. 1-2, pp. 12–20, 1994.

[68] F. Farzaneh, S. J. Riederer, and N. J. Pelc, "Analysis of T_2 limitations and off-resonance effects on spatial resolution and artifacts in echo-planar imaging," *Magnetic Resonance in Medicine*, vol. 14, no. 1, pp. 123–139, 1990.

[69] G. Johnson and J. M. S. Hutchison, "The limitations of NMR recalled-echo imaging techniques," *Journal of Magnetic Resonance (1969)*, vol. 63, no. 1, pp. 14–30, 1985.

[70] C. De Panfilis and C. Schwarzbauer, "Positive or negative blips? the effect of phase encoding scheme on susceptibility-induced signal losses in EPI," *NeuroImage*, vol. 25, no. 1, pp. 112–121, 2005.

[71] R. Deichmann, J. A. Gottfried, C. Hutton, and R. Turner, "Optimized EPI for fMRI studies of the orbitofrontal cortex," *NeuroImage*, vol. 19, no. 2, pp. 430–441, 2003.

[72] Q. X. Yang, B. J. Dardzinski, S. Z. Li, P. J. Eslinger, and M. B. Smith, "Multi-gradient echo with susceptibility inhomogeneity compensation (MGESIC): Demonstration of fMRI in the olfactory cortex at 3.0 T," *Magnetic Resonance in Medicine*, vol. 37, no. 3, pp. 331–335, 1997.

[73] G. H. Glover, "3D z-shim method for reduction of susceptibility effects in BOLD fMRI," *Magnetic Resonance in Medicine*, vol. 42, no. 2, pp. 290–299, 1999.

[74] R. J. Ordidge, J. M. Gorell, J. C. Deniau, R. A. Knight, and J. A. Helpern, "Assessment of relative brain iron concentrations using T_2-weighted and T_2*-weighted MRI at 3 Tesla," *Magnetic Resonance in Medicine*, vol. 32, no. 3, pp. 335–341, 1994.

[75] C. Hutton, A. Bork, O. Josephs, R. Deichmann, J. Ashburner, and R. Turner, "Image distortion correction in fMRI: A quantitative evaluation," *NeuroImage*, vol. 16, no. 1, pp. 217–240, 2002.

[76] V. Roopchansingh, R. W. Cox, A. Jesmanowicz, B. D. Ward, and J. S. Hyde, "Single-shot magnetic field mapping embedded in echo-planar time-course imaging," *Magnetic Resonance in Medicine*, vol. 50, no. 4, pp. 839–843, 2003.

[77] P. Jezzard and R. S. Balaban, "Correction for geometric distortion in echo-planar images from B_0 field variations," *Magnetic Resonance in Medicine*, vol. 34, no. 1, pp. 65–73, 1995.

[78] P. Jezzard and S. Clare, "Sources of distortion in functional MRI data," *Human Brain Mapping*, vol. 8, no. 2-3, pp. 80–85, 1999.

[79] Y. M. Kadah and X. Hu, "Simulated phase evolution rewinding (SPHERE): A technique for reducing B_0 inhomogeneity effects in MR images," *Magnetic Resonance in Medicine*, vol. 38, no. 4, pp. 615–627, 1997.

[80] J. L. R. Andersson, S. Skare, and J. Ashburner, "How to correct susceptibility distortions in spin-echo echo-planar images: application to diffusion tensor imaging," *NeuroImage*, vol. 20, no. 2, pp. 870–888, 2003.

[81] P. S. Morgan, R. W. Bowtell, D. J. McIntyre, and B. S. Worthington, "Correction of spatial distortion in EPI due to inhomogeneous static magnetic fields using the reversed gradient method," *Journal of Magnetic Resonance Imaging*, vol. 19, no. 4, pp. 499–507, 2004.

[82] D. Holland, J. M. Kuperman, and A. M. Dale, "Efficient correction of inhomogeneous static magnetic field-induced distortion in echo planar imaging," *NeuroImage*, vol. 50, no. 1, pp. 175–183, 2010.

[83] H. Chang and J. M. Fitzpatrick, "A technique for accurate magnetic resonance imaging in the presence of field inhomogeneities," *Medical Imaging, IEEE Transactions on*, vol. 11, no. 3, pp. 319–329, 1992.

[84] M. D. Robson, J. C. Gore, and R. T. Constable, "Measurement of the point spread function in MRI using constant time imaging," *Magnetic Resonance in Medicine*, vol. 38, no. 5, pp. 733–740, 1997.

[85] N.-k. Chen and A. M. Wyrwicz, "Correction for EPI distortions using multi-echo gradient-echo imaging," *Magnetic Resonance in Medicine*, vol. 41, no. 6, pp. 1206–1213, 1999.

[86] ——, "Optimized distortion correction technique for echo planar imaging," *Magnetic Resonance in Medicine*, vol. 45, no. 3, pp. 525–528, 2001.

[87] H. Zeng and R. T. Constable, "Image distortion correction in EPI: Comparison of field mapping with point spread function mapping," *Magnetic Resonance in Medicine*, vol. 48, no. 1, pp. 137–146, 2002.

[88] M. Zaitsev, J. Hennig, and O. Speck, "Point spread function mapping with parallel imaging techniques and high acceleration factors: Fast, robust, and flexible method for echo-planar imaging distortion correction," *Magnetic Resonance in Medicine*, vol. 52, no. 5, pp. 1156–1166, 2004.

[89] Q.-S. Xiang and F. Q. Ye, "Correction for geometric distortion and N/2 ghosting in EPI by phase labeling for additional coordinate encoding (PLACE)," *Magnetic Resonance in Medicine*, vol. 57, no. 4, pp. 731–741, 2007.

[90] O. Speck, J. Stadler, and M. Zaitsev, "High resolution single-shot EPI at 7T," *Magnetic Resonance Materials in Physics, Biology and Medicine*, vol. 21, no. 1, pp. 73–86, 2008.

[91] Y. M. Kadah and X. Hu, "Algebraic reconstruction for magnetic resonance imaging under B_0 inhomogeneity," *IEEE Transactions on Medical Imaging*, vol. 17, no. 3, pp. 362–370, 1998.

[92] P. Munger, G. R. Crelier, T. M. Peters, and G. B. Pike, "An inverse problem approach to the correction of distortion in EPI images," *IEEE Transactions on Medical Imaging*, vol. 19, no. 7, pp. 681–689, 2000.

[93] B. P. Sutton, D. C. Noll, and J. A. Fessler, "Fast, iterative image reconstruction for MRI in the presence of field inhomogeneities," *Medical Imaging, IEEE Transactions on*, vol. 22, no. 2, pp. 178–188, 2003.

[94] J. A. Fessler, S. Lee, V. T. Olafsson, H. R. Shi, and D. C. Noll, "Toeplitz-based iterative image reconstruction for MRI with correction for magnetic field inhomogeneity," *Signal Processing, IEEE Transactions on*, vol. 53, no. 9, pp. 3393–3402, 2005.

[95] G. X. Liu and S. Ogawa, "EPI image reconstruction with correction of distortion and signal losses," *Journal of Magnetic Resonance Imaging*, vol. 24, no. 3, pp. 683–689, 2006.

[96] M. V. W. Zibetti and A. R. De Pierro, "A new distortion model for strong inhomogeneity problems in echo-planar MRI," *Medical Imaging, IEEE Transactions on*, vol. 28, no. 11, pp. 1736–1753, 2009.

[97] A. M. Blamire, S. Ogawa, K. Ugurbil, D. Rothman, G. McCarthy, J. M. Ellermann, F. Hyder, Z. Rattner, and R. G. Shulman, "Dynamic mapping of the

human visual cortex by high speed magnetic resonace imaging," *Proceedings of the National Academy of Sciences of the United States of America*, vol. 89, no. 22, pp. 11 069–11 073, 1992.

[98] I. R. Young, I. J. Cox, D. J. Bryant, and G. M. Bydder, "The benefits of increasing spatial resolution as a means of reducing artifacts due to field inhomogeneities," *Magnetic Resonance Imaging*, vol. 6, no. 5, pp. 585–590, 1988.

[99] E. M. Haacke, J. A. Tkach, and T. B. Parrish, "Reduction of a T_2* dephasing in gradient field echo imaging," *Radiology*, vol. 170, no. 2, pp. 457–462, 1989.

[100] J. R. Reichenbach, R. Venkatesan, D. A. Yablonskiy, M. R. Thompson, S. Lai, and E. M. Haacke, "Theory and application of static field inhomogeneity effects in gradient-echo imaging," *Journal of Magnetic Resonance Imaging*, vol. 7, no. 2, pp. 266–279, 1997.

[101] A. Jesmanowicz, B. B. Biswal, and J. S. Hyde, "Reduction in GR-EPI intravoxel dephasing using thin slices and short TE." in *Proceedings of the International Society for Magnetic Resonance in Medicine*, 1999.

[102] K.-D. Merboldt, J. Finsterbusch, and J. Frahm, "Reducing inhomogeneity artifacts in functional MRI of human brain activation–thin sections vs gradient compensation," *Journal of Magnetic Resonance*, vol. 145, no. 2, pp. 184–191, 2000.

[103] Y. Z. Wadghiri, G. Johnson, and D. H. Turnbull, "Sensitivity and performance time in MRI dephasing artifact reduction methods," *Magnetic Resonance in Medicine*, vol. 45, no. 3, pp. 470–476, 2001.

[104] S. Robinson, C. Windischberger, A. Rauscher, and E. Moser, "Optimized 3T EPI of the amygdalae," *NeuroImage*, vol. 22, no. 1, pp. 203–210, 2004.

[105] P. S. F. Bellgowan, P. A. Bandettini, P. van Gelderen, A. Martin, and J. Bodurka, "Improved BOLD detection in the medial temporal region using parallel imaging and voxel volume reduction," *NeuroImage*, vol. 29, no. 4, pp. 1244–1251, 2006.

[106] K.-J. Jung, H. Peng, T. Zhao, G. Avidan, and M. Behrmann, "Recovery of signal loss due to an in-plane susceptibility gradient in the gradient echo EPI through acquisition of extended phase-encoding lines," *Magnetic Resonance Imaging*, vol. 28, no. 6, pp. 777–783, 2010.

[107] M. J. E. Golay, "Field homogenizing coils for nuclear spin resonance instrumentation," *Review of Scientific Instruments*, vol. 29, no. 4, pp. 313–315, 1958.

[108] R. Gruetter, "Automatic, localized in vivo adjustment of all first-and second-order shim coils," *Magnetic Resonance in Medicine*, vol. 29, no. 6, pp. 804–811, 1993.

[109] J. Shen, R. E. Rycyna, and D. L. Rothman, "Improvements on an *in Vivo* automatic shimming method (FASTERMAP)," *Magnetic Resonance in Medicine*, vol. 38, no. 5, pp. 834–839, 1997.

[110] J. Shen, D. L. Rothman, H. P. Hetherington, and J. W. Pan, "Linear projection method for automatic slice shimming," *Magnetic Resonance in Medicine*, vol. 42, no. 6, pp. 1082–1088, 1999.

[111] R. Gruetter and I. Tkac, "Field mapping without reference scan using asymmetric echo-planar techniques," *Magnetic Resonance in Medicine*, vol. 43, no. 2, pp. 319–323, 2000.

[112] K. M. Koch, D. L. Rothman, and R. A. de Graaf, "Optimization of static magnetic field homogeneity in the human and animal brain in vivo," *Progress in Nuclear Magnetic Resonance Spectroscopy*, vol. 54, no. 2, pp. 69–96, 2009.

[113] C. Juchem, T. W. Nixon, S. McIntyre, D. L. Rothman, and R. A. d. Graaf, "Magnetic field homogenization of the human prefrontal cortex with a set of localized electrical coils," *Magnetic Resonance in Medicine*, vol. 63, no. 1, pp. 171–180, 2010.

[114] J. L. Wilson, M. Jenkinson, I. de Araujo, M. L. Kringelbach, E. T. Rolls, and P. Jezzard, "Fast, fully automated global and local magnetic field optimization for fMRI of the human brain," *NeuroImage*, vol. 17, no. 2, pp. 967–976, 2002.

[115] E. Balteau, C. Hutton, and N. Weiskopf, "Improved shimming for fMRI specifically optimizing the local BOLD sensitivity," *NeuroImage*, vol. 49, no. 1, pp. 327–336, 2010.

[116] T. Ernst and J. Hennig, "Double-volume ^{1}H spectroscopy with interleaved acquisitions using tilted gradients," *Magnetic Resonance in Medicine*, vol. 20, no. 1, pp. 27–35, 1991.

[117] A. M. Blamire, D. L. Rothman, and T. Nixon, "Dynamic shim updating: A new approach towards optimized whole brain shimming," *Magnetic Resonance in Medicine*, vol. 36, no. 1, pp. 159–165, 1996.

[118] R. A. d. Graaf, P. B. Brown, S. McIntyre, D. L. Rothman, and T. W. Nixon, "Dynamic shim updating (DSU) for multi-slice signal acquisition," *Magnetic Resonance in Medicine*, vol. 49, no. 3, pp. 409–416, 2003.

[119] K. M. Koch, S. McIntyre, T. W. Nixon, D. L. Rothman, and R. A. de Graaf, "Dynamic shim updating on the human brain," *Journal of Magnetic Resonance*, vol. 180, no. 2, pp. 286–296, 2006.

[120] J. L. Wilson and P. Jezzard, "Utilization of an intra-oral diamagnetic passive shim in functional MRI of the inferior frontal cortex," *Magnetic Resonance in Medicine*, vol. 50, no. 5, pp. 1089–1094, 2003.

[121] R. Cusack, B. Russell, S. M. L. Cox, C. De Panfilis, C. Schwarzbauer, and R. Ansorge, "An evaluation of the use of passive shimming to improve frontal sensitivity in fMRI," *NeuroImage*, vol. 24, no. 1, pp. 82–91, 2005.

[122] R. A. Osterbauer, J. L. Wilson, G. A. Calvert, and P. Jezzard, "Physical and physiological consequences of passive intra-oral shimming," *NeuroImage*, vol. 29, no. 1, pp. 245–253, 2006.

[123] J. J. Hsu and G. H. Glover, "Mitigation of susceptibility-induced signal loss in neuroimaging using localized shim coils," *Magnetic Resonance in Medicine*, vol. 53, no. 2, pp. 243–248, 2005.

[124] N. Weiskopf, C. Hutton, O. Josephs, and R. Deichmann, "Optimal EPI parameters for reduction of susceptibility-induced BOLD sensitivity losses: A whole-brain analysis at 3T and 1.5T," *NeuroImage*, vol. 33, no. 2, pp. 493–504, 2006.

[125] J. Rick, O. Speck, S. Maier, O. Tuscher, O. Dossel, J. Hennig, and M. Zaitsev, "Optimized EPI for fMRI using a slice-dependent template-based gradient compensation method to recover local susceptibility-induced signal loss," *Magnetic Resonance Materials in Physics, Biology and Medicine*, vol. 23, no. 3, pp. 165–176, 2010.

[126] Z. H. Cho and Y. M. Ro, "Reduction of susceptibility artifact in gradient-echo imaging," *Magnetic Resonance in Medicine*, vol. 23, no. 1, pp. 193–200, 1992.

[127] G. H. Glover and S. Lai, "Reduction of susceptibility effects in BOLD fMRI using tailored RF pulses," in *Proceedings of the International Society for Magnetic Resonance in Medicine*, vol. 1994, Sydney, 1998, p. 298.

[128] V. A. Stenger, F. E. Boada, and D. C. Noll, "Three-dimensional tailored RF pulses for the reduction of susceptibility artifacts in T_2*-weighted functional MRI," *Magnetic Resonance in Medicine*, vol. 44, no. 4, pp. 525–531, 2000.

[129] ——, "Multishot 3D slice-select tailored RF pulses for MRI," *Magnetic Resonance in Medicine*, vol. 48, no. 1, pp. 157–165, 2002.

[130] C.-y. Yip, J. A. Fessler, and D. C. Noll, "Advanced three-dimensional tailored RF pulse for signal recovery in T_2*-weighted functional magnetic resonance imaging," *Magnetic Resonance in Medicine*, vol. 56, no. 5, pp. 1050–1059, 2006.

[131] C.-Y. Yip, D. Yoon, V. Olafsson, S. Lee, W. A. Grissom, J. A. Fessler, and D. C. Noll, "Spectral-spatial pulse design for through-plane phase precompensatory slice selection in T_2*-weighted functional MRI," *Magnetic Resonance in Medicine*, vol. 61, no. 5, pp. 1137–1147, 2009.

[132] J. Y. Chung, H. W. Yoon, Y. B. Kim, H. W. Park, and Z. H. Cho, "Susceptibility compensated fMRI study using a tailored RF echo planar imaging sequence," *Journal of Magnetic Resonance Imaging*, vol. 29, no. 1, pp. 221–228, 2009.

[133] P. A. Bandettini, A. Jesmanowicz, E. C. Wong, and J. S. Hyde, "Processing strategies for time-course data sets in functional MRI of the human brain," *Magnetic Resonance in Medicine*, vol. 30, no. 2, pp. 161–173, 1993.

[134] A. Prinster, C. Pierpaoli, R. Turner, and P. Jezzard, "Simultaneous measurement of ΔR_2 and ΔR_2^* in cat brain during hypoxia and hypercapnia," *NeuroImage*, vol. 6, no. 3, pp. 191–200, 1997.

[135] C. Schwarzbauer, T. Mildner, W. Heinke, M. Brett, and R. Deichmann, "Dual echo EPI - the method of choice for fMRI in the presence of magnetic field inhomogeneities?" *NeuroImage*, vol. 49, no. 1, pp. 316–326, 2010.

[136] C. Schwarzbauer and D. A. Porter, "Single shot partial dual echo (SPADE) EPI-an efficient acquisition scheme for reducing susceptibility artefacts in fMRI," *NeuroImage*, vol. 49, no. 3, pp. 2234–2237, 2010.

[137] R. A. Jones, T. Schirmer, B. Lipinski, G. K. Elbel, and D. P. Auer, "Signal undershoots following visual stimulation: A comparison of gradient and spin-echo BOLD sequences," *Magnetic Resonance in Medicine*, vol. 40, no. 1, pp. 112–118, 1998.

[138] M. J. Lowe, J. T. Lurito, V. P. Mathews, M. D. Phillips, and G. D. Hutchins, "Quantitative comparison of functional contrast from BOLD-weighted spin-echo and gradient-echo echoplanar imaging at 1.5 Tesla and $H_2{}^{15}O$ PET in the whole brain," *J Cereb Blood Flow Metab*, vol. 20, no. 9, pp. 1331–1340, 2000.

[139] D. G. Norris, S. Zysset, T. Mildner, and C. J. Wiggins, "An investigation of the value of spin-echo-based fMRI using a Stroop color-word matching task and EPI at 3 T," *NeuroImage*, vol. 15, no. 3, pp. 719–726, 2002.

[140] C. F. Schmidt, P. Boesiger, and A. Ishai, "Comparison of fMRI activation as measured with gradient- and spin-echo EPI during visual perception," *NeuroImage*, vol. 26, no. 3, pp. 852–859, 2005.

[141] P. W. Stroman, V. Krause, U. N. Frankenstein, K. L. Malisza, and B. Tomanek, "Spin-echo versus gradient-echo fMRI with short echo times," *Magnetic Resonance Imaging*, vol. 19, no. 6, pp. 827–831, 2001.

[142] S. Naganawa, D. G. Norris, S. Zysset, and T. Mildner, "Regional differences of fMRI signal changes induced by hyperventilation: Comparison between SE-EPI and GE-EPI at 3T," *Journal of Magnetic Resonance Imaging*, vol. 15, no. 1, pp. 23–30, 2002.

[143] L. M. Parkes, J. V. Schwarzbach, A. A. Bouts, R. H. R. Deckers, P. Pullens, C. M. Kerskens, and D. G. Norris, "Quantifying the spatial resolution of the gradient echo and spin echo BOLD response at 3 Tesla," *Magnetic Resonance in Medicine*, vol. 54, no. 6, pp. 1465–1472, 2005.

[144] L. Pauling and C. D. Coryell, "The magnetic properties and structure of hemoglobin, oxyhemoglobin and carbonmonoxyhemoglobin," *Proceedings of the National Academy of Sciences of the United States of America*, vol. 22, pp. 210–216, 1936.

[145] D. Norris, "Principles of magnetic resonance assessment of brain function," *Journal of Magnetic Resonance Imaging*, vol. 23, no. 6, pp. 794–807, 2006.

[146] S. Ogawa, R. S. Menon, D. W. Tank, S. G. Kim, H. Merkle, J. M. Ellermann, and K. Ugurbil, "Functional brain mapping by blood oxygenation level dependent contrast magnetic resonance imaging - a comparison of signal characteristics with a biophysical model," *Biophysical Journal*, vol. 64, no. 3, pp. 803–812, 1993.

[147] P. Fox, M. Raichle, M. Mintun, and C. Dence, "Nonoxidative glucose consumption during focal physiologic neural activity," *Science*, vol. 241, no. 4864, pp. 462–464, 1988.

[148] J. Hennig, T. Ernst, O. Speck, G. Deuschl, and E. Feifel, "Detection of brain activation using oxygenation sensitive functional spectroscopy," *Magnetic Resonance in Medicine*, vol. 31, no. 1, pp. 85–90, 1994.

[149] R. B. Buxton, K. Uludag, D. J. Dubowitz, and T. T. Liu, "Modeling the hemodynamic response to brain activation," *NeuroImage*, vol. 23, pp. S220–S233, 2004.

[150] J. Frahm, G. Kruger, K. D. Merboldt, and A. Kleinschmidt, "Dynamic uncoupling and recoupling of perfusion and oxidative metabolism during focal brain activation in man," *Magnetic Resonance in Medicine*, vol. 35, no. 2, pp. 143–148, 1996.

[151] R. B. Buxton, E. C. Wong, and L. R. Frank, "Dynamics of blood flow and oxygenation changes during brain activation: The balloon model," *Magnetic Resonance in Medicine*, vol. 39, no. 6, pp. 855–864, 1998.

[152] P. Jezzard, P. M. Matthews, and S. M. Smith, *Functional MRI: An Introduction to Methods*. Oxford: Oxford Univarity Press, 2001.

[153] R. M. Birn, "The role of physiological noise in resting-state functional connectivity," *NeuroImage*, vol. 62, no. 2, pp. 864–870, 2012.

[154] M. J. Lowe, B. J. Mock, and J. A. Sorenson, "Functional connectivity in single and multislice echoplanar imaging using resting-state fluctuations," in *2nd International Conference on Functional Mapping of the Human Brain*. Boston, Massachusetts: Academic Press Inc, 1996, pp. 119–132.

[155] ——, "Functional connectivity in single and multislice echoplanar imaging using resting-state fluctuations," *NeuroImage*, vol. 7, no. 2, pp. 119–132, 1998.

[156] D. Cordes, V. M. Haughton, K. Arfanakis, J. D. Carew, P. A. Turski, C. H. Moritz, M. A. Quigley, and M. E. Meyerand, "Frequencies contributing to functional connectivity in the cerebral cortex in "resting-state" data," *American Journal of Neuroradiology*, vol. 22, no. 7, pp. 1326–1333, 2001.

[157] M. Hampson, B. S. Peterson, P. Skudlarski, J. C. Gatenby, and J. C. Gore, "Detection of functional connectivity using temporal correlations in MR images," *Human Brain Mapping*, vol. 15, no. 4, pp. 247–262, 2002.

[158] M. E. Raichle, A. M. MacLeod, A. Z. Snyder, W. J. Powers, D. A. Gusnard, and G. L. Shulman, "A default mode of brain function," *Proceedings of the National Academy of Sciences of the United States of America*, vol. 98, no. 2, pp. 676–682, 2001.

[159] M. D. Fox, A. Z. Snyder, J. L. Vincent, M. Corbetta, D. C. Van Essen, and M. E. Raichle, "The human brain is intrinsically organized into dynamic, anticorrelated functional networks," *Proceedings of the National Academy of Sciences of the United States of America*, vol. 102, no. 27, pp. 9673–9678, 2005.

[160] P. Fransson, "Spontaneous low-frequency BOLD signal fluctuations: An fMRI investigation of the resting-state default mode of brain function hypothesis," *Human Brain Mapping*, vol. 26, no. 1, pp. 15–29, 2005.

[161] M. D. Greicius, B. Krasnow, A. L. Reiss, and V. Menon, "Functional connectivity in the resting brain: A network analysis of the default mode hypothesis," *Proceedings of the National Academy of Sciences of the United States of America*, vol. 100, no. 1, pp. 253–258, 2003.

[162] H. Laufs, K. Krakow, P. Sterzer, E. Eger, A. Beyerle, A. Salek-Haddadi, and A. Kleinschmidt, "Electroencephalographic signatures of attentional and cognitive default modes in spontaneous brain activity fluctuations at rest," *Proceedings of the National Academy of Sciences of the United States of America*, vol. 100, no. 19, pp. 11 053–11 058, 2003.

[163] M. D. Fox, M. Corbetta, A. Z. Snyder, J. L. Vincent, and M. E. Raichle, "Spontaneous neuronal activity distinguishes human dorsal and ventral attention systems," *Proceedings of the National Academy of Sciences*, vol. 103, no. 26, pp. 10 046–10 051, 2006.

[164] S. A. R. B. Rombouts, C. J. Stam, J. P. A. Kuijer, P. Scheltens, and F. Barkhof, "Identifying confounds to increase specificity during a "no task condition": Evidence for hippocampal connectivity using fMRI," *NeuroImage*, vol. 20, no. 2, pp. 1236–1245, 2003.

[165] J. L. Vincent, A. Z. Snyder, M. D. Fox, B. J. Shannon, J. R. Andrews, M. E. Raichle, and R. L. Buckner, "Coherent spontaneous activity identifies a hippocampal-parietal memory network," *J Neurophysiol*, vol. 96, no. 6, pp. 3517–3531, 2006.

[166] C. F. Beckmann, M. DeLuca, J. T. Devlin, and S. M. Smith, "Investigations into resting-state connectivity using independent component analysis," *Philo-*

sophical Transactions of the Royal Society B: Biological Sciences, vol. 360, no. 1457, pp. 1001–1013, 2005.

[167] J. S. Damoiseaux, S. Rombouts, F. Barkhof, P. Scheltens, C. J. Stam, S. M. Smith, and C. F. Beckmann, "Consistent resting-state networks across healthy subjects," *Proceedings of the National Academy of Sciences of the United States of America*, vol. 103, no. 37, pp. 13 848–13 853, 2006.

[168] M. De Luca, C. F. Beckmann, N. De Stefano, P. M. Matthews, and S. M. Smith, "fMRI resting state networks define distinct modes of long-distance interactions in the human brain," *NeuroImage*, vol. 29, no. 4, pp. 1359–1367, 2006.

[169] S. M. Smith, P. T. Fox, K. L. Miller, D. C. Glahn, P. M. Fox, C. E. Mackay, N. Filippini, K. E. Watkins, R. Toro, A. R. Laird, and C. F. Beckmann, "Correspondence of the brain's functional architecture during activation and rest," *Proceedings of the National Academy of Sciences of the United States of America*, vol. 106, no. 31, pp. 13 040–13 045, 2009.

[170] M. Greicius, "Resting-state functional connectivity in neuropsychiatric disorders," *Current Opinion in Neurology*, vol. 21, no. 4, pp. 424–430, 2008.

[171] S.-J. Li, Z. Li, G. Wu, M.-J. Zhang, M. Franczak, and P. G. Antuono, "Alzheimer disease: Evaluation of a functional MR imaging index as a marker," *Radiology*, vol. 225, no. 1, pp. 253–259, 2002.

[172] W. W. Seeley, R. K. Crawford, J. Zhou, B. L. Miller, and M. D. Greicius, "Neurodegenerative diseases target large-scale human brain networks," *Neuron*, vol. 62, no. 1, pp. 42–52, 2009.

[173] C. Sorg, V. Riedl, M. Mhlau, V. D. Calhoun, T. Eichele, L. Ler, A. Drzezga, H. Frstl, A. Kurz, C. Zimmer, and A. M. Wohlschlger, "Selective changes of resting-state networks in individuals at risk for alzheimer's disease," *Proceedings of the National Academy of Sciences of the United States of America*, vol. 104, no. 47, pp. 18 760–18 765, 2007.

[174] K. Wang, M. Liang, L. Wang, L. Tian, X. Zhang, K. Li, and T. Jiang, "Altered functional connectivity in early Alzheimer's disease: A resting-state fMRI study," *Human Brain Mapping*, vol. 28, no. 10, pp. 967–978, 2007.

[175] K. Wang, T. Jiang, M. Liang, L. Wang, L. Tian, X. Zhang, K. Li, and Z. Liu, "Discriminative analysis of early Alzheimers disease based on two intrinsically anti-correlated networks with resting-state fMRI," 2006, pp. 340–347.

[176] V. L. Cherkassky, R. K. Kana, T. A. Keller, and M. A. Just, "Functional connectivity in a baseline resting-state network in autism," *Neuroreport*, vol. 17, no. 16, pp. 1687–1690, 2006.

[177] D. P. Kennedy and E. Courchesne, "The intrinsic functional organization of the brain is altered in autism," *NeuroImage*, vol. 39, no. 4, pp. 1877–1885, 2008.

[178] C. S. Monk, S. J. Peltier, J. L. Wiggins, S.-J. Weng, M. Carrasco, S. Risi, and C. Lord, "Abnormalities of intrinsic functional connectivity in autism spectrum disorders," *NeuroImage*, vol. 47, no. 2, pp. 764–772, 2009.

[179] T. B. Jones, P. A. Bandettini, L. Kenworthy, L. K. Case, S. C. Milleville, A. Martin, and R. M. Birn, "Sources of group differences in functional connectivity: an investigation applied to autism spectrum disorder," *NeuroImage*, vol. 49, no. 1, pp. 401–14, 2010.

[180] F. X. Castellanos, D. S. Margulies, C. Kelly, L. Q. Uddin, M. Ghaffari, A. Kirsch, D. Shaw, Z. Shehzad, A. Di Martino, B. Biswal, E. J. S. Sonuga-Barke, J. Rotrosen, L. A. Adler, and M. P. Milham, "Cingulate-precuneus interactions: A new locus of dysfunction in adult attention-deficit/hyperactivity disorder," *Biological Psychiatry*, vol. 63, no. 3, pp. 332–337, 2008.

[181] L. Wang, C. Zhu, Y. He, Y. Zang, Q. Cao, H. Zhang, Q. Zhong, and Y. Wang, "Altered small-world brain functional networks in children with attention-deficit/hyperactivity disorder," *Human Brain Mapping*, vol. 30, no. 2, pp. 638–649, 2009.

[182] C. Z. Zhu, Y. F. Zang, M. Liang, L. X. Tian, Y. He, X. B. Li, M. Q. Sui, Y. F. Wang, and T. Z. Jiang, "Discriminative analysis of brain function at resting-state for attention-deficit/hyperactivity disorder," *Med Image Comput Comput Assist Interv*, vol. 8, no. Pt 2, pp. 468–75, 2005.

[183] C.-Z. Zhu, Y.-F. Zang, Q.-J. Cao, C.-G. Yan, Y. He, T.-Z. Jiang, M.-Q. Sui, and Y.-F. Wang, "Fisher discriminative analysis of resting-state brain function for attention-deficit/hyperactivity disorder," *NeuroImage*, vol. 40, no. 1, pp. 110–120, 2008.

[184] A. Anand, Y. Li, Y. Wang, J. Wu, S. Gao, L. Bukhari, V. P. Mathews, A. Kalnin, and M. J. Lowe, "Activity and connectivity of brain mood regulating circuit in depression: A functional magnetic resonance study," *Biological Psychiatry*, vol. 57, no. 10, pp. 1079–1088, 2005.

[185] ——, "Antidepressant Effect on Connectivity of the Mood-Regulating Circuit: An fMRI Study," *Neuropsychopharmacology*, vol. 30, no. 7, pp. 1334–1344, 2005.

[186] M. D. Greicius, B. H. Flores, V. Menon, G. H. Glover, H. B. Solvason, H. Kenna, A. L. Reiss, and A. F. Schatzberg, "Resting-state functional connectivity in major depression: Abnormally increased contributions from subgenual cingulate cortex and thalamus," *Biological Psychiatry*, vol. 62, no. 5, pp. 429–437, 2007.

[187] R. L. Bluhm, J. Miller, R. A. Lanius, E. A. Osuch, K. Boksman, R. Neufeld, J. Theberge, B. Schaefer, and P. Williamson, "Spontaneous low-frequency fluctuations in the BOLD signal in schizophrenic patients: Anomalies in the default network," *Schizophrenia Bulletin*, vol. 33, no. 4, pp. 1004–1012, 2007.

[188] Y. Zhou, M. Liang, L. Tian, K. Wang, Y. Hao, H. Liu, Z. Liu, and T. Jiang, "Functional disintegration in paranoid schizophrenia using resting-state fMRI," *Schizophrenia Research*, vol. 97, no. 1-3, pp. 194–205, 2007.

[189] J. R. Andrews-Hanna, A. Z. Snyder, J. L. Vincent, C. Lustig, D. Head, M. E. Raichle, and R. L. Buckner, "Disruption of large-scale brain systems in advanced aging," *Neuron*, vol. 56, no. 5, pp. 924–935, 2007.

[190] J. Damoiseaux, C. Beckmann, E. S. Arigita, F. Barkhof, P. Scheltens, C. Stam, S. Smith, and S. Rombouts, "Reduced resting-state brain activity in the "default network" in normal aging," *Cerebral Cortex*, vol. 18, no. 8, pp. 1856–1864, 2008.

[191] M. J. Lowe, M. D. Phillips, J. T. Lurito, D. Mattson, M. Dzemidzic, and V. P. Mathews, "Multiple sclerosis: Low-frequency temporal blood oxygen level-dependent fluctuations indicate reduced functional connectivity - initial results," *Radiology*, vol. 224, no. 1, pp. 184–192, 2002.

[192] H. Liu, R. L. Buckner, T. Talukdar, N. Tanaka, J. R. Madsen, and S. M. Stufflebeam, "Task-free presurgical mapping using functional magnetic resonance imaging intrinsic activity," *Journal of Neurosurgery*, vol. 111, no. 4, pp. 746–754, 2009.

[193] J. S. Shimony, D. Zhang, J. M. Johnston, M. D. Fox, A. Roy, and E. C. Leuthardt, "Resting-state spontaneous fluctuations in brain activity: A new paradigm for presurgical planning using fMRI," *Academic Radiology*, vol. 16, no. 5, pp. 578–583, 2009.

[194] M. S. Dagli, J. E. Ingeholm, and J. V. Haxby, "Localization of Cardiac-Induced Signal Change in fMRI," *NeuroImage*, vol. 9, no. 4, pp. 407–415, 1999.

[195] J. R. Brosch, T. M. Talavage, J. L. Ulmer, and J. A. Nyenhuis, "Simulation of human respiration in fMRI with a mechanical model," *IEEE Transactions on Biomedical Engineering*, vol. 49, no. 7, pp. 700–707, 2002.

[196] D. Raj, A. W. Anderson, and J. C. Gore, "Respiratory effects in human functional magnetic resonance imaging due to bulk susceptibility changes," *Physics in Medicine and Biology*, vol. 46, no. 12, p. 3331, 2001.

[197] V. Kiviniemi, J. Ruohonen, and O. Tervonen, "Separation of physiological very low frequency fluctuation from aliasing by switched sampling interval fMRI scans," *Magnetic Resonance Imaging*, vol. 23, no. 1, pp. 41–46, 2005.

[198] S. J. Peltier and D. C. Noll, "T_2* dependence of low frequency functional connectivity," *NeuroImage*, vol. 16, no. 4, pp. 985–992, 2002.

[199] M. Quigley, D. Cordes, P. Turski, C. Moritz, V. Haughton, R. Seth, and M. E. Meyerand, "Role of the corpus callosum in functional connectivity," *American Journal of Neuroradiology*, vol. 24, no. 2, pp. 208–212, 2003.

[200] J. M. Johnston, S. N. Vaishnavi, M. D. Smyth, D. Zhang, B. J. He, J. M. Zempel, J. S. Shimony, A. Z. Snyder, and M. E. Raichle, "Loss of Resting Interhemispheric Functional Connectivity after Complete Section of the Corpus Callosum," *The Journal of Neuroscience*, vol. 28, no. 25, pp. 6453–6458, 2008.

[201] F. M. Krienen and R. L. Buckner, "Segregated Fronto-Cerebellar Circuits Revealed by Intrinsic Functional Connectivity," *Cerebral Cortex*, vol. 19, no. 10, pp. 2485–2497, 2009.

[202] M. J. Turlough FitzGerald, G. Gruener, and E. Mtui, *Clinical Neuroanatomy and Neuroscience*, 5th ed. Philadelphia: Elsevier Saunders, 2007.

[203] K. J. Miller, K. E. Weaver, and J. G. Ojemann, "Direct electrophysiological measurement of human default network areas," *Proceedings of the National Academy of Sciences*, vol. 106, no. 29, pp. 12 174–12 177, 2009.

[204] K. J. Friston, J. T. Ashburner, S. J. Kiebel, T. E. Nichols, and W. D. Penny, *Statistical Parametric Mapping The Analysis of Funtional Brain Images*, 1st ed. Academic Press, 2007.

[205] M. Jenkinson, P. Bannister, M. Brady, and S. Smith, "Improved optimization for the robust and accurate linear registration and motion correction of brain images," *NeuroImage*, vol. 17, no. 2, pp. 825–841, 2002.

[206] K. J. Friston, K. J. Worsley, R. S. J. Frackowiak, J. C. Mazziotta, and A. C. Evans, "Assessing the significance of focal activations using their spatial extent," *Human Brain Mapping*, vol. 1, no. 3, pp. 210–220, 1994.

[207] R. A. Poldrack, J. A. Mumford, and T. E. Nichols, *Handbook of Functional MRI Data Analysis*, 1st ed. Cambridge University Press, 2011.

[208] D. M. Cole, S. M. Smith, and C. F. Beckmann, "Advances and pitfalls in the analysis and interpretation of resting-state fMRI data," *Frontiers in Systems Neuroscience*, vol. 4, 2010.

[209] K. J. Friston, A. P. Holmes, J. B. Poline, P. J. Grasby, S. C. R. Williams, R. S. J. Frackowiak, and R. Turner, "Analysis of fMRI time-series revisited," *NeuroImage*, vol. 2, no. 1, pp. 45–53, 1995.

[210] K. J. Worsley and K. J. Friston, "Analysis of fMRI time-series revisited - again," *NeuroImage*, vol. 2, no. 3, pp. 173–181, 1995.

[211] T. E. Lund, K. H. Madsen, K. Sidaros, W.-L. Luo, and T. E. Nichols, "Non-white noise in fMRI: Does modelling have an impact?" *NeuroImage*, vol. 29, no. 1, pp. 54–66, 2006.

[212] R. M. Birn, J. B. Diamond, M. A. Smith, and P. A. Bandettini, "Separating respiratory-variation-related neuronal-activity-related fluctuations in fluctuations from fMRI," *NeuroImage*, vol. 31, no. 4, pp. 1536–1548, 2006.

[213] G. H. Glover, T. Q. Li, and D. Ress, "Image-based method for retrospective correction of physiological motion effects in fMRI: RETROICOR," *Magnetic Resonance in Medicine*, vol. 44, no. 1, pp. 162–167, 2000.

[214] E. Zarahn, G. K. Aguirre, and M. D'Esposito, "Empirical analyses of BOLD fMRI statistics," *NeuroImage*, vol. 5, no. 3, pp. 179–197, 1997.

[215] P. M. Macey, K. E. Macey, R. Kumar, and R. M. Harper, "A method for removal of global effects from fMRI time series," *NeuroImage*, vol. 22, no. 1, pp. 360–366, 2004.

[216] K. Murphy, R. M. Birn, D. A. Handwerker, T. B. Jones, and P. A. Bandettini, "The impact of global signal regression on resting state correlations: Are anti-correlated networks introduced?" *NeuroImage*, vol. 44, no. 3, pp. 893–905, 2009.

[217] V. Kiviniemi, J.-H. Kantola, J. Jauhiainen, A. Hyvrinen, and O. Tervonen, "Independent component analysis of nondeterministic fMRI signal sources," *NeuroImage*, vol. 19, no. 2, pp. 253–260, 2003.

[218] P. Comon, "Independent component analysis, a new concept?" *Signal Processing*, vol. 36, no. 3, pp. 287–314, 1994.

[219] M. J. McKeown, S. Makeig, G. G. Brown, T. P. Jung, S. S. Kindermann, A. J. Bell, and T. J. Sejnowski, "Analysis of fMRI data by blind separation into independent spatial components," *Human Brain Mapping*, vol. 6, no. 3, pp. 160–188, 1998.

[220] C. F. Beckmann and S. A. Smith, "Probabilistic independent component analysis for functional magnetic resonance imaging," *IEEE Transactions on Medical Imaging*, vol. 23, no. 2, pp. 137–152, 2004.

[221] G. A. F. Seber and A. J. Lee, *Linear Regression Analysis*. Wiley Interscience, 1977.

[222] P. L. Purdon and R. M. Weisskoff, "Effect of temporal autocorrelation due to physiological noise and stimulus paradigm on voxel-level false-positive rates in fMRI," *Human Brain Mapping*, vol. 6, no. 4, pp. 239–249, 1998.

[223] E. Bullmore, M. Brammer, S. C. R. Williams, S. Rabe-Hesketh, N. Janot, A. David, J. Mellers, R. Howard, and P. Sham, "Statistical methods of estimation and inference for functional MR image analysis," *Magnetic Resonance in Medicine*, vol. 35, no. 2, pp. 261–277, 1996.

[224] M. W. Woolrich, B. D. Ripley, M. Brady, and S. M. Smith, "Temporal autocorrelation in univariate linear modeling of fMRI data," *NeuroImage*, vol. 14, no. 6, pp. 1370–1386, 2001.

[225] E. T. Bullmore, J. Suckling, S. Overmeyer, S. Rabe-Hesketh, E. Taylor, and M. J. Brammer, "Global, voxel, and cluster tests, by theory and permutation, for a difference between two groups of structural MR images of the brain," *IEEE Transactions on Medical Imaging*, vol. 18, no. 1, pp. 32–42, 1999.

[226] R. Adler, *The geometry of random fields*. New York: Wiley, 1981.

[227] K. J. Worsley, S. Marrett, P. Neelin, and A. C. Evans, "Searching scale space for activation in PET images," *Human Brain Mapping*, vol. 4, no. 1, pp. 74–90, 1996.

[228] K. J. Worsley, S. Marrett, P. Neelin, A. C. Vandal, K. J. Friston, and A. C. Evans, "A unified statistical approach for determining significant signals in images of cerebral activation," *Human Brain Mapping*, vol. 4, no. 1, pp. 58–73, 1996.

[229] Y. Benjamini and Y. Hochberg, "Controlling the false discovery rate: A practical and powerful approach to multiple testing," *Journal of the Royal Statistical Society. Series B (Methodological)*, vol. 57, no. 1, pp. 289–300, 1995.

[230] C. R. Genovese, N. A. Lazar, and T. Nichols, "Thresholding of statistical maps in functional neuroimaging using the false discovery rate," *NeuroImage*, vol. 15, no. 4, pp. 870–878, 2002.

[231] C. F. Beckmann, M. Jenkinson, and S. M. Smith, "General multilevel linear modeling for group analysis in FMRI," *NeuroImage*, vol. 20, no. 2, pp. 1052–1063, 2003.

[232] M. W. Woolrich, T. E. J. Behrens, C. F. Beckmann, M. Jenkinson, and S. M. Smith, "Multilevel linear modelling for FMRI group analysis using bayesian inference," *NeuroImage*, vol. 21, no. 4, pp. 1732–1747, 2004.

[233] A. J. Bell and T. J. Sejnowski, "An information-maximization approach to blind separation and blind deconvolution," *Neural Computation*, vol. 7, no. 6, pp. 1129–1159, 1995.

[234] A. Hyvärinen, J. Karhunen, and E. Oja, *Independent Component Analysis*. New York: John Wiley & Sons, 2001.

[235] V. D. Calhoun and T. Adali, "Unmixing fMRI with independent component analysis - using ICA to characterize high-dimensional fMRI data in a concise manner," *IEEE Engineering in Medicine and Biology Magazine*, vol. 25, no. 2, pp. 79–90, 2006.

[236] M. E. Tipping and C. M. Bishop, "Mixtures of probabilistic principal component analyzers," *Neural Computation*, vol. 11, no. 2, pp. 443–482, 1999.

[237] T. P. Minka, "Automatic choice of dimensionality for PCA," *MIT Media Laboratory Perceptual Computing Section Technical Report No. 514*, 2000.

[238] W. D. Penny, S. Roberts, and R. Everson, "ICA: Model order selection and dynamic source models," in *Independent Component Analysis: Principles and Practice*, S. Roberts and R. Everson, Eds. Cambridge Universtiy Press, 2001.

[239] N. Delfosse and P. Loubaton, "Adaptive blind separation of independent sources: A deflation approach," *Signal Processing*, vol. 45, no. 1, pp. 59–83, 1995.

[240] A. Hyvärinen and E. Oja, "A fast fixed-point algorithm for independent component analysis," *Neural Computation*, vol. 9, no. 7, pp. 1483–1492, 1997.

[241] ——, "Independent component analysis by general nonlinear Hebbian-like learning rules," *Signal Processing*, vol. 64, no. 3, pp. 301–313, 1998.

[242] Z. Malouche and O. Macchi, "Adaptive unsupervised extraction of one component of a linear mixture with a single neuron," *Neural Networks, IEEE Transactions on*, vol. 9, no. 1, pp. 123–138, 1998.

[243] A. Hyvärinen, "Fast and robust fixed-point algorithms for independent component analysis," *Neural Networks, IEEE Transactions on*, vol. 10, no. 3, pp. 626–634, 1999.

[244] M. Gaeta and J. L. Lacoume, "Source separation without prior knowledge: the maximum likelihood solution," in *EUSIPCO'90*, 1990, pp. 621–624.

[245] D. T. Pham, P. Garrat, and C. Jutten, "Separation of a mixture of independent sources through a maximum likelihood approach," in *EUSIPCO*, 1992, pp. 771–774.

[246] D. T. Pham, "Blind separation of instantaneous mixture of sources via an independent component analysis," *Signal Processing, IEEE Transactions on*, vol. 44, no. 11, pp. 2768–2779, 1996.

[247] D. T. Pham and P. Garat, "Blind separation of mixture of independent sources through a quasi-maximum likelihood approach," *Signal Processing, IEEE Transactions on*, vol. 45, no. 7, pp. 1712–1725, 1997.

[248] J. F. Cardoso, "Infomax and maximum likelihood for blind source separation," *Signal Processing Letters, IEEE*, vol. 4, no. 4, pp. 112–114, 1997.

[249] D. Obradovic and G. Deco, "Information maximization and independent component analysis: Is there a difference?" *Neural Computation*, vol. 10, no. 8, pp. 2085–2101, 1998.

[250] J. F. Cardoso, "Source separation using higher order moments," in *IEEE Int. Conf. on Acoustics, Speech and Signal Processing (ICASSP'89)*, Glasgow, 1989, pp. 2109–2112.

[251] ——, "Eigen-structure of the fourth-order cumulant tensor with application to the blind source separation problem," in *IEEE Int. Conf. on Acoustics, Speech and Signal Processing (ICASSP'90)*, Albuquerque, New Mexico, 1990, pp. 2655–2658.

[252] J. F. Cardoso and A. Souloumiac, "Blind beamforming for non-gaussian signals," *Radar and Signal Processing, IEEE Proceedings F*, vol. 140, no. 6, pp. 362–370, 1993.

[253] P. Comon and B. Mourrain, "Decomposition of quantics in sums of powers of linear forms," *Signal Processing*, vol. 53, no. 23, pp. 93–107, 1996.

[254] B. S. Everitt and E. T. Bullmore, "Mixture model mapping of brain activation in functional magnetic resonance images," *Human Brain Mapping*, vol. 7, no. 1, pp. 1–14, 1999.

[255] N. V. Hartvig and J. L. Jensen, "Spatial mixture modeling of fMRI data," *Human Brain Mapping*, vol. 11, no. 4, pp. 233–248, 2000.

[256] S. Smith, M. Jenkinson, C. Beckmann, K. Miller, and M. Woolrich, "Meaningful design and contrast estimability in FMRI," *NeuroImage*, vol. 34, no. 1, pp. 127–136, 2007.

[257] C. Triantafyllou, R. D. Hoge, G. Krueger, C. J. Wiggins, A. Potthast, G. C. Wiggins, and L. L. Wald, "Comparison of physiological noise at 1.5 T, 3 T and 7 T and optimization of fMRI acquisition parameters," *NeuroImage*, vol. 26, no. 1, pp. 243–250, 2005.

[258] K. Murphy, J. Bodurka, and P. A. Bandettini, "How long to scan? the relationship between fMRI temporal signal to noise ratio and necessary scan duration," *NeuroImage*, vol. 34, no. 2, pp. 565–574, 2007.

[259] G. Kruger, A. Kastrup, and G. H. Glover, "Neuroimaging at 1.5 T and 3.0 T: Comparison of oxygenation-sensitive magnetic resonance imaging," *Magnetic Resonance in Medicine*, vol. 45, no. 4, pp. 595–604, 2001.

[260] W. A. Edelstein, G. H. Glover, C. J. Hardy, and R. W. Redington, "The intrinsic signal-to-noise ratio in NMR imaging," *Magnetic Resonance in Medicine*, vol. 3, no. 4, pp. 604–618, 1986.

[261] G. Kruger and G. H. Glover, "Physiological noise in oxygenation-sensitive magnetic resonance imaging," *Magnetic Resonance in Medicine*, vol. 46, no. 4, pp. 631–637, 2001.

[262] H. Gudbjartsson and S. Patz, "The rician distribution of noisy MRI data," *Magnetic Resonance in Medicine*, vol. 34, no. 6, pp. 910–914, 1995.

[263] K. Worsley, "Statistical analysis of activation images," in *Functional MRI An Introduction to Methods*, P. Jezzard, P. M. Matthews, and S. M. Smith, Eds. Oxford: Oxford University Press, 2001.

[264] W. A. Fuller, *Measurement Error Models*. New York: Wiley, 1987.

[265] M. D. Fox and M. Greicius, "Clinical applications of resting state functional connectivity," *Frontiers in Systems Neuroscience*, vol. 4, p. 19, 2010.

[266] R. Johnson, J. Marchini, S. Smith, and C. Beckmann, "Independent component analysis of functional magnetic resonance imaging data using wavelet dictionaries," in *Independent Component Analysis and Signal Separation*, ser. Lecture Notes in Computer Science, M. E. Davies, C. J. James, S. A. Abdallah, and M. D. Plumbley, Eds. Springer Berlin Heidelberg, 2007, vol. 4666, pp. 625–632.

[267] S. M. Smith, "Fast robust automated brain extraction," *Human Brain Mapping*, vol. 17, no. 3, pp. 143–155, 2002.

[268] R. T. Constable, "Functional MR imaging using gradient-echo echo-planar imaging in the presence of large static field inhomogeneities," *Journal of Magnetic Resonance Imaging*, vol. 5, no. 6, pp. 746–752, 1995.

[269] Q. X. Yang, G. D. Williams, R. J. Demeure, T. J. Mosher, and M. B. Smith, "Removal of local field gradient artifacts in T_2*-weighted images at high fields by gradient-echo slice excitation profile imaging," *Magnetic Resonance in Medicine*, vol. 39, no. 3, pp. 402–409, 1998.

[270] R. T. Constable and D. D. Spencer, "Composite image formation in z-shimmed functional MR imaging," *Magnetic Resonance in Medicine*, vol. 42, no. 1, pp. 110–117, 1999.

[271] D. Cordes, V. M. Haughton, K. Arfanakis, G. J. Wendt, P. A. Turski, C. H. Moritz, M. A. Quigley, and M. E. Meyerand, "Mapping functionally related regions of brain with functional connectivity MR imaging," *American Journal of Neuroradiology*, vol. 21, no. 9, pp. 1636–1644, 2000.

[272] H. Gu, H. Feng, W. Zhan, S. Xu, D. A. Silbersweig, E. Stern, and Y. Yang, "Single-shot interleaved z-shim EPI with optimized compensation for signal losses due to susceptibility-induced field inhomogeneity at 3 T," *NeuroImage*, vol. 17, no. 3, pp. 1358–1364, 2002.

[273] Y. P. P. Du, M. Dalwani, K. Wylie, E. Claus, and J. R. Tregellas, "Reducing susceptibility artifacts in fMRI using volume-selective z-shim compensation," *Magnetic Resonance in Medicine*, vol. 57, no. 2, pp. 396–404, 2007.

[274] H. Marshall, J. V. Hajnal, J. E. Warren, R. J. Wise, and D. J. Larkman, "An efficient automated z-shim based method to correct through-slice signal loss in EPI at 3T," *Magnetic Resonance Materials in Physics Biology and Medicine*, vol. 22, no. 3, pp. 187–200, 2009.

[275] K. A. Heberlein and X. Hu, "Simultaneous acquisition of gradient-echo and asymmetric spin-echo for single-shot z-shim: Z-SAGA," *Magnetic Resonance in Medicine*, vol. 51, no. 1, pp. 212–216, 2004.

[276] J. Pauly, D. Nishimura, and A. Macovski, "A k-space analysis of small-tip-angle excitation," *Journal of Magnetic Resonance*, vol. 81, no. 1, pp. 43–56, 1989.

[277] A. W. Song, "Single-shot EPI with signal recovery from the susceptibility-induced losses," *Magnetic Resonance in Medicine*, vol. 46, no. 2, pp. 407–411, 2001.

[278] H. Guo and A. W. Song, "Single-shot spiral image acquisition with embedded z-shimming for susceptibility signal recovery," *Journal of Magnetic Resonance Imaging*, vol. 18, no. 3, pp. 389–395, 2003.

[279] T.-K. Truong and A. W. Song, "Single-shot dual-z-shimmed sensitivity-encoded spiral-in/out imaging for functional MRI with reduced susceptibility artifacts," *Magnetic Resonance in Medicine*, vol. 59, no. 1, pp. 221–227, 2008.

[280] K. A. Heberlein and X. P. Hu, "Auto-calibrating the z-shim for slice secific recovery of susceptibility losses," in *Proceedings of the International Society for Magnetic Resonance in Medicine*, Miami, 2005.

[281] G. M. Bydder and I. R. Young, "MR Imaging: Clinical Use of the Inversion Recovery Sequence," *Journal of Computer Assisted Tomography*, vol. 9, no. 4, pp. 659–675, 1985.

[282] T. W. Redpath and F. W. Smith, "Imaging gray brain matter with a double-inversion pulse sequence to suppress CSF and white matter signals," *Magnetic Resonance Materials in Physics, Biology and Medicine*, vol. 2, no. 3, pp. 451–455, 1994.

[283] ——, "Use of a double inversion recovery pulse sequence to image selectively grey or white brain matter," *British Journal of Radiology*, vol. 67, no. 804, pp. 1258–1263, 1994.

[284] J. Listerud, J. Mitchell, L. Bagley, and R. Grossman, "OIL FLAIR: Optimized interleaved fluid-attenuated inversion recovery in 2D fast spin echo," *Magnetic Resonance in Medicine*, vol. 36, no. 2, pp. 320–325, 1996.

[285] S. P. Meara, P. A. Boulby, and G. J. Barker, "Implementation of a double inversion-recovery sequence with an echo-planar imaging readout: Application

to functional magnetic resonance imaging," in *Proceedings of the International Society for Magnetic Resonance in Medicine*, Miami, 2005, p. 494.

[286] C. Lin, M. A. Bernstein, J. Huston, and S. Fain, "Measurements of T_1 Relaxation times at 3.0T: Implications for clinical MRA," in *Proceedings of the International Society for Magnetic Resonance in Medicine*, Glasgow, 2001, p. 1391.

[287] P. Wright, O. Mougin, J. Totman, A. Peters, M. Brookes, R. Coxon, P. Morris, M. Clemence, S. Francis, R. Bowtell, and P. Gowland, "Water proton T_1 measurements in brain tissue at 7, 3, and 1.5T using IR-EPI, IR-TSE, and MPRAGE: results and optimization," *Magnetic Resonance Materials in Physics, Biology and Medicine*, vol. 21, no. 1, pp. 121–130, 2008.

[288] J. M. Wild, W. W. Martin, and P. S. Allen, "Multiple gradient echo sequence optimized for rapid, single-scan mapping of R_2* at high B_0," *Magnetic Resonance in Medicine*, vol. 48, no. 5, pp. 867–876, 2002.

[289] A. M. Peters, M. J. Brookes, F. G. Hoogenraad, P. A. Gowland, S. T. Francis, P. G. Morris, and R. Bowtell, "T_2^* measurements in human brain at 1.5, 3 and 7 T," *Magnetic Resonance Imaging*, vol. 25, no. 6, pp. 748–753, 2007.

[290] R. R. Ernst and W. A. Anderson, "Application of fourier transform spectroscopy to magnetic resonance," *Review of Scientific Instruments*, vol. 37, no. 1, pp. 93–102, 1966.

[291] E. P. Duff, L. A. Johnston, J. Xiong, P. T. Fox, I. Mareels, and G. F. Egan, "The power of spectral density analysis for mapping endogenous BOLD signal fluctuations," *Human Brain Mapping*, vol. 29, no. 7, pp. 778–790, 2008.

[292] A. Barnes, E. T. Bullmore, and J. Suckling, "Endogenous human brain dynamics recover slowly following cognitive effort," *PLoS ONE*, vol. 4, no. 8, p. e6626, 2009.

[293] T. Van der Doef, F. O. Zelaya, S. Lee, A. Pauls, and M. Mehta, "Methylphenidate causes changes in the amplitude and latency of the breathhold response function," in *Proceedings of the International Society for Magnetic Resonance in Medicine*, Stockholm, 2010, p. 3520.

[294] A. Kastrup, G. Kruger, T. Neumann-Haefelin, and M. E. Moseley, "Assessment of cerebrovascular reactivity with functional magnetic resonance imaging: comparison of CO_2 and breath holding," *Magnetic Resonance Imaging*, vol. 19, no. 1, pp. 13–20, 2001.

[295] J. L. Marchini and B. D. Ripley, "A New Statistical Approach to Detecting Significant Activation in Functional MRI," *NeuroImage*, vol. 12, no. 4, pp. 366–380, 2000.

[296] M. Jenkinson and S. Smith, "A global optimisation method for robust affine registration of brain images," *Medical Image Analysis*, vol. 5, no. 2, pp. 143–156, 2001.

[297] K. R. A. Van Dijk, T. Hedden, A. Venkataraman, K. C. Evans, S. W. Lazar, and R. L. Buckner, "Intrinsic functional connectivity as a tool for human connectomics: Theory, properties, and optimization," *J Neurophysiol*, vol. 103, no. 1, pp. 297–321, 2010.

[298] A. Weissenbacher, C. Kasess, F. Gerstl, R. Lanzenberger, E. Moser, and C. Windischberger, "Correlations and anticorrelations in resting-state functional connectivity MRI: A quantitative comparison of preprocessing strategies," *NeuroImage*, vol. 47, no. 4, pp. 1408–1416, 2009.

[299] M. Dalwani, D. Cordes, J. R. Tregellas, I. Hamza, and Y. P. P. Du, "Improved resting-state mapping of the default mode activity in OFC using volume-selective z-shimming," in *OHBM*, Beijing, China, 2012.

[300] K. Shmueli, D. L. Thomas, and R. Ordidge, "Signal drop-out reduction in gradient echo imaging with a hyperbolic secant excitation pulse - an evaluation using an anthropomorphic head phantom," in *Proceedings of the International Society for Magnetic Resonance in Medicine*, Seattle, 2006, p. 2385.

[301] J.-Y. Park and M. Garwood, "Imaging pseudo-echoes produced by a frequency-swept pulse," in *Proceedings of the International Society for Magnetic Resonance in Medicine*, Kyoto, 2004, p. 534.

[302] J.-Y. Park, L. DelaBarre, and M. Garwood, "Improved gradient-echo 3D magnetic resonance imaging using pseudo-echoes created by frequency-swept pulses," *Magnetic Resonance in Medicine*, vol. 55, no. 4, pp. 848–857, 2006.

[303] J.-Y. Park and M. Garwood, "Spin-echo MRI using $\pi/2$ and π hyperbolic secant pulses," *Magnetic Resonance in Medicine*, vol. 61, no. 1, pp. 175–187, 2009.

[304] M. Fernandez-Seara and F. Wehrli, "Postprocessing technique to correct for background gradients in image-based R_2^* measurements," *Magnetic Resonance in Medicine*, vol. 44, no. 3, pp. 358–366, 2000.

[305] H. Dahnke and T. Schaeffter, "Limits of detection of SPIO at 3.0 T using T_2^* relaxometry," *Magnetic Resonance in Medicine*, vol. 53, no. 5, pp. 1202–1206, 2005.

[306] F. T. Hioe, "Solution of Bloch equations involving amplitude and frequency modulations," *Physical Review A*, vol. 30, no. 4, pp. 2100–2103, 1984.

[307] M. S. Silver, R. I. Joseph, and D. I. Hoult, "Selective spin inversion in nuclear magnetic resonance and coherent optics through an exact solution of the Bloch-Riccati equation," *Physical Review A*, vol. 31, no. 4, pp. 2753–2755, 1985.

[308] K. Shmueli, D. L. Thomas, and R. Ordidge, "Slice-selective spin-echo formation using hyperbolic secant RF pulses," in *Proceedings of the International Society for Magnetic Resonance in Medicine*, Toronto, 2003, p. 961.

[309] J. M. Warnking and G. B. Pike, "Bandwidth-modulated adiabatic RF pulses for uniform selective saturation and inversion," *Magnetic Resonance in Medicine*, vol. 52, no. 5, pp. 1190–1199, 2004.

[310] T. L. Davis, K. K. Kwong, R. M. Weisskoff, and B. R. Rosen, "Calibrated functional MRI: Mapping the dynamics of oxidative metabolism," *Proceedings of the National Academy of Sciences of the United States of America*, vol. 95, no. 4, pp. 1834–1839, 1998.